UNIVERSITÀ DEGLI STUDI DI TRIESTE

XXXI CICLO DEL DOTTORATO DI RICERCA IN NANOTECNOLOGIE

Experimental modeling of nanostructured and single metal atom supported catalysts at close-to-ambient conditions.

Settore scientifico-disciplinare: **FIS 03**

DOTTORANDO / A
MANUEL CORVA

COORDINATORE
PROF. LUCIA PASQUATO

SUPERVISORE DI TESI
PROF. ERIK VESSELLI

ANNO ACCADEMICO 2017/2018

Abstract

This Thesis work deals with the growth and characterization of model nanostructured surface systems in ultra-high vacuum environment (UHV, $< 10^{-9}$ mbar) and with their evolution at near ambient pressure (NAP, 0.1 - 100 mbar) conditions. The investigations are performed with the aid of specific *in situ* techniques in order to probe the structural, electronic, chemical and catalytic properties of the models.

The latter span from ordered lattices of metal nanoparticles to 2D metallorganic crystals, where stabilized mono-metallic centers act as the active cores. These systems, based on single metal atom centers, represent the main topic of this manuscript and they will be referred to as Single Metal Atom Catalysts (SMAC).

Non-linear optical infrared-visible sum frequency generation spectroscopy (IR-Vis SFG) is the main technique that I employed, as it allows to investigate the vibrational modes of molecules adsorbed on a surface from UHV to near ambient pressures. Scanning tunneling microscopy and X-Ray photoemission spectroscopy measurements corroborate the results and were acquired in the framework of several collaborations. I received fundamental scientific contributions from different theoretical groups, and their *ab initio* numerical simulations, discussed in the manuscript, were exploited for a better interpretation of the experimental results.

The discussion of the scientific findings will first focus on the evolution of graphene-supported Pt nanoclusters in CO atmosphere, varying both surface temperature and CO pressure to test the stability of the nanostructures. As degradation of this nanosystem occurs at realistic reaction conditions, the attention was shifted to the design and synthesis of model SMAC systems, where the single metal atom is stabilized in a metallorganic cage, thus preventing structural degradation. On proper substrates, metalated tetrapyrrolic molecules as Metal-Phthalocyanines (MPcs) and Porphyrins (MPs) self-assemble in ordered superstructures while exposing their mono-metallic cores. The resulting bidimensional ordered lattice of stabilized single metal atoms resembles several single-metal atom centers found in Nature. As these systems naturally work at ambient conditions, their biomimetic analogues may offer promising perspectives in the field of heterogeneous catalysis.
A first, prototype SMAC model system consisted of a single layer of Nickel tetraphenyl porphyrins (Ni-TPPs) deposited on the Cu(100) surface. We find evidence that, following to NO exposure, an oxygen-containing ligand is stabilized at the Ni sites already at UHV conditions and at room temperature. In a first picture we propose the assignment of the observed spectroscopic features to a hyponitrite moiety (N_2O_2). The interaction with NO is observed only on the NiTPP monolayer interacting with the underlying copper surface, showing that the substrate plays a major role, governing the properties of the nanostructured system through trans-effects associated with an intense surface-to-molecule charge transfer.
A single Iron Phthalocyanine (FePc) layer was instead considered for a model carbonylation reaction. The metalorganic molecules were deposited both on a single foil of graphene, grown on the Ir(111) surface (FePc/GR), and on an alumina ultra-thin film, grown on the $Ni_3Al(111)$

surface (FePc/alumina). In both cases, we exploited CO adsorption to probe the molecular active sites.
On the FePc/GR layer, IR-Vis SFG evidenced unexpected CO stretching modes in 10^0-10^1 mbar CO at 300 K. We ascribe the observed vibrational features to the production of long-lived molecular excitons (induced by the visible radiation). The long lifetime of these excitons and their efficient production through singlet-fission mechanisms represent intriguing findings for innovative organic devices for solar energy conversion. We also investigated the interaction of the same system with gas-phase CO_2 We found that oxidation of the underlying graphene support yields the control of the charge transfer to the active sites, thus reducing the threshold pressure for CO_2 adsorption and activation at 300 K by at least two orders of magnitude. As CO_2 catalytic conversion is hindered by its low reactivity, enhancing its adsorption to metal sites is crucial in the framework of the efficient conversion of this waste gas to valuable chemicals. A practical route to alter the mesoscopic properties of the single metal atom centers has been found, and in parallel we proved a novel graphene oxidation route employing molecular oxygen at near ambient pressure.
Concerning instead the FePc/alumina film, we demonstrated that decoration by Cu nanoclusters tunes the surface potential energy, inducing a different symmetry in the molecular overlayer lattice, scarcely affecting the reactivity of the metallic sites, as proved by the vibrational modes of adsorbed CO molecules. Thus, we succeeded in tailoring the motif of a self-assembled metallorganic layer while preserving its active sites properties.

Contents

Chapter 1

Introduction

In the quest for understanding and manipulating surface properties, nano-architected surfaces offer high prospects. They can act as the testing ground to improve existing technological materials, but also as the starting point for the development of innovative solutions in a variety of fields. Through this manuscript, we will discuss about the potentialities of nanostructured model surfaces and how they can be synthesized in controlled ultra-high vacuum environment (UHV). Moreover, we will infer how to access their properties with atomic-level detail even outside the controlled, but limiting, UHV environment.

Several examples and evidence will be presented about the subtle interactions, conversions, and evolution that may take place at a solid-gas interface. As these themes are deeply connected to the fascinating field of heterogeneous catalysis, we will exploit a brief discussion about catalysis as the perfect starting point to introduce the role of nanostructures. However, we have to mind the reader that this work will follow a strict surface physics approach and focus on the nano-architected surfaces, not on the (eventual) specific reaction.

1.1 Understanding surfaces through model systems: the case of heterogeneous catalysts.

Catalysis is defined as the increase in the rate of a chemical reaction due to the participation of an external substance, the catalyst, and has been known and studied for at least two centuries.[1] In the last decades, catalysis has become of utmost importance to the worldwide economy.
It allows to convert raw (and even waste) material into valuable chemicals and fuels, in an economical, efficient, and non polluting manner.[2] The industrial applications are countless, from pharmaceutical to chemical, petrochemical, and even agrarian industry.[2–5] Catalysis is relevant in many high-impact activities: for example, it plays a central role in the treatment of exhaust gases in engines,[6,7] in the cleaning mechanism by laundry detergents,[8,9] in the production of food[10] and fertilizers.[11] Furthermore, catalysis is actually a crucial process for life itself, since many biological mechanisms are enhanced by enzymes, that are very specific catalysts found in Nature.[1,12]

From a technical point of view, a catalyst is an active chemical spectator, taking part into a reaction without being consumed.[13] To start a specific process, in fact, some chemical reactions must overcome a potential barrier, even though the reaction itself is energetically favored (i.e. the total free energy of the products is lower than the total free energy of the reactants). This potential barrier is usually described in terms of the activation energy, that is the energy that must be provided to the system in order to allow the reaction to take place. The role of a catalyst is to speed up the reaction by lowering the height of the activation

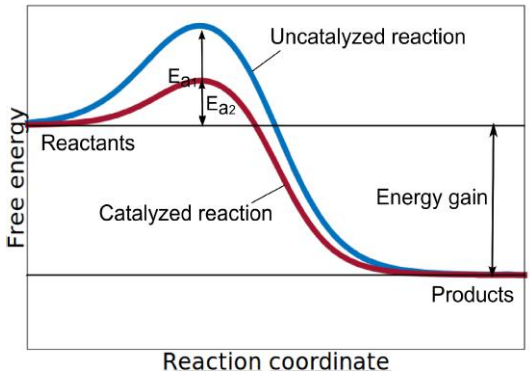

Figure 1.1: A schematic representation of the action of a catalyst. Image from Ferrari *et al.*.[16]

barrier. This is therefore accomplished by changing the kinetics of the process, i.e. the temporal scale of the reaction, while both the thermodynamics and the equilibrium states are left untouched. In Fig. 1.1 a schematic representation of the concept of catalysis is given: the blue line shows the uncatalyzed reaction, the red line the catalyzed one, characterized by a lower activation energy.[14,15] Nonetheless, the goal of a catalyst is not to simply accelerate whatever reaction, but to perform this task with high selectivity. It has to be sensitive to the chemical composition of the reactants, and rule out undesired side-reactions. Even those which could be the most energetically favored.

Catalysts can be divided in two general classes: homogeneous catalysts, where the reactants and the catalysts are in the same phase, or heterogeneous catalysts, where the reactants and the catalysts are in different phases, usually solid/liquid or solid/gas.

1.1.1 Heterogeneous catalysts, model surfaces and the *material* gap.

With respect to the homogenoeus class, heterogeneous catalysis is the most widespread (it has been estimated that over 90% of chemical processes are performed on heterogeneous catalysts[17]) and nowadays its study is a well established branch of surface science. The main advantage with respect to homogeneous catalysts is that solid catalysts can be easily separated from the reactants and products of the overall reaction. In addition, heterogeneous catalysts usually endure extreme working conditions better than their homogeneous analogues, allowing for longer lifetimes before deactivation.[18] Moreover, the solid surface may allow the deposition and immobilization of different catalytic substances, ensuring that they are not dispersed within the reaction products. This diversification opens a vast playground, eventually allowing to reach the desired selectivity (see Fig. 1.2).

Despite their wide range of applications, industrial catalysts are not trivial to characterize and represent a formidable challenge. Heterogeneous catalysts employed in industrial reactors are typically polycrystalline, and in order to achieve high surface areas they usually contain particles with sizes in the nanometer scale (see Fig. 1.3).[2] This introduces a variety of different surface sites, and the difficulty of identifying the active centers (i.e. the specific positions on the surface where the reactants effectively interact with the catalyst) of the reaction of interest has not to be underestimated. On top of this, the catalytic activity of a surface may involve several side-reactions taking place only at the surface, therefore not detectable among the reactants and products present in the reactor (the closed environment in which the reaction takes place under controlled conditions).[19]
In order to precisely deconvolve the information, and achieve a complete and reliable characterization of the catalytic activity, accurate **model systems** have to be investigated. Their

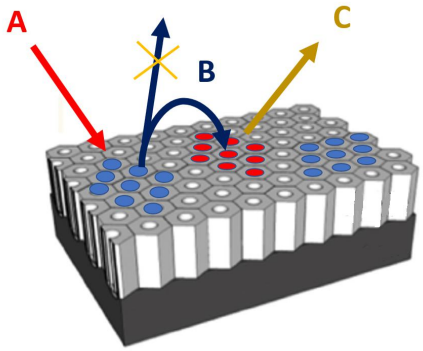

Figure 1.2: A cartoon representing how selectivity can be induced by dispersing non-equivalent catalytic materials on a supporting surface. The unwanted intermediate B is converted into the desired chemical C. Modified image from Mijangos *et al.*.[20]

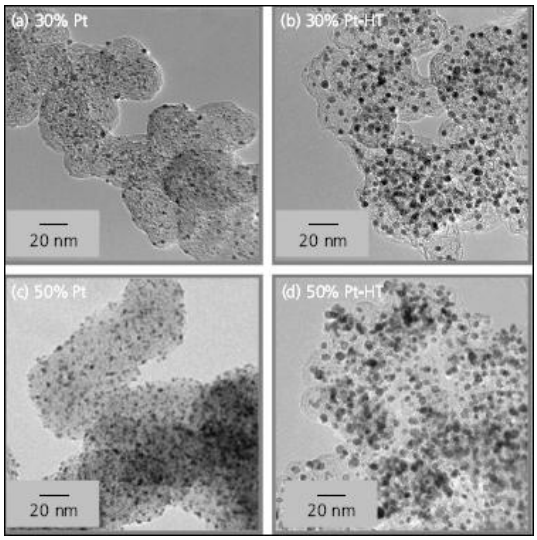

Figure 1.3: Transmission electron microscopy (TEM) images of a platinum catalyst with 30% or 50% metal loading (top-bottom), before and after heat treatment (HT) (left-right). Image from Matsutani *et al.*.[21]

role is fundamental: knowledge about the details of a reaction can yield the design of new, high-efficient systems, where highly desirable requirements such as efficiency, stability, selectivity and cheapness are maximized.[2] In the 1960s, with the advent of surface science techniques, the first model systems were studied: simple reactions on single-crystal metal surfaces.[22] In surface physics studies, highly controlled model surfaces are prepared and characterized in UHV conditions ($\sim 1 \times 10^{-10}$ mbar pressure) down to the single-atom level. The aim is to control and access the elementary and fundamental interactions yielding the macroscopic catalytic behavior of a solid surface. However, a long way had yet to be paved towards the understanding of the role of nanometric structures at real surfaces. Originally, attention was focused on the structure of low-Miller-index clean single-crystal surfaces and their interaction with gas molecules. However, single crystal model surfaces are not able to mimic the properties of a realistic solid surface, characterized by micro and nanometric structures: this represents the so called *material gap*. Thus, to bridge this gap new degrees of complexity were introduced in a controlled way: stepped surfaces, bi-metallic and oxide single crystals, and ultimately supported nanoparticles. The latter may represent the best modelling

of the surface of a real catalyst, broadly presenting features in the nanometer scale.[23] However, with complexity, new issues arose.

1.1.2 Reducing the dimensionality of surface structures: a path towards single metal atoms.

It is nowadays well-known that the activity of a solid interface dramatically depends on the size of the structures it exhibits: typically, the specific activity increases with the surface-to-volume ratio(as depicted in Fig. 1.4).[24,25] Adding to the goal of mimicking realistic surfaces, this led to a continuous effort towards the synthesis and investigation of nanostructures.

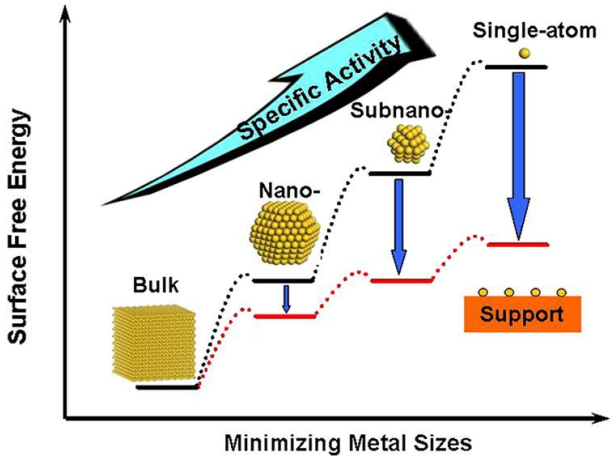

Figure 1.4: Schematic representation of the effect of the catalyst's dimension on its free energy and activity. Image from Yang *et al.*.[24]

Reducing the dimensionality of the active media has two main effects: firstly, the decrease in the atomic coordination number leads to a higher number of unsaturated chemical bonds, thus explaining the increase in chemical activity. But then, quantum effects become not-negligible as approaching nanometer scales. Discretization of the energy levels must be taken into account, up to the eventual opening of HOMO-LUMO gaps even for metal aggregates. This effect can drastically influence the overall properties of the material.[22,26] As an example, gold, that is usually chemically inert, shows an extraordinary reactivity when downsized to the nanometer scale.[27,28]

Between nanometric systems, supported metal nanoclusters are widely investigated. They indeed represent a model system well reproducing heterogeneous catalysts used in industrial process, generally constituted by active-metal nanoparticles dispersed onto a supporting, high surface-area matrix (see Fig. 1.3). However, nanoclusters attracted undisputed attention also in several different fields and applications, from optics to medicine, from energy production to electronics. This results from their unique properties, stemming from their finite small size. As a matter of fact, in the case of nanoparticles not only do their structure, electronic, magnetic, and optical properties change with size, but also new properties arise as a result of quantization effects, at variance with their bulk counterparts.[29,30] In the size regime below 2 nm quantum properties dominate, and nanoclusters of that size exhibit discrete electronic levels, like atoms do (see Fig. 1.5).[31,32]

Surfaces obtained through a dispersion of metal nanoclusters immobilized over a substrate have the advantage of being industrially reproducible while still being accessible to surface science techniques.[33] Nevertheless, most nanoclusters present a broad size distribution, and irregular morphology. This yields multiple active sites with different performances, which can

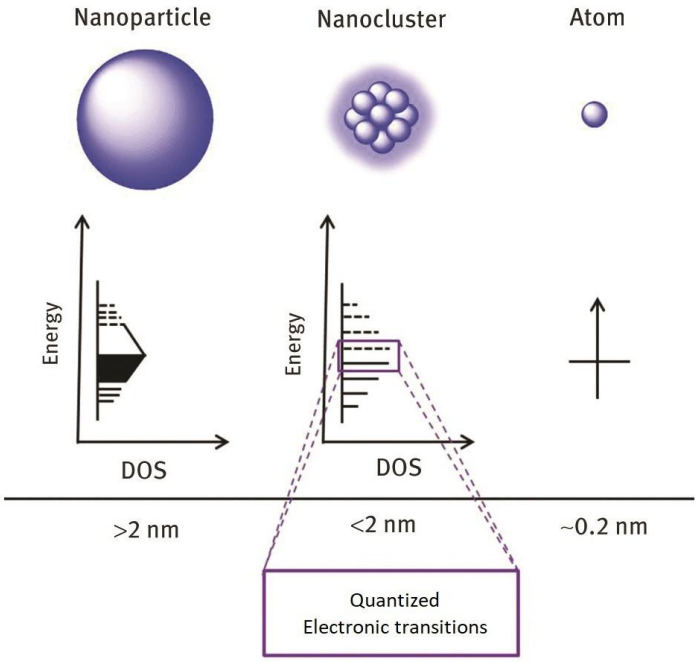

Figure 1.5: Schematic representation of the formation of discrete electronic energy levels on the way from bulk to atoms. Image from Das *et al.*.[32]

hardly be efficiently controlled. This heterogeneity might affect the properties of the catalysts, introducing unwanted side reactions.[24] But most of all, the atomic-level understanding of such a system becomes, in most of the cases, unaffordable.
To overcome this limit, a suitable support is necessary to synthesize cluster-based model surfaces. A common problem in cluster catalysis research is that samples are usually characterized by very low cluster densities to avoid coalescence of randomly arranged clusters. An ideal system would instead consist of a regular array (of large extension) of equally sized and spaced clusters, found in an identical environment; an example can be seen in Fig. 1.6. Similar cluster superlattices would allow to access and tune the single clusters properties, determining a well-defined collective response from the additive contributions of all the almost identical clusters (as might be of interest for magnetic applications or in catalysis) or obtaining a collective coherent response (as in optics). The support can not only stabilize, but also modify geometric and electronic properties of metal particles, and the interaction with the substrate becomes more and more important while the cluster size decreases. Among the most common supports, major interest is deserved by oxides surfaces, ultrathin oxide films on metals, and carbon allotropes (amorphous carbon, graphite, carbon nanotubes, and graphene) as novel and promising, highly tunable materials (we will discuss specific examples in the following of this manuscript).

Intriguingly, it is possible to further downsize the dimensionality of the metallic active media, reaching the ultimate limit: single metal atoms. If stabilization of such entities is achieved, a Single Metal Atom Catalyst (SMAC) can be synthesized.[24] SMACs offer a very specific activity while employing the minimum quantity of (costly) material: uniform single atom dispersions allow to achieve high selectivity, since all sites have the same physical and chemical properties. Despite being a recent tool in the field of catalysis, many applications have already been found for SMACs, including oxidation, hydrogenation, and carbonylation

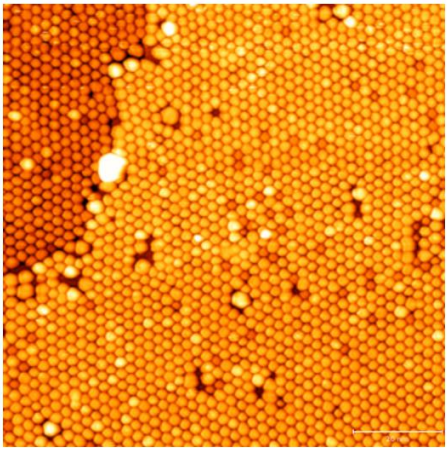

Figure 1.6: Scanning Tunnelling Microscopy (STM) image of a Pt cluster superlattice grown on Gr/Ir(111), characterized by a high degree of order. Image size: 100×100 nm^2; V_{bias} = 1 V, I = 30 pA; Pt coverage: 0.74 ML with respect to underlying Ir(111).

reactions.[24,34]

Decreasing the coordination of catalytic atoms, however, also has some downsides. As for nanoclusters, stabilization is a major issue (smaller particles form aggregates via surface diffusion due to the enhancing of the particles' surface free energy). In order to prevent aggregation, SMACs can be stabilized by other structures. A first possibility, straightforwardly from the nanoclusters case, is to deposit single atoms on specific substrates (metal oxides, graphene, porous materials) presenting well-defined anchoring sites. The anchoring must be neither too strong (or deactivation of the single atoms might be encountered) nor too weak (or diffusion and coalescence might take place at working conditions). Unfortunately, this approach encounters severe applicative limitations. A limited number of supporting materials is available, and usually the same support is not adequate for different metals. This limits the choice of the active materials. Moreover, even in this case, control over the single atoms requires sophisticated techniques, not suitable for practical industrial applications.[24]
Another interesting approach would consist in employing chemical methods, in which larger aggregates contain and stabilize single-metal atoms in their structure. Through surface reactions, these aggregates could be able to anchor the metal onto the substrate.[24] However, the choice of the stabilizing cages is critical, as the single metal atoms have to still be active in the obtained arrays.

Ultimately, a path to access the synthesis of SMAC model systems is indeed available. In fact, a viable solution could be provided by Nature. Following a biomimetic approach, it is possible to self-assemble metal-organic frameworks (MOFs) exposing single metallic atom embedded in supporting organic cages.

1.2 Biomimesis and Single Metal Atom Catalysts (SMAC)

Biomimesis embraces the concept of translating biological mechanisms and functions into applications for countless technological fields, from engineering to architecture, from chemistry to electronics.[35–37] Nature has evolved over billion of years, optimizing high-performing processes. The core idea of biomimesis is then that these high-efficiency mechanisms may inspire solutions to modern puzzles.[38–41]

In Nature, structures are commonly built following bottom-up, self-assembly processes, where small (nanometric) building blocks spontaneously interact and form larger, well-defined

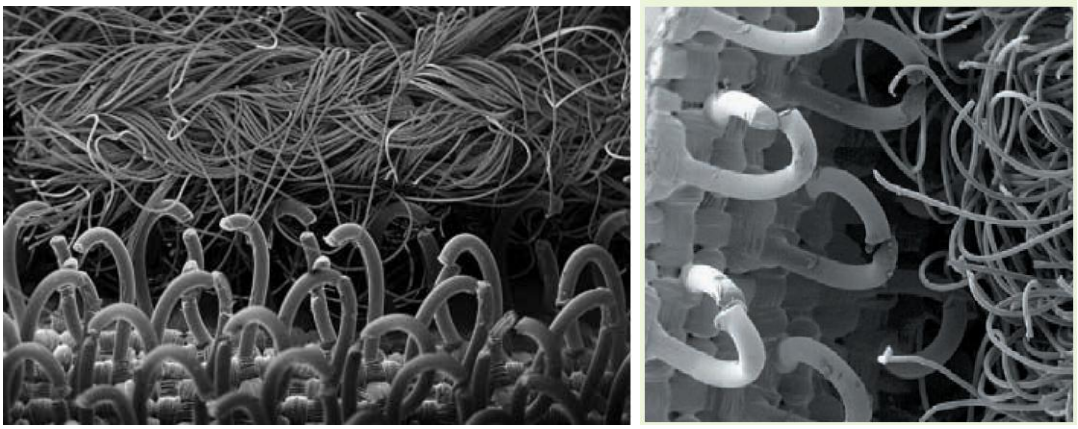

(a) (b)

Figure 1.7: (a) Scanning electron microscopy image of cocklebur hooks and loops that inspired the velcro design (shown in b). 370 μm view. Images from Brushan *et al.*.[37]

structures.[42] Therefore, biomimetic concepts could ideally produce intriguing results in nanotechnologies: while controlling surfaces at the nanoscale is far from trivial (as we discussed above), a self-assembly process can yield structures with nanometric ordering but even on the mesoscopic scale (with evident appeal for technological applications).
Nature offers several examples of single metal atom containing systems. In acetogenic bacteria, the CO dehydrogenase enzyme (CODH) is involved in the efficient conversion between carbon oxides (CO, CO_2). In particular, the CO_2 to CO conversion is promoted and exploited as a source of carbon for the organism's growth. The CODH enzyme presents five metal-containing clusters, and one of them shows a single Ni atom (shown in Fig. 1.8, left).[43] On the basis of Fourier transform infrared (FTIR) studies, it has been proposed that this is the active site for the reduction of the carbon dioxide molecule.[12,43] Other examples are hemoglobin and myoglobin, proteins developed by vertebrates to sustain aerobic life.[44] Hemoglobin efficiently carries oxygen from the lungs to the tissues and contributes to the transport of carbon dioxide back to the lungs. Myoglobin, instead, is located in muscles and provides a reserve supply of oxygen.[44] Their ability to bind oxygen depends on a specific prosthetic group: the heme group, consisting of an organic matrix stabilizing a central iron atom (see Fig. 1.8, center).[44] Moreover, we have to mention that the chlorophyll A group, a photoreceptor present in most green plants, possesses a single magnesium atom bound to an organic square structure (see Fig. 1.8, right).

A selected characteristic links these macromolecules, employed in a variety of reactions and organisms: a natural molecular cage stabilizes a single metal atom, which acts as the actual reactivity center. It is evident that single metal atoms and MOFs are able not only to regulate chemical conversion, but also offer other intriguing prospects. Finally, it is important to stress that, as an example in the case of catalysis, room temperature and near ambient pressures represent almost ideal working conditions, for affordability and stability reasons. This makes biomimetic metallorganic molecules even more appealing, since most of biological processes naturally developed in these conditions.

Indeed, Nature presents numbers of active centers incorporated into larger structures, acting both as supports and stabilizers for the centers themselves. Moreover, the organic back-bone may exert regulatory functions and handles the interaction with other molecules.[12] Another consequence of the presence of this external structure adds to the sintering prevention: when such macromolecules are deposited on a substrate, the organic skeleton may open

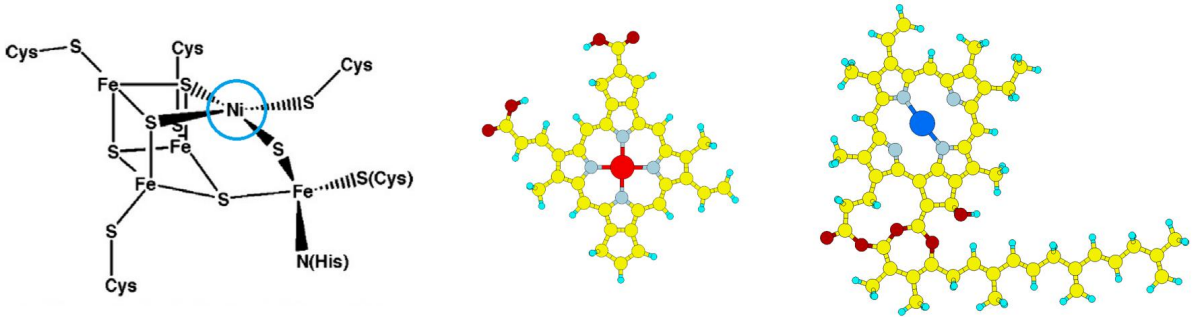

Figure 1.8: From left to right, a schematic representation of the Ni-containing cluster of the CODH enzyme (image from Ragsdale *et al.*[12]), of the heme group and of the chlorophyll A structure (images from Ferrari *et al.*[16]). Colour scheme: yellow is C, cyan is H, gray is N, red is O, blue is Mg and scarlet is Fe.

up to the possibility of assembling in ordered structures. In these cases, if the confined single atom shows the desired properties, ordered arrays of equivalent active centers can be assembled, as desired. Therefore, the choice of the proper metallorganic framework and support is of utmost importance for the synthesis of biomimetic ordered SMAC-arrays, and will be discussed in the following chapter when introducing the specific scientific investigations.

As one of the main targets of the investigation presented in this thesis will concern the interaction of the synthesized nanostructured surfaces with gaseous phases, we will spend some words about the interaction between natural occurring single metal based biomolecules and simple reactants.

1.3 The interaction of small molecules with single metal centers.

The *heme* group is a perfect example of the multiple tasks that can be performed by metal-organic structures containing single metal atoms.
It is in fact at the core of several biological processes, first of all in the determination of the oxygen transport properties of hemoglobin in aerobic organisms. In fact, it is at the iron atoms of the heme groups that oxygen reversibly binds and therefore can be efficiently delivered from the lungs to the tissues (see Fig. 1.9c).[44]

Moreover, the heme group is found also in the cytochrome-c (cyt c, see Fig. 1.9a), a hemeprotein present in every aerobic organism. It is involved in biological processes entailing an electron transfer associated with the reversible variation of its metallic ion oxidation state:

$$\mathrm{Fe(III)} \rightleftharpoons \mathrm{e^-} + \mathrm{Fe(II)}. \tag{1.1}$$

Apart from its role in the electron transfer in the cellular respiratory chain, the cyt c was demonstrated to have an antioxidant function, favouring elimination of byproducts of the normal aerobic metabolism that are harmful for the cell, as $O_2{}^-$ and H_2O_2. In its oxidized form Fe(III) it reacts with $O_2{}^-$ with production of O_2, in its reduced form Fe(II) it reacts with H_2O_2 producing H_2O.

Another fascinating system is the family of the cytochrome P450, in particular the nitric oxide reductase (P450nor) class (see Fig. 1.9b). These enzymes functionally differ from the rest of the P450s, as they play an important role in the denitrification processes in fungi. In the specific, the NO reductase converts the highly toxic NO to less dangerous N_2O taking

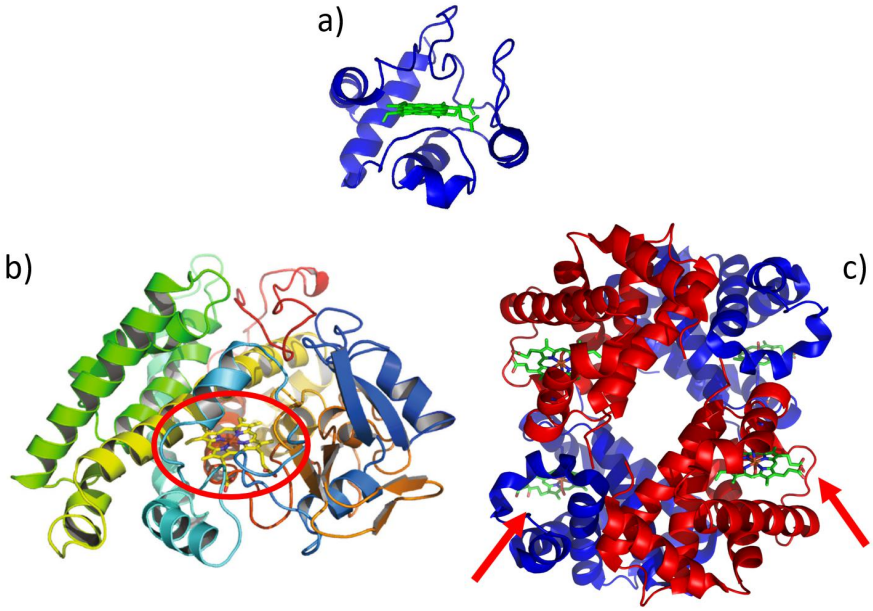

Figure 1.9: Cartoons representing (a) the cytochrome c (the protein structure is reported in blue, the heme group in green; image from Zuliani *et al.*[45]), (b) the cytochrome P450nor2 (image from Li *et al.*[46]), and (c) the hemoglobin (four heme groups are present, image from Berg *et al.*[44]).

advantage of the reduced Nicotinamide Adenine Dinucleotide (NADH) or the Nicotinamide Adenine Dinucleotide Phosphate (NADPH) molecules as direct electron donors.[46]

In this manuscript, we will focus on prototype reactions involving the adsorption and conversion of carbon and nitrogen oxides (CO, NO, CO_2). Their chemistry is broadly investigated, mostly due to their role in the exhaust treatment of post-combustion processes.[6,7,47] However, biological structures have evolved to operate at biological conditions. Even though this represents a positive aspect concerning their possible applicabilities, it is far from a trivial task to adequately characterize them at the atomic-level detail in close-to-ambient environment.

To clarify this issue, let us consider CO adsorption on metal phthalocyanines (MPcs), planar molecules resembling the heme group. CO adsorption represents a prototype reaction step due to its stoichiometric simplicity,[48] and allows to investigate the active sites of a surface. Moreover, it continues to attract great attention, as for example in the attempt to alleviate the CO poisoning effect on methanol and hydrogen fuel cell electrocatalysts.[49] Several measurements were performed to investigate carbon monoxide interaction with metallized porphyrins and phthalocyanines.[50] However, even though the iron atom present in the heme group can interact with CO 200-fold stronger than with oxygen,[44] only recently new literature appeared about the carbonylation of metal-Pcs at temperatures higher than ∼140 K in UHV environment.[51] This is due to the low adsorption energy of the CO molecules on MPcs: carbon monoxide immediately desorbs from the surface if temperature is not sufficiently low. However, by raising the CO partial pressure it is possible to increase the rate of adsorption, balancing the desorption process. Therefore, at higher pressure a non-negligible average population of adsorbed CO molecules can be measured (further details about the adsorption and desorption processes are reported in Appendix 6.2).

A significant message arises: the properties of bio-inspired SMACs systems may be unveiled only by leaving the ultra-high vacuum of classic surface-science approaches and reaching the near ambient pressure regime. This adds to an already existing challenge involving

surface-science investigations, and generally referred to as the issue of the *pressure gap*.

1.4 The pressure gap: a quest for *in situ* and *operando* approaches.

As we mentioned, the first step to accurately depict the properties of applicative surfaces is the UHV synthesis of model systems realistically reproducing their features. In addition, innovative (maybe bio-inspired) model structures may suggest new strategies to solve existing technological issues or lead to the discovery of new fascinating properties. However, it has to be kept in mind the strong relationship between a surface and the environmental parameters, first of all pressure and temperature. In particular, profound modifications are expected while leaving the controlled UHV conditions and entering the realm of near ambient pressure ($10^{-2} - 10^{3}$mbar). Higher pressures yield a significant contribution of the gas-phase chemical potential. Two examples are provided by methanol adsorption on Pd(111) and CO adsorption on Ni(110). Upon methanol dosing, the molecule's C-O bond is efficiently broken on palladium at 5 mbar while at UHV conditions there is no evidence of C-O cleaving.[52] In the second experiment, at 400 K (111)-microfacets are formed on the nickel (110) surface exposed to 2 bar CO pressure, while at $\sim 10^{-7}$ mbar the Ni(110) surface is intact.[53] It is clear that many orders of magnitude of difference in pressure create a fundamental uncertainty in how far the phenomena observed in vacuum can be transferred to other environments.
In the quest for depicting surface properties at atomic-level detail, surface evolution can not be neglected and has to be tackled in situ and *operando*, meaning at the conditions of interest and as the evolution is proceeding.

Near-ambient pressure investigations The application of the considerations developed hitherto to the investigation of the catalytic properties of a surface results in the following: a model catalyst must be placed in ideal reactors and investigated with continuity from UHV to mild but realistic pressure conditions. However, these conditions represent a challenge for most conventional surface physics techniques. This is usually referred to as the *pressure gap* of surface science: the lack of experimental techniques that offers atom-detailed information outside UHV.

High pressure chambers, experimental setups, and investigation techniques are constantly improved in order to fill the void in the investigation range. In this framework, the development of experimental setups allows nowadays to perform Scanning Tunneling Mycroscopy (STM), Transmission Electron Microscopy (TEM), and X-Ray Photoemission Spectroscopy in the near ambient pressure regimes ($\sim$ 1 mbar), and new surface-sensitive techniques allow to directly investigate surfaces in a broad range of parameters. Such is the case of Polarization-Modulation Infrared Reflection Adsorption Spectroscopy (PM-IRAS) and Infrared-Visible Sum Frequency Generation Vibrational Spectroscopy (IR-Vis SFG). IR-Vis SFG exploits non-linear optics and symmetry arguments in order to collect information only and directly from the interfaces, and the details will be presented thoroughly in this thesis work.

Chapter 2

Experimental methods

Our aim is first the sinthesys of nanostructured surfaces, then the characterization of their evolution due to the interaction with a gas mixture of known (simple) composition. In order to complete these tasks both conventional surface physics techniques and reliable near ambient pressure spectroscopies are employed. While the first allow to finely characterize the as-prepared nanometric features in UHV environment, NAP spectroscopies grant access to information pertaining the interaction of the nano-architected interfaces with gas phases.

In this chapter, the main experimental methods exploited in this thesis work are presented. We review the theoretical framework of the underlying physical processes for Infrared-Visible Sum Frequency Generation (IR-Vis SFG) and Near Ambient Pressure X-ray Photoemission Spectroscopy (NAP-XPS). Moreover, we discuss some details concerning the experimental setups.

Concerning additional techniques exploited to respond to specific questions pertaining single scientific cases, they will be briefly introduced in the corresponding Chapter.

2.1 IR-Vis SFG spectroscopy

A key step in understanding surface evolution at increasing environmental pressure is the identification of the adsorbed species. First of all, intriguingly for applications in heterogeneous catalysis, the detection of adsorbed molecules different from the reactants demonstrates a surface catalytic activity. Secondly, changes in the adsorption properties offer information of utmost interest, even in the case of simple adsorption/desorption processes (which could almost be intended as the simplest prototype reactions). As an example, surface reconstruction can be followed inspecting the evolution of the adsorption sites. In addition, changes in the adsorption pressure threshold (further details are presented in Appendix 6.2) may allow to determine if specific treatments of the surface are effective or not.
Concerning the adsorbates, either single atoms, molecules, or molecular moieties can be considered. A valuable tool to access them is vibrational spectroscopy, which allows the identification and characterization of the adsorbed molecular species by determining the vibrational modes of the system under analysis. However, techniques accessing vibrational information as Infrared Reflection Adsorption Spectroscopy (IRAS) and High Resolution Electron Energy Loss Spectroscopy (HREELS) are not always sufficient to characterize a heterogeneous catalysts. In fact, outside vacuum conditions the deconvolution of the surface-related signal (coming from the molecular moiety interacting with the surface and ultimately containing the information of interest) from contributions coming from the gas phase may not be straightforward.

Among all the available vibrational spectroscopies, Infrared-Visible Sum Frequency Genera-

tion (IR-Vis SFG) spectroscopy received increasing interest in the last decades.[54–56] Its appeal stems from its intrinsic surface specificity: the provided vibrational information pertains solely the species adsorbed at a surface. This property arises from symmetry arguments concerning the second order susceptibility, to which the emitted SFG signal is intimately connected (the details will be described below). As centrosimmetric homogeneous phases (gaseous, liquid or even solid) can't contribute to the SFG signal, the IR-Vis SFG technique can be ideally applied for the characterization of the vibrational modes of chemical species adsorbed at catalytic surfaces while the catalyst is in action (*operando*) in atmospheric pressure or even in liquid environment (*in situ*).

2.1.1 Theoretical background

The probe in IR-Vis SFG spectroscopy consists of two light beams at different frequencies interacting in a medium characterized by a second-order nonlinear susceptibility tensor $\chi^{(2)}$, and generating a wave at the sum of their frequencies $\omega_{SFG} = \omega_1 + \omega_2$. In order to acquire an SFG vibrational spectrum of molecules adsorbed onto a solid surface, two laser pulses are spatially and temporally overlapped at the sample termination. One input beam is in the visible range (ω_{VIS}), and the second beam in the mid-IR (ω_{IR}, see Fig. 2.1). In this description, the IR-beam frequency is tunable and when it is tuned through a vibrational resonance of the adsorbate it induces a vibrational transition from the ground to an excited state. The visible beam induces then a second transition to a higher-energy electronic virtual state. When the high-energy virtual state relaxes, a photon is generated at the frequency ω_{SFG} that corresponds to the sum of the frequencies of the incident optical fields, resulting in a signal in the visible region (see Fig. 2.1). By tuning the wavelength of the IR beam and monitoring the intensity of the SFG output, a vibrational (vibronic) spectrum of the surface is obtained.[57]

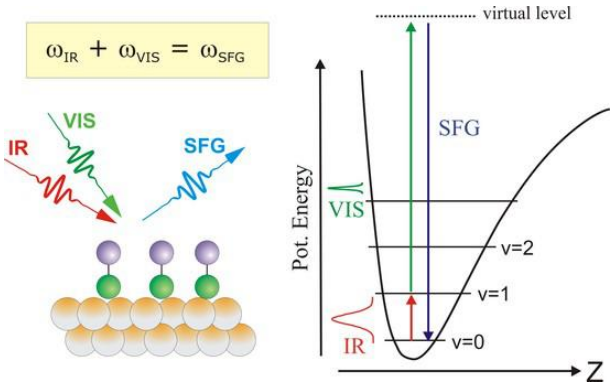

Figure 2.1: On the left side, two laser beams at IR and Vis frequency impinge on a surface and a signal at the sum of the frequencies is generated. On the right, schematic representation of a SFG transition.

SFG as a non-linear optical effect

The phenomenon at the basis of IR-Vis SFG spectroscopy, namely the Sum Frequency Generation, is a nonlinear optical effect that is observed when intense radiation interacts with matter. In the following, we will follow the presentation implemented by Lambert and assume the electric dipole approximation while describing the interaction of light with matter.[56] Within this approximation, magnetic and multipoles contributions are neglected. Moreover, as a further assumption the dipoles induced in matter are solely related to the applied macroscopic field, disregarding contributions stemming from neighbor induced dipoles.

In this framework, when light interacts with matter the associated electric field $\mathbf{E}$(t) influences the electron motion and induces an electric dipole moment proportional to the field amplitude. Its density (i.e. dipole per unit volume) is the polarization $\mathbf{P}$(t). In the case of conventional linear optics, i.e. when the amplitude of the radiation electric field is several order of magnitude weaker than the electric fields in matter (10^9 V/m), the induced polarization is approximated as a linear function of the electric field strength, usually described by the relationship

$$\boldsymbol{P}(t) \simeq \epsilon_0 \chi^{(1)} \boldsymbol{E}(t) \tag{2.1}$$

where $\chi^{(1)}$ is known as the linear susceptibility and $\epsilon_0 = 8.85 \times 10^{-12}$ C/Vm is the permittivity of free space.
In the case of pulsed laser radiation, the electric field amplitude may reach values even higher than 10^{12} V/m and the linear approximation holds no more. The optical response has to be described instead by Eq.[2.2], that is expressing the polarization as a full power series in the field strength E(t):

$$\begin{aligned} \boldsymbol{P}(t) &= \epsilon_0 \left[\chi^{(1)} \boldsymbol{E}(t) + \chi^{(2)} \boldsymbol{E}^2(t) + \chi^{(3)} \boldsymbol{E}^3(t) + \dots \right] \\ &= \boldsymbol{P}^{(1)}(t) + \boldsymbol{P}^{(2)}(t) + \boldsymbol{P}^{(3)}(t) + \dots \end{aligned} \tag{2.2}$$

The quantities $\chi^{(2)}$ and $\chi^{(3)}$ are known as second- and third-order nonlinear optical susceptibility tensor, respectively. Their components are considerably weaker than $\chi^{(1)}$, and therefore in the case of weak electric fields Eq.[2.1] is a good approximation of the induced polarization.

We shall now instead consider the term $\boldsymbol{P}^{(2)}(t)$ in Eq.[2.2], and refer to it as the second-order nonlinear polarization. While reporting the full derivation in Appendix 6.4, we state that, in the case of an impinging electric field originated by the superposition of two fields modulated at $\omega_1 = \omega_{IR}$ and $\omega_2 = \omega_{Vis}$, $\boldsymbol{P}^{(2)}(t)$ can be deconvoluted in 5 different components, each modulating at a different frequency.[56] Among these terms, we focus our attention on the sum frequency generated term $\boldsymbol{P}^{SFG}(t)$, that is the component which modulates at the sum frequency $\omega_{SFG} = \omega_{IR} + \omega_{Vis}$, and we report its i cartesian component in Eq.[2.3], where summation over the j,k indexes is implied.

$$P_i^{SFG}(t) = \frac{1}{2} \epsilon_0 \chi^{(2)}_{ijk} E_{1,j} E_{2,k} + c.c. \tag{2.3}$$

$\boldsymbol{P}^{SFG}(t)$ determines the production of the SFG radiation measured in the IR-Vis SFG experiments, which in turn is intimately related to the properties of the second order susceptibility tensor $\chi^{(2)}$.
Eq.[2.3] allows us to show that in centrosymmetric media (i.e. possessing a center of inversion) the $\chi^{(2)}$ nonlinear susceptibility must vanish, and therefore **centrosymmetric phases can never contribute to the production of the SFG signal**. Let us apply the parity symmetry to Eq.[2.3]: P_i, $E_{1,i}$, and $E_{2,j}$ change sign since the polarization and electric fields are polar vectors. Conversely $\chi^{(2)}_{ijk}$, possessing the same symmetry of the centrosymmetric material, is preserved under inversion. Hence we find:

$$\begin{aligned} -P_i^{SFG}(t) &= \frac{1}{2} \epsilon_0 \sum_{jk} \chi^{(2)}_{ijk} (-E_{1,j})(-E_{2,k}) + c.c. \\ &= \frac{1}{2} \epsilon_0 \sum_{jk} \chi^{(2)}_{ijk} E_{1,j} E_{2,k} + c.c. \end{aligned} \tag{2.4}$$

By comparing Eq.[2.3] and Eq.[2.4] we see that $\chi^{(2)}_{ijk} = 0$ must hold.
Although most of isotropic media possess inversion symmetry, the boundary between two

materials (e.g. a solid crystal and a gas) is inherently non-centrosymmetric and, therefore, sum-frequency active. The information acquired through SFG spectroscopy is thus intrinsically surface specific.
In a compact notation, the term $\boldsymbol{P}^{SFG}$ can be written as

$$\boldsymbol{P}^{SFG} = \epsilon_0 \chi^{(2)} \boldsymbol{E}_1 \boldsymbol{E}_2 \tag{2.5}$$

However, following what presented in Eq.[2.3] and Appendix [6.4], in the following we project this quantity onto its cartesian components (i.e. in the laboratory frame) in order to extract information about the non-linear susceptibility $\chi^{(2)}$ from the measured SFG.

IR-Vis SFG in reflection geometry

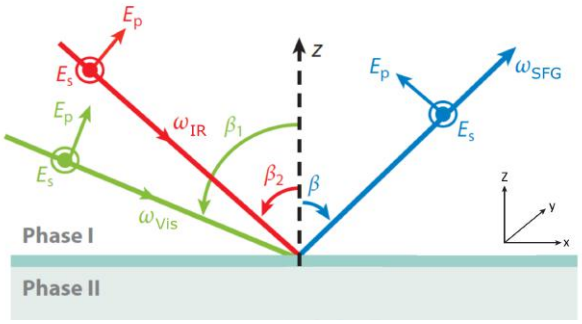

Figure 2.2: The plane of incidence is the page. Modified image from Wang *et al.*.[58]

In Fig. 2.1 and 2.2 the scheme of a typical IR-Vis SFG measurement in reflection geometry is reported. When describing an electromagnetic wave of generic frequency incident on a planar surface, it is possible to split its associated electric field $\boldsymbol{E}^I$ into components that are parallel (p) and perpendicular (s) to the plane of incidence. Considering the axis system and the beam geometries of Fig. 2.2, the magnitudes of the x, y and z components of the incident electric field, either visible or IR, are

$$E_x^I = \pm E_p^I \cos\beta \tag{2.6a}$$
$$E_y^I = E_s^I \tag{2.6b}$$
$$E_z^I = E_p^I \sin\beta \tag{2.6c}$$

where E_p and E_s are non negative and the positive sign in Eq.[2.6a] is employed if the projection of $\mathbf{E}_p$ lays along the positive x direction. The formalism now used follows that of Lambert *et al.*.[56] The total electric field present at the interface is the sum of the fields of the incident and reflected beams.

$$\begin{aligned} E_x &= E_x^I + E_x^R = E_x^I + r_p E_x^I = \pm(E_p^I \cos\beta - r_p E_p^I \cos\beta) \\ &= \pm E_p^I (1 - r_p)\cos\beta \\ E_y &= E_y^I + E_y^R = E_y^I + r_s E_y^I = E_s^I (1 + r_s) \\ E_z &= E_z^I + E_z^R = E_z^I + r_p E_z^I = E_p^I \sin\beta + r_p E_p^I \sin\beta \\ &= E_p^I (1 + r_p)\sin\beta \end{aligned} \qquad \begin{pmatrix} r_p = \dfrac{E_p^R}{E_p^I} \\ \\ r_s = \dfrac{E_s^R}{E_s^I} \end{pmatrix} \tag{2.7}$$

where r_s and r_p are the Fresnel amplitude coefficients for reflection in the s and p polarization, respectively, and the negative sign in the expression of $\mathrm{E_x}$ is related to the negative projection

of $\mathbf{E}_p^R$ along $\hat{x}$. Taking advantage of Equations[2.7], the generic SFG polarization in Eq.[2.3] may be now expressed in terms of the intensity of the incident beams (where the I superscript has been dropped for simplicity and $i = x, y,$ or z):

$$P_i^{SFG} = \frac{1}{2}\epsilon_0 \sum_{jk} \chi^{(2)}_{ijk} K_{Vis,j} E_{Vis,p/s} K_{IR,k} E_{IR,p/s} \qquad \begin{pmatrix} K_i = \pm(1 - r_p)\cos\beta \\ K_j = (1 + r_s) \\ K_k = (1 + r_p)\sin\beta \end{pmatrix} \tag{2.8}$$

The nonlinear induced polarization generates a surface bound SFG electric field. The resulting SFG light is emitted from the interface at a specific angle determined by the conservation of the wavevector components parallel to the interface, the so-called phase matching condition:

$$k_{Vis}\sin\beta_{Vis} + k_{IR}\sin\beta_{IR} = k_{SFG}\sin\beta_{SFG} \tag{2.9}$$

To relate the emitted SFG electric field $\mathbf{E}^{SFG}$ to the induced polarization and to take into account phase matching, nonlinear SFG Fresnel (complex) factors, or L factors, are employed:

$$E_i^{SFG} = L_i P_i^{SFG} \tag{2.10}$$

The L factors are not explicitly reported here though they can be found, together the K factors introduced in Eq.[2.8], in the work of Lambert *et al.*.[56] It has to be stressed that both L and K terms depends on the specific angles adopted in the experimental geometry ($\beta_{SFG/Vis/IR}$) and on the refractive index of the interface.

The intensity of the SFG light emitted from the surface and subsequently detected can be expressed as the square modulus of the $\mathbf{E}^{SFG}$ field:

$$\begin{aligned} I_p^{SFG} &\propto \left|E_x^{SFG}\right|^2 + \left|E_z^{SFG}\right|^2 \\ &\propto \left|L_x P_x^{SFG}\right|^2 + \left|L_z P_z^{SFG}\right|^2 \\ I_s^{SFG} &\propto \left|E_y^{SFG}\right|^2 \\ &\propto \left|L_y P_y^{SFG}\right|^2 \end{aligned} \tag{2.11}$$

With specific incident polarization combinations it is possible to selectively probe particular components of the susceptibility tensor, reducing the number of terms in the summation in Eq.[2.11]. In fact, from Eq.[2.8] we have that

$$\begin{aligned} P_x &\propto \sum_{jk} \chi^{(2)}_{xjk} K_{Vis,j} E_{Vis,p/s} K_{IR,k} E_{IR,p/s} \\ P_y &\propto \sum_{jk} \chi^{(2)}_{yjk} K_{Vis,j} E_{Vis,p/s} K_{IR,k} E_{IR,p/s} \\ P_z &\propto \sum_{jk} \chi^{(2)}_{zjk} K_{Vis,j} E_{Vis,p/s} K_{IR,k} E_{IR,p/s} \end{aligned} \tag{2.12}$$

and it can be noticed that selecting the polarization of the incoming/outgoing fields (i.e. ruling out different $E_{B,p/s}$, B=(SFG/Vis/IR) components) we probe different components of the $\chi^{(2)}$ tensor.

The notation for the order of the three beams polarization is SFG beam - Vis beam - IR beam. As an example, *ssp* corresponds to the measurement of *s*-polarized SFG light, after *s*-polarized Vis light and *p*-polarized IR light have impinged on the sample.

Mind that for metallic substrates the reflectivity in the infrared spectral region is often particularly high, and it may be shown that the incident beam results in a large surface **E** field in the z direction, but negligible fields in the x and y directions.[56] Therefore with metal substrates only p IR polarized light is employed.

Modeling SFG spectra

Although the second order response of the system is in general characterized by more than one component of the susceptibility tensor, it is common practice to describe it by a single "effective" scalar susceptibility, including also the L and K factors. We suggest the reader more comprehensive works for a systematic description, which however falls outside the scope of this manuscript.[54,58,59] For an interface with adsorbed molecular species, this "effective" susceptibility is given by

$$\chi^{(2)}_{eff} = \chi^{(2)}_{sub} + \chi^{(2)}_{ads} \tag{2.13}$$

where $\chi^{(2)}_{sub}$ accounts for the response of the substrate while $\chi^{(2)}_{ads}$ accounts for the response of the adsorbed species.

For dielectric surfaces $\chi^{(2)}_{sub}$ is typically negligible. Conversely, for metal surfaces, $\chi^{(2)}_{sub}$ can be of a significant magnitude due to surface plasmon resonances. Therefore, a considerable fraction of the SFG signal could be generated in this way, though it will be largely invariant with the IR frequency. For this reason, $\chi^{(2)}_{sub}$ is usually approximated to be a constant, in general complex-valued, and it is common practice to refer to it as to the non-resonant part of the second-order susceptibility, $\chi^{(2)}_{NR}$. On the other hand, $\chi^{(2)}_{ads}$ is expected to vary considerably as the frequency of the infrared laser beam is tuned through a molecular resonance. Accordingly, $\chi^{(2)}_{ads}$ is referred to as the resonant part of the second-order susceptibility, $\chi^{(2)}_{R}$.

An exact expression for $\chi^{(2)}_{R}$ accounting for its tensorial nature can be calculated using the time-dependent perturbation theory, see the work of Wang *et al.*,[58] and further details about its modeling (considering its dependency on the molecular susceptibility tensor β) will be discussed in the following section.
Here, we consider that it is possible, while approximating to a single effective scalar term, to express $\chi^{(2)}_{eff}$ in terms of different surface contributions.[58,60,61] We write $\chi^{(2)}$ in Eq.[2.13] as

$$\begin{aligned}\chi^{(2)}_{eff}(\omega_{IR}) &= A^{(NR)}e^{i\phi} + \sum_{\nu} \frac{A^{(R)}_{\nu} e^{i\phi_\nu}}{\Omega_\nu - i\Gamma_\nu - \omega_{IR}} \\ &= e^{i\phi}\left(A^{(NR)} + \sum_{\nu} \frac{A^{(R)}_{\nu} e^{i\Delta\phi_\nu}}{\Omega_\nu - i\Gamma_\nu - \omega_{IR}}\right)\end{aligned} \tag{2.14}$$

where $\chi^{(2)}_{NR}$ and $\chi^{(2)}_{R}$ have been expressed in terms of the following parameters: $A^{(NR)}$ and $A^{(R)}_{\nu}$ are real-valued amplitudes, the ν-sum runs over the resonance frequencies Ω_ν, Γ_ν are the damping constants related to the excitation lifetime (the full width at half maximum is FWHM $= 2\Gamma_{nu}$), ω_{IR} is the infrared frequency of the impinging laser beam, and $\Delta\phi_\nu$ is the relative phase shift of the ν-th vibrational resonant mode with respect to the non-resonant background. Intuitively (further discussion will follow in the next section), the amplitude $A^{(R)}_{\nu}$ of the ν-th vibrational mode depends on the adsorbate concentration (number density N) and the product of the vibrational and electronic transition moments of the specific molecular transition (T_ν and M_ν respectively)

$$A^{(R)}_{\nu} \propto N T_\nu M_\nu \tag{2.15}$$

Adopting the aforementioned approximated form $\chi^{(2)}_{eff}$, and considering the expressions in Eq.[2.11] and [2.12], the intensity of the SFG light emitted from the surface as a function of the incident IR frequency is then be expressed as:

$$I_{SFG}(\omega_{IR}) \propto \left| A^{(NR)} + \sum_{\nu} \frac{A^{(R)}_{\nu} e^{i\Delta\phi_\nu}}{\Omega_\nu - i\Gamma_\nu - \omega_{IR}} \right|^2 I_{Vis} I_{IR}(\omega_{IR}) \tag{2.16}$$

In Eq.[2.16] it is anticipated that, while the intensity of the impinging visible radiation is constant (apart from time-dependent fluctuations due to intrinsic setup instabilities and drifts), the intensity of the IR radiation may strongly depend on the frequency ω_{IR}. This is related to the way the IR radiation is generated, and will be explained in the technical section below. To properly obtain the peak parameters from the I_{SFG} signal, the latter has to be normalized by I_{IR} first. Moreover, a Gaussian broadening may be added to the line profile in order to take into account for both experimental contributions (such as the line width of the laser beams and the energy resolution of the detector) and inhomogeneity in the adsorbed species population (see Eq.[2.17]).[55]

$$\frac{1}{\sqrt{2\pi}\sigma}\int dy I_{SFG}(\omega_{IR}-y)e^{-\frac{y^2}{2\sigma^2}} \tag{2.17}$$

It is common practice to extract the chemical information of the adsorbed molecular species by numerically fitting the experimental spectrum according to Eq.[2.16] by means of least-square methods, after having normalized by I_{IR} and I_{Vis}. In this way it is possible to get the non resonant amplitude $A^{(NR)}$ and the resonance parameters: frequencies Ω_ν, widths Γ_ν, phase shifts $\Delta\phi_\nu$, and amplitudes $A_\nu^{(R)}$.

As a concluding remark we have to spend some words about the K and L Fresnel factors appearing in Eq.[2.8] and [2.10]. Backus *et al.*[62] showed that in the case of the metal-water interface the role of the Fresnel factors is far from negligible. As such terms where included in the expression of $\chi^{(2)}_{eff}$ in Eq.[2.13], the resonant term (depending on the system of interest) could not be constant at different infrared frequencies. Therefore, during the investigation performed in the following chapters, we preemptively collected the reference spectra of the pristine substrates. Then, this reference has been used to normalize the SFG data collected at different working conditions, whenever necessary. However, it has to be stressed that the modulation introduced by the Fresnel factors span over hundreds of wavenumbers.[62] Therefore, it can be easily distinguished from the resonant terms described in Eq.[2.14].

Molecular Hypepolarizability

As discussed above and presented in Eq.[2.16], modulations of I_{SFG} occur mainly due to the resonant term of second-order non-linear susceptibility, which changes significantly with IR wavenumber and is therefore the main responsible for the vibrational information obtained from a SFG spectrum. In the specific, the resonant macroscopic susceptibility tensor $\chi^{(2)}_R$ may be expressed as the orientational average of the molecular polarizability tensor β (defined in the molecular-frame coordinate system) of the molecules adsorbed at the interface.[58] As the frequency of the infrared laser beam is tuned through a resonance of the microscopic β components, a modulation in the SFG signal intensity is produced. A description of the complete mathematical relationship between β and $\chi^{(2)}_R$ can be found elsewhere,[56,58] but here we limit to a brief presentation of the model.

When working with molecules, it is more convenient to employ a molecular bound coordinate system (a,b,c) that can differ from the surface bound Cartesiam system. The two frames can be converted into one another with the rotation transformation $R(\theta)R(\Phi)R(\psi)$, defined by the Euler angles (θ,Φ,ψ) that describe the molecular system with respect to the Cartesian one, see Fig. 2.3. In a comparable manner to χ^2, $\beta_{\alpha\beta\gamma}$ is a tensor of 27 components (α,β and γ are indices that assume the values of (a,b,c)) describing the non-linear response of the molecule at all incident and emitted E field polarization combinations. Following the approach presented by Wang *et al.*,[58] the molecular polarizability presents several components

$\beta_{\nu,\alpha\beta\gamma}$, associated with a particular molecular vibration ν. The sum of all the non-zero $\beta_{\nu,\alpha\beta\gamma}$ components describes the complete response of the molecule to the visible and infrared E fields (a non resonant term can be present and contribute).

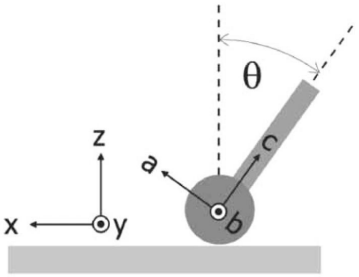

Figure 2.3: Schematic representation of a molecule adsorbed at an angle θ to the surface normal. The surface and molecular bound axis systems are related by a simple rotation matrix with a Euler angle of θ (image from Lambert *et al.*[56]).

According to the definition of macroscopic average, χ^2_{ijk} is a sum over all the $\beta_{\alpha\beta\gamma}$ of the adsorbed molecules in a given volume. The sum may be written as follows:

$$\chi^2_{ijk} = \frac{N}{\epsilon_0} \sum_{\alpha\beta\gamma} \langle R(\theta) R(\Phi) R(\psi) \beta_{\alpha\beta\gamma} \rangle \tag{2.18}$$

A quantum mechanical expression for $\beta_{\alpha\beta\gamma}$ may be derived using perturbation theory. A simplified, but meaningful equation applicable when ω_{IR} is near a vibrational resonance and ω_{Vis} is far from the frequency of electronic transitions is reported here:

$$\beta_{\alpha\beta\gamma} = \frac{1}{2\hbar} \frac{M_{\alpha\beta} A_\gamma}{(\omega_\nu - \omega_{IR} - i\Gamma)} \tag{2.19}$$

where ω_{IR} is the frequency of the tuneable infrared beam, ω_v is the frequency of the vibrational resonance, and Γ is the relaxation time of the vibrationally excited state involved in the resonance. $M_{\alpha\beta}$ and A_γ are the Raman and infrared transition moments, respectively. Eq. 2.19 reveals the SFG selection rule: for a transition to occur, it must be both Raman and infrared active. We stress the attention on the the different α, β, γ indexes of the Raman (M) and infrared (A) transition moments.

2.1.2 Analysis of the SFG spectra

As not all the readers may be familiar with the intensity plots of the SFG signal, here we present the procedure followed in this work to analyze and show the IR-Vis SFG data.

Presenting SFG data: intensity or amplitude plots. As a first step, the "raw" SFG signal has to be normalized by the smoothed impinging IR and Vis signal intensities. This allows to remove artifacts resulting from modulations of the impinging IR and Vis laser intensities. Possible sources are instabilities in the source laser, variations in the air water content that may induce unwanted adsorption in the IR signal, and intrinsic modulations of the IR signal due to its production, as it requires the rotation of nonlinear crystals.

Each spectrum is then analysed by least-square fitting of the data with the SFG profile

$$\frac{I_{SFG}(\omega_{IR})}{I_{Vis} I_{IR}(\omega_{IR})} \propto \left| A^{(NR)} + \sum_k \frac{A_k^{(R)} e^{i\Delta\phi_k}}{\omega_k - \omega_{IR} - i\Gamma_k} \right|^2 \tag{2.20}$$

Note that the factor which, if included, could turn the proportionality in Eq.[2.20] into an equality, is usually not considered as it is usually hardly accessible, first of all because of its deep relationship with the optical alignment that may change day by day. As we will mainly focus on the resonant contributions and their evolution as function of parameters as for example background pressure, temperature, and substrate preparation, throughout this manuscript we present the normalized signal in arbitrary units (arb. units). In addition, whenever explicitly indicated a further normalization to the value of the non-resonant background will be implemented.

Each SFG spectrum is described by 1+4×N parameters (N being the number of resonances), namely the non resonant amplitude $A^{(NR)}$ and the resonance parameters: frequencies ω_k, Lorentian linewidths Γ_k, phase shifts $\Delta\phi_k$ and amplitudes $A_k^{(R)}$.

During the analysis of SFG intensity spectrum, we plot the normalized SFG signal (dots) together with the best fit (lines) according to the above intensity function (Eq.[2.20]). A selected example coming from Corva *et al.*[63] is reported in Fig. 2.4 (panel a), where the SFG intensity data in the C-O stretching region obtained upon exposure of the Ir(111) surface to 10^{-1} mbar CO_2 are reported.

There are different possible approaches to the visualization of the data fitting results. Eq.[2.20] expressed in terms of the second-order susceptibility

$$\frac{I_{SFG}(\omega_{IR})}{I_{Vis}I_{IR}(\omega_{IR})} \propto \left|\chi^{(2)}\right|^2 = \left|\chi^{(2)}_{Nres} + \chi^{(2)}_{Res}\right|^2 \tag{2.21}$$

can be rewritten in order to highlight the physics information content of interest. Indeed, the real and imaginary components of the refraction index describe the scattering and absorption properties of a system, respectively, and can be readily obtained for the resonant part:

$$\begin{aligned}\chi^{(2)}_{Res}(\omega_{IR}) &= \Re\left[\chi^{(2)}_{Res}\right] + i\Im\left[\chi^{(2)}_{Res}\right] \\ &= \Re\left[\sum_k \frac{A_k^{(R)}e^{i\Delta\phi_k}}{\omega_k - \omega_{IR} - i\Gamma_k}\right] + i\Im\left[\sum_k \frac{A_k^{(R)}e^{i\Delta\phi_k}}{\omega_k - \omega_{IR} - i\Gamma_k}\right]\end{aligned} \tag{2.22}$$

and separately represented in an amplitude (not intensity) plot (Fig. 2.4, panel b). Alternatively, the real (Fig. 2.4, panel c) and imaginary (panel d) amplitudes can be displayed for each k-th resonance separately

$$\begin{aligned}\chi^{(2)}_{Res,k}(\omega_{IR}) &= \Re\left[\chi^{(2)}_{Res,k}\right] + i\Im\left[\chi^{(2)}_{Res,k}\right] \\ &= \Re\left[\frac{A_k^{(R)}e^{i\Delta\phi_k}}{\omega_k - \omega_{IR} - i\Gamma_k}\right] + i\Im\left[\frac{A_k^{(R)}e^{i\Delta\phi_k}}{\omega_k - \omega_{IR} - i\Gamma_k}\right]\end{aligned} \tag{2.23}$$

thus representing each contribution to the resonant amplitudes. The above plotting choices yield equivalent visualization of the information determined with the data least-square fitting procedure and allow speculating about the signal amplitudes.[59,64]

However, it is known that if N resonances are present in an SFG spectrum, up to 2^N equivalent sets of parameters can be obtained from data fitting according to Eq.[2.20].[60] This occurs since we actually measure intensities and not amplitudes. We here propose and adopt throughout this work to plot the deconvoluted intensities (not amplitudes) contributing to the effective SFG signal (Fig. 2.4, panel e), thus providing also visual information about the contribution of each resonance to the overall intensity. For each *k-th* component we display, coherently with the experimental and best fit SFG intensity curves, the following function

$$I_{SFG,k}(\omega_{IR}) \propto \left|A^{(NR)} + \frac{A_k^{(R)}e^{i\Delta\phi_k}}{\omega_k - \omega_{IR} - i\Gamma_k}\right|^2 \tag{2.24}$$

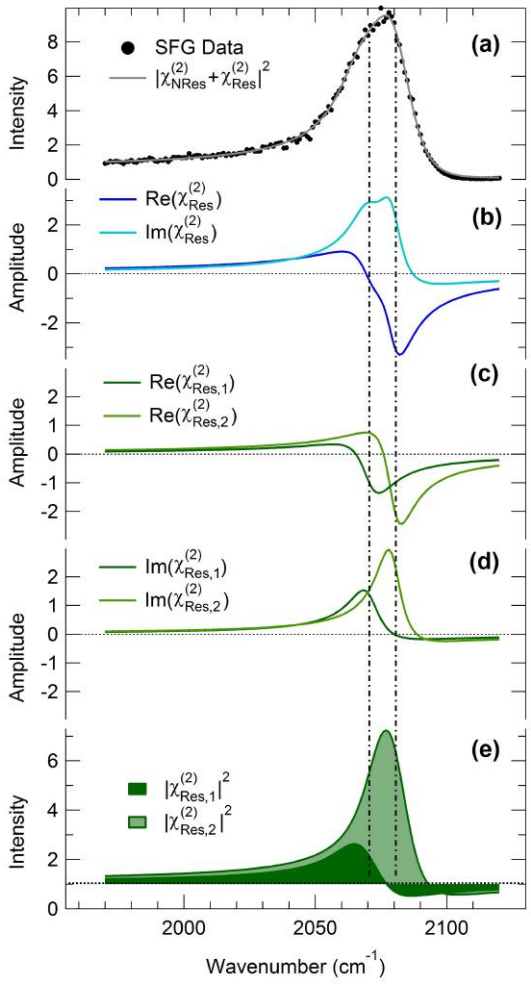

Figure 2.4: Analysis and interpretation of SFG data: (a) sample SFG intensity spectrum in the C-O stretching region upon exposure of Ir(111) to CO_2 (dots) and best-fit (grey line); (b) plot of the real and imaginary parts of the resonant susceptibility obtained from the least-square fit of the data; (c) plot of the real part of the resonant susceptibility for each resonance, obtained from the least-square fit of the data; (d) plot of the imaginary part of the resonant susceptibility for each resonance, obtained from the least-s quare fit of the data; (e) plot of the full intensity for each resonance, obtained from the least-square fit of the data, where the color-filling highlights the intensity modulation with respect to the non-resonant background (horizontal dashed line); vertical dashed lines show the position of the resonances as from the data fitting procedure; amplitude and intensity values (y axis) are in arbitrary units.

This intensity expression accounts for interference between each resonance and the non-resonant background, while interference among resonances is not accounted for. The latter, indeed, is already visualized in the fitting curves according to Eq.[2.20]. With reference to Fig. 2.4, panel (e), the horizontal dashed line shows the non-resonant background level, while the color-filling of the curves shows the signal intensity modulation with respect to the non-resonant background. The vertical dashed lines show the actual positions of the resonances (ω= 2071 cm^{-1}; ω=2080 cm^{-1}) coming from the data fitting procedure.

2.1.3 The VISpLab: SFG at the University of Trieste.

The aim of this technique is the characterization of adsorbed species present on a surface. A necessary requirement consists, indeed, in having complete control over surface conditions: the presence of contaminants could strongly influence the system, hindering the synthesis of the nano-architectures and their characterization. Precise control can be achieved working in Ultra-High Vacuum (UHV) conditions, namely preparing the sample in an appropriate chamber kept at a pressure of $\sim 10^{-10}$ mbar. Simple arguments from kinetic theory of gases explain why such a threshold value, and are presented in Appendix 6.1.

The SFG setup was therefore coupled with a UHV system, which allows sample preparation in a controlled environment. Both the laser setup and the chamber are described in the following, however concerning the details of the optical setup we refer to Appendix 6.5.

The spectrometer. SFG measurements were performed at the Visible and Infrared Spectroscopy Laboratory (VISpLab, University of Trieste) exploiting a customized setup purchased from the Lithuanian laser manufacturing company EKSPLA. All the system components are computer controlled through custom LabVIEW software. Briefly, the setup is composed by:

1. A *chiller*;

2. A *PL2230 Series Laser* with a free-standing power supply: it generates the vertically polarized fundamental radiation characterized by picosecond optical pulses at 1064 nm (IR, 9398.5 cm^{-1}) The duration of each pulse is $\sim$ 30 ps, with a repetition rate of 50 Hz and a maximum pulse energy of 25 mJ. The peak power of the fundamental radiation, defined as $P = E/\Delta t$ (E being the maximum pulse energy and Δt the pulse duration), is $P_{fund} \simeq 1GW$;

3. A *Harmonics Unit H500*: it generates the second harmonic radiation at 532 nm (Vis, 18797 cm^{-1}). Its output beams are three: one from the original IR radiation (6 mJ of maximum pulse energy) and two Vis beams. One is directly used in the SFG experiment and has a maximum pulse energy of 1 mJ and a peak power $P_{Vis} \simeq 33MW$, while the other exhibits a maximum pulse energy of 9 mJ and is used to generate the tunable IR radiation;

4. An *Optical Parametric Generator PG501/DFG1P*: it mixes one Vis beam with the original IR radiation in order to obtain the 2300$\div$10 000 nm (1000$\div$4347.8 cm^{-1}) tunable mid-IR radiation which will be used in the SFG experiment together with the remaining 532 nm Vis radiation; the measured pulse average energy is $\simeq$ 200 mJ, which corresponds to a peak power $P_{IR} \simeq 7MW$;

5. The *SFG box*: here the polarization of the tunable mid-IR and the Vis beam are selected and the beams are spatially overlapped on the sample, generating a SFG signal in the 432-505 nm range. Knowing that the beam diameter is $\simeq$ 1 mm, the maximum

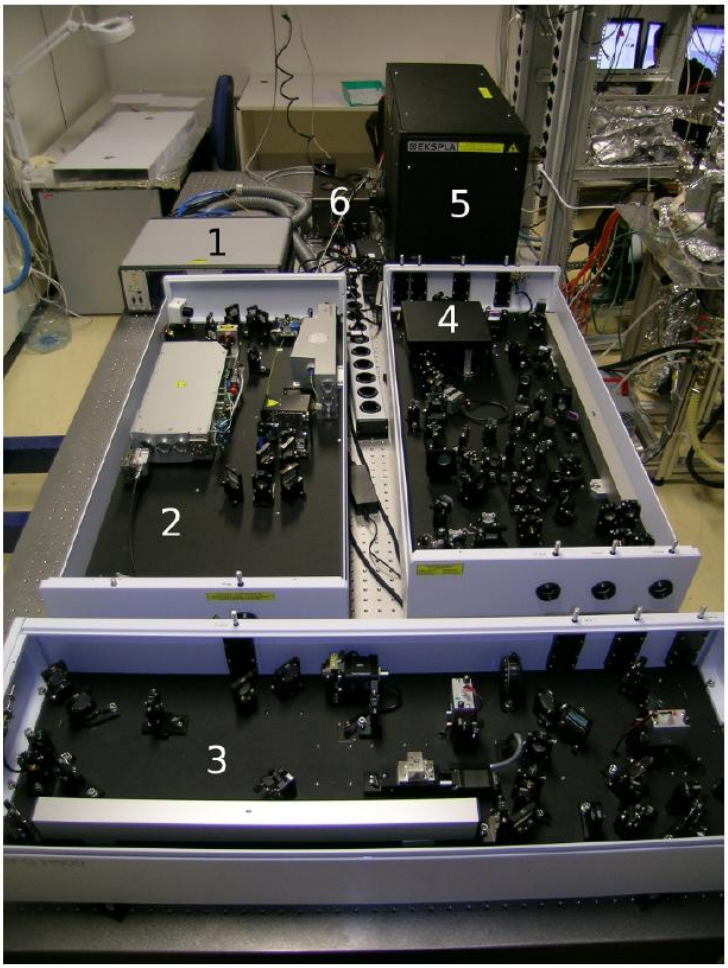

Figure 2.5: Top view of the SFG system a the Visible and Infrared Spectroscopy Laboratory (VISplab) at the University of Trieste, Italy: power supply (1), laser source (2), harmonics unit (3), parametric generator (4), SFG box (5), monochromator and detector (6).

irradiance on the sample is $I_{Vis} \simeq 7.2 \times 10^6\,\mathrm{MWm^{-2}}$ and $I_{IR} \simeq 1.8 \times 10^6\,\mathrm{MWm^{-2}}$ for the Vis and IR radiation, respectively.

6. A *monochromator*, a MS200 Czerny-Turner type with single grating turret.

The UHV chamber

The UHV chamber employed in the SFG measurements presented in this manuscript consists, see Fig. 2.8, of a cylindrical amagnetic stainless steel chamber, hereafter named *preparation chamber*, with 30 cm diameter, an inverted- Y shaped *pumping section* (10), (12) and a *high-pressure cell* (HP cell) designed for the SFG experiment. The three sections are made independent through gate valves. The pumping section is located below the preparation chamber and hosts at the end of the two arms a cryogenic pump (10) coupled with a titanium sublimation pump and an ion pump (12). The preparation chamber is also pumped by a turbo molecular pump (4) which, in turn, is prepumped by a diaphragm pump. When the gate valve between the preparation chamber and the pumping section is open, a background pressure of 5×10^{-11} mbar can be achieved. The HP cell is located behind the preparation chamber and coupled with the SFG box. A fast entry lock loading system (5) is also present: it allows to load the sample into the UHV system without the need to break the vacuum. It is independently pumped by a turbo pumping station (11), i.e. a turbo molecular pump coupled with a backing pump for the pre-pumping, that grants a background pressure better than 10^{-8} mbar. A magnetic transfer arm (7) is employed for loading/unloading the sample-holder from the fast entry lock and from the two manipulators, namely that of the preparation chamber and that of the HP cell.

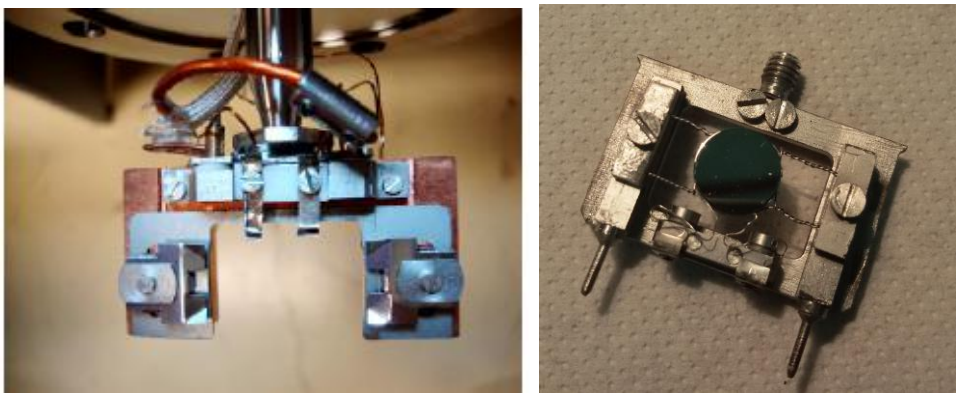

Figure 2.6: On the left, the sample receiver of the SFG setup (two of them are present, one in the preparation chamber and one in the high pressure cell). On the right, the sample holder.

The sample-holder (Fig. 2.6, right), once plugged into its receiver (Fig. 2.6, left), allows to heat the sample resistively in UHV (at 1 bar) up to 1300 K (700 K). The sample is held through the twisting of a single tantalum wire (0.2 mm diameter) in four points around the sample circumference. Such mounting technique allows to minimize the mechanical stress due to the wire thermal expansion and contraction thus granting a much longer life. The sample temperature is measured through a K-type chromel-alumel thermocouple that is spot-welded at the back of the sample.

The HP cell (or SFG cell), Fig. 2.7, is a steel cylinder (6 cm diameter) with two barium fluoride (BaF_2) windows, one for the incident IR and Vis beams and the other one for the outgoing SFG beam. The incidence angle of the IR and Vis beams is not normal to the window

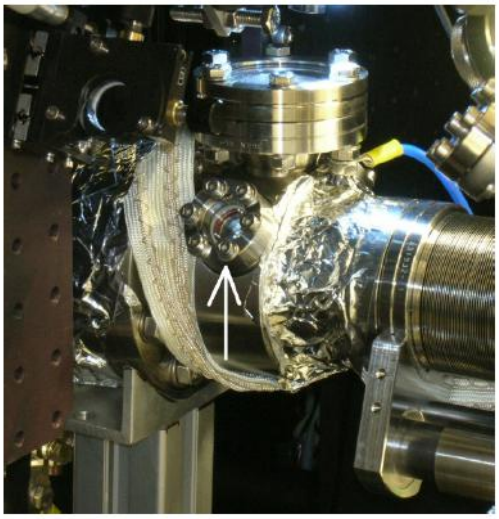

Figure 2.7: Overview of the high pressure cell. The white arrow points the entrance window for the IR and Vis beams.

in order to avoid back reflection into the SFG setup that may cause damage to the optics. BaF_2 windows were chosen because they allow transmission in the $1000 \div 4000$ cm^{-1} spectral range with nearly 100% efficiency. They can sustain a pressure difference up to 1 bar. The SFG cell is equipped with its own manipulator that provides, besides the (x; y; z) translations and the polar rotation, also the possibility to tilt the sample. The pressure is measured through a full range cold cathode pressure gauge that works in the $5 \times 10^{-9} - 1 \times 10^{3}$ mbar range. A gas line which can handle up to three different gases is provided. The SFG cell can be independently pumped by the scroll pump (9) and by the turbo pumping station (11).

The preparation chamber is dedicated to the preparation and pre- and post- reaction characterization of samples. It is equipped with the instrumentation needed to perform low energy electron diffraction (LEED) (6), a mass spectrometer (2), an ion gun that allows to sputter the sample, and a gas line (8) that allows the desired gas(es) to be dosed on the sample. A retractable quartz balance and an evaporator equipped with two resistively heated quartz pockets are also present, and used to evaporate on the sample surface known quantities of metals or molecules (Physical Vapor Deposition, PVD). The top part of the preparation chamber ends with the manipulator (1): it provides four degrees of freedom, the three translations (x; y; z) and the polar rotation.

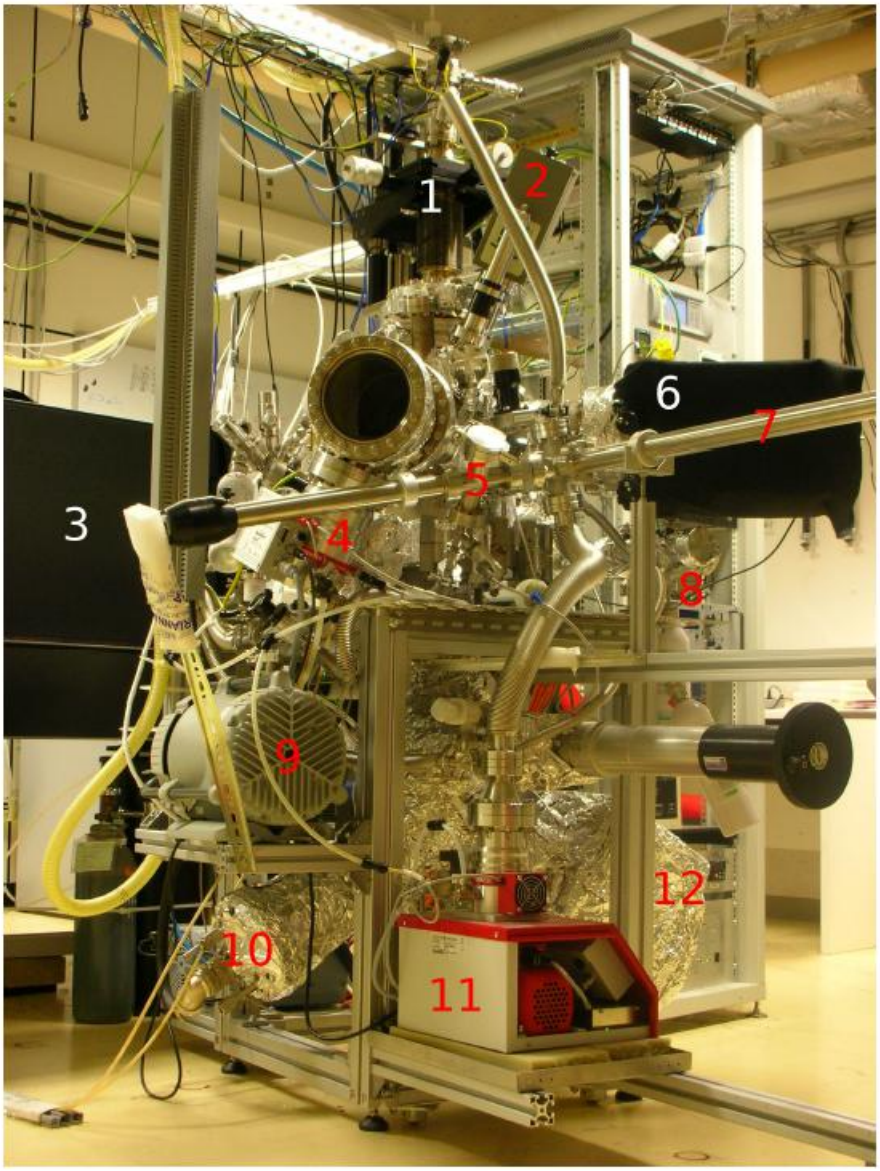

Figure 2.8: Overview of the preparation chamber, equipped with a manipulator (1), a mass spectrometer (residual gas analyser, RGA) (2), a turbo molecular pump (4), a fast entry lock loading system (5), the setup for low energy electron diffraction (LEED) (6), a magnetic transfer arm (7) to move the sample-holder from the fast entry lock to the preparation chamber and to the high pressure chamber, a gas line (8), a scroll pump (9), a cryogenic pump (10), a turbo pumping station (11) and a ionic pump (12). The SFG box can be seen (3).

2.2 Near-ambient pressure XPS (NAP-XPS)

Most of the findings that will be presented in the following Chapters were understood by complementing the vibrational information obtained through IR-Vis SFG spectroscopy with chemical information achieved employing X-ray photoelectron spectroscopy (XPS), a photon-in/electron-out technique. XPS is a technique commonly employed only in vacuum due to the short mean free path of electrons through a gas phase. However, after a review of its theoretical background, in the following we will discuss about the technical expedients letting it operate even at near ambient pressure conditions.

2.2.1 X-ray photoelectron spectroscopy

X-ray photoelectron spectroscopy is one of the most common surface science techniques for the analysis of the surface chemical composition of solids. The physical process on which XPS is based is electron photoemission: a photon of energy $h\nu$ is sent on the surface of a solid and gets adsorbed by an electron with a binding energy E_b below the vacuum level. Such electron can emerge from the solid, into the vacuum level, with a kinetic energy

$$E_k = (h\nu - E_b). \tag{2.25}$$

In this simple picture, the energy distribution of the electrons photoemitted from a solid should reproduce the energy distribution of electrons within the solid, only shifted up by $h\nu$.

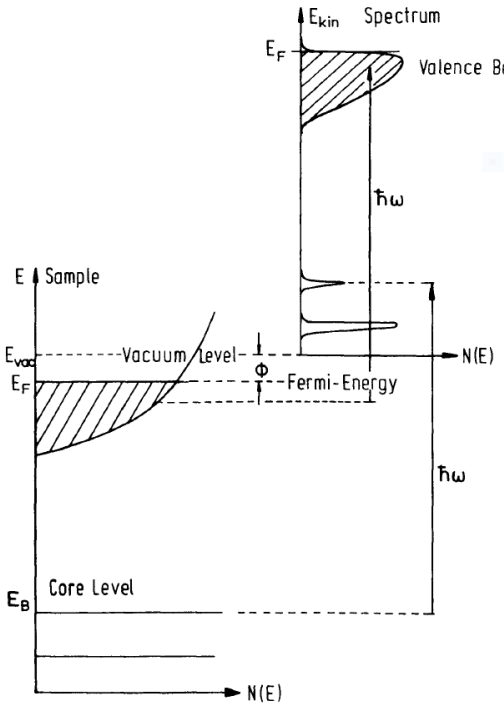

Figure 2.9: Energy scheme of a photoemission experiment: relation between the energy levels in a solid and the photoelectrons energy distribution. Image from Hüfner *et al.*.[65]

It is common practice to refer binding energies to the Fermi level, so to have an absolute reference for energies. Determination of the vacuum level, in fact, relies on the accurate knowledge of the work function of the material and the contact potentials of the experimental set-up.[66] In this case, the kinetic energy can be written as

$$E_k = (h\nu - E_b^f - \phi_0) \tag{2.26}$$

where E_b^f is the binding energy referred to the Fermi level and ϕ_0 the work function of the solid.

From a theoretical point of view, the photoemission process can be treated with time-dependent perturbation theory. A semiclassical approach is conventionally adopted, meaning that apart from the electromagnetic field, which is treated classically, the theory is developed in the quantum mechanical framework.[67] The unperturbed system, a solid, is subject to the time-independent Hamiltonian H_0 and, at the instant $t_0 = 0$, it is perturbed by a monochromatic electromagnetic field (of energy $\hbar\omega$, with $\omega = 2\pi\nu$). As a consequence, the Hamiltonian is given by the sum of H_0 with a time-dependent term $H_I(t)$ that describes the perturbation ($\mathbf{r}$ indicates the position on the electron)

$$H(\mathbf{r}, t) = H_0(\mathbf{r}) + H_I(\mathbf{r}, t). \tag{2.27}$$

The interaction Hamiltonian can be written as follows

$$H_I(\mathbf{r}, t) = \frac{e}{2mc}(\mathbf{A} \cdot \mathbf{p} + \mathbf{p} \cdot \mathbf{A}) - e\phi + \frac{e^2}{2mc^2}(\mathbf{A} \cdot \mathbf{A}) \tag{2.28}$$

where $\mathbf{A}$ and ϕ are the vector and scalar potential, $\mathbf{p}$ is the momentum operator.[65] The perturbation depends explicitely on time through $\mathbf{A}$. In the Coulomb gauge, so with $\phi = 0$ and $\nabla \cdot \mathbf{A} = 0$, and neglecting the quadratic $\mathbf{A}^2$ which represents the two photon scattering process, $H_I(\mathbf{r}, t)$ can be simplified as follows

$$H_I(\mathbf{r}, t) = \frac{e}{mc}(\mathbf{A} \cdot \mathbf{p}). \tag{2.29}$$

Starting from here, it is possible to calculate the photoionization cross-section w for a transition from a N-electron initial state ψ_i, to a final state ψ_f in which a core electron has been ejected. The resulting expression for w is

$$w \propto \frac{2\pi}{\hbar} |\langle \psi_f | H_I | \psi_i \rangle|^2 \delta(E_f - E_i - \hbar\omega) \tag{2.30}$$

From equation 2.30, it is clear that only when the photon energy matches the energy difference between the final and the initial state of the system, the transition may occur. Moreover, the modulus squared term yields the selection rules for the transition. If the initial state is described by a one-electron wavefunction with quantum numbers (n, l, m) and, similarly, the final state by a wavefunction with (l', m') (in which n' has been omitted as the electron is in the continuum), then the evaluation of the angular integrals in the matrix element leads to the selection rules

$$\begin{cases} l' = l \mp 1 \\ m' = m, m \mp 1 \end{cases} \tag{2.31}$$

Thus, for example, for any particular l value of the initial state, the final state will contain a coherent sum of two states with angular momentum $(l + 1)$ and $(l - 1)$.

It is important to point out that the cross sections depend on the radial part of the wave function, which is directly defined by the value assumed by the quantum numbers n and l. As it's clearly demonstrated in Fig. 2.10, given a photon energy, the cross section is different for each electron within the same atom. Of course the cross section is also dependent on the atomic number of the element considered.

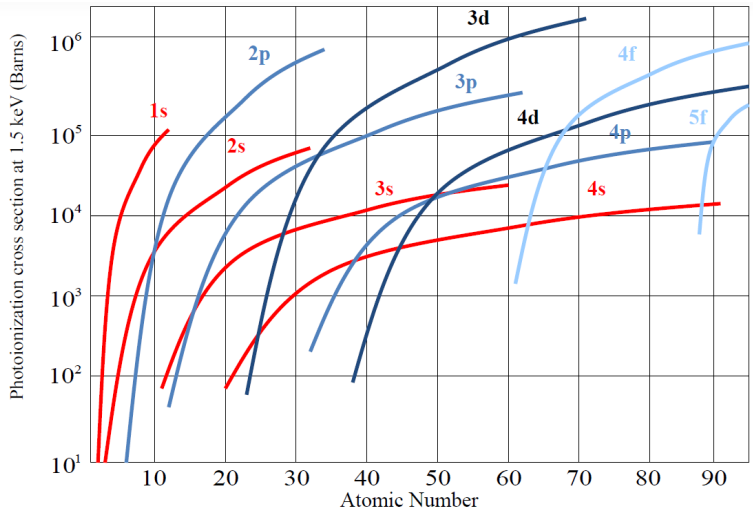

Figure 2.10: Photoionisation cross-section at 1.5 keV as a function of the atomic number. Image from Hüfner *et al.*.[65]

Interatomic relaxation shift

When the energies of core levels are investigated with high energy resolution, it is found that differences in binding energy between two non-equivalent atoms of the same species can be detected. These energy differences are called *chemical shifts* and depend on the bonding environment around the atom and, in particular, on its oxidation state. To explain chemical shifts, further understanding of the relation between the binding energy and the electronic configuration of a photoionized atom is necessary

The binding energy E_b of an electron k undergoing photoemission from a n-electron atom within a solid is given by the difference in energy between the final and initial states of the atom, that is

$$E_b(k) = E_f(n-1) - E_i(n). \tag{2.32}$$

If there were no rearrangement of all of the spectator electrons, Koopmans' approximation would hold. In this case the initial state atomic wavefunction ψ_i could be written as

$$\psi_i(n) = \varphi_j \Psi_j(n-1) \tag{2.33}$$

where φ_j is the wavefunction of the electron that will be removed and Ψ_j is the wavefunction on the (n-1)-electron ion. Instead, the final state wavefunction ψ_f of the ion would be

$$\psi_f(n-1) = \Psi_j(n-1). \tag{2.34}$$

Consequently, the binding energy of the electron that gets photoemitted would be given by the unique value $E_b = -\epsilon_j$, where ϵ_j is the energy of the j-th energy level of the initial state, and only one peak would be expected in the photoelectron spectrum.

Yet, this approximation is too rough, since electrons cannot be treated as frozen in their configuration; a more sophisticated picture is required. The final state, achieved by removing one electron, corresponds to an ionic state in which a hole exists in place of the ejected photoelectron. This does not correspond to the ground state of the final ionic state. The electrons in the ionized atom, but also those on neighbouring atoms, can relax in response to the ionization event and, thereby, lower the energy of the final state. These relaxation phenomena lead to reconsider the description of the final state wavefunction. In fact, it should

be written in terms of the s eigenstates of the ion with a core hole in the j-th orbital.

$$\psi_f(n-1) = \Phi_{js}(n-1) \tag{2.35}$$

The fact that a relaxation of the ion core occurs in the final state, means that the wavefunction $\Psi_j(n-1)$ is not an eigenstate of the ion. Therefore, it must be projected onto the actual eigenstates of the ion Φ_{js}. This results in the formation of one or more possible final state wavefunctions, yielding therefore to multiple eigenvalues and final state energy values. In terms of photoelectron spectrum this means that there will be a main peak, but also additional ones, called *satellite lines*.

From the above discussion, it is clear that both initial state and final state effects influence the binding energy. Initial state effects are caused by chemical bonding, which influences the electronic configuration in and around the atom. For this reason, the energetic shift caused by initial state effects is known, as mentioned before, as *chemical shift*. This energy shift strongly depends on the oxidation state of the atom, and, usually, the binding energy increases with the oxidation state; in fact the greater the electronegativity of an atom, the higher the binding energy. This can be understood on the basis of simple electrostatics. The first ionization energy of an atom is always lower than the second, as the higher the effective positive charge on the atom, the higher the binding energy of the photoelectron. Most of the atomic relaxation results from rearrangement of outer shell electrons, while the inner ones, possessing higher binding energy, scarsely contribute. The material's conductivity determines the extra-atomic relaxation. In a conducting material such as a metal, valence electrons are free to move from one atom to a neighbouring one and screen the hole created by photoionization. In an insulator, the electrons do not possess such mobility, so they react by being polarized by the core hole. Hence, the magnitude of the extra-atomic relaxation in metals is greater than that of insulators.

Surface sensitivity

Photoemission-spectroscopy gains its surface sensitivity from the fact that electrons have a high cross section for inelastic scattering with matter. This is showed by the data in Fig.

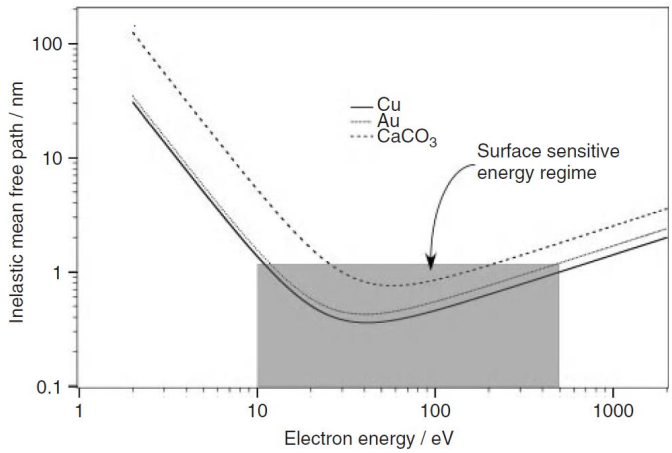

Figure 2.11: The universal curve of electron mean free path in solid matter.

2.11, which reports the inelastic mean free path of electrons as a function of the electrons energy in a solid. The curve in Fig. 2.11 is known as the universal curve because its shape doesn't depend strongly on the chemical identity of the solid. Photoelectrons emitted with a

kinetic energy between 10 and 1000 eV are particular suitable for surface elemental analysis, as their mean free path is below $\sim$ 10 Å.

NAP-XPS

As it was reported above, X-ray photoelectron spectroscopy is a surface-sensitive technique. XPS spectra are obtained by irradiating a material with a beam of X-rays, while, simultaneously measuring the flux and the kinetic energy of electrons that escape from the surface of such material. The X-ray source and the electron energy analyzer require ultra high vacuum conditions in the analysis chamber ($P \leqslant 10^{-8}$ mbar). In fact, once photoelectrons are emitted from the sample surface, they undergo elastic and inelastic collisions from atoms or molecules in the gas-phase.[68] The electron mean free path λ_e, or the average distance between collisions, depends on their energy and the gas pressure P in the chamber. Fig. 2.12 reports the variation of λ_e as a function of the electron energy in an oxygen gas environment. For electrons of 400

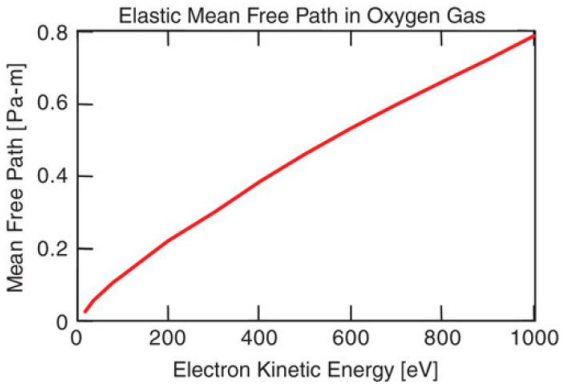

Figure 2.12: Electron elastic mean free path through an oxygen gas environment as a function of kinetic energy. Ten Pa-meter represents the same number of molecules as approximately 1 monolayer, if condensed on a surface. Image from Salmeron *et al.*.[68]

eV kinetic energy, λ_e is about 4 mm when the oxygen pressure is $\sim$1 mbar (similar values are found for other gases). Since λ_e is inversely proportional to P, its value decreases to about 30 μm at 100 mbar, which makes collection of unscattered electrons very challenging. The count rate of detected photoelectrons decreases exponentially with sample-analyzer distance. Therefore, λ_e at high pressure needs to be maximized in order to limit XPS signal loss. For these reasons, it is difficult to conduct investigations of surfaces under applicative conditions, namely in the presence of gases, such as in the case of interfacial chemical reactions in electrochemistry or catalysis.

With Near Ambient Pressure XPS (NAP-XPS), some issues in the experimental set-up are addressed, allowing to operate even in near ambient pressure (up to a few tens of mbar). The sample is kept inside a NAP cell equipped with a skimmer which acts as passage channel for the generated photoelectrons. They are forthwith directed into the energy analizer, passing through differential pumping stages which reduce the pressure by several orders of magnitude, so to diminish electron scattering. The skimmer opening diameter must meet both the necessity of high photoelectron flux and low pressure in the energy analizer chamber while maintaining the desired pressure on the sample. Accounting for gas flow and pressure distribution conditions in the geometry of a commercial setup, the aforementioned constraints are satisfied with a skimmer opening of about $\sim$ 0.3 mm, and a skimmer-sample distance 0.3 mm.

2.2.2 Lineshape and data analysis

Modeling XPS spectra

The basic lineshape of a photoemission process is given by a Lorentzian function.[69] The natural line width is determined by the lifetime of the core hole left by photoelectron in the ionized atom, which is related, via the Heisemberg principle, to the probability of the core hole to be filled by an electron in a lower binding energy level. The more decay channels through which electrons can fill the core hole, the shorter it's life time. As schematically pictured in Fig. 2.13, decay channels can be, for instance, Auger or radiative processes.

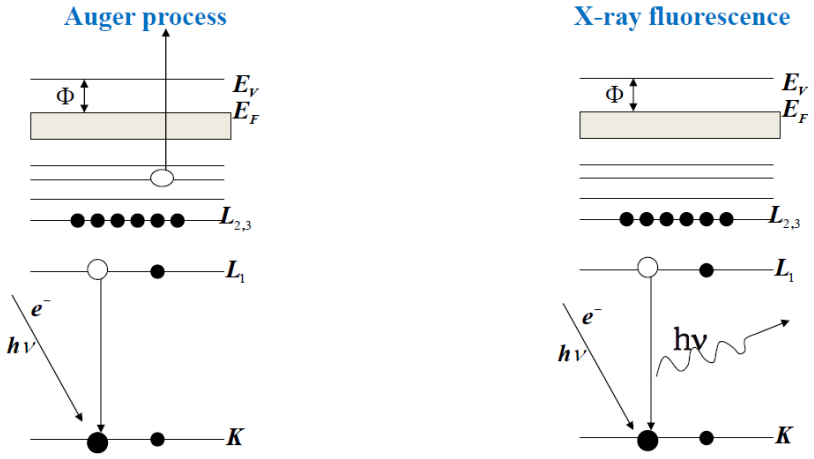

Figure 2.13: Energy level diagram showing the filling of a core hole, giving rise Auger electron emission on the right, to (X-ray) photon emission on the left.

Given Γ the intrinsic peak width, and τ the core hole lifetime, the uncertainty relation states that

$$\Gamma = \frac{h}{\tau} \tag{2.36}$$

where h is the Planck constant. The photoemission peak lineshape is therefore generally expressed as

$$I_{\mathrm{Lor}}(E_{\mathrm{kin}}) = I_0 \frac{\frac{\Gamma}{2\pi}}{(E_{\mathrm{kin}} - E_0)^2 + \frac{\Gamma^2}{4}} \tag{2.37}$$

where the Full Width at Half Maximum (FWHM) is denoted by Γ and E_0 is the position for the maximum intensity I_0.
The experimental energy resolution (related to both the photon source and the energy analizer), the excitation of phonons in the solid, and the intrinsic sample inhomogeneity contribute to a Gaussian broadening of the photoemission peak.

Moreover *shake-up* and *shake-off* events may impact on the lineshape with an asymmetry contribution. When ejected, a photoelectron may cease part of its energy to other valence electrons, thus creating electron-hole pairs at the Fermi level, (*shake-up* event). But also other electrons can be emitted as a consequence of core ionization (*shake-off* event). In both cases, the actual photoelectron kinetic energy is lowered, thus the XPS peak has an asymmetric tail at higher binding energy.

The most common parametrization for the core-level lineshape in photoemission spectra, including all the previously mentioned physical effects, is a Doniach-Sunjic function convoluted with a gaussian.[70] The mathematical expression for a Doniach-Sunjic, Eq.[2.38], is basically a lorentzian function with an asymmetry parameter α

$$I_{\mathrm{DS}}(E_{\mathrm{kin}}) = I_0 \frac{\Gamma_E(1-\alpha)}{\left((E_{\mathrm{kin}}-E_0)^2+\frac{\Gamma^2}{4}\right)^{\frac{1-\alpha}{2}}}\zeta(E_{\mathrm{kin}}) \tag{2.38}$$

where α is the asymmetry parameter, Γ_E is the Euler Gamma function, and

$$\zeta(E) = cos\left[\frac{\pi\alpha}{2} + (1-\alpha)\tan^{-1}\left(\frac{E_0-E}{\Gamma/2}\right)\right] \tag{2.39}$$

Data analysis

In order to have an absolute energy reference, the binding energies of each spectrum were calibrated with respect to the Fermi energy of the sample (see discussion in subsection 2.2.1). All spectra were then normalized to the background intensity at the lower binding energy side, to exclude the effect of possible photon beam flux fluctuations and to account for different alignment geometries as well as gas phase adsorption. Depending on the specific sample, a linear or Shirley[71,72] background was subtracted, to rule out the effects of inelastic scattering of photoelectrons.

The spectra were analysed with a fitting procedure based on χ^2 square minization. As explained earlier, the fitting function is a Doniach-Šunjic profile convoluted with a Gaussian. Each peak is described by five parameters: the Lorentzian linewidth (Γ), the asymmetry parameter (α), the Gaussian linewidth (G), the intensity (I_0), and the binding energy position (E_0).

It is also worthy to note that XPS signals originating from levels with orbital angular momentum $l \geq 1$ ($l,\ p,\ d\ldots$ levels) are doublets, as a consequence of spin-orbit coupling. In fact, there are two possible states associated with the quantum numbers (l,s) if $l \geq 1$ (for electrons $s = \frac{1}{2}$), characterized by the two possible values of the total orbital momentum j

$$j = l \mp s. \tag{2.40}$$

The peaks in the doublet will also have a specific area ratio R, based on the degeneracy d_j of each state, given by $d_j = sj + 1$. In particular

$$R = \frac{A_{l+s}}{A_{l-s}} = \frac{2(l+s)+1}{2(l-s)+1} \tag{2.41}$$

where A_j is the area of a peak corresponding to the state with orbital quantum number j.

2.2.3 A NAP-XPS setup.

The NAP-XPS spectra presented in this thesis were collected at the NAP-XPS laboratory located at the Charles Univesity in Prague. We describe it in the following this commercial setup as an example.

Analysis chamber

The system is subdivided into the analysis and preparation chambers, communicating through a gate valve, with NAP and UHV manipulators respectively.
The analysis chamber is equipped with an X-ray radiation source, which emits Al Kα radiation ($h\nu = 1486.6$ eV) that is subsequenlty monochromatized.

A hemispherical electron energy analizer allows collection of XPS spectra at NAP conditions thanks to a differential pumping system equipped with electrostatic lenses for focusing, see

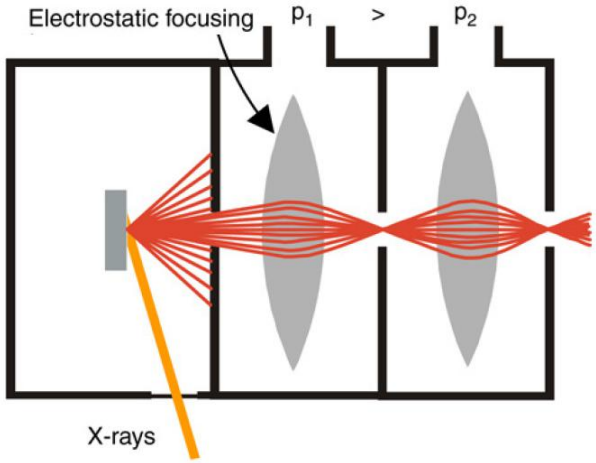

Figure 2.14: Schematic representation of differential pumping system used for photoelectron spectroscopy in ambient gas pressures. Electrostatic lenses refocuses the electron trajectories into the apertures connecting the differential pumping stages. Image from Salmeron *et al.*.[68]

the schematic representation reported in Fig. 2.14. This guarantees a pressure drop from 10^{-3} bar (NAP) to $10^{-7}/10^{-8}$ bar. In Fig. 2.15 we show a picture of the electron energy analyzer with the skimmer, the pumping and the focusing stage.

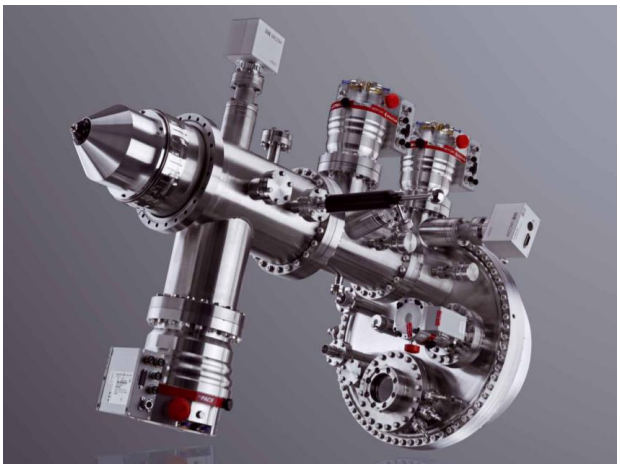

Figure 2.15: Electron energy analyzer with differential pumping system. Image from SPECS website.[73]

The Analysis chamber is also equipped with a quadrupole mass spectrometer, used for monitoring the composition of the residual gas atmosphere inside the NAP cell (QMS), a high resolution CCD camera to facilitate sample approach and positioning in the NAP cell and wobblestick to transfer the sample between the UHV manipulators and the NAP cell.
NAP measurements are carried out in the inner NAP cell, that is docked to the entrance aperture of the analyzer during measurements with a dedicated manipulator in a cell-in-chamber design.

NAP cell with gas inlet system

The NAP cell is represented in Fig. 2.16. It is fitted on a 3-axis manipulator in the NAP load lock chamber separated from Analysis chamber by a gate valve.

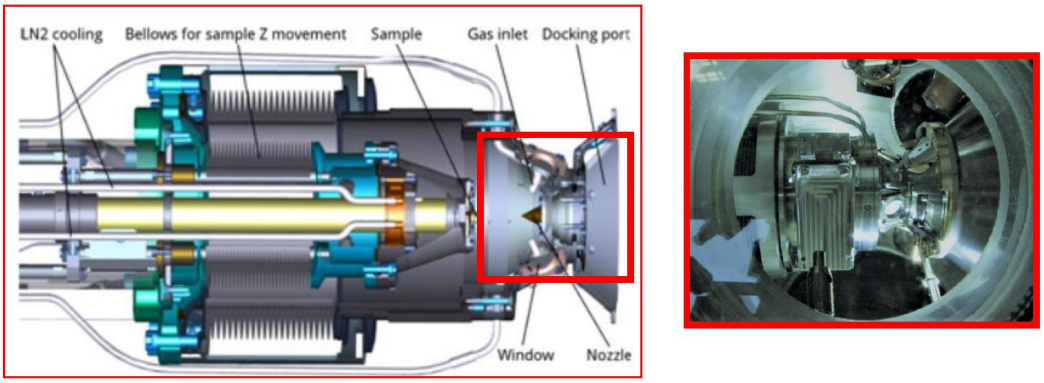

Figure 2.16: Schematic representation of the NAP cell on the left; a picture of the section higlighted in red, on the right. Both images are reprinted from SPECS manual.

The manipulator enables movement of the NAP cell through the gate valve to the Analysis chamber and docking of the NAP cell to the entrance aperture of the analyzer. The NAP cell is made of stainless steel and it is fitted with a sample holder stage, a loading door and a skimmer for photoelectrons with a 0.3 mm opening.

The sample is placed in a vertical position in the sample holder stage and it is grounded. The sample holder is also fitted by a K-type thermocouple to measure the sample temperature; a second K-type thermocouple is mounted permanently on the sample holder stage.

Sample heating is achieved through an external filament placed at the back side of the sample holder stage, outside the NAP cell. The external filament heats the back side of the sample holder stage by electron bombardment; the heat from the stage is then conductively transferred to the sample holder and the sample. The maximal reachable temperature of a sample in the NAP cell is 850 K. Also, at high temperature and in oxidizing atmosphere, formation of MoO_3 from the sample holder could lead to contamination of sample surface. To avoid this the temperature should not exceed $\sim$ 800 K. The sample holder stage has an inner circuit for the cooling of the sample by air/LN_2. The minimal sample temperature achievable by LN_2 cooling is 200 K.

Gases can be introduced into the NAP cell through three independent gas lines. The pressure in the NAP cell is monitored by a capacitance gauge with a working range from 0.03 – 133 mbar. The 0.3 mm skimmer separates the high pressure region of the NAP cell and the low-pressure region of the pre-lens system of the electron energy analyzer: it serves as a passage for photo-electrons generated from the sample. The drop of pressures across the skimmer is roughly of five orders of magnitude and the maximal pressure in the NAP cell depends on the gas type, for nitrogen or similar gases it is 20 mbar. However, the recommended maximal pressure for the photoemission experiment, with respect to the attenuation of the photo-electrons by the gas phase, is up to 5 mbar (N_2 or equivalent gas). The NAP cell is pumped by the skimmer itself continuously and additionally by an outlet (roughly of the same conductivity as the skimmer) fitted with a back pressure controller pumped by a turbomolecular pump.

The sample needs to be brought close to the skimmer for the NAP-XPS measurement. Approach and sample positioning is controlled by a high resolution camera through viewports installed on the NAP cell. The sample-skimmer working distance is approx. 0.3 mm. X-rays enter the NAP cell through an Al coated Si_3N_4 window (100 nm thick).

Chapter 3

Supported nanoparticles: The case of Pt clusters on graphene

We begin here the discussion of the research activity performed during this PhD project. We start tackling a model nanostructured system composed by dispersed Pt nanoclusters stabilized on a single layer of graphene. In the framework of this manuscript, this scientific case represents a "showcase" of the metodology of investigation followed during the research activity. We will present how the support must be properly characterized and tested, allowing the deconvolution of the information pertaining the substrate from that of the supported nanostructures. Then, we will introduce how we characterize the nanostrucutered surfaces in their pristine condition. Finally, we will present how the nanosystem evolves when progressively brought to realistic operative conditions by increasing both pressure and temperature.

3.1 Characterization of the support: graphene monolayer at mbar CO pressure.

We first introduce the support employed for the synthesis of the nanocluster array: a single layer of graphene grown on the Ir(111) single crystall termination. But, more importantly, we present the side-investigations required to describe how the pristine support (prior to the synthesis of the nanostructured features) evolves under extreme (from a surface physics point of view) conditions. This approach is necessary to achieve reliable information, discerning the effect of the nanostructures from the evolution of the substrate.

The Ir(111) single crystal was cleaned in the preparation chamber (see Section 2.1.3) by sputtering cycles at room temperature (Ar^+, 1.5 keV) followed by thermal annealing up to 1300 K, yielding a sharp (1×1) LEED pattern with a very low background intensity (see Fig. 3.1, left). I collected a IR-Vis SFG spectrum in the 1900÷2120 cm^{-1} spectral range at room temperature upon exposure of the Ir(111) surface to 4 mbar of carbon monoxide (see Fig. 3.1, right). A single peak is observed at 2085 cm^1. It is assigned to the stretching mode of CO molecules adsorbed on-top of the iridium atoms. No other resonances are observed.

Following a well-established recipe, the graphene sheet was grown through thermal cracking of ethylene (C_2H_4) on the Ir(111) surface. Firstly, ethylene was adsorbed at room temperature till saturation (6 L, where 1 L = 10^{-6} Torr*s) and thermally decomposed in ultra high vacuum at 1300 K, yielding the first graphene seeds. Then, chemical vapour deposition (CVD) was employed in order to increase the graphene coverage towards 1 ML. Two thermal cycles between 500 and 1300 K were performed in 5×10^{-8} mbar and 1×10^{-7} mbar C_2H_4,

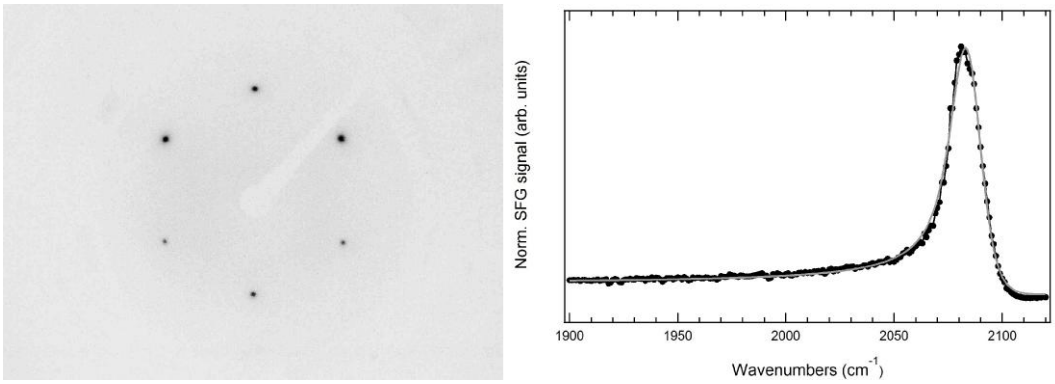

Figure 3.1: On left panel, a LEED pattern of the Ir(111) surface at 320 K (115 eV). On the right panel, IR-Vis SFG spectrum in the C-O stretching region collected *in situ* at 4 mbar CO on the Ir(111) single crystal termination [λ_{Vis} = 532 nm; ppp polarization].

respectively. After the last cycle, at $\sim$ 1125 K ethylene was evacuated and the sample cooled in UHV environment.
The obtained graphene single-sheet quality was checked through LEED, which revealed a sharp Moirè pattern (see Fig. 3.2, left panel). Moreover, we show in Fig. 3.2, right, an STM image of a graphene single foil obtained following this recipe.

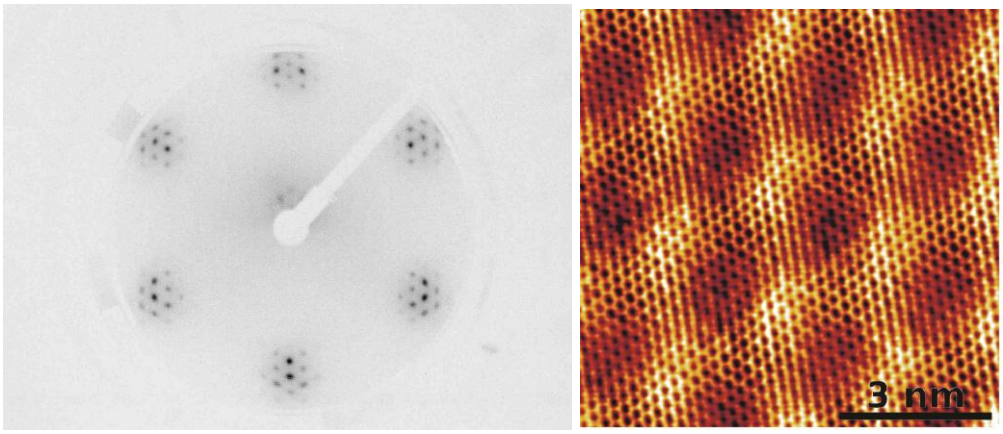

Figure 3.2: On the left, a LEED pattern of graphene at 335 K (85 eV). On the right, an STM image of the graphene single foil obtained on the Ir(111) surface following the recipe reported in Section 3.1. Image taken under UHV conditions at 4 K [V_{bias} = +0.1 V, I = 1 nA].

A SFG spectrum of the graphene single foil was collected in UHV environment at room temperature in the 1500÷1700 cm^{-1} spectral range (see Fig. 3.3, were its best fitting curve is also shown). Only one peak is present at 1610 cm^{-1}, and we assign it to the G band, associated with the doubly degenerate in-plane Transverse Optical (iTO) and Longitudinal Optical (iLO) phonon mode at the Brillouin zone center (see Fig. 3.4).[74]

In order to test the graphene quality and to investigate the presence of vibrational fingerprints due to possible contaminants ($Ni(CO)_4$ may form when stainless steel is exposed to high pressures of CO), I exposed a single foil of graphene at room temperature to 4 mbar of carbon monoxide. Spectra have been collected in the 1500÷1700 cm^{-1} and 1900÷2100 cm^{-1} ranges before and *in situ* during CO exposure. The collected spectra are reported in Fig. 3.3, after normalization with respect to the IR and Vis impinging signals. No peaks are present in the C-O stretching region, and the vibrational fingerprint of the optical phonon of

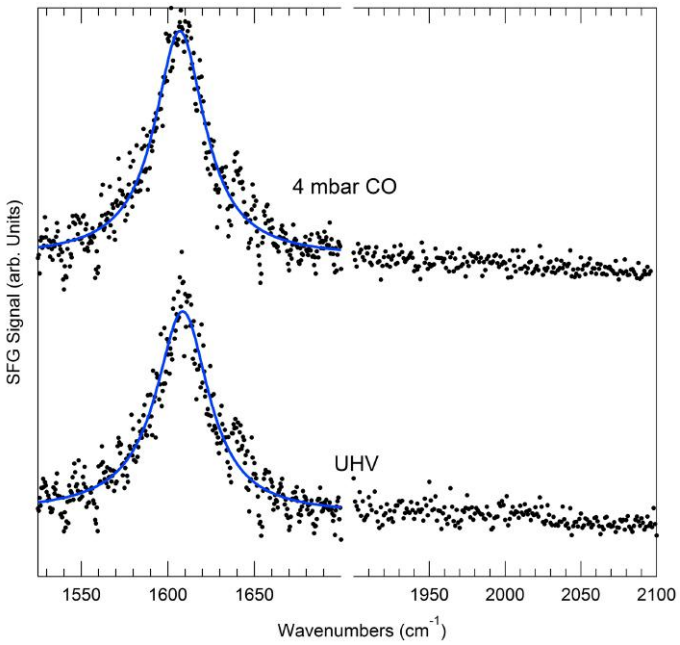

Figure 3.3: IR-Vis SFG spectra of Ir(111)-supported graphene in UHV conditions and in 4 mbar CO pressure. A single peak is present at ∼1610 cm^{-1} (left) while in the C-O stretching region (right) no features are detectable [λ_{Vis} = 532 nm; ppp polarization].

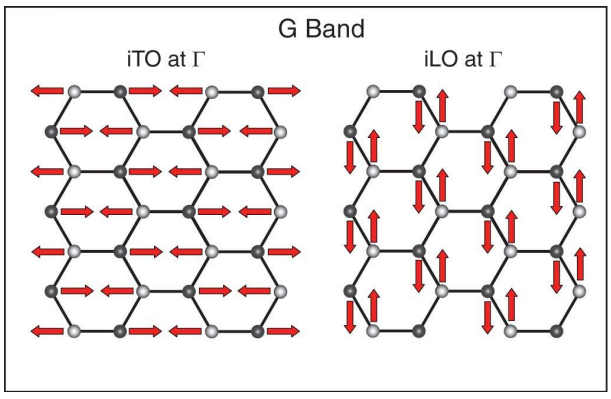

Figure 3.4: Representation of the In-plane Optical Transverse and Longitudinal (iTO and iLO) graphene phonon modes at the center of the Brillouin zone. Image from Malard *et al.*.[74]

graphene undergoes negligible modifications upon CO exposure.
Previous literature works report CO to intercalate under an incomplete (0.9 ML) graphene sheet grown on the Ir(111) surface, creating a coexistence of areas covered by intercalated graphene and non-intercalated ones.[75] The adsorption geometries and the induced chemical shift on the binding energy of the iridium $4f_{7/2}$ core level demonstrated high similarities between CO adsorbed on clean Ir(111) and CO intercalated under graphene.[75]
On the basis of these similarities, we expected to be able to detect and characterize intercalated CO in SFG measurements. However, we did not detect any fingerprint in the C-O stretching region spectrum of graphene exposed to CO (see Fig. 3.3, right). We consider this as a proof of the good quality of our graphene single foil, which was not subject to intercalation during the measurement. Moreover, the absence of contaminants able to adsorb on graphene is confirmed, together with the non-reactivity of graphene itself with respect to carbon monoxide.

3.2 Pt Nanoclusters on graphene/Ir(111).

Small metallic clusters are known to display structural, electronic, and chemical properties that are peculiar with respect to the corresponding bulk analogues.[76,77] Quantum-size effects may even yield nonmetallic behavior and the availability of reactive under-coordinated sites makes cluster-based catalytic systems of widespread interest. In the case of platinum, highly active and selective catalysts for the oxidation of propane have been successfully engineered on SnO and Al_2O_3 supports by exploiting few atoms Pt nanoparticles.[76] Pt concave sites are found to be very active for oxygen reduction, while isolated single Pt atoms play an important role in the CO oxidation and water-gas shift reactions.[78–80] For these applications, the practical realization of stable systems with very precise control on the clusters size distribution is extremely important.[81]

In this view, the support has a fundamental role for the growth and anchoring of the metal particles, and important research efforts are dedicated to the investigation of optimal templates within the families of both oxides and supported graphene (GR).[82] More specifically, the weakly interacting GR/Ir(111) system is one of the most studied models since the Moiré-induced geometric and chemical corrugation of GR, caused by the lattice mismatch with the underlying Ir termination, provides an optimal template on which metal particles can be grown in an essentially regular hexagonal array. Physical vapor deposition of Pt atoms at room temperature yields indeed a self-assembled cluster lattice, with particles adsorbed in the hcp sites of the GR Moiré unit cell and stable up to 400 K for small sizes and up to 650 K for large sized particles.[83] Deposition of 0.05 ML Pt/GR/Ir(111) yields the development in the C 1*s* core level spectra of a broad shoulder at the higher binding energy side of the main graphene peak.[84] The GR sheet undergoes deformation due to the cluster pinning, yielding a sp^2 to sp^3 rehybridization of GR carbon atoms squeezed at the Pt-Ir interface.[85] The main graphene C 1*s* peak is also shifted by +50 meV with respect to the bare sheet, due to Pt doping. Upon exposing the clusters to 10 L of CO, the rehybridization shoulder diminishes in intensity and the main C 1*s* peak shifts back to its original position. Clusters formed by less than ten atoms are unstable upon CO sticking and diffuse and coalesce yielding a Smoluchowski ripening effect.[84]

A time-resolved investigation reveals that the aforementioned changes in the spectroscopic signals set in already before the onset of clusters mobility. Therefore, CO adsorption influences the graphene rehybridization beneath the clusters before sintering. However, it is found that CO adsorption at on-top Pt sites does not compete for the same electronic density involved in the binding of Pt to the GR support, which takes place through the Pt($5d_{3z^2\text{-}r^2}$)-C($2p_z$) interaction. Instead, Density Functional Theory (DFT) calculations ascribe the observed

mobility to the adsorption of CO in bridge Pt sites at the borders of the clusters. However, population of bridge sites was not observed under UHV conditions,[84] at variance with the Pt/GR/Rh(111) case,[86] thus leaving this issue partly unsolved. Due to the applicative potential of GR-supported Pt catalysts, the morphological changes induced by adsorption are a crucial issue and have therefore been thoroughly investigated under vacuum conditions,[84,86–89] while for Pt single crystal terminations CO adsorption has been investigated also in the near ambient pressure (NAP) regime.[90,91]

In the following, I report a combined spectroscopic, microscopic, and theoretical investigation of the adsorption of CO on the Pt clusters grown on GR/Ir(111) at pressures from UHV up to 1 mbar. While I mainly contributed to the collection and analysis of the experimental spectroscopic and microscopic data, the theoretical DFT calculations and simulations were obtained through a collaboration with the International Center of Theoretical Physics (ICTP) and the theoretical group of the condensed matter physics section of the Physics Department of the University of Trieste.

The combined results provide evidence for the adsorption of CO in both top and bridge configurations on Pt clusters, with the population of several non-equivalent sites, spanning from first to second-layer terraces, to borders and edges, depending on the particle size and morphology and on the adsorption conditions. Upon heating above 420 K, CO spillover to the underlying Ir(111) surface is observed, catalyzed by the presence of the Pt particles.

3.2.1 UHV synthesis of the Pt nanoclusters

In order to thoroughly characterize the ordered array of Pt nanoparticles for the adsorption of carbon monoxide, we firstly applied the known growth recipes by evaporating Pt atoms from the physical vapor phase on the graphene Moiré at room temperature. By means of STM, we characterized the size distributions of the clusters for selected Pt loadings, namely 0.05, 0.09, 0.25, 0.75, and 1.5 ML. Our results are both qualitatively and quantitatively in agreement with recent literature concerning the cluster morphology and the Moiré filling factor,[89] thus providing a reliable starting point for the characterization at NAP conditions.

In Fig. 3.5, we plot a set of STM images with different lateral scales (from top to bottom: 50×50, 25×25, and 7×7 nm^2) for the five coverage values, together with the distributions of the cluster dimensions (bottom). The actual number of atoms was obtained in the following way: the apparent volume of each cluster, which depends on the shape and the electronic structure of the cluster itself and of the STM tip, was extracted by means of 2D profiling and z-cutting of the images, followed by a renormalization to the nominal Pt coverage. The latter was calibrated by imaging Pt ad-islands on the bare Ir(111) clean surface, in analogy to previous literature.[89]

For Pt loadings below a quarter of a monolayer, the cluster size distribution is found to be unimodal, with a single peak at 7 and 9 atoms per cluster for 0.05 and 0.09 ML Pt, respectively (Fig. 3.5, bottom, and Fig. 3.6, panel d). The Moiré filling factor (Fig. 3.6, panel a) grows rapidly to 80% and the superlattice mainly consists of single-layer clusters (Fig. 3.6, panel b). At 0.25 ML, 1- and 2-layer clusters coexist, with (average) sizes of 14 and 30 atoms, respectively, and almost saturate the Moiré, the distribution of the sizes becoming bi-modal. This peculiar feature of the cluster size distribution was not reported in previous literature.[84,89] Interestingly, each of the families of the largest clusters (0.25, 0.75, and 1.5 ML Pt) shows indeed a size distribution with two peaks, the second positioned at about twice the size of the first one (as evident both in Fig. 3.5, bottom panel, and in Fig. 3.6, panel d). This suggests that the largest clusters for each Pt loading originate from the coalescence of two adjacent smaller particles.

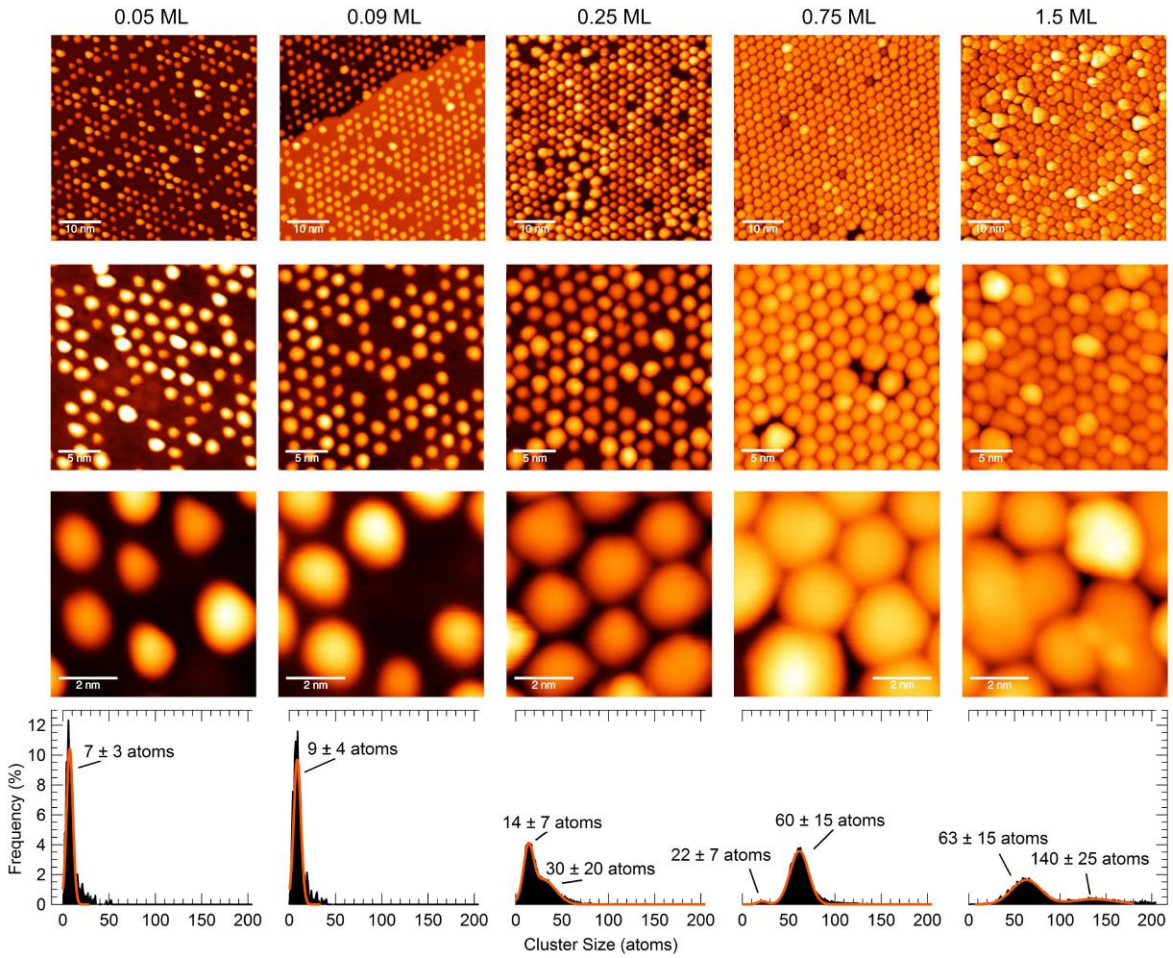

Figure 3.5: Selected STM images collected at 77 K after depositing Pt at room temperature on a single graphene layer on Ir(111); Pt loadings span from 0.05 to 1.5 ML (from left to right) and different image sizes are shown (from top to bottom: 50×50, 25×25, and 7×7 nm^2, respectively; V_{bias} = +1.0 V, I = 20-100 pA depending on image); in the bottom panel, corresponding size distributions (cluster size frequencies) are shown as obtained upon averaging on the whole STM images dataset: continuous lines represent fitting curves with Gaussian profiles (position and width of the peaks are reported in the text labels).

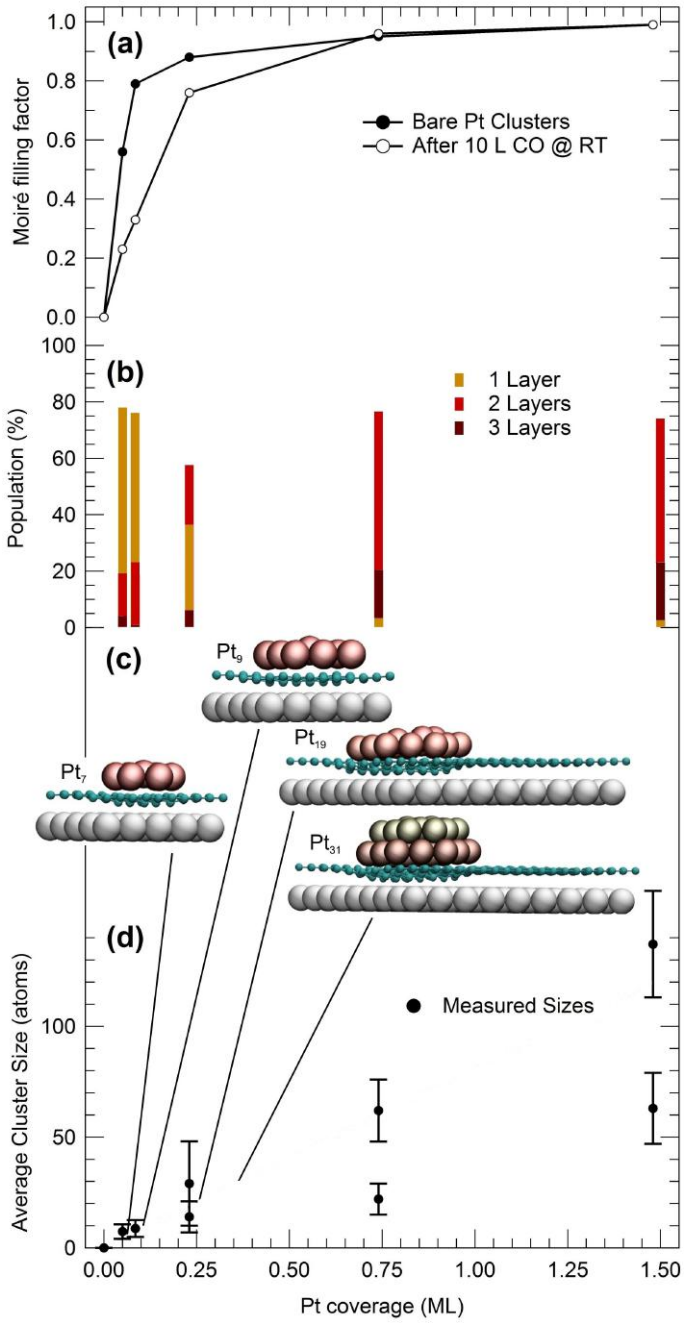

Figure 3.6: (a) Moiré filling factor prior and after exposure of the Pt clusters to 10 L CO at room temperature; (b) cluster height population of the bare Pt clusters (the bars are intended to start from zero and have been overlapped); (c) fully relaxed DFT models for clusters of 7, 9, 19, and 31 Pt atoms on GR/Ir(111) – color legend: Ir-white, GR-green, Pt-brownish (tone depending on height and layer); (d) measured average clusters sizes: they were obtained from the distributions plotted in the bottom panel of Fig. 3.5; data obtained from STM images.

Computational investigation of Pt_n morphology. From the *ab initio* calculations we found that for Pt_n nanoclusters with n>7 the aggregation in the hcp region is preferred (by 0.2 eV for Pt_9: $E_{ads\ hcp}$ = 10.43 eV, $E_{ads\ fcc}$ = 10.23 eV), but for smaller nanoclusters there is no preference between the two regions. These findings suggest high mobility of very small Pt aggregates, and are consistent with the absence of nanoclusters with n<5 in the experimental observation, even at very low coverage. From the experiments at 0.75 ML, 100% of the Moiré hcp sites are mostly populated by 2-layer clusters assuming evident hexagonal shape. At the highest investigated coverage (1.5 ML), coalescence between clusters growing in adjacent cells is dominant and evident from the images. Comparison between 1-layer and 2-layer configurations has been computationally carried out for clusters of various sizes. In line with the experimental observations, it has been found that there is a preference for 1-layer arrangement in aggregates with n<20 (Fig. 3.6, panel c).

CO adsorption on Pt_n cluster. Exposure of the former superstructures to 10 L of CO (10^{-7} mbar) at room temperature yields CO adsorption at the particles and mobility enhancement, thus promoting further coalescence. The filling factor decreases to almost half of the initial value for the smallest clusters, while larger particles are less influenced (Fig. 3.6, panel a). In Fig. 3.7, selected STM images of the CO-covered Pt clusters are shown for three Pt loadings. A regular structural pattern can be observed on the surface of the clusters (Fig. 3.7, insets), showing hexagonal symmetry. On the basis of previous observations on Pt single crystal surfaces, we conclude that the pattern is associated with CO molecules adsorbed at terminal Pt sites in a $(\sqrt{3}\times\sqrt{3})$ R30°-CO superstructure with a local CO coverage of 0.33 ML.[92]

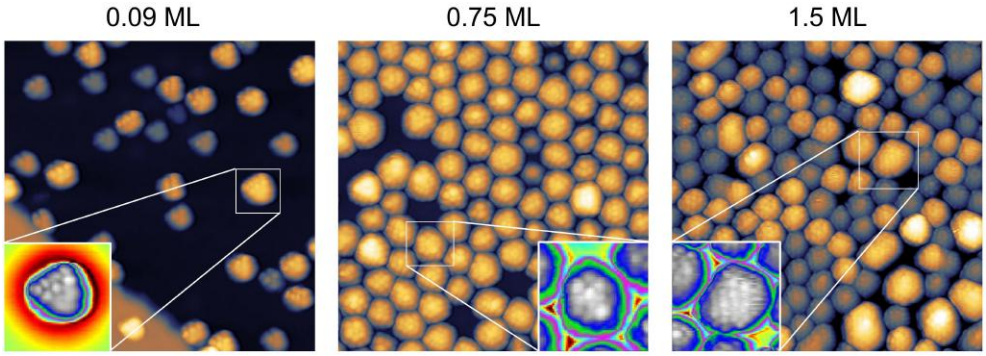

Figure 3.7: STM images collected at 77 K after exposure of the Pt clusters to 10 L CO at room temperature (pCO = 10^{-7} mbar); insets (zoomed) show selected clusters with enhanced color contrast to highlight the CO-induced corrugation [25×25 nm^2, V_{bias} = +0.1 V, I = 50 pA].

The DFT simulation of a 31 Pt atom cluster, structurally relaxed in the hcp adsorption region on the graphene Moiré, and covered with 8 CO molecules adsorbed at Pt in on-top configuration of both the surface layer and edge sites, is reported in the top panel of Fig. 3.8. The adsorption of CO induces a buckling in the cluster's structure and repulsive dipole interactions between the ad-molecules yield a tilt of the molecular axes. The agreement between the experimental and simulated STM image can be appreciated from the figure, where the CO superstructure cell is highlighted in orange. A less bright halo surrounds the clusters in the observed STM image. Interestingly, our simulated images reproduce also this feature: some molecules adsorb in bridge sites across the first and second Pt layers, pointing laterally and therefore appearing lower and darker than those adsorbed in top sites in the uppermost Pt layer and forming the brighter $(\sqrt{3}\times\sqrt{3})$ R30° superstructure. Computationally, we extensively investigated the effect of CO adsorption at nanoclusters of different size. As

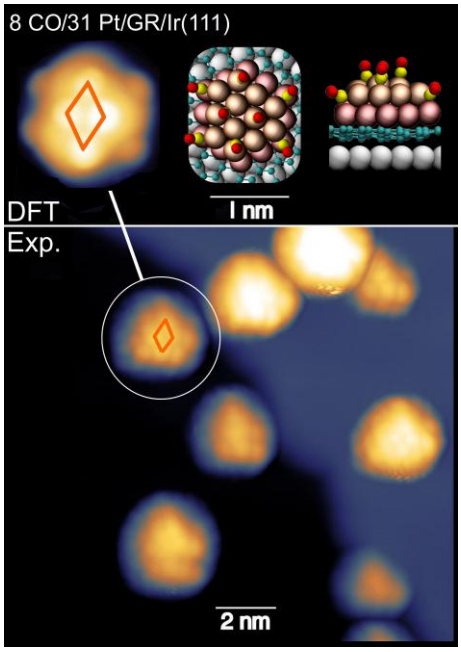

Figure 3.8: Comparison between experimental STM imaging of CO-covered Pt clusters (large image) and DFT simulations (upper panel, left) of a 31 atoms Pt cluster hosting 8 CO molecules; the upper panel on the right shows the model (top and side views) of the fully relaxed cluster structure, including the graphene sheet and the underlying Ir(111) terminal layer; the orange parallelograms indicate the $(\sqrt{3}\times\sqrt{3})$ R30°-CO unit cell (see text for details).

selected examples, we show in Fig. 3.9 the DFT optimized structures of Pt_4 (top) and Pt_{19} (bottom) clusters for increasing CO coverage (from left to right). The calculated adsorption energy E_{ads} referred to one CO molecule is also reported in Fig. 3.9. For high CO coverage on Pt_{19}, a sizeable reduction of E_{ads} is found, from 2.28 eV to 1.64 eV, due to intermolecular repulsion. Much smaller variations are found in case of Pt_4, from 2.00 to 2.13 eV at most, since the CO molecules have enough space to tilt and reduce their mutual repulsion. For CO adsorption on the Pt(111) single crystal surface, we obtain E_{ads} values ranging from 2.06 (zero coverage limit) down to 1.8 and 1.39 eV, in case of 0.5 and 1.0 ML (full coverage), respectively. Therefore, the presence of the GR/Ir(111) support seems to improve the affinity of Pt with respect to CO, yielding an overbinding effect.

Pt_n restructuring. Our calculations for supported Pt_4 nanoclusters show that their structure is almost unaffected by the adsorption of a single CO molecule (Fig. 3.9, top panels). Analogously, Pt_{19} is almost flat in absence of CO and the adsorption of a molecule does not have relevant effects on the cluster shape, apart from a local lifting of the CO bonded Pt atoms (Fig. 3.9, lower panels). However, the scenario changes with the adsorption of more CO molecules. When 12 CO molecules are adsorbed, the cluster is restructured, assuming a dome shape, with the central Pt atoms pulled up. The effect is even more evident with the adsorption of 17 CO molecules. The restructuring reduces the number of Pt atoms bonded to graphene, making the nanocluster-graphene interaction weaker. The strong affinity of Pt towards CO may explain the overall energy gain upon CO adsorption and reconstruction of nanoclusters, overcompensating the removal of Pt-GR bonds. As a rule of thumb, while the average strength of the Pt-GR bond is of the order of 1 eV in a flat nanocluster of 5 to 21 atoms, the average adsorption energy of CO is about twice (from 1.6 to 2.2 eV depending on the CO coverage, see Fig. 3.9). The repulsion between the adsorbed CO molecules may

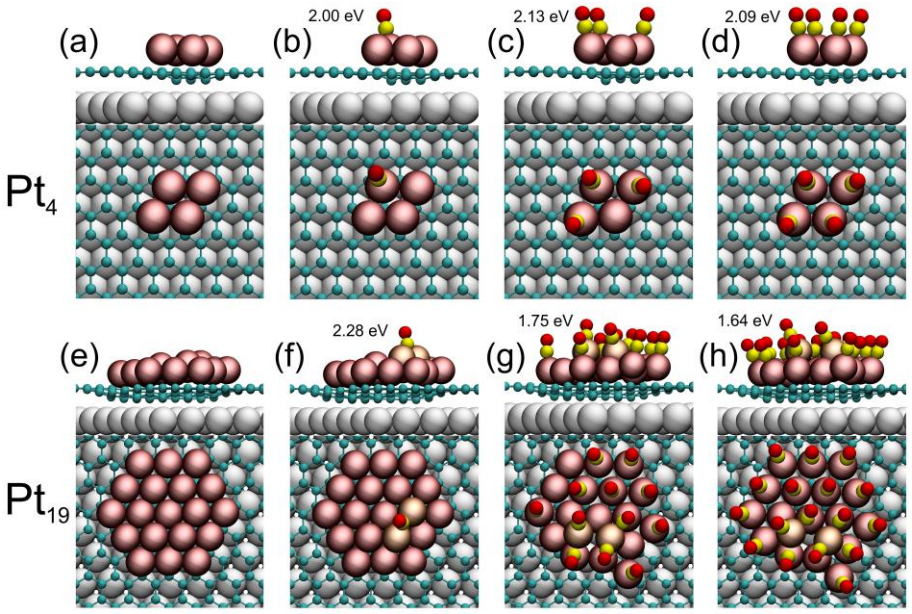

Figure 3.9: Fully relaxed DFT models for clusters of 4 (top, from a to d) and 19 atoms (bottom, from e to h) at increasing CO coverage (from left to right, specifically: 0, 1, 3, 4 CO on Pt_4 and 0, 1, 12, 17 CO on Pt_{19}) – color legend: Ir-white, GR-green, Pt-brownish (tone depending on height), C in CO-yellow, O in CO-red. The average CO-Pt binding energy is also reported.

induce the nanocluster restructuring, since a dome-like shape allows larger CO-CO distances and tilting with respect the adsorption on a perfectly flat Pt island. We can therefore argue that the mechanism described above is likely to cause an increased mobility and consequently the observed Smoluchowski ripening. The peculiar shape of restructured nanoclusters allows the adsorption of CO in different configurations, mainly in non-equivalent top sites (with Pt atoms that are either directly bound to graphene or not) and in bridge sites, as in the case of the Pt_{31} nanoclusters with intermediate CO coverage (Fig. 3.8, top panel). This result provides a qualitative rationale for the different peaks in SFG spectra that will be discussed in the following.

3.2.2 Towards near ambient pressure

IR-vis SFG vibronic spectroscopy measurements of the C-O stretching resonance were performed *in situ* upon exposure of the ordered Pt clusters at room temperature to carbon monoxide pressures progressively increasing from 10^{-8} to 1 mbar. Fig. 3.10 displays the SFG data together with the best fit and the deconvolution of the resonances according to the procedure described in the methods sections. Four non-equivalent stretching modes (Pi, i = 1÷4), corresponding to CO molecules adsorbed in non-equivalent sites, are observed, depending on the adsorption conditions.

Two vibrational features are observed for the lowest Pt coverage (0.05 ML) in 10^{-8} mbar CO: P_2 at $\omega_2 = 1975$ cm^{-1} (green) and P_3 at $\omega_3 = 2039$ cm^{-1} (violet), blue-shifting with increasing pressure up to 2000 and 2071 cm^{-1}, respectively. At first glance a single broad and dispersive spectral feature may be used for the best fit of the observed SFG intensity modulation. However, it is found that two features are necessary to accurately reproduce the experimental data, thus confirming the presence of two distinct contributions. In addition, a third peak, P_1 (yellow), with very low intensity and dispersive lineshape is observed at $\omega_1 = 1845$ cm^{-1}.

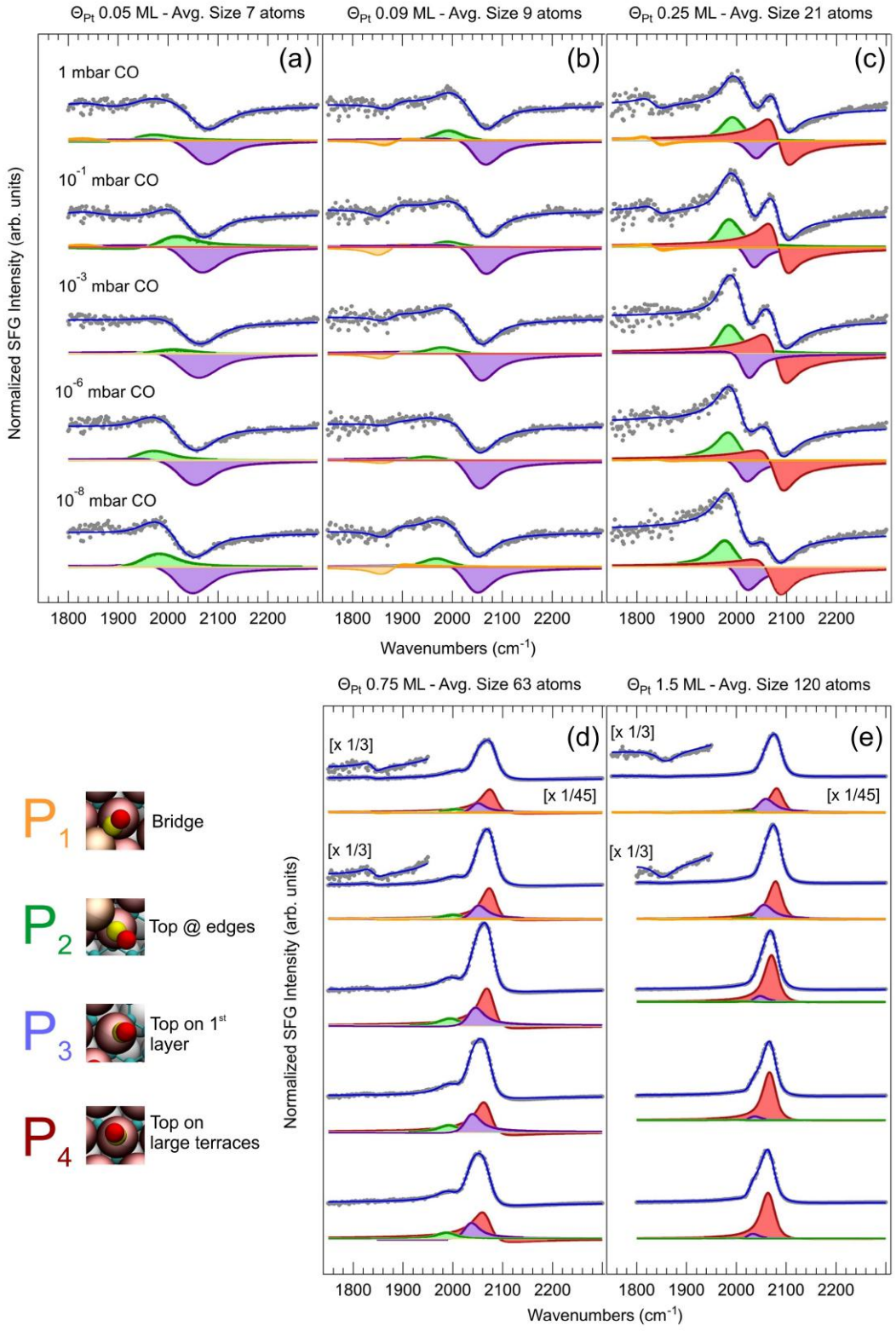

Figure 3.10: IR-vis SFG spectra in the C-O stretching region collected at room temperature *in situ* for increasing Pt cluster size (from a to e) and for increasing CO pressure (from bottom to top in each of the panels) spanning from UHV to NAP conditions. Data (grey dots) and the results of the least-squares fitting (blue lines) are shown; color-filled curves represent deconvoluted intensity modulations with respect to the non-resonant background (see text for further details); the labeling and color mapping of the deconvolution is shown in the bottom left part of the figure, together with pictorial models for the non-equivalent CO adsorption sites [λ_{Vis}= 532 nm; ppp polarization].

Table 3.1: Positions of the C-O stretching resonances together with literature referencing and proposed assignment. Models of the adsorption sites are depiscted in the last column and are intended as exemplative only.

Resonance	Energy (cm^{-1})	Reference (cm^{-1})	Assignment (adsorption site)	
P_1	1840-1870	1845-1855[96–98]	Pt-bridge	
P_2	1980-2010	2000[94]	Pt-top @ edge, corners	
P_3	2015-2060	2065-2078[99,100]	Pt-top @ borders, 1st layer terraces	
P_4	2060-2090	2072-2104[96–101]	Pt-top @ terraces of large clusters	
P_5	2040-2057	2063-2079[51,63]	Ir-top, intercalated under graphene	
P_6	1880	-	Pt-bridge	

A significant Gaussian broadening of the whole spectrum is also found (σ= 25 cm^{-1}), suggesting a consistent structural and chemical inhomogeneity, in agreement with the STM measurements.

A similar situation is observed also for 0.09 ML Pt, with ω_1 = 1871 cm^{-1}, ω_2 = 1969-1993 cm^{-1}, and ω_3 = 2041-2057 cm^{-1}, respectively, while the Gaussian broadening reduces to σ= 15 cm^{-1}. At 0.25 ML Pt a fourth feature P_4 (red) appears in the ω_4 = 2076-2087 cm^{-1} range, depending on the CO pressure, and the inhomogeneity contribution further decreases to σ= 11 cm^{-1}. The intensity of the fourth resonance increases by almost one order of magnitude when further increasing the Pt cluster size up to 1.5 ML, while no additional features appear.

As a general trend, the lineshape analysis of the IR-vis SFG signal reveals a relevant weakening of the observed Gaussian broadening, from 25 down to 7 cm^{-1}, for increasing Pt loading. This is in agreement with the STM images that show an increased degree of order of the superlattice for larger particles. In addition, higher CO pressures yield a typical, progressive blue-shift of the stretching features, consistently with a denser CO phase at the clusters' surface and with the CO-induced coalescence of adjacent particles.

Inequivalent, cluster-size dependent adsorption sites. The line positions and the assignment of the SFG resonances are reported in Table 3.1. The position of the resonances can provide precious information about the strength of the CO bonding to the metal, and thus about the adsorption site. Upon adsorption on Pt, the C-O stretching frequency is red-shifted with respect to the gas-phase value, due to the weakening of the C-O molecular bond. This is readily understood on the basis of the bonding mechanism, well described within the framework of the Blyholder model.[93–95] The hybridized states between CO and Pt originate from the σ electron donation from the 5σ orbital of CO to the vacant $6sp$ conduction band of Pt and from the π back-donation from the $5d$ of Pt to the vacant antibonding $2\pi^*$ orbital of CO. The latter is mainly responsible for the weakening of the C-O bond and hence the red-shift with respect to the resonance at 2170 cm^{-1} of free CO.[93] In the case of adsorption

on Pt, a simple model can be obtained by considering the coordination number. The lower the Pt coordination number, the stronger the Pt-CO interaction, thus the stronger the electron back-donation and the weaker the C-O bond.[94] On the basis of the above considerations and with reference to established literature, we then attribute the highest energy feature P_4 to CO molecules adsorbed on top of Pt atoms in the middle of (111) terraces on multi-layer clusters (Pt-Pt coordination 9).[96–101] Indeed, P_4 grows for Pt loadings higher than 0.25 ML when 2-layer clusters start growing. Consequently, we associate P_3 with CO at on top Pt sites of (111) terraces of single-layer clusters (Pt-Pt coordination 6) at 0.05 and 0.09 ML Pt coverage. For thicker clusters, we attribute this feature to CO adsorbed on top of edge Pt atoms at the borders of the first layer of the cluster (Pt-Pt coordination number 7).[99–101] P_2 instead gives a negligible contribution to SFG spectra from small clusters, while its intensity grows for higher Pt loadings. By applying the same reasoning, we conclude that it is due to CO molecules on top of edge Pt atoms on single-layer clusters and of corner atoms on multi-layer clusters (Pt-Pt coordination 4 and 3).[94] Lastly, P_1 is the lowest energy feature that we observe, almost exclusively for high CO pressures and with growing intensity for larger cluster sizes. Under high CO coverage conditions (> 0.5 ML), carbon monoxide adsorbs on (111) terraces forming a c(4×2) superstructure, so that also bridge sites get populated.[92,98,101] For CO adsorbed in this configuration both the IR and Raman cross-sections are smaller, thus explaining the lower intensity with respect to molecules at terminal Pt sites.[98] We therefore attribute P_1 to CO molecules at bridge Pt sites.

In our SFG spectra we observe that progressively larger (111) facets associated with CO-induced ripening of the clusters,[84] yield a more homogeneous system and smaller Gaussian contributions to the spectral inhomogeneity broadening. From the fitting procedure the phase of the resonances with respect to the non-resonant background can also be obtained. In Fig. 3.11 we therefore plot the relative phase ϕ_4 as a function of the system and adsorption pressure, and ϕ_4 together with ϕ_5 as a function of the temperature (details in the following). As it can be directly observed also by eye when looking at the raw SFG spectra, we measure a clockwise rotation of the phase for increasing CO pressure, temperature, and cluster size, thus with the progressive formation of larger (111) Pt facets. If we exclude geometric contributions due to a change in the average orientation of the CO dipole, this effect may by associated with the electronic transition that is involved in the resonant SFG vibronic process. This issue has already been investigated by means of doubly-resonant SFG spectroscopy on the CO/Pt(111) system,[93] and the charge-transfer state associated with the C-O stretching mode was found to be at 2.51 eV, with a bandwidth of 0.83 eV, thus close to and compatible with our visible beam excitation (532 nm, 2.33 eV). The resonance involves the transition from the $5d$ to the $6sp$ orbital of Pt hybridized with the 5σ orbital of CO. Therefore, changes in the Pt electronic configuration due to cluster restructuring may be indirectly reflected in the apparent resonance's phase. The latter may be interpreted as a spectroscopic fingerprint of the dispersion and ripening of the clusters' superlattice when CO is exploited as a probe molecule.

3.2.3 The issue of thermal and chemical stability: CO spillover to the Ir(111) surface

Vibronic information in 0.1 mbar CO. When heating the system above room temperature in 10^{-1} mbar CO, several changes are observed in the SFG spectra. In Fig. 3.12 we plot the C-O stretching region measured in the 300-575 K range for 0.05 (left) and 0.25 ML (right) of Pt on graphene. Let us consider Fig. 3.12. From 425 K the P_4 component (red) is replaced by P_5 (light red), with a noticeable phase change and with a burst in amplitude (notice that the spectra at 500 and 575 K have been divided by two in order to fit into the

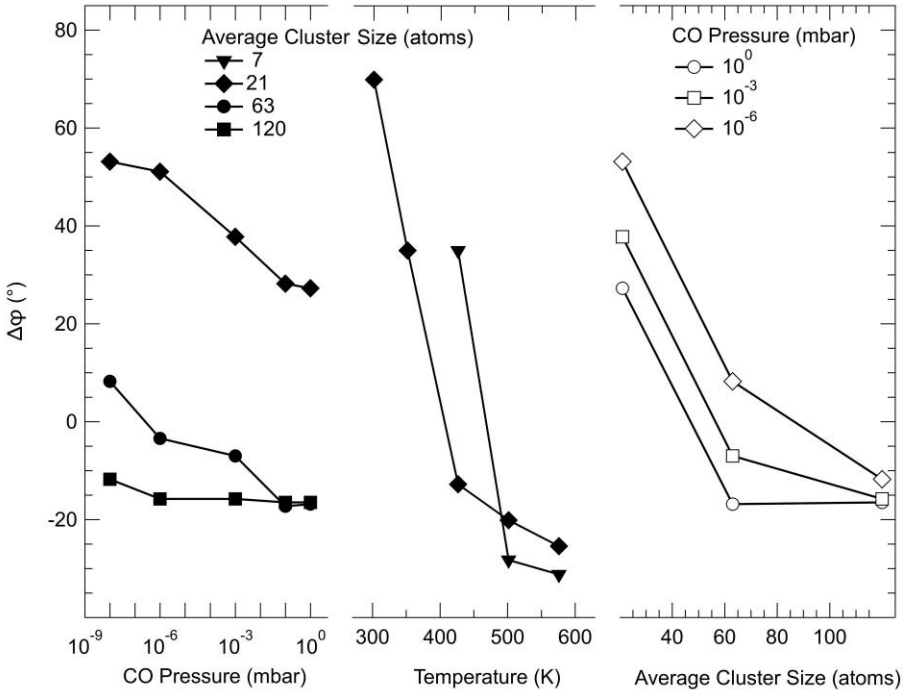

Figure 3.11: Relative phase of the IR-Vis SFG C-O stretching resonances with respect to the nonresonant background for different cluster sizes as a function of CO pressure at room temperature (left), sample temperature in 10^{-1} mbar CO (center), and as a function of the cluster size at different CO pressures (right).

panel), showing a red-shift of about 50 cm^{-1} down to the 2040-2057 cm^{-1} range, depending on the conditions. While the phase shift mostly occurs at low temperature (Fig. 3.11, central panel), the red-shift of the peak is more gradual with temperature. The first effect can be ascribed to a change in the electronic structure of the adsorption site, compatibly with the spillover of CO from the Pt clusters to the Ir surface, while the red-shift is associated with temperature-related anharmonic coupling with the CO frustrated translation modes,[102] as already observed for CO/Ir(111), where the C-O stretching mode is observed in the 2063-2079 cm^{-1} interval,[63] close to the values we find here. The intensity burst of P_5 may instead be associated with the progressive growth of densely packed CO islands at the Ir(111) surface, as observed in the case of CO intercalation at the GR/Ir interface.[75] CO adsorption on Pt (111) islands at near ambient pressure conditions would instead yield a sharp resonance at about 2100 cm^{-1}, thus at higher energy.[96,103] In parallel, in the case of the large clusters, a new and broader component (P_6 - cyan) grows at about 1880 cm^{-1}, most probably associated with thermal induced loss of registry and inhomogeneity of CO in bridge Pt sites.[96]

Near Ambient Pressure XPS in 0.1 mbar CO In order to better understand the observed behavior, we also collected NAP-XPS spectra. In Fig. 3.13 we plot the C 1s (a and b) and Pt $4f_{7/2}$ regions (c) measured at room temperature (bottom) and at 420 K (top) in 10^{-1} mbar CO on the bare graphene (a) and on the 0.25 ML Pt on graphene systems (b and c). In the former case, no CO adsorption occurs and there is no evident change upon heating in the C 1s lineshape at 284.1 eV associated with graphene, apart from an increased Gaussian broadening due to thermal effects. No C-O stretching features are observed in the SFG spectra either. Since CO does not stick on graphene, this indicates that a perfect and complete graphene single layer was grown and that no CO intercalation occurred. Indeed,

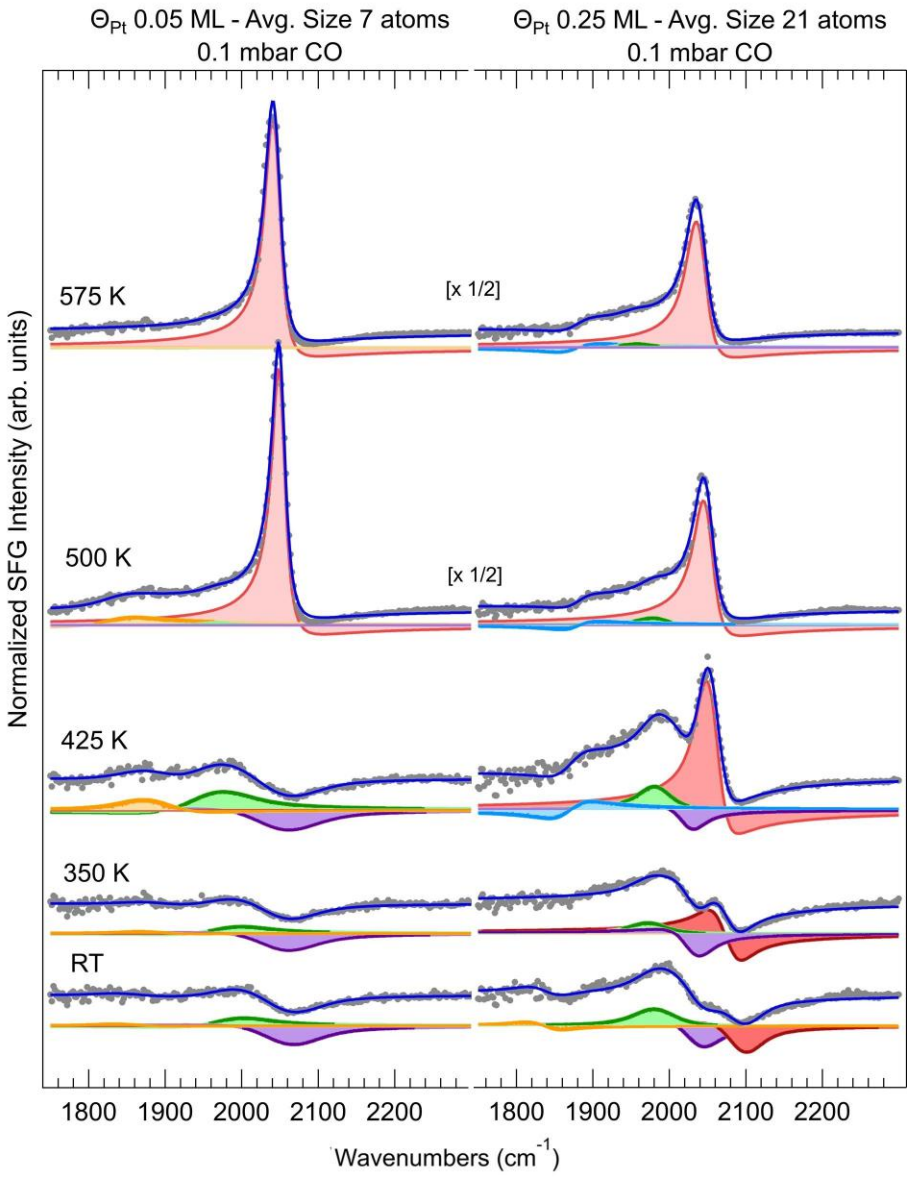

Figure 3.12: IR-vis SFG spectra in the C-O stretching region collected *in situ* at 10^{-1} mbar CO as a function of the sample temperature for 0.05 ML (left) and 0.25 ML Pt (right), respectively [λ_{Vis} = 532 nm; ppp polarization].

when the graphene sheet is defective or incomplete, small molecules like CO and O_2 have been observed to intercalate and adsorb at the underlying Ir(111) surface at near ambient pressure conditions.[75,104]

When the Pt clusters are present (Fig. 3.13b, bottom), instead, a broad rehybridization shoulder appears in the C 1*s* spectrum at higher binding energy (yellow peak), at the expense of the intensity of the peak at 284.1 eV. This is in remarkable agreement with CO adsorption

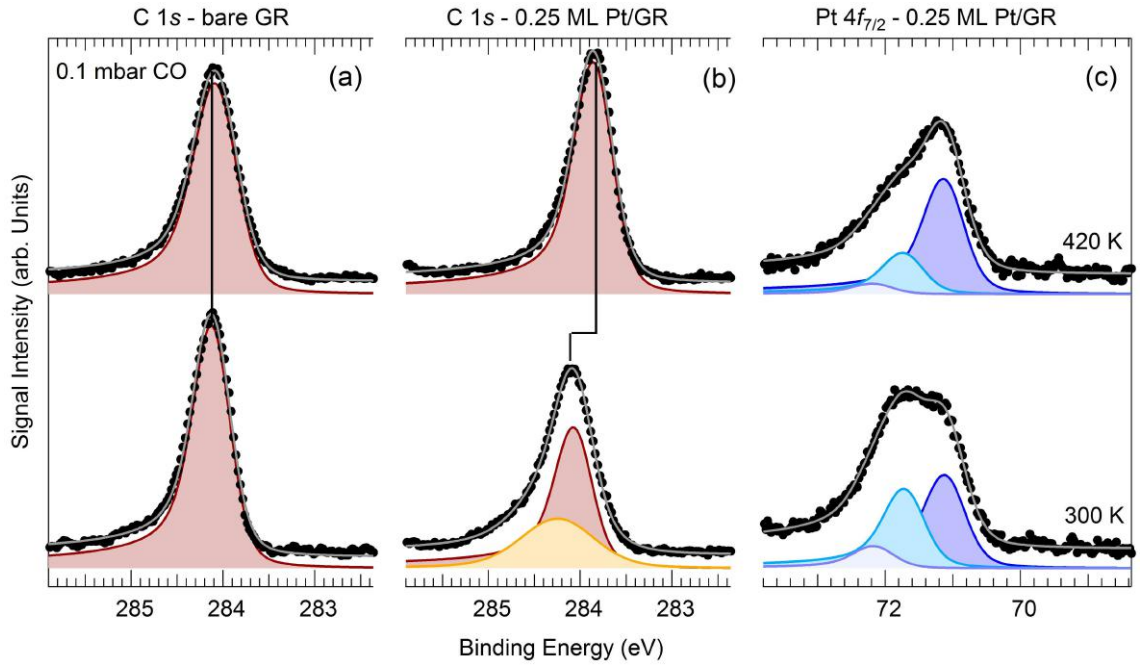

Figure 3.13: NAP-XPS spectra in 10^{-1} mbar CO collected at room temperature (bottom) and at 420 K (top): C 1*s* region (a) from the bare graphene sheet on Ir(111); C 1*s* (b) and Pt $4f_{7/2}$ (c) regions of Pt clusters (0.25 ML Pt on graphene) [hν = 1486.6 eV, PE = 10 eV].

on the same system under UHV conditions.[89] The broad feature is attributed to the non-equivalent sp^3 C atoms of graphene in between the Pt clusters and the underlying iridium surface.[84,85,88,89] Upon heating, we observe a -0.3 eV shift of the main graphene component (284.1 eV) to lower binding energy (283.8 eV), while the high binding energy feature is not visible any more. A shift of -0.3 eV of the graphene C 1*s* peak has already been observed at near ambient pressure in the case of intercalation of CO between the graphene and the Ir(111) surface, where the $(\sqrt{3}\times\sqrt{3})$ R30°-CO/Ir(111) superstructure is formed.[75,105] We thus conclude that, upon annealing, Pt catalyzes the intercalation of CO to the underlying metal surface. Consistently, we find that the C 1*s* feature at 286.3 eV associated with CO (see Fig. 3.14) grows in intensity upon annealing from room temperature to 420 K. Pt $4f_{7/2}$ core level spectra collected *in situ* provide further insight (Fig. 3.13, panel c). It is already known that the geometric and chemical inhomogeneity of Pt atoms combined in a small cluster structure show a progression of different Pt 4*f* chemical shifts.[85] Indeed, while Pt ad-islands on the bare Ir(111) surface yield a single sharp contribution at 70.88 eV, in the case of a single layer 19 Pt atom cluster on the graphene sheet the spectrum spans 1 eV in binding energy, with a principal contribution at about 70.8 eV. Adsorption of CO on a nanostructured Pt surface at 10^{-1} mbar was found to induce, besides the bulk Pt $4f_{7/2}$ component at 71.10 eV, the growth of two spectroscopic features shifted by +0.60 and +1.05 eV, associated with terrace and low-coordinated Pt atoms bound to CO.[91] A similar upshift of the Pt core level binding energy upon adsorption of CO was already observed on our same system under UHV

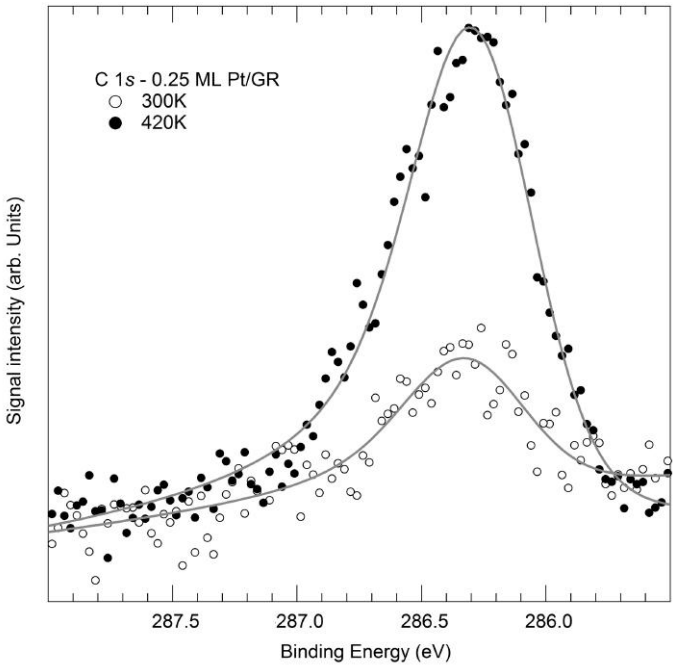

Figure 3.14: C 1s core level spectra in the CO region at 0.1 mbar CO for the 0.25 ML Pt/GR system.

conditions.[89] As shown in panel c of Fig. 3.13, the same components as in the case of the stepped Pt surface were successfully used to deconvolve the Pt spectra presented here. It is important to note that the higher binding energy components were found to grow in intensity with increasing CO pressure from 10^{-9} to 10^{-1} mbar in the case of CO-induced rippling of a single crystal Pt surface, yielding nanometer sized clusters.[91]

In the present case of Pt clusters on the GR/Ir(111) template, upon annealing we observe a decrease in the intensity of the core level shifted components, compatibly with a cluster coalescence process. It has indeed already been shown, in the case of Rh clusters grown on the same support,[106] that a bulk-related metal core level component is already observable for clusters of 60-80 atoms and accounts for about 50 % of the signal after temperature-induced coalescence of 0.37 ML Rh clusters, thus supporting our assignment of the 71.10 eV feature to bulk-coordinated Pt atoms. The mechanism for CO intercalation is unexplained yet: the increased intensity of the Pt $4f_{7/2}$ component at 71.10 eV at the expense of the CO-induced features is compatible with the formation of larger Pt agglomerates, while the graphene network is catalytically opened to allow CO spillover to the GR/Ir(111) interface. Remarkably, previous STM investigations have demonstrated that Pt clusters (0.25 ML Pt) are stable on GR/Ir(111) up to 400 K, whereas coalescence sets in for higher temperature.[82] Cycles of CO adsorption at room temperature followed by oxidation at 575 K on this system under UHV conditions (10^{-7} mbar) have shown that the Pt clusters undergo reversible shape changes, with a decreased radius and increased thickness in presence of CO with respect to the clean system, in a breathing-like cycle.[88] In any case, no degradation of the underlying graphene sheet has been observed under these vacuum conditions, at variance with our near ambient pressure experiments where Pt particles promote diffusion of CO under the graphene sheet. Temperature-induced cluster intercalation has been observed for strong interacting graphene systems like GR on Ru, Ni, and Rh, but to our knowledge this was not observed at the Ir surface, even if a possible role of gas phase reactants was suggested.[87] In the present case, we observe the disappearance of the high binding energy feature in the C 1*s* XPS spectrum of GR at 420 K (Fig. 3.13, panel b, top), possibly indicating that the sp^3 C atoms at the

Pt-Ir interface are not present any more, or at least are reduced in number. This may be a further confirmation that the CO-Pt interaction is stronger than the Pt-GR interaction, the latter being further weakened upon adsorption of CO, similarly to what proposed under UHV conditions.[89] Alternatively, it may also be compatible with the intercalation of the Pt clusters under GR, but further investigations are necessary to confirm this latter interpretation.

3.2.4 Conclusions

Our results put in evidence the importance of our systematic NAP approach, allowing us to add new important considerations even in the well-established research area of dispersed Pt nanoclusters and nanoparticles.

We studied the adsorption of CO from UHV to near ambient pressure on a regular array of Pt nanoclusters supported by graphene/Ir(111). By means of a combination of experimental techniques (*in situ* non-linear photon in – photon out spectroscopy, photon in – electron out spectroscopy, microscopy), and numerical simulations based on *ab initio* methods, we find that both terminally and bridge bonded CO species populate non-equivalent sites of the clusters, spanning from first to second-layer terraces, to borders and edges, depending on the particle size and morphology and on the adsorption conditions. A significant restructuring of the clusters is observed upon CO adsorption at room temperature, promoting particles sintering for small clusters and reshaping for large ones. In the latter case, Pt atoms in the center of the cluster are lifted upon binding with CO and a progressively lower Pt-Pt coordination is observed for increasing CO coverage. Above room temperature, Pt clusters catalyze the spillover of CO at 10^{-1} mbar to the underlying graphene/Ir(111) interface, permanently modifying the initial nanostructured system.

Chapter 4

Activity of model single-site catalysts: chemistry and quantum effects

After putting in evidence possible limitations of catalytic systems based on dispersed nanoparticles, we start in the following chapter the discussion about a different category of model nanostructured systems, the so-called Metal-Organic Frameworks (MOF). As introduced in Section 1.2, in particular we will focus on bio-inspired SMAC model systems.

While in Section 4.1 we introduce how they can be synthesized in vacuum conditions employing specific molecules presenting the structure of the already discussed heme group, in the following of the Chapter we will present two examples of the activity of the resulting surfaces. Not only the interaction with simple gas phases of NO and CO will be discussed, but we will exploit the scientific cases also to focus on the role of the support and of cooperativity in the case MOF systems.

4.1 SMAC systems from self-assembling metallorganic molecules.

The synthesis of SMAC systems can be quite straightforward in UHV conditions if an accurate choice of the metallorganic molecules and of the supporting template is adopted. Exploiting heated crucibles to evaporate molecular films on the desired support, it is possible to take advantage of flat metallorganic molecules containing a single metal atom, like metalated Porphyrins and Phthalocyanines. On the proper substrate, these molecules can not only adsorb parallel to the surface (allowing their single metal atom core to interact with the gas phase), but also self-assemble in ordered lattices. As the organic backbone already stabilizes the metal sites, the supporting substrate can be selected without concern about sintering. In addition, the support itself can be exploited as an additional parameter to drive and tune the electronic, self assembly, and catalytic properties of the nanoarchitected SMAC system.

4.1.1 Tetra-Phenyl Porphyrins (TPPs).

Porphyrins stand out from other organic molecules hosting single metal atoms because of their structural and thermal stability properties. Their planar structure offers indeed the perfect framework for surface-science studies, as they adsorb on a variety of substrates while exposing their monometallic center.[107] The simplest example of a porphyrin is porphin (Fig. 4.1a), a planar hetero-macrocycle consisting of four pyrrole moieties linked by methin groups. In the non-metalated form, two pyrrolic hydrogen atoms saturate the porphin

ring.[108,109] However, porphin is quite rare as peripheral substituents can be easily added. New compounds are formed, as protoporphyrin IX (the precursor of heme groups, see Fig. 4.1b) and Octaethylporphyrins (Fig. 4.1c). In particular, another compound named tetra-phenyl porphyrin (TPP, Fig. 4.1d) is formed when four phenyl groups are added at the methine bridges.

Among the properties of all porphyrinic complexes, metalation is of peculiar interest: it is a naturally occurring phenomenon that can be attained for most elements in the periodic table.[110–112] The square-planar coordination environment given by the nitrogen atoms at the center of the macrocycle can indeed host a metal atom, that substitutes the two hydrogen atoms.

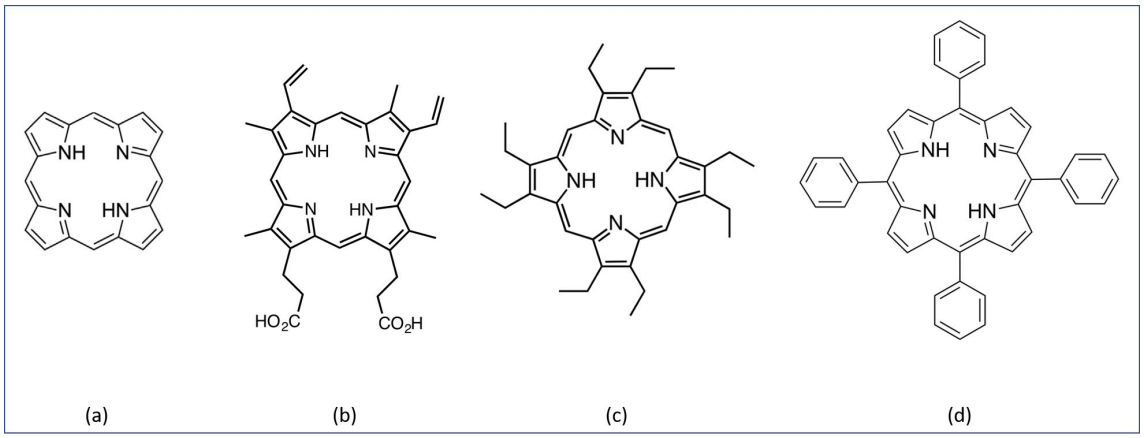

Figure 4.1: Schematic representation of a Porphyn (a), a Protoporphyrin IX (b), an Octaethylporphyrin (c) and a Tetra-Phenyl Porphyrin (TPP). Image from Gottfried *et al.*.[107]

For $3d$ metal ions, the ionic radius well matches the available space between the coordinating nitrogen atoms, thus keeping intact the planar structure of the molecule. For larger metal ions, saddling of the structure usually occurs.[113] In the adsorbed state, metalated porphyrins (or Metal Porphyrins, MPs) usually strongly interact with the substrate, resulting in a modification of the chemical, electronic, and magnetic properties of the metal center. Furthermore, the planarity of the molecules grants access to the ions from both sides of the molecular plane, so that both cis- and trans-coordination to ligands may occur (see Fig. 4.2), depending on the adsorption geometry.

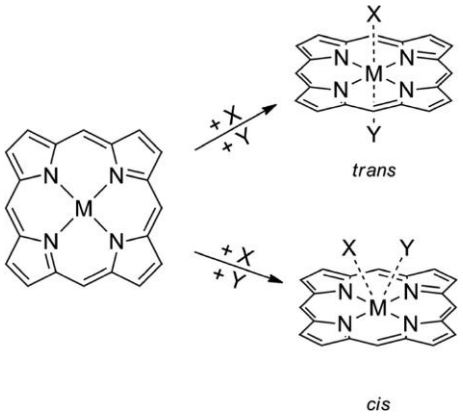

Figure 4.2: Schematic representation of ligation for a Metal Porphyrin: both trans- and cis-coordination can be achieved. Image from Gottfried *et al.*.[107]

Metalation has been investigated with great interest because these metal centers represent unsatured units for charge transfer and ligation of adducts.[114] The metal center axial coordination site that points away from the surface can interact with a ligand (or more than one), or be the active center of a reactive process.[113] When a ligand binds with the metal center, a competition for the strongest bond is established between the ligand itself and the substrate (this is generally referred to as the *trans effect*), modifying once more the charge distribution of the whole complex.[115,116] The variety of metal complexes, added to the availability of different substrates and axial ligands, offers many possible arrangements and tunable properties. Depending upon the characteristics of both substrate and ligands, very different total charge distributions may be produced resulting in different interaction strengths with aforementioned ligands.
The number of functions that exploit porphyrins and metallocomplexes, both naturally occurring in biology and tailored in science and technology, are countless.[107] As far as the SMACs approach to heterogeneous catalysis is concerned, applications for porphyrins have already been found. CoTPPs supported on TiO_2 were used to catalyse the reduction of nitric oxides with CO.[117,118] (Cl)FeTPP anchored on carbon nanotubes were employed in the oxidation of hydrocarbons and sulphides in water,[119] whereas Fe, Cu, Co and Ni porphyrins were tested for the electroreduction of CO_2.[120,121]

In order to maximize the interaction with the substrate, the adsorption of TPPs is usually parallel to the surface but with the phenyl rings exhibiting a tilt away from the surface. The rotational motion of the phenyl rings is coupled to a saddle-shape deformation of the macrocycle, by which the rotational barrier is reduced.[122–124]

4.1.2 Metal- Phthalocyanines (MPcs).

Phthalocyanines (Pc) closely resemble the porphyn derivates, but their central ring consists of a porphyrazin group. In the latter case, nitrogen replaces the carbon atom of the methin bridges. In addition, phthalocyanines exhibit four benzenic rings at the periphy of the pyrrolic groups, forming 4 isoindolic moieties (see Fig. 4.3).
Phthalocyanines, in close analogy to porphyrins, can accommodate and stabilize single transition metal atoms, forming what is generally referred to as Metal-Phthalocyanines (MPcs). While exposing the catalytic core, they are reported to strongly bind to metallic substrates and even on weak-interacting substrates. This is the case of adsorption on graphene, where the interaction takes place through a π-bonding between the aromatic rings of the Pcs and the graphene sheet. Almost no distortion of the molecular plane is reported in this case.[125] On the contrary, on metal substrates the metal-metal interaction may prevail and yield a distortion of the planar geometry.[107,114]

Both porphyrins and phthalocyanines are able to self-assemble in ordered film structures whose arrangement (depending both on the nature of the metallic centre and on the supporting substrate, but also on the coverage[126]) can be tuned, resulting from an interplay between molecule-molecule and molecule-substrate interactions.
An example is the adsorption in the submonolayer regime of iron phthalocyanines (FePcs) on the Ag(110) surface. Two stable energetically degenerate but structurally distinct rectangular c(10×4) and p(10×4) domains are formed by FePcs deposited on the Ag(110) surface in the submonolayer coverage, and they coexist even after prolonged annealing up to 520 K. However, if a complete monolayer is formed, the thermal treatment converts the molecular lattice into an oblique $(1\pm4,4\mp3)$ superstructure.[126] In Fig. 4.4 the distinct, coverage-dependent configurations are reported.
The role of the support can be appreciated in the case of adsorption of iron phthalocyanines on a graphene single foil grown on the Ru(001) surface. At low coverage, dispersed single

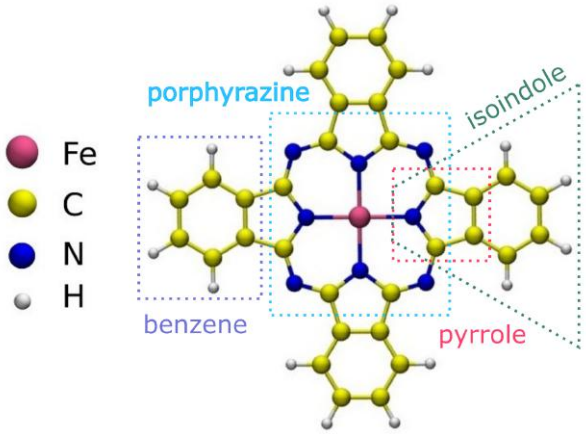

Figure 4.3: Stick and ball schematic representation of an iron phthalocyanine.

molecules and isolated chains were observed, while increasing the coverage to 0.75 ML yields a Kagome lattice following the Moirè structure pattern of the underlying graphene sheet (see Fig. 4.5).[127] Thus, a correct choice of growth parameters allows to obtain well-ordered layers of evenly spaced monoatomic metal-active centres, resulting in a stable SMAC model.

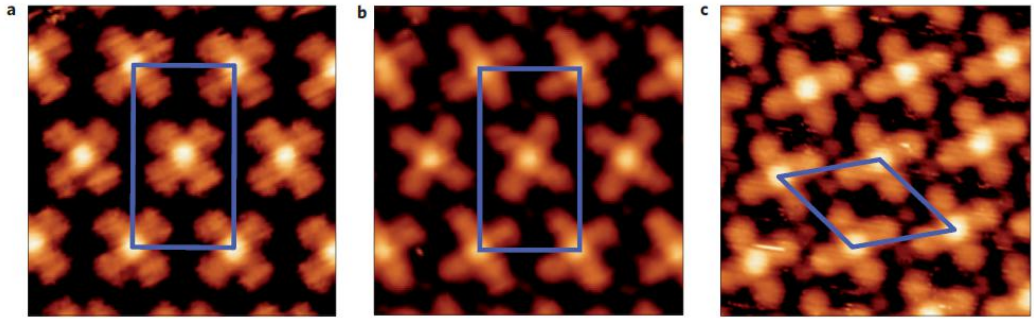

Figure 4.4: (5,2×5,2 nm^2) STM images of: **a)** rectangular c(10×4) structure (V_{sample} = 0.365 V, I=0.20 nA), **b)** rectangular p(10×4) structure (V_{sample} = 0.537 V, I=1.00 nA), and **c)** oblique (1±4,4∓3) structure (V_{sample}=0.029 V, I =0.15 nA). Figure from Sedona *et al.*.[126]

It has to be pointed out that porphyrins and phthalocyanines are reported to posses a high thermal stability. Especially, phthalocyanines undergo sublimation and then decomposition between 500 and 800 K.[128] Thin films can be therefore readily prepared by Physical Vapour Deposition, sometimes referred to as Organic Molecular Beam Epitaxy (OMBE), in vacuum. However, the stability and reactivity of the achieved metal-organic layer has to be investigated, both in the UHV environment and in operative catalytic conditions. In the following we will discuss two investigations pertaining adsorption of simple diatomic molecules (NO and CO, respectively) on ordered lattices of metalated tetrapyrrolic rings.

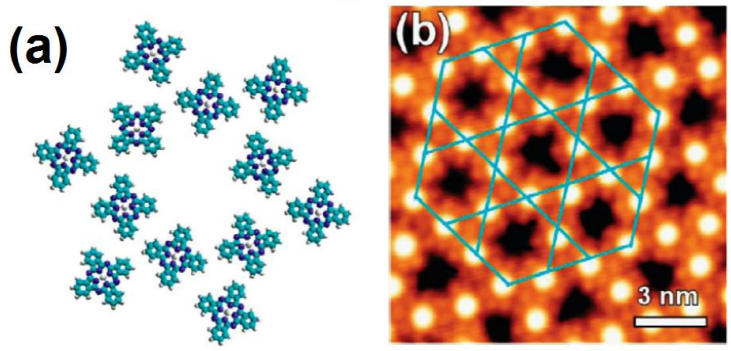

Figure 4.5: FePc on graphene/Ru(0001): STM images obtained after RT deposition of 0.75ML of FePc on graphene/Ru(0001).(a) Structural model of the Kagome lattice, (b) Details of the Kagome lattice of FePc with unit cell (marked with blue lines). Figure from Mao *et al.*.[127]

4.2 Hyponitrite synthesis on Nickel tetraphenyl porphyrins (N_2O_2-NiTPP/Cu(100).

The first SMAC system that we introduce is constituted by a layer of nickel tetraphenyl porphyrin (NiTPP) molecules deposited on the Cu(100) single crystal surface. This system presents a strong charge transfer from the substrate that alters the molecular electronic and catalytic properties.[129] We show in the following that, probably resulting from such charge redistribution, a single or a double layer of NiTPP exhibit a completely different response with respect to NO adsorption. While the multilayer (which is not in contact with the metallic surface) is almost not affected by NO exposure, the single NiTPP layer interacts with NO at room temperature already at UHV-compatible pressures. We then present, supported by experimental data and numerical simulations, an hypothesis about how at the Ni centers NO may be efficiently catalyzed, forming a new species (possibly hyponitrite - N_2O_2) stabilized at the single Ni sites. For these reasons, the NiTPP/Cu(100) SMAC system may represent a perfect biomimetic model system of several enzymatic centers found in Nature catalyzing the conversion of toxic NO to useful compounds. Moreover, as its activity is already observed at UHV conditions, it also represents a perfect model system for systematic surface science investigations.

4.2.1 Mimicking NO conversion in enzymes: NO adsorption at Ni sites.

Enzymes can be considered as the perfect prototype of the fundamental active structures in biological systems. As they are characterized by high binding selectivity and efficiency, an increasing number of researchers are looking at them as blueprints for novel synthetic catalysts.[130] Intriguingly, the key constituents of several enzymatic reaction centers involved in methanogenesis,[131] catalytic oxidation,[132] and nitric-oxide reduction[133] are metal-containing tetrapyrroles, closely related to the central ring of porphirins and phthalocyanines. Nitric oxide reductase (NOR) enzymes, such as NorBC and Cytochrome P450,[46,134] take advantage of the selectivity provided by this reactive core.

One of the mechanisms proposed in the description of the NO conversion process in NOR involves, in the intermediate step, the formation of a hyponitrite (N_2O_2) moiety, resulting from the coupling of two NO molecules.[134] However, as far as we know this species has been directly detected only upon stabilization under cryogenic conditions (70 K),[135,136] whereas examples of stable N_2O_2 at room temperature, close to the ambient environment, have not

been reported.

The fundamental quantity ruling the average residence time of a molecule at a surface is the adsorption energy (see Appendix 6.2). Values in the range of the eV are demanded in order to ensure stability of an adsorbate at room temperature in UHV conditions. As an example, in the case of mono-carbonylation of a FePc monolayer an adsorption energy of only few tens of meV has been measured. Thus, a mean non-negligible population of adsorbed CO species can be detected at room temperature only in the mbar pressure range.[51] Another example concerns again CO adsortpion on metalated tetrapyrrolic centers: cis-dicarbonyl adsorption schemes were observed on metal-supported porphyrins (two CO per MP) only at 20 K, as the system results unstable at higher temperatures.[137]

In the specific case of NO adsorption, for metal-supported porphyrin arrays, it is commonly accepted that only a single NO molecule coordinates to the porphyrin metal center.[115,138,139] Therefore, the proposed pathway leading to N_2O_2 formation through NO di-cordination would be hardly accessible at room temperature. However, in the following we will present evidence about why the NiTPP/Cu(100) interface is a unique model system, where the mono-coordination scheme may represent only the first step.

Room temperature stable adsorption.

While my contribution mainly focused on the IR-Vis SFG measurements and will be presented in the following, in the framework of a larger collaboration (with the research groups of the NanoESCA and ALOISA beamline at the Elettra synchrotron radiation facility) we highlighted the changes in the organic film upon adsorption of nitric oxide employing also STM and XPS techniques.

The clean Cu(100) surface was prepared by cycles of Ar^+ ion sputtering at 2.0 keV, followed by annealing at 800 K. The absence of contaminants was checked by XPS. The ordering of the surface and molecular layer was investigated by means reflective high-energy electron diffraction (RHEED) method during XPS experiments and low-energy electron diffraction (LEED) in the case of IR-Vis SFG measurements. A few mg of NiTPP (Porphyrin Systems) were loaded into a quartz crucible of a home-made Knudsen cell type evaporator and thermally evaporated at ∼520 K onto the copper substrate kept at room temperature. For XPS and IR-Vis SFG measurements, the molecular coverage has been calibrated with a quartz microbalance.

It is known from the literature that NiTPPs sublimated and self-assembled on Cu(100) at room temperature, under ultra-high vacuum conditions (UHV), show a partial filling-up of their lowest unoccupied molecular orbitals (LUMOs) up to LUMO+3, favoured by the close proximity of the porphyrin macrocycle (∼2 Å) to the copper surface.[129] This charge rearrangement at the organic/metal interface affects the properties of the NiTPP film, possibly enhancing its reactivity. We tested the NiTPP array model system by exposing it to an increasing dose of nitric oxide, while keeping the sample at room temperature (RT). All the measurements were carried out under UHV conditions (base pressure $\sim 1\times10^{-10}$ mbar) and the sample was exposed to NO using partial pressures in the range between 5×10^{-7} to 5×10^{-6} mbar).

Due to the strength of the molecule-substrate interaction, the STM contrast of a NiTPP molecule arises from the phenyl substituents that are strongly tilted upwards, preventing the macrocycle to be resolved by the STM tip. For this reason, the overall appearance of the porphyrin is mainly dominated by four asymmetric bright lobes (phenyl legs) with a dark depression in the centre (macrocycle).[129] In Fig. 4.6 we present a high resolution low-temperature STM image taken after exposing the NiTPP/Cu(100) surface to 2000 L of NO at room temperature. Circular protrusions appear at the centre of the porphyrin

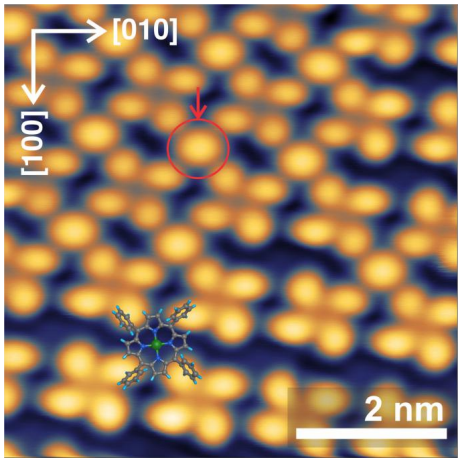

Figure 4.6: High resolution STM image of the NiTPP/Cu(100) film after NO exposure of 2000 L. Circular protrusions appear at the Ni atom position (circled in red) while some molecules remain unchanged. STM image parameters: V_{bias} = -1.0 V, I = 0.1 nA, image size 5.5×5.5 nm^2. T= 4 K.

macrocycles and their number increases with the NO dose. Some of them can be removed by the tip during the raster scanning of the surface, as revealed by comparing the forward and backward STM images. We associate these new features to NO molecules bound to the macrocycle.[138,140] Notably, neither observable changes in the unit cell nor in the orientation of the NiTPP with respect to the substrate were observed upon exposure of the molecular system to the nitric oxide. No features different from circular protrusion were found on the pristine molecules after NO exposure in the range 60-4000 L. Even though it is widely accepted that NO binds directly to the chelated metal ion in the macrocycle, XPS spectra of the Ni $2p_{3/2}$ core level shell provide valuable information on the NO-Ni interaction, allowing also to quantify the number of active centres involved in the adsorption process.

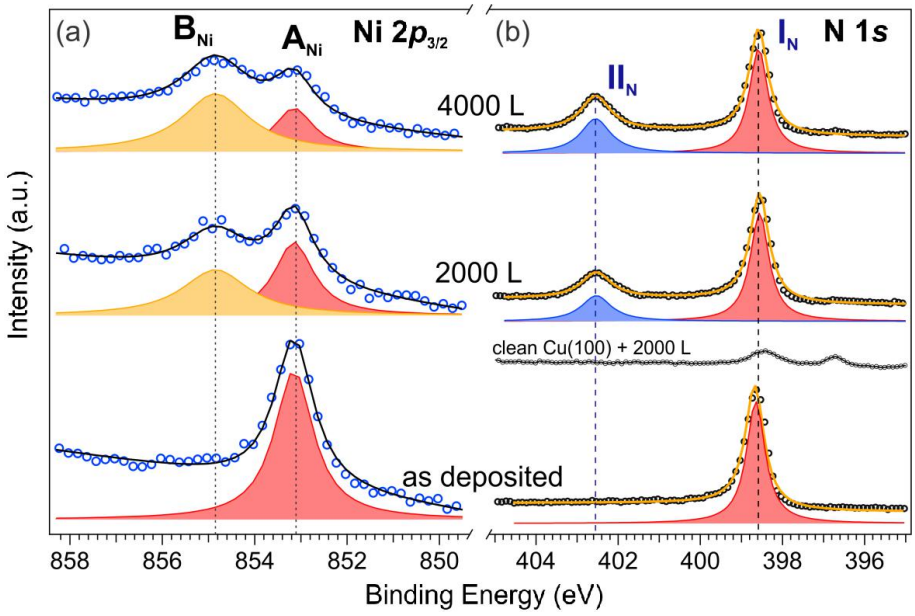

Figure 4.7: (a) Ni $2p_{3/2}$ and (b) N 1s core level photoemission spectra (experimental data and fits) of NiTPP/Cu(100) before and after exposure to 2000 L and 4000 L of NO. N 1s region measured after the exposure of clean copper to 4000 L (black curve) also is shown in panel (b). Photon energies: Ni $2p_{3/2}$ hν = 1000 eV and N 1s hν = 515 eV.

Fig. 4.7a (bottom) shows the Ni $2p_{3/2}$ core level spectrum of the pristine NiTPP self-assembly on Cu(100). The binding energy, as well as the full width half maximum of the peaks, were determined using a Doniach-Šunjić lineshape,[70] convoluted with a Gaussian in order to account for energy resolution, temperature, and heterogeneity effects. The main Ni $2p_{3/2}$ peak (A_{Ni}) at a binding energy of 853.15 eV (Lorentzian FWHM ∼1 eV) is assigned to the core level of the central Ni ion in a formal +1 oxidation state. Remarkably, the low valence state of nickel resembles the one of the cofactor F430,[141] confirming the system as a biomimetic model.

After NO exposure, a new feature (B_{Ni}) arises at a higher binding energy (854.85 eV, see Fig. 4.7a, middle). Increasing the NO dose, this component grows at the expense of A_{Ni}. We therefore associate B_{Ni} to the Ni atoms directly interacting with the nitrogen monoxide, in line with our STM analysis. Moreover, the B_{Ni} binding energy shift witnesses the oxidation of the nickel atom as a consequence of the interaction with the adsorbed NO molecules.
By properly fitting the Ni $2p_{3/2}$ core level, we were able to carry out a semi-quantitative analysis of the spectra upon NO dosage. Neglecting in a first approximation photoelectron diffraction contributions, by comparing the Ni $2p_{3/2}$ spectra after exposure of the NiTPP/Cu(100) film to 2000 and to 4000 L NO, we found that about 50% and 75% of the NiTPP molecules host nitrogen species, respectively.

In order to obtain further insight into the NO coordination, we followed the changes in the N 1s core level induced by the corresponding NO exposures of the NiTPP/Cu(100) film. The XPS spectra are presented in Fig. 4.7b. Quantitative parameters, such as binding energy position, Lorentzian FWHM and area of the peaks were obtained using a Voigt line shape in the best fitting procedure. The N 1s spectrum of the pristine NiTPP covered surface shows a single sharp peak at 398.65 eV (I_N), assigned to the core level ionization of the four nitrogen atoms of the macrocycle. Its binding energy is in good agreement with previously reported values for similar systems.[142,143] Then, the molecular film was exposed to NO and a new spectral feature (II_N) appears at 402.55 eV (see Fig. 4.7b, middle top). We tentatively associate II_N to the nitrogen of the NO molecules bound to the Ni atom of the macrocycles.

A control experiment, where the bare copper surface is exposed to nitrogen monoxide under the same experimental conditions, excludes a direct NO-copper interaction. The corresponding XPS spectrum is reported in Fig. 4.7b (middle low, black curve). Here, two components at binding energies of 398.4 eV and 396.7 eV, respectively, contribute to the N 1s core level. The former is associated to NO molecules bound to the copper surface,[144] while the latter to the atomic nitrogen resulting from the NO dissociation, respectively.[145,146]
An almost negligible residual contribution from atomic N can be detected also in the XPS spectrum shown in Fig. 4.7c, top, suggesting that the NiTPP layer does not fully saturate the copper substrate, allowing the NO dissociation to take place at the few uncovered areas or at the surface defects. The presence of adsorbed nitrous oxide (N_2O) moieties, which can be formed by disproportionation of NO at the surface, is excluded in the present case, because of the absence of the spectroscopic N 1s fingerprints at 402 and 406 eV associated with the latter species.[145,146]

The issue of the NO/NiTPP ratio.

We consider now the relative concentration of the different nitrogen species. Since four nitrogen atoms in each NiTPP molecule contribute to I_N, the ratio between II_N and I_N peak areas can be used to estimate the amount of NO molecules adsorbed on the organic film. Remembering that not all the NiTPP molecules interact with NO (from Ni 2p 50% and 75% for 2000 L and 4000 L, respectively) we would expect the II_N/I_N ratio to be 0.25 for adsorption of a single NO at each porphyrin (i.e. upon saturation). Our data, however,

yield intensity ratios of about 0.4 and 0.5 for exposures of 2000 and 4000 L, respectively, which are not compatible with the adsorption of a single NO but, surprisingly, suggest that actually two NO molecules bind to each NiTPP. It must be noted that cross-section differences and scattering processes, neglected in the present analysis, cannot account for such a large discrepancy between the expected and measured values of the intensity ratios. Moreover, density functional calculations (discussed below) and the large linewidth (1.75) eV of the II_N feature (which may arise from two inequivalent nitrogen species adsorbed at theNi atom) confirm this picture.

4.2.2 IR-Vis SFG: insights about NO adsorption geometry.

Unfortunately, from the XPS data it was not possible to unravel the NO-Ni bonding configuration, nor get final evidence considering the number of adsorbed NO molecules per Ni atom. For this reason, a systematic characterization by means of IR-Vis SFG spectroscopy has been performed, investigating the evolution of the vibrational spectra varying the NiTPP surface coverage and the NO exposure.

The NiTPP vibrations: a complex, coverage-dependendt spectral landscape.

The NiTPP monolayer on the Cu(100) surface exhibits a large variety of vibronic features. In summary, we can distinguish two spectral zones, associated with the internal modes of the macrocycle and of the phenyl groups (1200-1700 cm^{-1}), and with several non-equivalent C-H stretches in the phenyl terminations (2800-3100 cm^{-1}). In the former region we resolve features at 1277, 1304, 1316, 1434, 1437, 1483, 1573, and 1593 cm^{-1}, while in the latter region we observe resonances at 2856, 2907, 3007, 3046, 3069, and 3086 cm^{-1}, due to the geometric distortion of the phenyl groups and their interaction with the metal surface and the neighbouring molecules. A table has been prepared with a detailed mode assignment, and can be found in the Appendix 6.6 in Table 6.1.[147–149] In the following we will discuss about the evolution of these regions in dependence with NiTPP coverage, annealing temperature, and NO exposure.

Upon adsorption on the Cu(100) surface at room temperature, NiTPPs self assemble in ad islands that grow in size with the surface NiTPP coverage.[150] We focus on the low energy vibronic region, where three distinct spectroscopic features develop when depositing up to 1.0 $\pm$0.1 ML of NiTPP (Fig. 4.8) at 1276, 1304, and 1315 cm^{-1}.

The first fingerprint is associated, on the basis of previous literature (Table 6.1),[147–149] with both macrocycle and phenyl vibrations. In particular the N-C and C-Ph stretching are involved in the former case, while the CH bending in the latter. The second peak at 1304 cm^{-1} originates instead from skeletal modes of the macrocycle only, and in particular from the pyrrolic half-ring. Finally, contributions from both the phenyl out of plane movements and from the pyrrolic quarter ring give origin to the feature at 1315 cm^{-1}.

In Fig. 4.8 it can be noticed that, for increasing NiTPP surface coverage, the central feature is less affected by the growing island size, thus indicating that the macrocycle is influenced to a smaller extent. The phase relative to the nonresonant background of this resonance changes from 300° at 0.5 $\pm$0.1 ML to 350° at 1.00 $\pm$0.1 ML (Fig. 4.8a). Instead, the modes involving contributions also from the peripheral phenyl groups undergo larger phase shifts (of 70° and 90°, respectively), suggesting changes in the electronic environment. This is also further supported by the large increase observed in the resonant to nonresonant amplitude ratios (Fig. 4.8b), well beyond the contribution from the surface coverage alone, and ascribed to dipole matrix effects at the origin of the SFG signal in relation with both geometric and electronic structure changes.

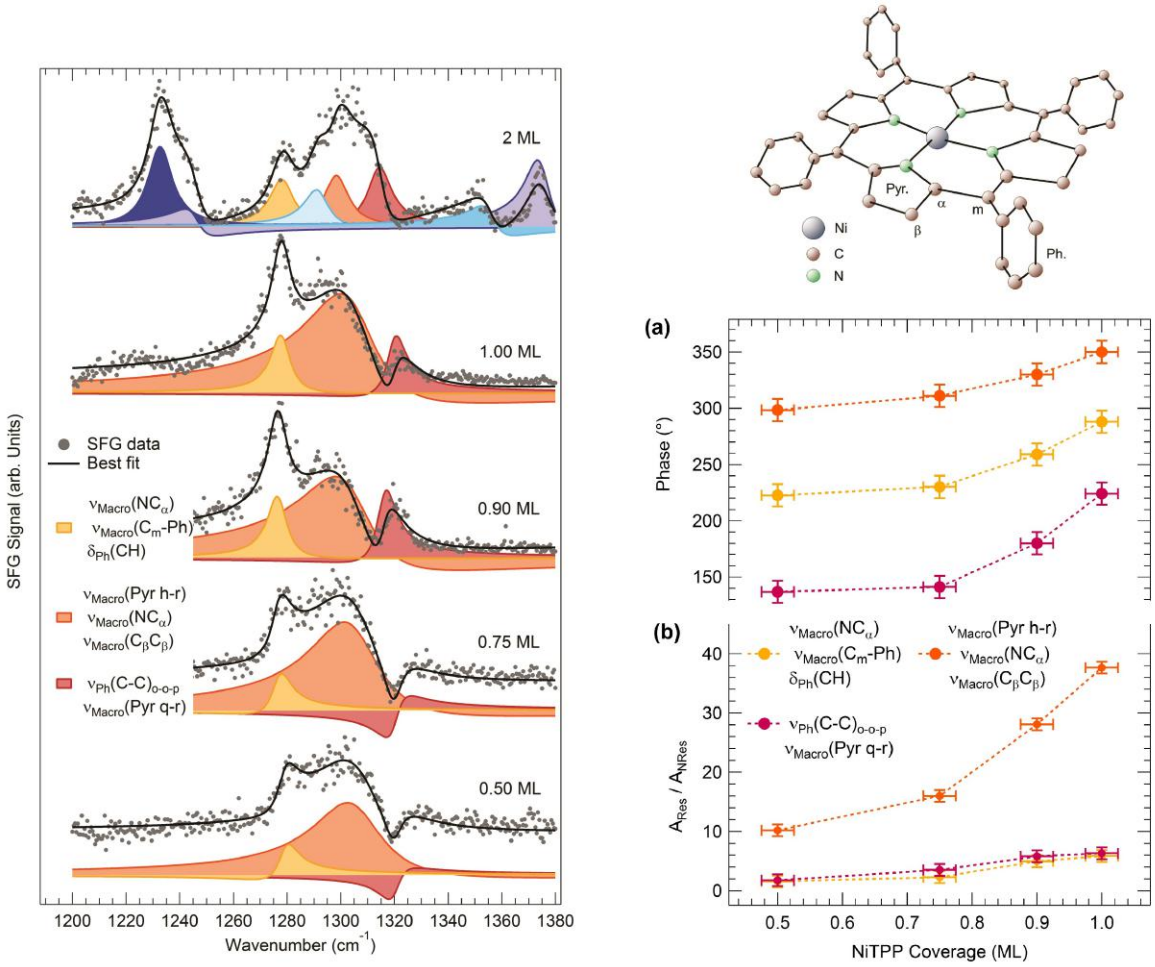

Figure 4.8: On the left side, IR-Vis SFG spectra collected at room temperature in the low-energy region for progressively increasing NiTPP coverage (0.5 – 2.0 ±0.1 ML). The normalized signal (grey dots) is shown together with the best fit (black lines) and the deconvolution (color filled profiles), according to the model lineshape described in the Methods [λ_{Vis} = 532 nm; ppp polarization].
On the right panel, in the top part of the figure, a scheme of the NiTPP molecule is depicted with the labelling of the C atoms and of the relevant molecular groups (H atoms are not shown). Dependence of the observed IR-Vis SFG phase (a) and amplitude (b) on the NiTPP surface coverage in the 0.5 – 1.0 ±0.1 ML range for the low energy modes as obtained from the deconvolution of the spectra reported in the left panel.

When the second layer develops (Fig. 4.8, top spectrum), five additional resonant features are visible in the vibronic spectrum at 1232, 1246, 1291, 1356, and 1374 cm^{-1}, respectively. Both phenyl groups and the macrocycle contribute to these peaks, as it can be seen in Table 6.1, witnessing a very different environment with respect to the interface layer, as expected on the basis of charge transfer effects.[129]

Annealing of 0.9 ±0.1 ML of NiTPP reveals good stability of the layer up to 400 K (Fig. 4.9). Above this temperature, major modifications occur in the vibronic spectra, including frequency and phase shifts, and the growth of an additional resonance at 3033-3035 cm^{-1}, thus showing that the layer undergoes structural changes, including dissociation of the molecules, above 400 K.

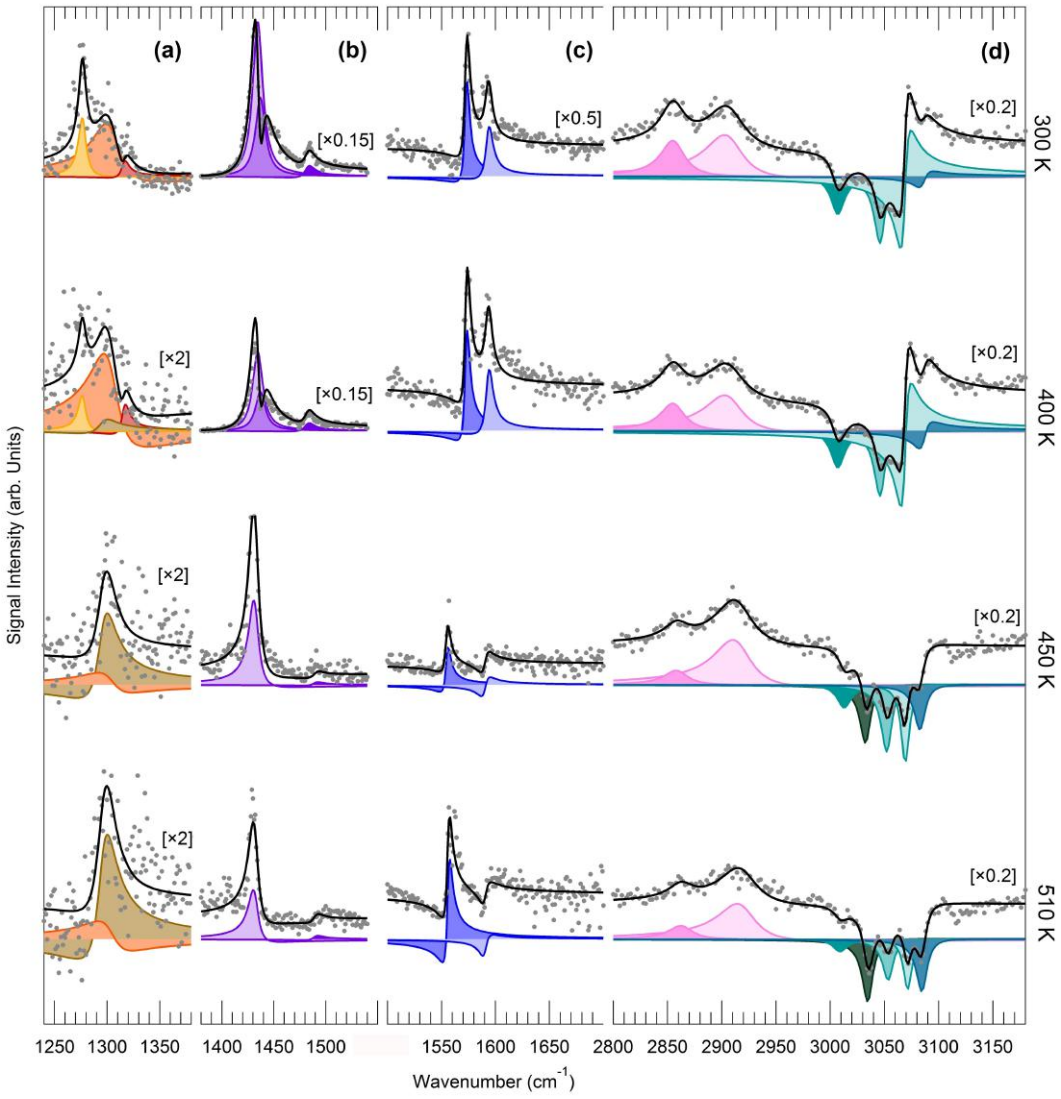

Figure 4.9: IR-Vis SFG spectra collected upon stepwise annealing of 0.9 ±0.1 ML NiTPP/Cu(100). The normalized signal (grey dots) is shown together with the best fit (black lines) and the deconvolution (color filled profiles). Note that intensity scaling factors have been applied to selected spectra for best visual comparison [λ_{Vis} = 532 nm; ppp polarization].

NO exposure and the hyponitrite hypothesis.

Upon NO adsorption at room temperature (see Fig. 4.10), four intense, additional spectral features progressively appear at 1319, 1365, 1602, and 3101 cm^{-1} (green deconvolution profiles in Fig. 4.10), accompanied by a significant evolution of the resonant modes already present and associated with the porphyrin and phenyl vibrations described above. This can be explained by both geometric and electronic modifications upon the NO-Ni ligation.

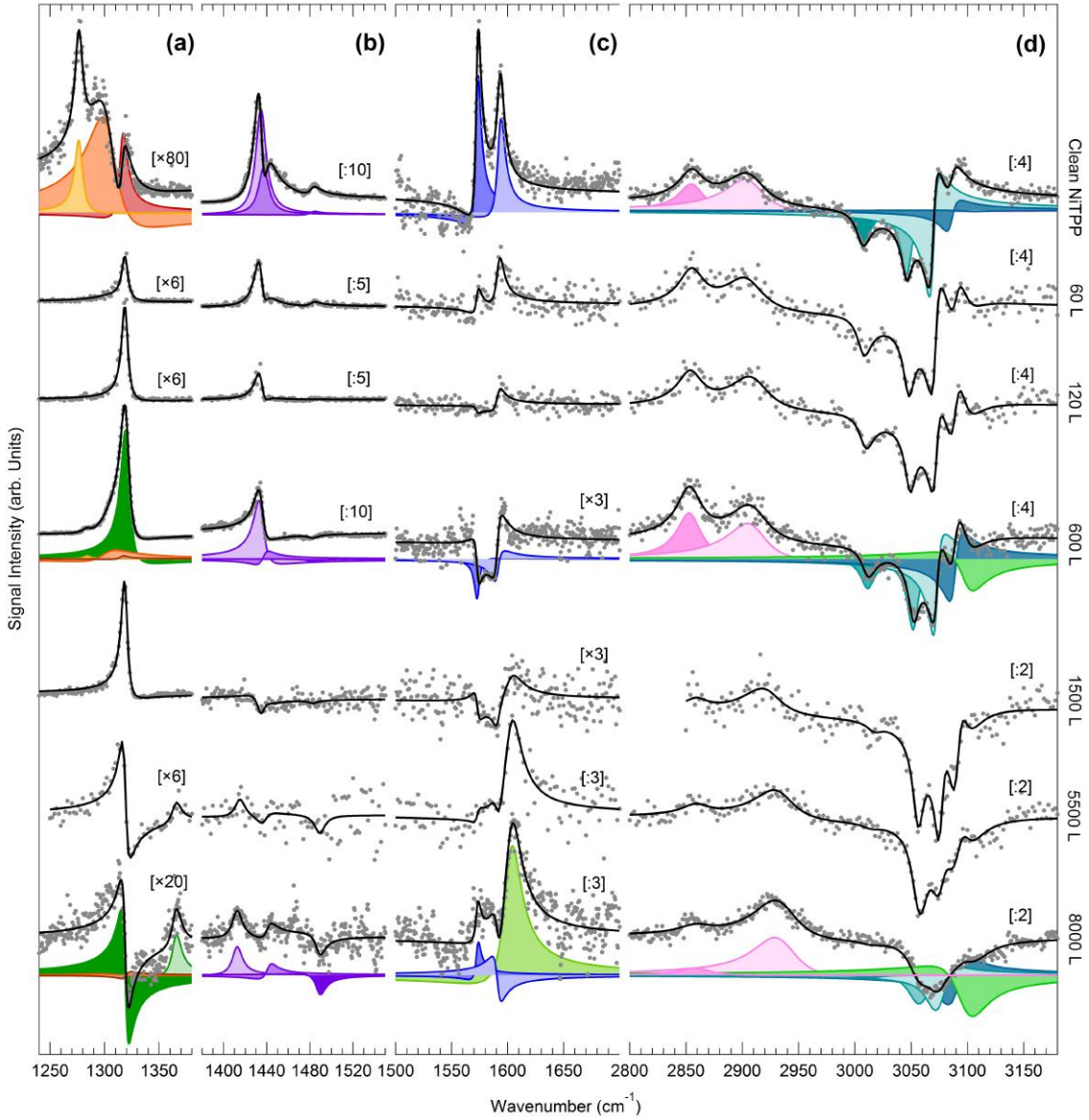

Figure 4.10: IR-Vis SFG spectra of the observable vibronic modes upon exposure of 0.9 ±0.1 ML of NiTPP/Cu(100) to nitric oxide at room temperature. The normalized signal (grey dots) is shown together with the best fit (black lines) and the deconvolution of the resonant components (color filled profiles), according to the model lineshape described above [λ_{Vis} = 532 nm; ppp polarization]. Note that intensity scaling factors have been applied to selected spectra for best visual comparison [NO exposure range: 0 – 8000 L, from top to bottom].

The resonance at 3101 cm^{-1} is associated with the $C_\beta H$ stretching mode of the pyridinic moiety slightly modified upon NO adsorption.[147] The appearance instead of the three features at 1320, 1365, and 1602 cm^{-1} can be explained in a tentative picture where the first one is

associated with the internal N-N stretch and the latter two with the internal N-O stretch of non-equivalent NO groups of a stabilized hyponitrite species, in agreement with the literature.[151–155] The attribution of the modes to the symmetric and asymmetric stretching of a dinitrosyl complex in a NO cys di-coordination configuration can be instead ruled out, yielding consistently different stretching frequencies.[156]

The formation of the N_2O_2 complex at the central Ni atom evidently contributes to an induced geometric distortion of the macrocycle and of the surrounding phenyl terminations, together with a rearrangement of the local electronic structure. As exposure increases, this results in the profound changes observed in the vibronic spectra with respect to the clean NiTPP overlayer. In particular, we observe that, after an initial decrease, the amplitude of the non-resonant background increases by an order of magnitude during the NO uptake (Fig. 4.11). This reveals an evolution in the surface density of states close to the Fermi energy, associated with the plasmonic resonances induced by the impinging visible light. The initial decrease of the non-resonant amplitude is observed independently from the NiTPP surface loading, namely 0.5, 0.75, and 1.0 ±0.1 ML (Fig. 4.11, left panel).

Intriguingly, if we investigate the NO adsorption behavior on a multilayer of NiTPPs, we observe that no evidence of nitrogen monoxide adsorption can be observed after 600 L exposure (see Fig. 4.11, right panel). Indeed, the charge transfer from the metal to the supported metal-organic framework appears as a prerequisite to enhance the reactivity of Ni centers.

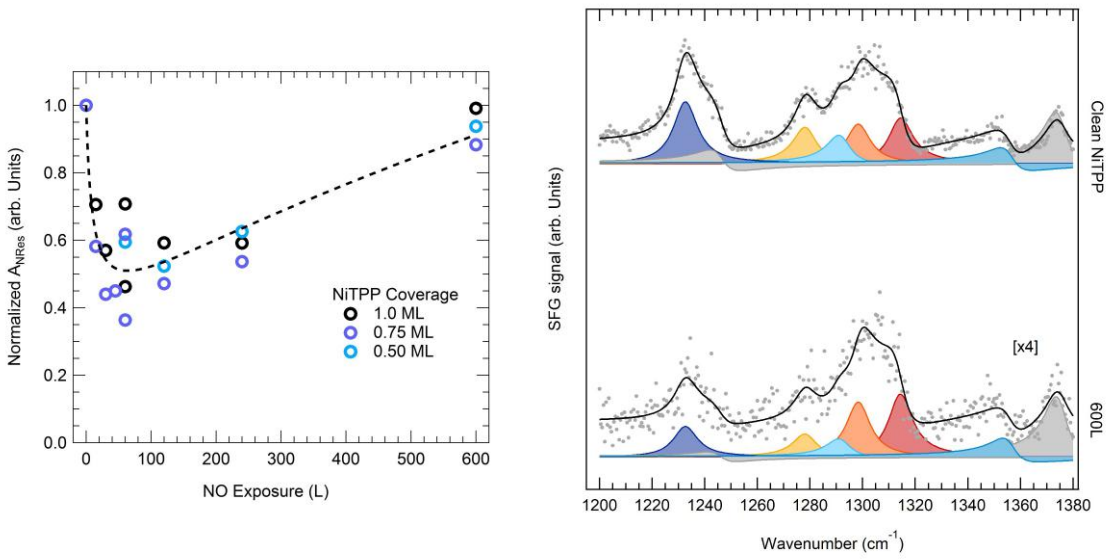

Figure 4.11: On the left: dependence of the normalized non resonant background on the NO exposure at room temperature for different initial NiTPP surface coverage values. On the right, IR-Vis SFG spectra of a NiTPP multilayer collected at room temperature in UHV condition before and after a NO exposure of 600 L [λ_{Vis} = 532 nm; ppp polarization].

We have further analyzed the SFG signal amplitude of the N-N stretch mode at 1319 cm^{-1} as a function of the exposure to NO in Fig. 4.12a. We can notice that the isotherm uptake profile is poorly compatible with a Langmuir shape. Moreover, while the adsorbed complex with two NO molecules is very stable at room temperature, its formation requires long exposures, calling for a very low sticking coefficient, possibly associated with an activated adsorption mechanism. On the basis of the above observations, we fitted the NO uptake by means of the Hill model (see Fig. 4.12a and Appendix 6.3),[157] obtaining a value of 3 ±

1 for the Hill coefficient which is indicative of a cooperative adsorption process where the adsorption of a first NO favors the uptake of a second NO at the same Ni site.

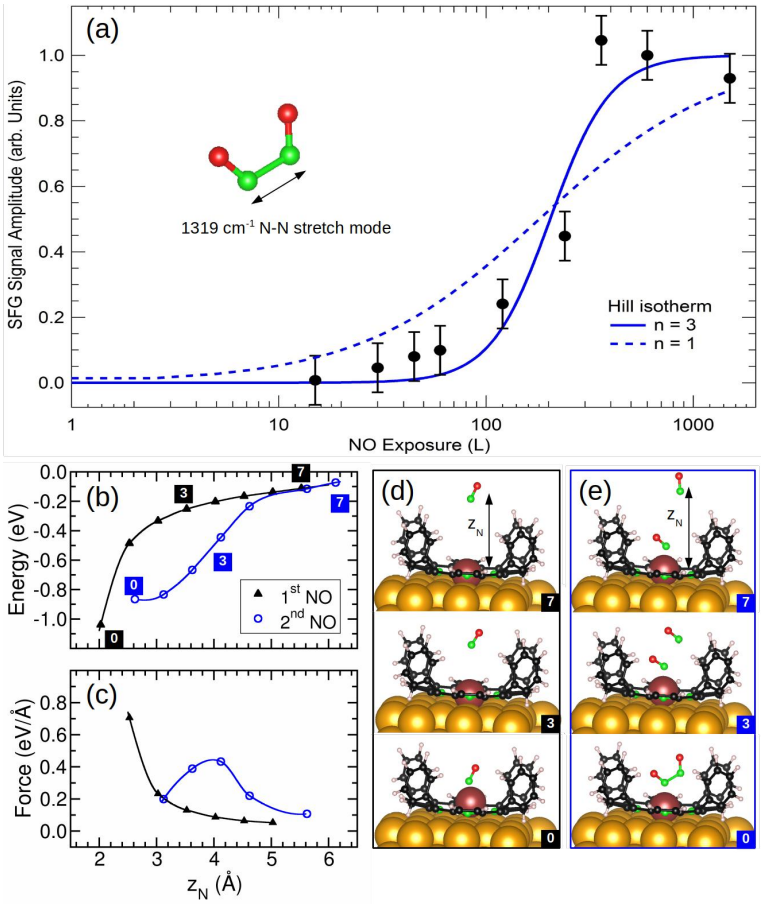

Figure 4.12: (a) Amplitude of the 1319 cm-1 N-N stretch mode as function of the NO exposure (symbols) with fits according to Hill model (lines). (b) DFT total energies and (c) forces acting on NO as a function of the vertical distance of N from the plane of the macrocycle for the approach of the 1st (blue circles) and 2nd (black triangles) NO molecule. Panels (d) and (e) show corresponding snapshots of the adsorption process as indicated by the label in (b).

4.2.3 DFT simulations supporting the N_2O_2 hypothesis.

The adsorption scenario of two NO molecules sitting on a single NiTPP site is further corroborated by density functional calculations, obtained through a collaboration with the Physics Department and the Center for Nanointegration Duisburg-Essen (CENIDE) at the University of Duisburg-Essen.

Based on the previously determined adsorption configuration of NiTPP on Cu(100),[129] we have obtained the most favourable adsorption geometries and energies of a singly and doubly occupied Ni-site, as depicted in the bottom panels (d) and (e) of Fig. 4.12. For the adsorption of the first NO, we find a binding energy of 1.05 eV while the uptake of the second NO lowers the energy by another 0.92 eV, as illustrated in Fig. 4.12b. These numbers alone would not explain the details of the cooperative mechanism, due to the similar energy values associated to each NO adsorption (see Appendix 6.3). However, the preferred adsorption of a second NO on a NO-preoccupied Ni site, rather than an empty Ni site, may be explained by the significantly enhanced range of the force which pulls an approaching NO molecule towards a

site with an already adsorbed NO (Fig. 4.12c).

It is also worth noting that the spin state of the Ni atom undergoes characteristic changes upon NO adsorption. The magnetic moment on Ni, which is 1 for the empty NiTPP/Cu(100) site, gets quenched after the first NO molecule has been adsorbed. Upon uptake of the second NO, the spin on Ni switches back to 1, accompanied by a charge transfer from the NiTPP to the hyponitrite. The partial negative charging of the N_2O_2 unit also results in a shortening of the N-N bond length for which we find 1.56 Å in the adsorbed state. Intriguingly, the observed changes in the spin state of Ni are reminiscent of a previously reported cooperative binding mechanism of CO in a metal organic framework containing Fe-centers.[158] However, in that MOF system, the cooperative mechanism relies on the coupling of spins on neighbouring Fe atoms which are only 3.36 Å apart, while in our NiTPP monolayer, the Ni-Ni distance of 12.7 Å is too large for such an effect. Also, the previously reported cooperative adsorption of CO in the MOF does not involve the uptake of more than one CO molecule at a given metal site. Thus, the cooperative adsorption mechanism reported here for NO on NiTPP is of a different origin and is likely due to guiding force-field arising from the first adsorbed NO molecule.

4.2.4 Conclusions.

In conclusion, we provide evidence that a Ni(I)TPP array interacts with nitric oxide already at UHV-compatible pressure and at room temperature. Moreover, we highlight the possibility that hyponitrite species are readily catalyzed and stabilized at the single Ni sites. A multi-technique approach combining X-ray photoemission and infrared-visible sum-frequency generation vibronic spectroscopies, supported by STM measurements and density function calculations was demanded due to the system complexity. In particular, while the XPS core level spectra taken at the N 1s show an excess of nitrogen concentration, unexplained if we assume that only one NO adsorbs per NiTPP, the IR-Vis SFG spectroscopy measurements identify specific vibrational modes compatible with hyponitrite species. In fact, three new vibrational features appear upon exposure of the NiTPP film to NO: two can be associated to the internal N-O stretch of two non-equivalent NO groups, while the last one may be related to an internal N-N stretch. Measuring the evolution of the N-N stretch amplitude as a function of the exposure to NO results in an isotherm uptake profile compatible with a cooperative adsorption process, i.e. the adsorption of a first NO may favor the formation of a N_2O_2 molecule at the same Ni site. DFT calculations support this complex mechanism. While determining the adsorption energy, in line with stabilization at UHV and 300 K, they also demonstrate that the force pulling an approaching NO molecule towards a site with an already adsorbed NO can act at significantly larger distances compared to the one generated by a free Ni site. The stabilization of hyponitrite at room temperature may unveil the catalytic properties of the NiTPP molecular array, opening a pathway towards heterogeneous catalysis exploiting biomimetic platforms.

4.3 Carbonylation of Iron phthalocyanines (CO-FePc/GR/Ir(111)).

While in the previous Section we demonstrated that the charge transfer between the NiTPP layer and the Cu(110) surface is a prerequisite to activate the interaction between NO and single Ni atom sites, in this Section we switch off the interaction with the support and take advantage of CO adsorption as a probe. While discussing the role of cooperativity in MOFs, we employ a single sheet of graphene as a decoupling buffer layer to obtain an almost non-interacting, highly ordered lattice of FePc molecules. We demonstrate that, by means of ligand adsorption (CO), it is possible to detect long-lived Frenkel excitons in this self-assembled 2D molecular system via their effect on the vibrational spectrum of the ligand itself, even at room temperature and near ambient pressure. Non-linear optical SFG spectroscopy emerges as a unique tool for this kind of investigation, as it mimics a pump-and-probe experiment, and may pave the way for the simultaneous controlled generation and characterization of localized excitons in a 2D metalorganic system on a laboratory scale.

4.3.1 Excitons and spin crossover mechanism.

The absorption of visible light in a material can lead to the formation of excitons, i.e. pairs composed of an excited electron and the associated hole. Biological systems exploit excitons in nanoscale systems to harvest and funnel energy to chemical reaction centers, demonstrating that good control over excitonic properties and dynamics may lead to crucial results in biomimetic optoelectronic, photovoltaic, and photocatalytic applications. But excitons are difficult to control and characterize, as the excited system tends to relax back to its initial conditions annihilating the electron-hole pair. Reducing electron-hole pair recombination is therefore essential to produce long-lived excitons, maximizing the efficiency of the energy transport process. Stable excitons in molecular systems have been observed in recent years, with lifetimes up to hundreds of picoseconds at room temperature.[159] The mechanism determining the coherence time is based on the coupling between the exciton and the bath of surrounding nuclear motions. Indeed, in organic frameworks a strong coupling can be observed between molecular, nuclear, and electronic dynamics,[160] resulting in a vibronic manifold with high density of states that can facilitate mixing, allowing fast internal conversion transitions.[161,162] Another important contribution to the exciton lifetime originates from the occurrence of spin transitions, yielding metastable states. Indeed, if a switch in the spin configuration of the molecule occurs (the so-called spin crossover), the system can be trapped in a spin-excited, non-equilibrium state.

In several iron(II) complexes, spin crossover transitions can be induced by thermal excitation, but light-induced excited spin state trapping (LIESST) through a multiple-step mechanism has also been observed.[163,164]

Long-lived excitons: the heme group. The search for materials capable of trapping excited states even at room temperature has started long ago and some promising systems have already been identified.[163,165] The role of ligand fields in the light-induced spin change process was also discussed.[164,165] As an interesting example, superparamagnetic properties at room temperature were recently found for hemozoin nanocrystals. Hemoglobin is converted into this heme polymer by the malaria protozoan that causes degeneration of the erythrocytes.[166] Hemozoin shows Fe-porphyrazine complexes in which the Fe^{3+} ion is embedded in a $C_{4\nu}$ crystal field, thus inducing a splitting of the d-states that can be populated in a low- or in a high-spin configuration, with an exchange interaction between the electron-spin states that exceeds, at room temperature, k_BT.

Singlet Fission. Another crucial parameter is the efficiency of the excitation mechanism, intrinsically related to the physical and electronic properties of the excitonic media. When, considering a singlet ground state condition, light is exploited to induce a singlet-triplet transition as in the LIESST mechanism, the triplet generation process may be associated with an inter-system crossing or singlet fission mechanisms, thus involving a short-lived, intermediate singlet excited state that relaxes through a cooperative path involving adjacent chromophores.[167] In the latter case, light absorption generates a spin-singlet exciton that converts within few hundreds of femtoseconds into a pair of spin-triplet excitons residing at neighboring sites.[161] The two generated spin-triplet excitons initially correlate to form an overall spin-singlet state, globally yielding a spin-allowed transition whose efficiency in not hindered as aforementioned fast spin-preserving channels are now accessible. Singlet fission does not occur in single, isolated small-molecules, since at least two adjacent sites are needed to accommodate the triplet excitation products.[167] Moreover, for singlet fission to be spontaneous, the singlet excitation energy needs to be more than twice the triplet excitation energy. So far, these processes have been observed only in nanocrystals or thin films, but not in a purely 2D system as described here. Exciton multiplication by singlet fission could indeed yield practical applications by improving the efficiency of photovoltaic devices,[167,168] as well as the adsorption properties of gas sequestration and conversion devices by exploiting cooperative mechanisms.[158]

Synthetic 2D crystal and excitons at near ambient pressure. It would be of both fundamental and technological interest to mimic the above electron- and spin-transition properties in controlled synthetic (model) systems. For this purpose, we exploit metalorganic 2D films and crystals,[169] which can be obtained by self-assembly methods on a weakly interacting and convenient support like graphene, yielding a π–conjugated system. For triplet exciton formation to take place, it is crucial that the intermolecular coupling is on the one hand strong enough to ensure efficient singlet fission and on the other hand weak enough to allow fast diffusion and separation of triplets.[167] Singlet excitons are short-lived and might be delocalized over more than one site in a 2D crystal, whereas triplet excitons are long-lived, and tend to be localized on a single molecular site.[167] The ability of excitons to diffuse reduces the recombination chances, making molecular crystals efficient systems for singlet fission processes.[167] In the specific case, we have chosen to adsorb Fe-phthalocyanines (FePc) under UHV conditions on a single, complete graphene (GR) sheet grown on the Ir(111) single crystal termination (see Fig. 4.13 A). The FePc molecules are thermally stable,[128,170,171] weakly couple to the GR support,[125] and form a well-ordered 2D crystal with almost square symmetry (Fig. 4.13 B, C). However, depending on the deposition parameters the ordered FePc lattice can be disrupted and disordered domains can be created. In Fig. 4.13 D we report a boundary between two domains of different degree of order.

We exposed this system to a near to atmospheric pressure (up to 12 mbar) of carbon monoxide. By exploiting IR-Vis SFG, I monitored the evolution of the C-O stretching intensity as a function of the CO pressure at room temperature, thus following the FePc carbonylation process *in situ*. In the following, we will show that IR-Vis SFG acts as a pump-and-probe experiment, generating long-lived excitons, which are detected by their effect on the vibrational modes of the CO ligand. This approach offers considerable advantages over other methods, being able to investigate the system *in situ* at near-atmospheric conditions.[107,114] Intriguingly, in UHV environment phthalocyanines have already shown nonequilibrium spin crossover properties that can be locally controlled by means of the tip of a scanning tunneling microscope after adsorption at cryogenic temperature on a substrate that crucially affects the spin state of the central metal atom.[172–174] As an alternative, adsorption and thermal

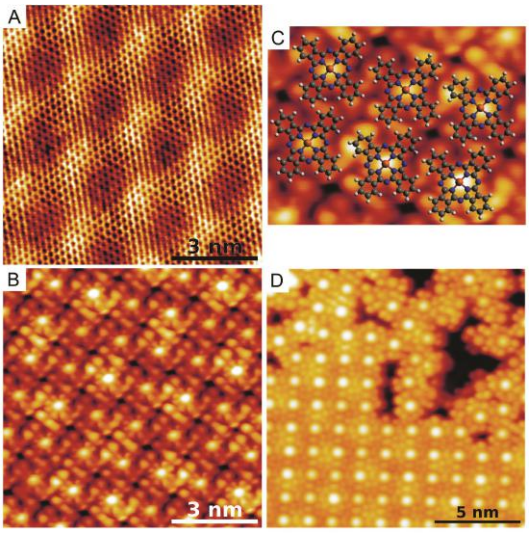

Figure 4.13: Structural characterization of the FePc/GR system. (A) STM image of bare graphene on Ir(111). (B) STM image of the FePc single, well-ordered layer on graphene and (C) the structural model of the molecules. (D) A boundary between ordered and disordered domains. All images were taken under UHV conditions at 4 K [(A) V_{bias} = +0.1 V, I = 1 nA; (B-C) V_{bias} = -2.0 V, I = 0.2 nA; (D) V_{bias} = -2.0 V, I = 0.1 nA].

desorption of small ligand molecules that interact with the four-fold coordinated metal center were employed to tune the magnetic coupling of metalorganic complexes to substrates.[139,169,175] The light-induced switching can be exploited to generate a nonequilibrium or metastable molecular electronic and spin configuration, since the optical pumping yields excitation of the metal-to-ligand charge transfer that rapidly decays to a high-spin state.[176]

4.3.2 An unexpected vibrational multiplicity

A FePc monolayer has been deposited under UHV conditions on the single, complete GR sheet on the Ir(111) single crystal termination. The almost square lattice, characterized by an angle of 87° (Fig. 4.13 B, C), similar to the case of CoPcs,[177] has lattice vector lengths of 14.1 and 13.6 Å. The FePc monolayer lattice is rotated by 13° with respect to the underlying GR sheet, while the molecules are rotated by 18° with respect to the FePc lattice. Depending on the exact procedure (FePc deposition and post-annealing temperature), the prepared layers may show the co-existence of both ordered and disordered domains (Fig. 4.13 D).

As mentioned, together with DFT results obtained in the framework of our research group, we took advantage of the IR-Vis SFG technique to fully investigate the room temperature adsorption of CO on a single layer of FePc molecules *in situ* at near ambient pressure.
The IR-Vis SFG spectra, collected at a pressure spanning from UHV to 12 mbar of CO, are reported in Fig. 4.14. The growth of four distinct vibronic features in the C-O stretching region for the 2D FePc/GR crystal is evident, while only a single feature was observed for the multilayer, as detailed below. Any vibrational fingerprint can no longer be detected if the UHV condition is recovered (see Fig. 4.14, top spectrum). This demonstrates the weak interaction between CO and the FePcs, at variance with the stable NO adsorption discussed in the previous Section 4.2.

We remember the reader that a complete, bare GR sheet is not active towards CO adsorption and passivates the underlying Ir metal surface. Intercalation of CO under the GR sheet would produce a very intense vibronic signal in the 2040-2080 cm^{-1} range, as discussed

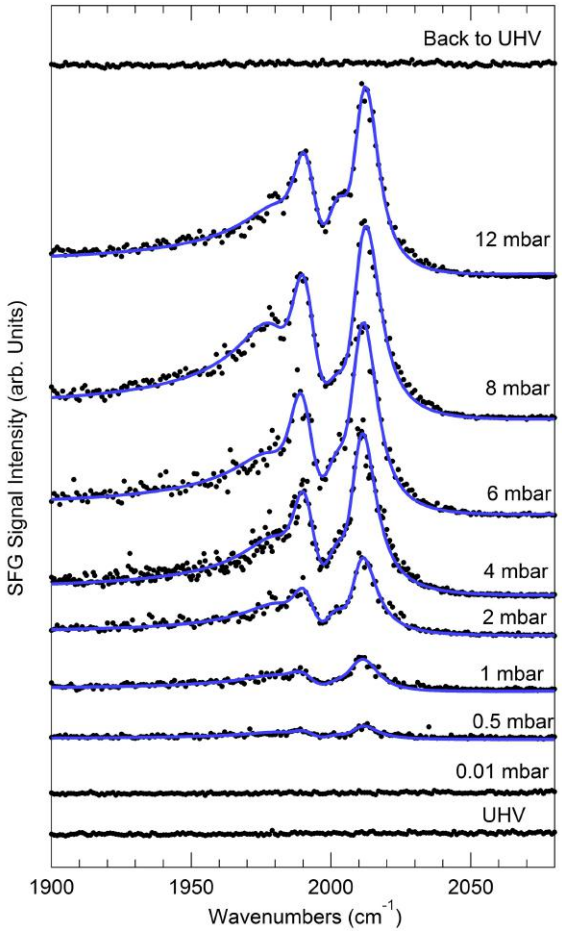

Figure 4.14: IR-Vis SFG spectra of in the C-O stretching region of the carbonylated FePc monolayer on graphene as a function of pressure, from UHV to 12 mbar and back to UHV conditions, from bottom to top. The spectra were collected at room temperature [λ_{Vis} = 532 nm, ppp polarization].

in Section 3.1 and 3.2.[75,178] Instead, on the 2D FePc/GR/Ir(111) crystal the observed features progressively develop in the 2000 cm^{-1} region.

Due to the large distance between Fe centers at which the CO molecules bind, a contribution of coverage-dependent non-linear dipole effects to the SFG intensity can be ruled out, indicating that the observed IR-Vis SFG signal can be exploited to measure the CO uptake on the Fe centers (Fig. 4.15). By fitting the experimental data with an established Langmuir adsorption kinetic model (dashed line in Fig. 4.15), we obtain a CO-Fe binding energy of -0.3±0.1 eV.

In parallel, a thorough set of *ab initio* calculations were performed in order to get a deeper understanding of the system (see Appendix 6.8). Concerning the CO adsorption energy, we obtain a theoretical value of -0.34 eV for a single CO ligand adsorbed at each iron center (mono-coordination), in perfect agreement with the experimental data, and find that further CO adsorption beyond mono-coordination is strongly endothermic. The experimental uptake profile is very similar to that reported for FePcs adsorbed at the bare Ir metal surface,[51] and the saturation pressure at room temperature is in line with working gas partial pressures of heme systems in Nature.[44] In addition, by means of *ab initio* thermodynamics we computed the (CO)FePcs saturation curve (blue line in Fig. 4.15). The remarkable agreement further confirms the proper description of the CO bonding mechanism.
We also find from our calculations that the carbonylation of the FePc quenches the spin of the molecule, i.e. the total spin of the (CO)FePc is S = 0, at variance with the FePc molecule

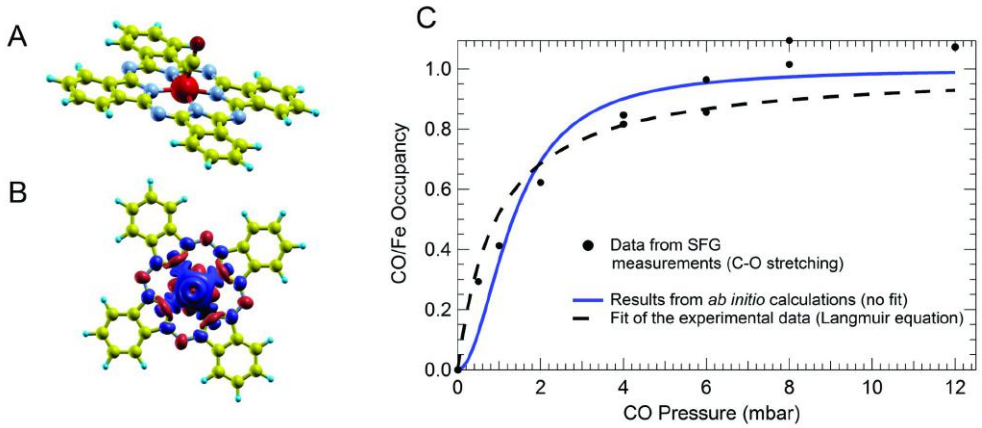

Figure 4.15: Carbonylation of the FePc monolayer on graphene. (A) Adsorption geometry for a single CO molecule on FePc. (B) Spin polarization ($\rho_{up} - \rho_{down}$) for the triplet obtained in DFT+U (blue: negative values; red: positive values). (C) Relative coverage of the adsorption sites of a layer of FePc molecules as a function of the CO pressure. The experimental data (dots) are affected by an error of roughly ± 0.1 on the vertical axis. The theoretical curve (blue, solid line) is obtained within the framework of a pure *ab initio* approach, while the experimental data are fitted by a Langmuir isotherm (black, dashed line).

without the CO ligand (S = 1), in agreement with the literature.[179] Therefore, the expected ground state is a singlet state (paired electrons).

A detailed analysis of the IR-Vis SFG C-O stretch fingerprint (Fig. 4.16) identifies four contributions at 1986, 1992, 2005, and 2011 cm^{-1}. The surface density of the Fe centers is very low due to the large size of the FePc molecules (about 0.03 ML with respect to the underlying Ir metal surface). Despite this, we managed to measure the resonant signal due to the strong CO dipole and the graphene-enhanced scattering. In the present case we have used $\lambda_{Vis} = 532$ nm (photon energy: 2.33 eV), thus matching a typical singlet excitation energy.[167] The degree of order of the layer strongly affects the resonant lineshape, as can be observed from the two spectra plotted in Fig. 4.16, showing a remarkable change of the relative peaks intensities and a Gaussian broadening for the disordered system (from 0.8 to 2.3 cm^{-1}), while all other lineshape parameters including line positions remain constant.

In contrast, carbonylation of a FePc multilayer (3D crystal) adsorbed on the same graphene sheet yields a single resonant peak at 2012 cm^{-1} with a different relative phase with respect to the non-resonant background (Fig. 4.17 A and B). The multiplet is therefore an inherent feature of the 2D system.

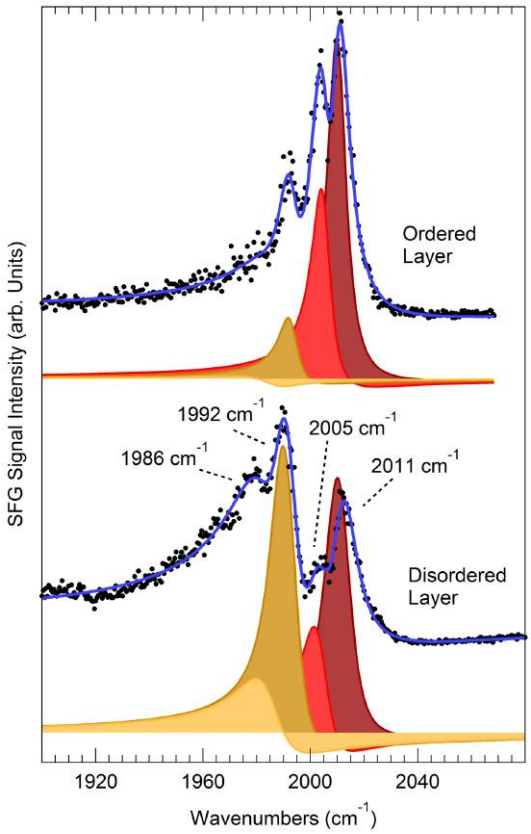

Figure 4.16: IR-Vis SFG intensity spectra of the C-O stretching region collected *in situ* at room temperature in 10 mbar CO on the ordered (top) and disordered (bottom) FePc monolayer on graphene. Experimental data (black dots) are represented, together with the results of the best fit (blue lines) and the interference of each resonance with the non-resonant background according to the effective susceptibility, as described in the text ($\lambda_{Vis} = 532$ nm; ppp polarization).

A Vis-induced vibrational multiplicity: PM-IRAS spectra.

I performed analogous measurements by means of Polarization-Modulation Infrared Reflection Absorption Spectroscopy (PM-IRAS), for which a broadband mid-IR radiation beam is shined on the sample surface,[52] thus inducing pure vibrational transitions instead of vibronic excitations. Further details about the employed experimental setup and about the technique can be found in Appendix 6.7. The PM-IRAS spectra obtained upon room temperature carbonylation of the FePc multi- and mono-layers on GR are reported in Fig. 4.17 C and D, respectively. At variance with the corresponding vibronic (SFG) spectra, only one peak appears in both cases, at 2008-2009 cm^{-1}. This clearly associates the vibronic splitting observed by IR-Vis SFG with the electronic transitions induced by the impinging visible light. The small experimental discrepancy in the vibrational energies (2-4 cm^{-1}) between SFG and IR experiments is likely due to the anharmonic coupling of the C-O stretch to frustrated lateral modes.[103]

In the following, we discuss possible scenarios of interpretation. Trans-coordination and ligand environment effects in heme carbonyls have been found to induce shifts in the C-O stretching mode (of the same order as the ones we measure: 5-10 cm^{-1}), both in model and in biologic systems.[116,180,181] A varying coordination of the Fe atom to the underlying graphene sheet and an inhomogeneous coupling contribution, depending on non-equivalent adsorption geometries of the FePc molecules with respect to the graphene Moiré, cannot account for

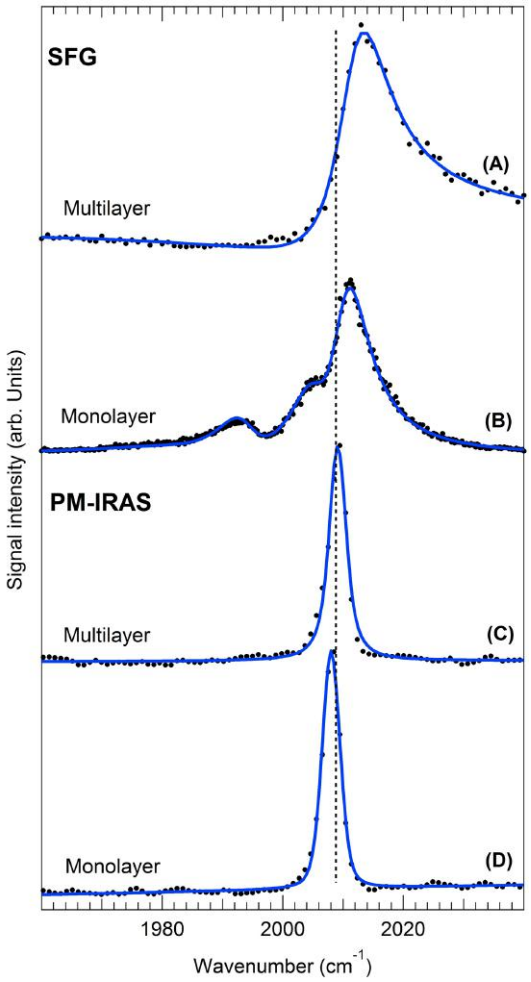

Figure 4.17: Vibrational vs vibronic fingerprints of the C-O stretching mode for the carbonylated FePc monolayer. Comparison between IR-Vis SFG (A and B) and PM-IRAS (C and D) intensity spectra collected *in situ* at room temperature in 10 mbar CO in the C-O stretching region for the carbonylated FePc monolayer (B and D) and multilayer (A and C) on graphene. For the IR-Vis SFG spectra, λ_{Vis} = 532 nm and ppp polarization were used.

the observed multiplet since it is absent in pure IR measurements. The measured splitting can neither be ascribed to multiple CO coordination, since the symmetric and antisymmetric stretching modes in Fe poly-carbonyls would be separated by several tens of wavenumbers, at variance with the observed splitting of only a few cm^{-1}. Consistently, the absence of the splitting in our pure IR spectra excludes these interpretations. Finally, as mentioned, our DFT calculations confirm that only mono-coordination is energetically possible. Further details concerning the derivation of the theoretical adsorption curve plotted in Fig. 4.15, and further discussion about other discarded hypotheses are reported in Appendix 6.8. However, the following picture emerges as the only one explaining all the presented evidence: the vibronic multiplicity observed in the IR-Vis SFG spectra is intimately related to the creation of long-lived excitons excited by the visible radiation.

Excitons in a FePc crystal in UHV.

In order to investigate the lifetime of the excited electronic states of the heterostack induced by visible radiation, we studied the electron dynamics of the FePc monolayer on GR/Ir(111) by means of Time-Resolved Two-Photon Photoemission (TR-2PPE). Further details about the experimental setup and technique can be found in Appendix 6.7. The experiments were performed at room temperature in order to correlate with the IR-Vis SFG results. However, due to the nature of the photoemission process involving low kinetic energy photoelectrons, we investigated the system in ultra-high vacuum conditions, thus without adsorbed CO. We employed a 515 nm pump pulse to create a transient population of excitonic states that were subsequently probed by a 257.5 nm pulse.[182]

Two transient states were detected, see Fig. 4.18. A short-lived excited state (SL - $\tau_{SL} < 570$ fs), located 1.3 eV above the Fermi level, was found to decay in long-lived, lower energy states (LL - $\tau_{LL} = 28 \pm 8$ ps) at $(E - EF) \leq 0.6$ eV. We associate the SL state with the electrons excited in the FePc LUMO, supported by previous STS measurements in literature.[183] A precise determination of the energy position of the LL state was not possible, because the first 0.5 eV above the secondary electron cut-off were not accessible in the current experimental set-up due to detector saturation. Nevertheless, an upper binding energy limit of 0.6 eV could be obtained. Our findings on this system are in agreement with previous four wave mixing measurements performed on FePcs in a dimethylsulfoxide solution, yielding a short-lived state (<170 fs) decaying in a longer lifetime state (≃40 ps),[184] and with other pump-probe investigations.[185]

It has to be stressed that the long-lived LL state is highly related to spin crossover mechanisms: its lifetime value (28 ± 8 ps) is way higher than common lifetimes related to internal conversion mechanisms, but also too small if compared to common lifetimes of fluorescent channels.[186] This is in line with previous observations, reporting the low fluorescent yield of metal-phthalocyanines.[187,188]

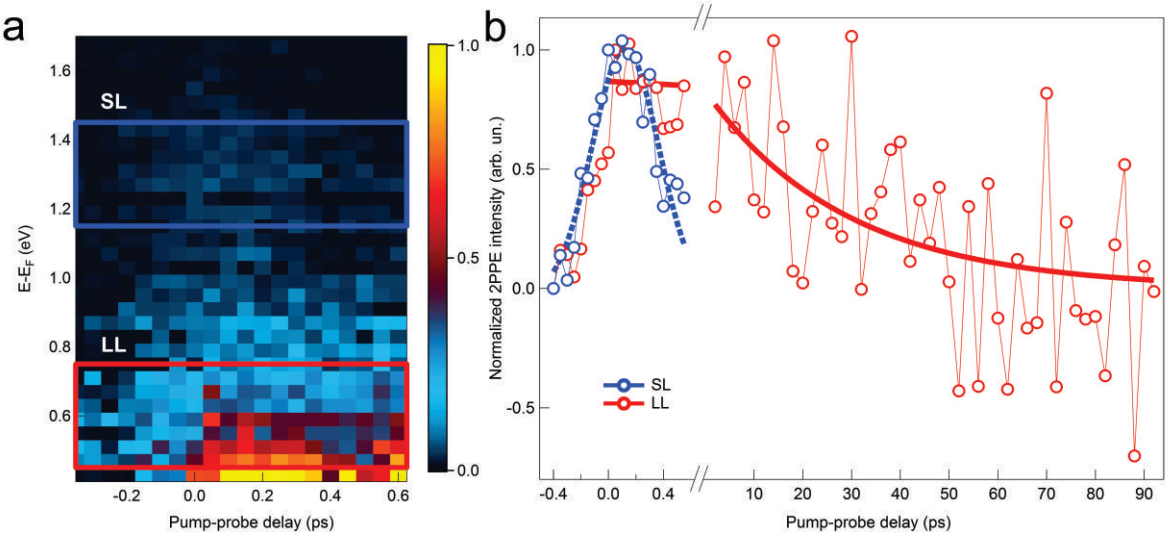

Figure 4.18: (a) Pseudo-color plot of the TR-2PPE spectra for the FePc monolayer on Gr/Ir(111). The color scale represents the normalized photoemission intensity. The spectra were recorded with $h\nu_1 = 2.4eV$ (pump) and $h\nu_2 = 4.8eV$ (probe). The integrated intensities for the two regions delimited by the blue (SL) and red (LL) contours are displayed in (b). SL (blue markers) has been fitted with a Gaussian peak (blue, dashed line), while for LL (red markers) an exponential decay (red, solid line) has been adopted.

4.3.3 CO adsorption and spin-excited states.

To explain both experimental and theoretical evidences, we propose that the observed SFG vibrational splitting is associated with contributions from excited triplet electronic molecular states (unpaired electrons) that are populated upon exposure to the visible light beam, similar to a LIESST scenario. We calculated the vibrational modes for the singlet ground state and for two different triplet states and obtained vibrational frequencies of 2016, 2049, and 2055 cm^{-1}, respectively. The calculated splitting is comparable to the splitting among peaks in the SFG spectrum, spanning about 30 cm^{-1} and with a separation between adjacent features of 6 cm^{-1}. The increase in the C-O stretching frequency calculated for the triplet states with respect to the ground configuration is consistent with the fact that CO adsorption is weakened, in agreement with an electron back-donation mechanism according to the Blyholder model of CO bonding, making this molecule an ideal probe of the local electron density. The multiplet of observed non-equivalent resonances agrees can be explained within the framework of a crystal ligand field theory picture, in which a C4ν symmetry system is expected to split its energy levels. The latter geometry applies indeed to the carbonylated FePc, since binding of CO lifts the Fe atom from the molecular plane, inducing a symmetry break that activates the singlet fission process, as recently observed.[168] Indeed, the dependence of the relative intensity of the peaks on the ordering of the 2D crystal can be associated with quantum cooperative interactions between the interacting molecules within the framework of a singlet-fission origin of the triplet excited states, allowing for subsequent triplet diffusion and minimizing recombination.[167] In the present case, the CO molecule adsorbed at the Fe center acts both as a ligand and as a vibrational identifier.

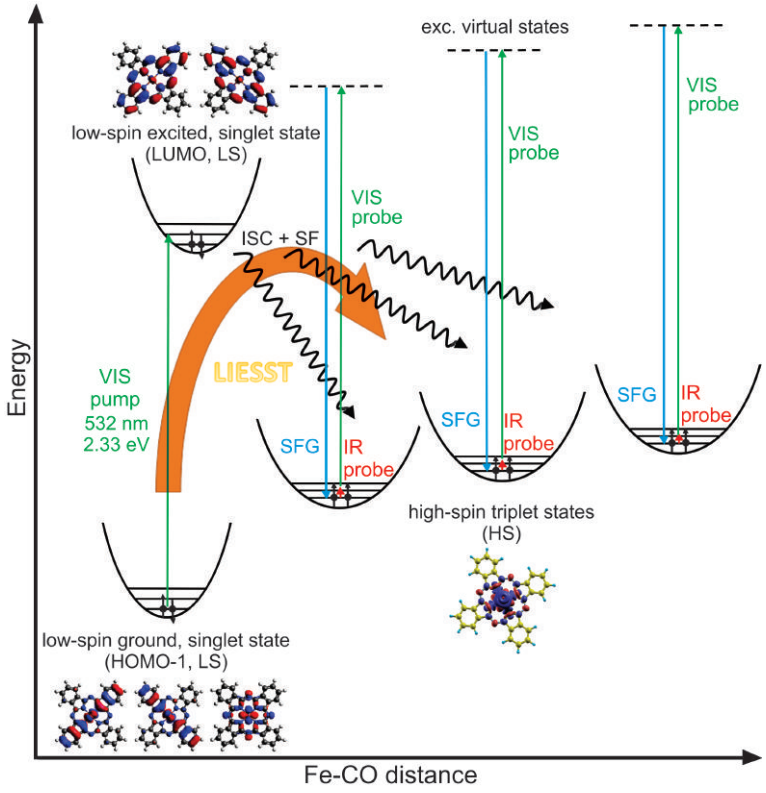

Figure 4.19: Jablonski diagram of the exciton formation mechanisms. The visible radiation yields excitation of the fundamental low-spin (LS) state into an excited singlet configuration, followed by fast relaxation into long-lived triplet high-spin (HS) states through inter-system crossing (ISC) and singlet fission (SF) mechanisms.

Corroborated by our *ab initio* DFT simulations, we can propose the mechanism depicted in the Jablonski diagram of Fig. 4.19. The visible radiation excites the system from a low-spin ground, singlet state (s = 0) to an excited singlet state (HOMO-1 to LUMO transition). The latter cooperatively decays via a singlet fission process to high-spin triplet states that can then be probed by means of IR-Vis SFG.
Time-resolved 2PPE experiments yield lifetimes of less than 570 fs (SL) and of 28 ± 8 ps (LL), respectively, for the two corresponding excited states of the decarbonylated FePc/GR, in line with results obtained on similar molecules.[182,189–192] This explains why the SFG measurements are able to catch the population of the most stable configuration (LL), since the IR and Vis pulses have a similar duration (30 ps). Moreover, 2PPE experiments associate the two excited states with energies of 1.3 and <0.6 eV, respectively. This further supports our findings since, as observed in the introduction, for singlet fission to be spontaneous, the singlet excitation energy needs to be more than twice the triplet excitation energy.[167]

4.3.4 Conclusions

We discussed how a self-assembled carbonylated metalorganic 2D crystal supported on graphene, upon exposure to visible light at room temperature, can sustain long-lived excitons (tens of ps). Both the presence of the graphene layer and the 2D network are essential for the stabilization of the excitons, which is why they are not observed on the multilayer (see Fig. 4.17). This is due to the peculiar mechanisms involved in the LIESST process, including singlet fission that relies on the appropriate interaction between neighboring centers.

This work shows that IR-Vis SFG spectroscopy is a unique tool for this kind of investigation as it mimics a pump-and-probe experiment. Visible radiation generates excitons that can be simultaneously detected through their effect on the internal stretching mode of the adsorbed carbon monoxide ligand, a convenient and accurate way to control, investigate and characterize complex processes in metalorganic molecules in which electronic and nuclear degrees of freedom interact in non-trivial ways.

Chapter 5

Atomic-level control and tuning of model single-site catalysts

While in the previous Chapter we discussed about examples of the activity of SMAC systems differing both in the employed metallorganic bricks and the underlying support, in this Chapter we will demonstrate that it is possible to actively tune the structural and electronic properties of a monolayer of FePc molecules by modifying the supporting surface. First, we will discuss an example about how the adsorption motif of adsorbed metallorganic molecules can be changed almost without affecting their adsorption properties, therefore affecting the ***structure*** *of the metal-organic framework. In the second part, we will instead present a novel route to achieve a strong enhancement of the interaction of CO_2 with the iron centers of an array of FePcs, thus modifying the* ***chemical*** *properties of the adsorbed molecular layer.*

5.1 Tailoring self-assembly: iron phtalocyanines on alumina ($FePc/Al_2O_3$)

In the last decade, adsorption of metallorganic molecules on solid surfaces represented an inspiring playground for the nano-designed synthesis of advanced materials characterized by tunable electronic, magnetic, and catalytic properties.[107,114,126] In fact, the self-assembly properties of metal-organic molecules offers tunable nanometric building blocks for the construction of stable and efficient nano-architectures.[193] Even though manipulation of single molecules allows to observe fascinating local phenomena yielding single molecular switches and molecular rotors,[114] the path for extending such precise manipulation on the larger, applicative scale is quite hazy. Conversely, exploiting the long-range self-assembly process of specific adsorbed molecules already suggested attracting synthetic model systems for innovative technological devices. As an example, Sedona *et al.* found that inequivalent self-assemblies of iron phthalocyanine (FePc) molecules on the Ag(110) surface result in different catalytic properties towards the oxygen reduction reaction.[126] Efforts were spent to search and characterize highly ordered molecular assemblies self-assembled on suitable substrates, yielding vast literature.[107,114]

Phthalocyanine adsorption and potential energy surface. Even restricting our attention to metal-phthalocyanine (MPc) molecules only, in consideration of their fascinating electronic properties, high thermal stability, and employment in the synthesis of bio-mimetic systems,[51,114,128] a variety of adsorption structures were reported both on metallic and less active surfaces.[128,193–196] As adsorption may deeply modify the electronic, magnetic, and

conformational structure of the metallorganic adsorbates, attention has been devoted to the investigation of less interacting substrates to be exploited as decoupling layers preserving the desired features of the tectons. As discussed in the previous chapter, the adsorption of MPc molecules on almost decoupled, free standing monolayer graphene (GR/Ir(111)) represents a perfect example, widely investigated with both microscopy and spectroscopy tools.[125,128,170] Graphene efficiently decouples the MPc lattice from the support, and negligibly influences the self-assembly, yielding an almost-quadratic molecular lattice, independent from the substrate symmetry.[125,128,194] This results first of all from the smooth potential energy surface of the GR/Ir(111) foil, but also from the MPc-GR bond, governed by delocalized π orbitals interactions. However, an opposite behavior can be found on the GR grown on the Ru(0001) surface. Even though the nature of the supporting layer does not change with respect to the previous case, the intense corrugation of the carbon layer modulates the potential energy surface.[127] As a result, substrate-molecule interactions can overwhelm the inter-molecular forces, and the symmetry and periodicity of the substrate deeply affect the self-assembly process. This implies that tuning the corrugation of the potential energy surface by means of controlled surface functionalization allows to select different self-assembled molecular lattices, by changing neither the employed molecules, nor the support. This possibility has been already demonstrated for the aforementioned MPc/GR/Ir(111) system. In fact, Bazarnik *et al.* report that a priori Co- or Fe-intercalation under the graphene carpet enhances its corrugation, consequently affecting the molecule-substrate interaction and yielding a sharp transition from quadratic to slightly distorted honeycomb lattices.[197]

5.1.1 Alumina ultra-thin film on $Ni_3Al(111)$

But graphene is not the only decoupling film suitable for surface functionalization. In fact, other ultra-thin epitaxial layers can also be employed, e.g. oxide layers. In particular, the alumina bi-layer grown on the $Ni_3Al(111)$ single crystal termination represents an intriguing support, well-known for its nano-templating role for the controlled growth of metal nanoclusters.[198–200] Briefly summarizing, the highly ordered ultrathin alumina film, formed by an oxygen-terminated, non-stoichiometric O-Al-O-Al stacking sequence, shows a $(\sqrt{67} \times \sqrt{67})$R12.2° unit cell and hosts specific nucleation sites for the ordered growth of metal nanoparticles. Two superstructures were previously identified by means of Scanning Tunneling Microscopy (STM) and Atomic Force Microscopy (AFM).[201–203] The first is a regular pattern of oxygen and aluminum vacancies ("holes") that reach the buried metallic interface and form the so-called geometric *dot* structure, yielding the same periodicity of the oxide unit cell (the distance between two "holes" is therefore of 4.16 nm). The second superstructure is a regular hexagonal pattern with 2.4 nm periodicity (referred to as the *network* structure).[201,203]

Metal nanocluster and FePc deposition. In the case of the self-assembled growth of Cu, V, and Pd nanoparticles, the *network* structure does not play a role.[198,199] In fact, only the "holes" (the *dot* sites) act as preferential nucleation sites for the growth of the nanoclusters, trapping single metal adatoms deposited at the oxide surface from a physical vapor phase. In contrast to the regular, controlled growth of metal clusters, no ordering effect of the ultra-thin alumina layer on deposited metal phthalocyanines has been previously observed: CuPcs hardly form ordered structures even at monolayer coverage, where the formation of the second layer starts before the first one is completed. Moreover, the thermal stability of the adsorbed layer is poor, as above 350 K complete desorption occurs.[204] However, we show that the controlled growth of a metal cluster lattice finely modifies the surface potential energy of the oxide film, thus ideally steering the adsorption properties of the adsorbed molecular layer. Pursuing a fine control over the self-assembly properties by means of pre-deposition of metal nanoclusters,

and looking for thermal stability well above 350 K, we performed a thorough characterization of an adsorbed layer of FePcs, as described in the following. Since the functionality of several biological systems like enzymes is based on metallic monoatomic cores (Fe, Ni, Mg, Cu...), in this work Cu nanoclusters will be employed to functionalize the alumina surface. In this way, while tailoring the surface order obtained by self-assembly processes, we will also provide a model to synthesize bio-inspired bimetallic 0D metallorganic alloys.

5.1.2 Cu nanoclusters, FePc deposition and potential energy surface.

The $Ni_3Al(111)$ single crystal termination was cleaned by standard UHV sputtering-annealing cycles (Ar+/Ne+, 1170 K). Following established recipes, controlled oxidation of the surface yields a high-quality ultra-thin alumina layer.[201] In the detail, surface oxidation was accomplished through three annealing cycles to 1000 K in 2×10^{-7} mbar O_2 followed by UHV annealing to 1070 K. Metal and molecular depositions were performed under UHV conditions with the oxide surface kept at room temperature. FePcs were purchased from TCI Europe with a purity above 98% and sublimated from a heated quartz crucible. Cu clusters were synthesized by room temperature self-assembly at the oxide surface after phys-ical vapor deposition.

STM images collected at Vbias = +3.2 V on the pristine alumina surface show the regular honeycomb pattern of the *network* structure (Fig. 5.1a), in agreement with the literature.[202] Deposition of a few % of a monolayer of Cu at room temperature apparently results in no major changes, apart from the appearance of few intense protrusions (Fig. 5.1b). We ascribe them to a minority of larger Cu clusters that coexist with a majority population of small cluster, which are homogeneously distributed but cannot be discerned due to low contrast at this bias, similarly to the case of Pd seeds previously reported.[203] Indeed, the metal nanoparticles seed at specific sites of the oxide superstructure (in particular, the "holes" or *dot* sites) and, for few atoms particles only, tiny contrast differences can be observed upon STM imaging.[203] An example of the height profiles obtained from the STM imaging of the Cu-seeded alumina film is shown in Fig. 5.1, in agreement with what expected from previous literature.[203] Concerning the origin of the larger clusters that we observe, Asar *et al.* showed that, in the case of Cu, the cohesion energy increases with cluster size.[200] Consequently, an increase in the cluster dimension induces an increase in the probability of its further growth, yielding the observed appearance of few larger clusters. The latter phenomenon influences the cluster distribution, yielding a broader size variability for the Cu clusters at variance with other deposited metals.[198,205] Therefore, the average cluster size that we indicate in the following is estimated from the known coverage of deposited Cu atoms with respect to the density of nucleation sites.

We now focus on the adsorption of FePc molecules at room temperature, both on the pristine and on the Cu-decorated ultrathin oxide film described above. Starting from the low-coverage regime, we investigate adsorption and arrangement of FePcs in the 10^{-2}-10^{-1} ML range (the coverage is referred to the Ni_3Al termination). Previous literature addresses that metal-phthalocyanines hardly form ordered layers on the alumina surface under these conditions. For growing loadings, the coverage distribution at the surface is far from being homogeneous, yielding coexistence of mono- and multi- layers.[204] Thus, in the following we will only distinguish between low and high local coverage conditions (around 0.01 and 0.08 ML, respectively).

At low coverage FePc molecules, adsorbed on the pristine alumina surface at room temperature and imaged with Vbias = +2.0 V at 77 K, appear with a bright center (the iron atom) surrounded by four lobe-protrusions assigned to the benzopyrrole groups (Fig. 5.2a). The underlying alumina film can also be distinguished, contributing to the contrast with the

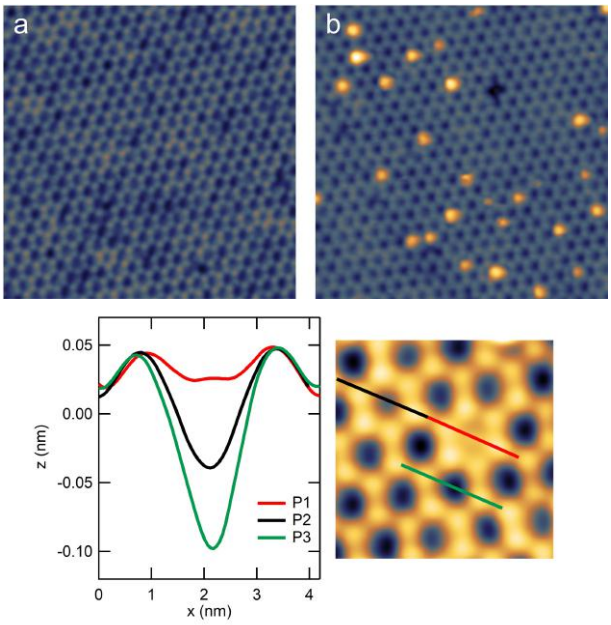

Figure 5.1: STM images of (a) the pristine and (b) the Cu-decorated alumina film [T = 77 K; V_{bias} = +3.2 V; 45 × 45 nm^2; (a) I = 50 pA and (b) I = 2 pA]. In the bottom panel, a zoom-in [9.8 × 9.8 nm^2] with cut-profiles of the cluster nucleation sites (*dot* structure) evidencing a non-equivalent filling depending on the size of the Cu nanoparticles, as observed in the case of Pd nucleation.[203]

features associated with the alumina *network* structure. When compared with the ultra-thin alumina lattice, no specific preferential adsorption site is found for the single FePc molecule. Small aggregates of two or three molecules are observed, possibly witnessing the presence of attractive intermolecular lateral interactions. A similar behavior has been observed also for CuPcs on the same substrate.[204] By means of DFT calculations we find indeed that the FePc-alumina bond involves the delocalized molecular orbitals of the benzenic and pyrrolic groups. In the presence of Cu clusters, we find that the bright protrusions, corresponding to the larger Cu particles, act as preferential coalescence sites for the FePc molecules (Fig. 5.2b). We also find no proof for adsorption of the FePc molecules on-top of these clusters (Fig. 5.2c) since STM images do not reveal the presence of any structural modulation in the z direction over the particles. Instead, the presence of the small Cu clusters seeds, anchored at the "holes" of the alumina superstructure (undiscernible also at this bias), does not seem to influence either the appearance of the FePcs, or the adsorption geometry.

The role of surface potential energy. At higher FePc coverage, instead, Cu clusters strongly influence the self-assembly of the molecular layer. On the pristine alumina, FePc molecules assemble forming a locally-ordered structure characterized by a supercell matching that of the underlying alumina film, yielding a $(\sqrt{67} \times \sqrt{67})$R12.2° regular pattern (Fig. 5.3a) with a local FePc coverage of 0.09 ML, corresponding to 6 FePcs molecules per alumina unit cell. In coincidence with the *dot* sites of the alumina structure we find missing FePc molecules in the self-assembled monolayer (the site is marked with a hexagon in Fig. 5.3a). Due to the hexagonal symmetry of the assembly, in the following the structure will be referred to as the "Hexagonal Structure" (HexS). Here, the inter-molecular interactions are overwhelmed by the adsorbate-surface interactions, at variance with what has been observed for FePcs deposited on the Cu(111) and Au(111) single crystal terminations, or on a weakly coupled graphene sheet.[125,128,195,196] In fact, at first glance the C3ν symmetry of the underlying

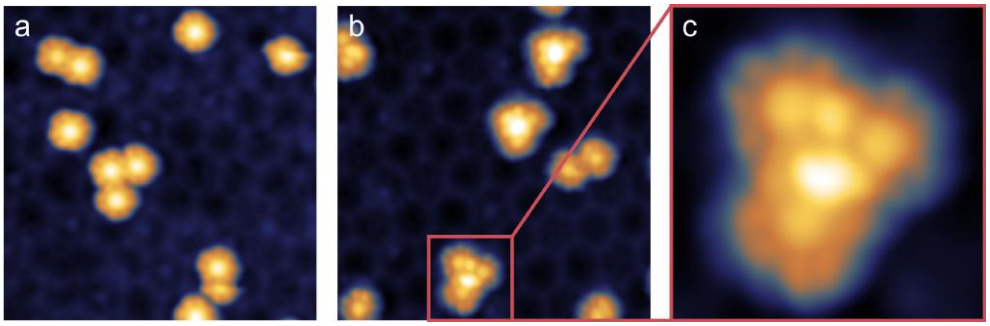

Figure 5.2: STM images at low local coverage (< 0.010 ML) of FePcs on (a) the pristine and (b) the Cu-decorated alumina film showing how the large Cu clusters act as coalescence sites for the molecules. [V_{bias} = +2.0V; 19 × 19 nm^2; (a) I = 10 pA and (b) I = 7 pA]. The molecular aggregate shown in (c) evidences how FePcs avoid on-top adsorption on large Cu clusters [V_{bias} = +2.0 V, 5 × 5 nm^2; I = 7 pA].

ultra-thin alumina film is reproduced by the adlayer. The FePc "vacancies" characterizing the HexS form a periodic lattice with a unit cell parameter of 4.16 nm, in registry with the $(\sqrt{67} \times \sqrt{67})$R12.2° alumina unit cell. The six molecules surrounding each molecular vacancy form, within the experimental resolution, a hexagon with diagonals of 3.1 nm and rotated by $21 \pm 1°$ with respect to the vacancies-joining vectors (Fig. 5.3a).

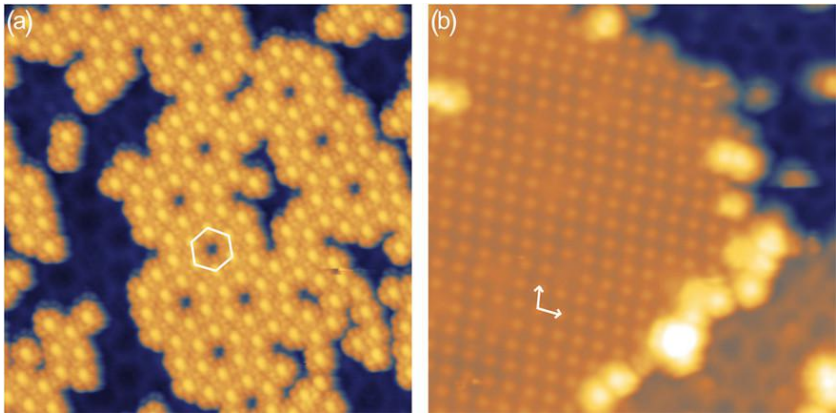

Figure 5.3: STM images (a) of the hexagonal FePc assembly (HexS) on the pristine alumina film and (b) of the almost square lattice (SquS) formed on the Cu-decorated alumina surface [high local coverage, above 0.089 ML; V_{bias} = +2.0V, 30 × 30 nm^2; I = 5 pA].

DFT computations (obtained in the framework of a collaboration with the International Center of Theoretical Physics (ICTP) and the theoretical group of the condensed matter physics section of the Physics Department of the University of Trieste) evidence a major role of the adsorbate-surface interactions in defining the symmetry and geometry of the assembled monolayer. Indeed, adsorption of the FePc is much disfavored at a *dot* site (the calculated molecule-surface bond energy is only 0.61 eV) with respect to the oxygen-terminated regions (2.8 eV) (Fig. 5.4, top panels). The high corrugation of the potential energy surface thus influences the self-assembly, and lateral inter-molecular interactions have to undergo symmetry constraints that are induced by the substrate, as observed in the case of the FePc Kagomé lattice on the highly corrugated graphene on Ru(0001).[127]

From DFT calculations combined with experimental STM results we obtained the position of each FePc within the HexS unit cell as depicted in Fig. 5.5, where the structural model is superimposed on the experimental microscopy image. The model corresponds to the DFT

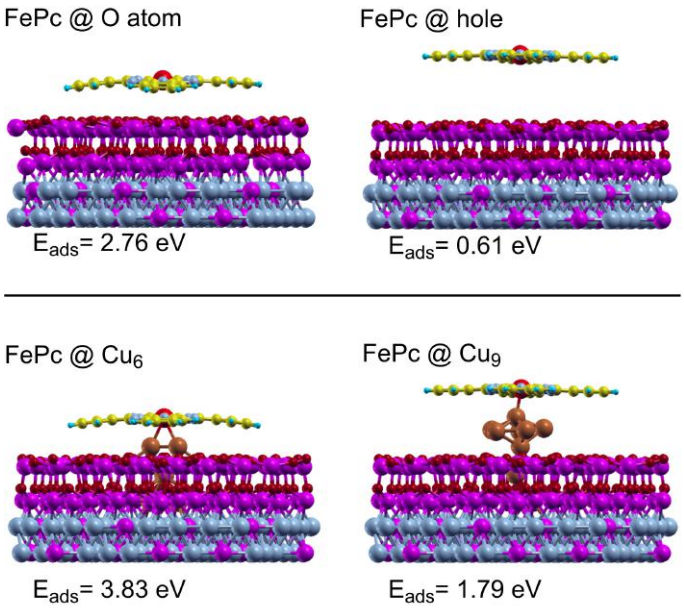

Figure 5.4: Stick and ball model of the simulated adsorption geometries of a FePc molecule on the pristine (top panel) and Cu-decorated alumina thin film (bottom panel). Color legend: Ni, grey; Al, purple; O, dark red; Fe, red; C, yellow; N, light blue; H, blue; Cu, orange.

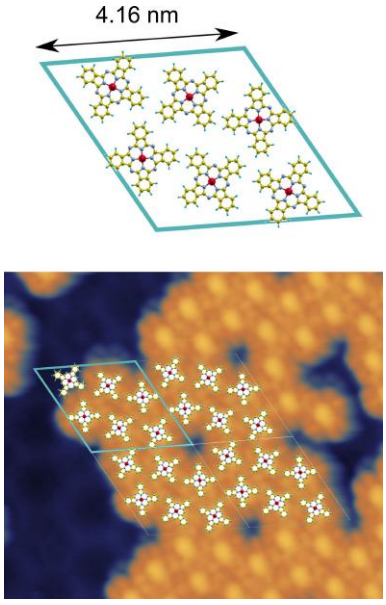

Figure 5.5: Model unit cell for the hexagonal structure of the FePc/Al_2O_3 system (top). At the bottom, a (2×2) cell superimposed on an experimental STM image.

fully-relaxed structure, in which the constraints about the relative molecular orientation were lifted, with the metallic cores pinned, instead, at the positions extracted from the experimental STM images. The bias-dependent appearance of the FePc molecules in the STM images was also simulated and the results were compared with the corresponding experiments (Fig. 5.6a).

Pre-seeding of the alumina support by small Cu clusters yields a smoothing of the potential energy surface, making also the *dot* sites favorable for adsorption of the FePcs. In fact, on the Cu-decorated ultra-thin oxide film, FePcs adopt a denser adsorption structure, with a coverage of 0.106 ± 0.007 ML, and characterized by a quasi-quadratic unit cell ($\alpha = 98 \pm 3°$) with unit vectors $a_1 = 1.40 \pm 0.05$ nm and $a_2 = 1.50 \pm 0.05$ nm (Fig. 5.3b), the latter rotated by $20 \pm 2°$ with respect to the underlying alumina, thus yielding an incommensurate superposition. The pseudo-C4ν symmetry is typical of densely-packed Pc domains in which lateral molecule-molecule interactions prevail.[107,114] We refer to this structure as the "Square Structure" (SquS). Glide planes are observed in the STM images, consisting in a 21 ± 3 % shift along a_2, but with no regular periodicity along a_1. It is reasonable that some strain release is necessary to accommodate the quasi-quadratic unit cell of the SquS on the underlying hexagonal alumina termination. DFT calculations confirm that the role of the Cu seeds is to allow adsorption of the ad-molecules also at the *dot* sites. Indeed, an adsorption energy of 3.83 eV is obtained for the binding of the FePc to a Cu_6 cluster at the *dot* site (Fig. 5.4). This energy is even higher than that for adsorption at the oxygen-terminated sites (2.76 eV).

By close-looking at the STM images, we also find that a minority population of molecules in the SquS shows a different appearance as a function of the applied bias (Fig. 5.6b-c). Interestingly, the central bright protrusion associated with the mono-metallic Fe core (Fig. 5.6a) is absent (Fig. 5.6c). The position of these "dim" molecules does not match the "holes" (*dot* sites) of the underlying alumina unit cell, thus excluding a contribution from the Cu clusters anchored at that sites, with a periodic and relative distance of 4.16 nm. A contribution from larger clusters can also be excluded, since they would be clearly imaged as observed at low coverages (Fig. 5.2b). Initially, this effect had no counterpart in our numerical STM simulations that at any bias yield a bright central protrusion associated with the Fe atom (Fig. 5.6a), even by increasing the size of the underlying Cu cluster (not shown). However, Cu clusters have to play a role, as these "dim" molecules are observed only on the Cu pre-seeded system. The dim molecules do not show up either when FePcs are deposited on a graphene substrate, i.e. another weakly interacting support.[206]
To explain this observation, we propose two possible pictures. The minority species could be associated with Pc molecules that have undergone de-metalation at the Cu clusters. A similar appearance of Pc molecules upon STM imaging has indeed been observed on the graphene surface.[207] Accordingly, our simulated STM images of Pcs adsorbed either on the oxygen sites of the pristine oxide or at the Cu clusters show analogous appearances (Fig. 5.6c). An alternative explanation may be instead ascribed to the interaction between the Fe centers and the underlying O atoms. As the molecular pseudo-C4ν array and the oxide C3ν structure are not in registry, several different, non-equivalent adsorption configurations of the Fe centers with respect to the oxygen-terminated surface are forced by the lateral constraints, yielding the formation of the glide planes discussed above as a stress-release phenomenon. While considering the catalytic effect of the FePc/Ag(110) system on the oxygen reduction reaction, Sedona *et al.* observed the FePc molecules to show a dim, but still metalated center when the Fe atom interacts with two oxygen atoms in specific adsorption geometries.[126] Therefore, also in the present case the "dim" molecules may bind to two oxygen atoms of the underlying oxygen-terminated alumina support.
We do not explore further the details of this effect in this report that is manly focused on the structural tunability induced by Cu. In any case, it is clear that the forced population of

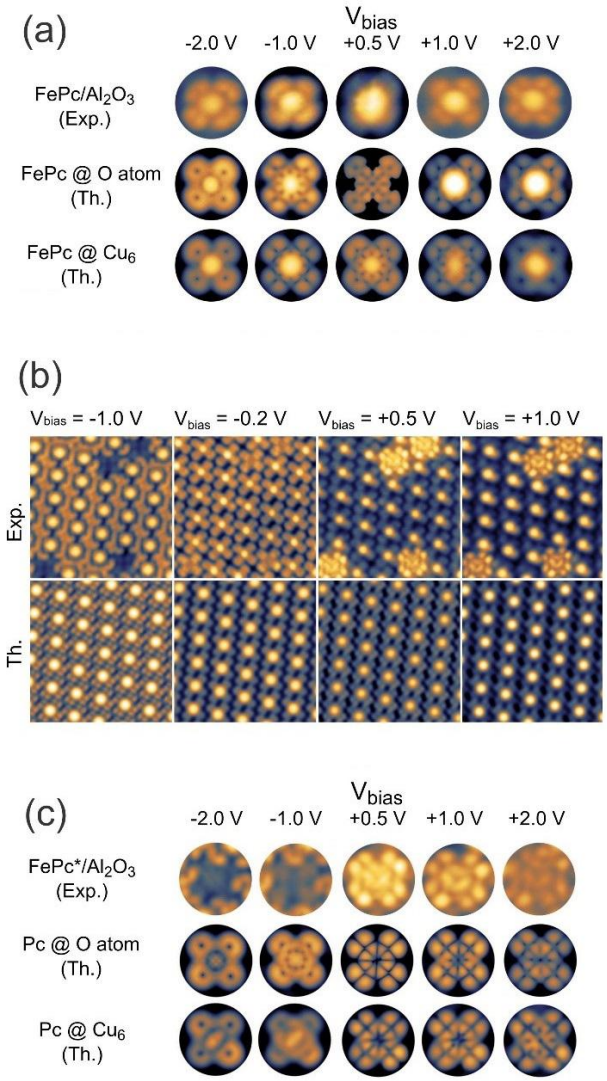

Figure 5.6: Comparison between experimental (Exp.)and DFT-simulated (Th.) bias-dependent appearance of the FePc molecules at different adsorption sites. Top panel (a): isolated FePc molecules on the FePc/Cu/Al_2O_3 surface; DFT simulations confirm negligible differences between the FePc adsorbed on the oxide or on the Cu clusters. Middle panel (b): STM images of the SquS recorded at the indicated bi-as at fixed position, compared with simulations of a free-standing FePc layer with the proper periodicity. Bottom panel (c): "dim" FePc molecules appearing in the SquS; the disappearance of the central bright protrusion is reproduced by simulating a de-metalated Pc molecule adsorbed either on the oxide surface or on a small Cu cluster.

specific adsorption sites by the FePc molecules in the square array yields also new minority states.

5.1.3 Cu nanoclusters: the interaction with the FePcs.

DFT and XPS: depicting the FePc-Cu interaction. While the role of the Cu metal clusters on the supramolecular self-assembly is evident, the FePc-cluster interaction needs further insight. As already pointed out, the bias-dependent appearance upon STM imaging of the FePcs is not affected by the presence of Cu seeds (Fig. 5.6a). The computed density of states projected on the benzenic carbon atoms, on the nitrogen atoms, and on the Fe center suggests that the bonding of the molecules to the Cu nanoparticles yields a rearrangement of the electronic structure, involving the whole molecule but in particular the Fe $3d$ states (Fig. 5.7). Interestingly, the molecule is more perturbed upon adsorption at small clusters. This reflects in a trend in the adsorption energies, i.e. in the strength of the FePc-Cu bond, changing from 3.83 eV to only 1.79 eV by increasing the Cu nanoparticle size from 6 to 9 atoms (Fig. 5.4). This is also confirmed by the absence of FePc molecules adsorbed at the large Cu particles, as from the STM images.

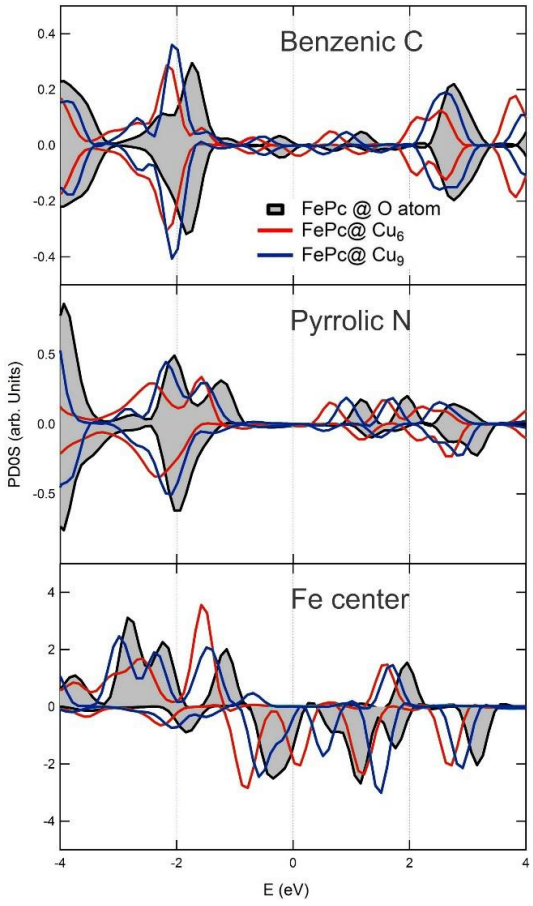

Figure 5.7: Calculated DOS projected onto (from top to bottom) the p states of all C atoms of the benzenic rings, the p states of all N atoms of the pyrrolic rings, and the d states of the central Fe atom; different colors refer to FePc molecules at different adsorption sites.

In order to shed further light on the FePc-Cu interaction, we performed X-ray photoelectron spectroscopy measurements of the C and N $1s$ core level regions at low (0.04 ML) FePc coverage for increasing, selected Cu loadings (0.09, 0.15, and 0.23 ML, yielding average Cu cluster sizes

of 6, 10, and 15 atoms, respectively). Photoemission spectra were collected at the Materials Science Beamline end-station at the ELETTRA synchrotron facility through a Specs Phoibos 150 high-luminosity electron-energy analyzer. C and N 1*s* core level regions were measured at normal emission (selecting 400 and 500 eV incident photon energies, respectively) and normalized at the lower binding energy side background. The data were analyzed by least-square fitting with Voigt profiles, taking into account a linear background. The experimental spectra and their deconvolution, as obtained by least square fitting, are shown in Fig. 5.8. In order to extract the most reliable information, constraints on the fitting parameters were imposed aiming at reducing the number of free parameters (see Appendix 6.9 for further details). Concerning the N 1*s* core level region (left), it is known that FePcs adsorbed on several substrates exhibit two features that are in most cases energetically unresolved and are centered at about 399 eV with a relative shift of 0.3-0.5 eV.[170] They are associated with the two non-equivalent nitrogen atoms in the tetrapyrrolic ring.[128,196] Accordingly, we fitted the N 1*s* spectrum of FePc molecules deposited on the pristine alumina surface with two Voigt-shaped features of equal intensity centered at 399.3 and 399.0 eV, respectively.

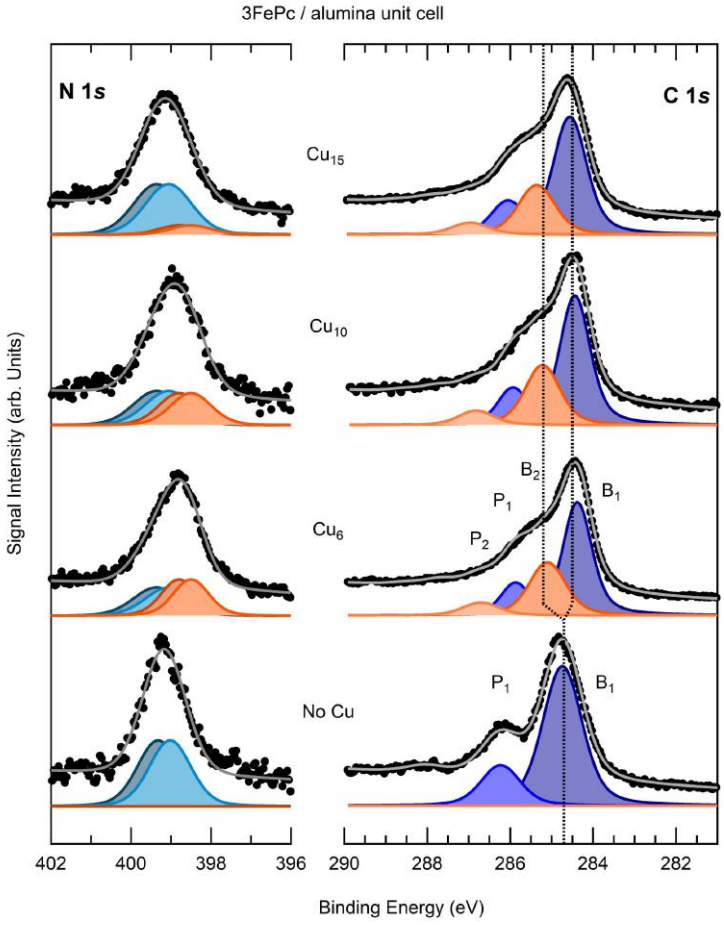

Figure 5.8: Left panel: N 1*s* spectra collected at 300 K at fixed FePc coverage for increasing Cu loading, from bot-tom to top [hν = 500 eV]. Right panel: C 1*s* core level region [hν = 400 eV]. Data (black dots) and the results of the least-square fitting procedure (grey lines) are shown together with the color-filled curves representing the deconvolution of each contribution. Blue and orange colors refer to FePc/Al_2O_3 and FePc/Cu/Al_2O_3 molecules, respectively. The dashed lines indicate the average positions of the B1 and B2 features, displaying fine energy shifts as a function of the Cu cluster size.

When Cu is pre-deposited, we observe an apparent broadening of the spectral feature,

accompanied by a shift towards lower binding energies. Indeed, the experimental data are adequately deconvoluted in the latter case by two pairs of peaks, i.e. the former doublet plus a new doublet at 0.6 eV lower binding energy, attributed to FePc species in contact with Cu. The signal intensity of this doublet progressively decreases for increasing Cu cluster size. Therefore, from the core level spectra and in agreement with both STM images and DFT calculations, we can conclude that the FePc-Cu interaction is progressively weakened at increasing cluster sizes. The new FePc population is also observed in the corresponding C 1*s* spectra, shown in the right-panel of Fig. 5.8. In the C 1*s* spectrum of FePc molecules deposited on the bare alumina film (bottom-right spectrum), two adiabatic features can be clearly resolved. In line with the literature, we associate the two peaks with the carbon atoms forming the benzenic (B1) and pyrrolic (P1) groups, respectively.[196] At closer inspection, see Fig. 5.9, the spectrum reveals the presence of an additional feature appearing at higher binding energy and ascribed to inelastic shake-up effects (S1). The presence of another non-adiabatic

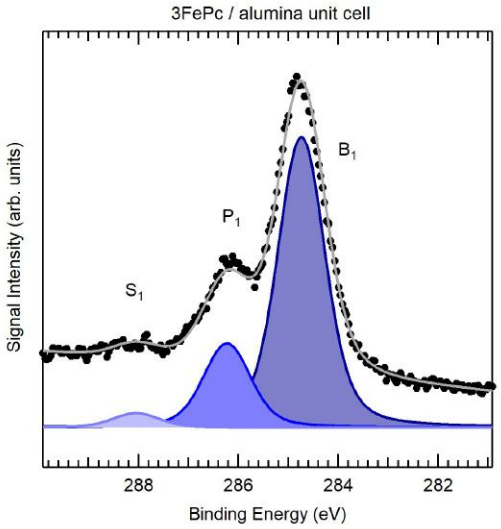

Figure 5.9: C 1*s* spectrum collected at 300 K of the FePc molecules deposited on the pristine Al_2O_3 surface. The highest binding energy feature (S) is ascribed to non-adiabatic adiabatic features and has been properly considered in the least-square fitting throughout the manuscript.

peak close to the pyrrolic signal is known from high-energy resolution experiments, but this latter feature is definitely not resolved in our case.[208] Therefore, we adequately reproduce the C 1*s* spectrum of the FePc/Al_2O_3 system with a triplet of peaks, constrained in a first approximation to a common Lorentzian linewidth ($\gamma = 0.4$ eV) and yielding binding energies of 284.7 eV (B1), 286.2 eV (P1), and 288.0 eV (S1). For clarity, in Fig. 5.8 and 5.10 we report only the deconvolution of the benzenic and pyrrolic peaks. When the surface is pre-covered with Cu clusters, the spectra are successfully fitted by means of two sets of triplets, associated with the FePc molecules interacting with the oxide surface (B1 and P1) and with the Cu clusters (B2 and P2), in analogy to the case of the N 1*s* peaks. The former C 1*s* triplet is rigidly shifted to lower binding energy by 0.2 eV with respect to the pristine alumina case, while the latter appears at higher binding energy (+0.7 eV).

Enhancing FePc thermal stability through the Cu clusters. Tackling the effect of the clusters on the thermal stability of the FePc layer, a step by step annealing up to 600 K was performed and C 1*s* spectra were collected at room temperature after each annealing. On the left side of Fig. 5.10, the carbon core level region of 0.04 ML FePc deposited on the pristine

and on the 0.15 ML Cu-decorated alumina thin film are reported, while in the right panel we plot the total integrated intensity for different Cu loadings, normalized to the pre-annealing signal, versus the annealing temperature. On the bare alumina the molecular layer appears to

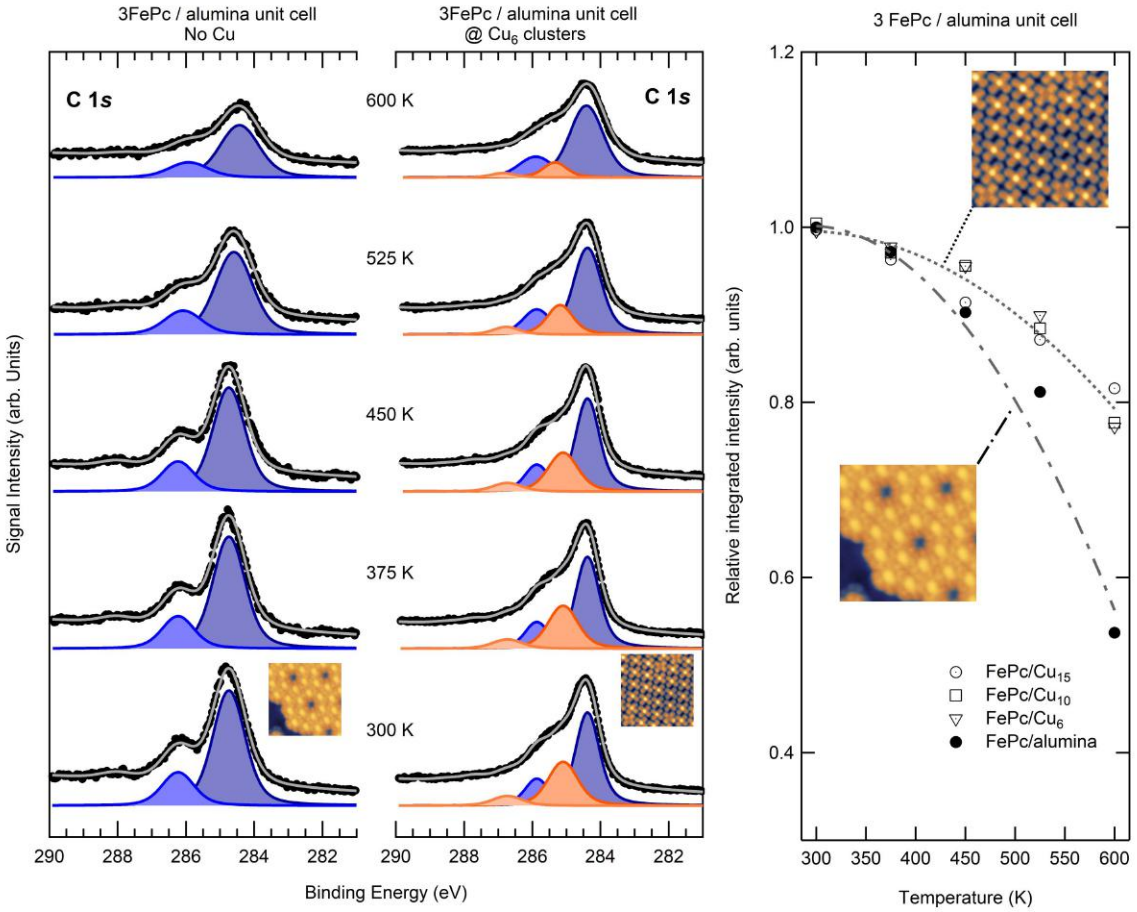

Figure 5.10: On the left side, C 1*s* core level region evidencing the difference in thermal stability of the FePc layers deposited on the pristine (left) and on the Cu-decorated Al_2O_3 surface (right), represented by the STM images of the HexS and SquS structure respectively. Spectra were collected at 300 K after each annealing step. Only the results from the measurements on the Cu_6 system are reported, but analogous effects have been observed also for Cu_{10} and Cu_{15} and are summarized in the right-most panel: the plot of the relative integrated intensity shows the temperature stabilization effect of the Cu clusters on the 2D FePc monolayer. Dotted lines are drawn to guide the eye.

be quite stable up to 450 K, as only a XPS intensity loss of around 10% occurs. Above that temperature, a progressive reduction of the signal within a wide temperature range (46% at 600 K) takes place, accompanied by a Gaussian broadening of the spectral features (from 0.59 to 0.95 eV). This reasonably suggests desorption and progressive, partial decomposition of the molecular structure, similarly to the case of FePcs suported on a single graphene sheet.[128] In the presence of the Cu seeds, the effects of temperature are weakened, yielding, to a certain extent, a stabilization of the FePc layer (the XPS signal reduction is limited to 20% at 600 K). We observed no dependence (Fig. 5.10, right panel) of this stabilization effects on the cluster size (experimentally estimated average sizes of 6, 10, and 15 Cu atoms/cluster) thus associating the thermal stability to the molecule-molecule lateral interactions in the SquS overstructure.

Insights about the FePc core: CO adsorption at NAP. After proving the effect of the Cu seeds on the structure and on the thermal stability of the molecular layer, we finally investigated possible effects of the Fe-Cu interaction on the adsorption properties of the single metal atom core of the Pc. Due to the weak interaction of the central metal atom with small ligands, we switched to near ambient pressure conditions in order to populate the adsorption sites at room temperature.[114] IR-Vis SFG experiments were performed *in situ* at 5 mbar. It is known from the literature that CO adsorption may be exploited as a probe to identify the active sites of nanostructured surfaces and infer about their evolution.[178] At room temperature, significant population of the Fe atoms by CO occurs on the FePc molecules only in the millibar pressure regime.[51] Thanks to the surface-sensitivity of *in situ* IR-Vis SFG vibronic spectroscopy, we characterized the cluster-size dependence of the FePc active sites with CO as a chemical probe. Adsorption of CO on the bare alumina thin film and consequent formation of carbonate species is not expected even at the mbar regime.[209] On the other hand, small Cu clusters promote CO adsorption and decomposition even under ultra-high vacuum conditions and liquid nitrogen temperature, yielding accumulation of atomic carbon via the Boudouard process.[199] For this reason, preliminary check measurements were performed on the pristine and on the Cu-decorated alumina surfaces, confirming that no CO-related features can be detected unless FePc molecules are deposited.

In Fig. 5.11, SFG spectra collected in the intra-molecular FePc and C-O stretching regions are reported. The data were obtained at 0.04 ML FePc coverage, yielding 3 molecules per

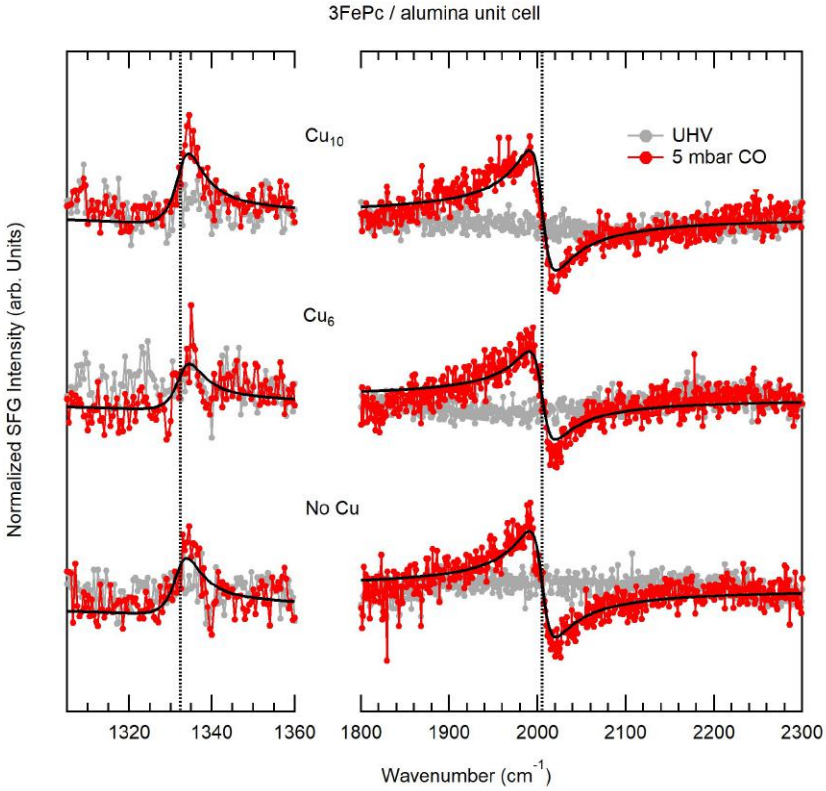

Figure 5.11: *In situ* IR-Vis SFG spectra [ppp polarization, $\lambda_{Vis} = 532$ nm] collected at 300 K in the C-O and intra-molecular C-C stretching regions, right and left panels, respectively. Data (dots) and the results of the least-square fitting procedure (black lines) are shown. While data pertaining the UHV condition are reported in grey, red dots refer to measurements collected *in situ* in 5 mbar CO. Spectra were collected for fixed FePc coverage and increasing Cu loading, from bottom to top.

alumina unit cell, and for increasing Cu loading (0.09 and 0.15 ML, corresponding to 6 and 10 Cu atoms/cluster). Grey lines and markers represent the reference spectra obtained under UHV conditions, while red data correspond to the measurements in 5 mbar CO. In the lower energy region, the internal modes of the organic macrocycle are expected to show up, but only when the molecular plane is not parallel to the crystal surface or some deformation of the molecule occurs in order to yield a dipole-active component parallel to the surface normal.[125] This is not the case for the FePcs deposited both on the bare and on the Cu-seeded alumina. Instead, a peak appears at 1333 cm^{-1} when the molecular layer is exposed to CO. This feature is assigned to the rocking and scissoring modes of the benzenic rings of the macrocycle.[125] The appearance of this feature is thus ascribed to a significant deformation of the FePc plane upon CO adsorption. Considering the C-O stretching region, a single feature is observed at 2005 cm^{-1} upon CO exposure, reversibly disappearing as soon as the system is brought back to UHV conditions. We assign it to the internal stretching mode of single CO molecules interacting with the monometallic cores of the metallorganic framework. We observe no dependence on the Cu loading for both features, neither in the position, nor in the relative phase with respect to the non-resonant background. Intensity differences are within the experimental error of the FePc coverage, therefore non-significant. Since for Pt clusters on graphene the evolution of the active sites strongly modifies both the resonant frequencies and the relative phase,[178] we conclude that both the folding and the active sites of the FePc molecules are quite insensitive to the Cu clusters.

5.1.4 Conclusions

We have shown how to influence the FePc adsorption structure on the ultra-thin alumina layer grown on the $Ni_3Al(111)$ surface by artificially controlling the corrugation of the potential energy surface of the support, which is flattened by the pre-deposition of Cu clusters. The idea exploits the switching of the self-assembly process from a molecule-substrate to a molecule-molecule interaction scheme. A FePc-Cu_n bond is established and leads to evident changes in the molecular core-level spectra. By increasing the cluster-size ($n \geq 9$) the bond weakens and the larger the clusters, the lower the adsorption energy. CO adsorption on the FePc molecules occurs at room temperature at near ambient pressure regimes, but it is not influenced by the presence of Cu. However, the presence of the metal clusters strongly enhances the surface thermal stability of the adsorbed FePc molecules. Therefore, we demonstrate as it is possible to select different adsorption motifs and enhance the stability without affecting the adsorption properties of the molecular layer, at least concerning the CO ligand.

5.2 CO_2 at the phthalocyanine/graphene heterostack (CO_2-FePc/GR)

As mentioned above, in this last Section we demonstrate that it is possible to activate CO_2 binding to a 2D crystal of iron phthalocyanines supported by a single foil of graphene. The graphene template, modified by molecular oxygen exposure, act as a tuning knob activating the adsorption properties of the metallorganic layer. The resulting model system acts as a reversible carbon dioxide getter, mimicking many features of complex biological system but on an artificial nanostructured surface.

5.2.1 CO_2 adsorption and activation.

It is nowadays widely established that carbon dioxide is a greenhouse gas produced in large amounts by human activity, and recycling it on a massive scale through chemical conversion is one of the key challenges humankind has to face.[210–213] The closed shell nature of the molecule makes it poorly reactive, with small binding energies on reactive centers that could catalytically convert it and peculiar molecular activation mechanisms associated with a substrate to adsorbate charge transfer.[214–216] For this reason developing materials for conversion of carbon dioxide is a central issue, and nano-architected surfaces, presenting regular arrays of CO_2-specific adsorption sites, may yield innovative results.

A stable bond. In the CO_2 molecule, the carbon and oxygen atoms are bound in linear geometry through an *sp* hybridization of the four carbon atomic orbitals $2s$, $2p_x$, $2p_y$, and $2p_z$.[217,218] The first dissociation energy (D^0) is approximately 532 kJ/mol (5.5 eV), whereas to decompose the H_2 molecule an energy of 436 kJ/mol (4.5 eV) is needed.[219] Such strong bonding can be explained through the molecular orbitals (MO) model: of the resulting 10 linear combinations of the atomic *s* and *p* orbitals, only the bonding and non-bonding molecular orbitals are occupied (see Fig. 5.12).

CO_2 has therefore to be activated in order to convert it to other useful chemicals, i.e. its bonds must be weakened. Again in a MO scheme, it is predicted that charge (electrons) donation to the molecule will result in the population of the anti-bonding molecular orbitals. Destabilization will then occur, as observed in the CO_2^- anion: in order to "accommodate" the extra electron, the molecule assumes a bent geometry and part of the *sp* hybridization is lost. As reported by Taifan *et al.*,[218] the acquisition of an extra electron induces a bending of the O-C-O angle to 135°, while the C-O distance increases from 1.16 to 1.23 Å. Interestingly, the frequency of the antisymmetric stretching mode shifts from 2405 to 1764 cm^{-1} for the CO_2 and $CO_2{}^-$ molecule, respectively.

If carbon dioxide adsorbs on a surface and charge transfer from the substrate occurs, then the molecule may participate to reactions. This is what takes place in UHV conditions on the Ni(110) surface, as it was demonstrated by means of high resolution XPS and electron energy loss spectroscopy (HREELS).[216,220] CO_2 physisorption was observed at 87 K. Upon heating the sample above 110 K, spectroscopic data indicate the presence of chemisorbed CO_2 together with adsorbed CO and oxygen species, originated by the dissociation of the activated carbon dioxide.

Catalysis on biomimetic metal sites On what can be considered antithetic to single crystal surfaces and in general to artificial systems, living organisms developed strategies to deal with this problem efficiently, through the production of specialized biomolecules. Acetogenic bacteria exploit for example dedicated enzymes for the fixation and conversion of

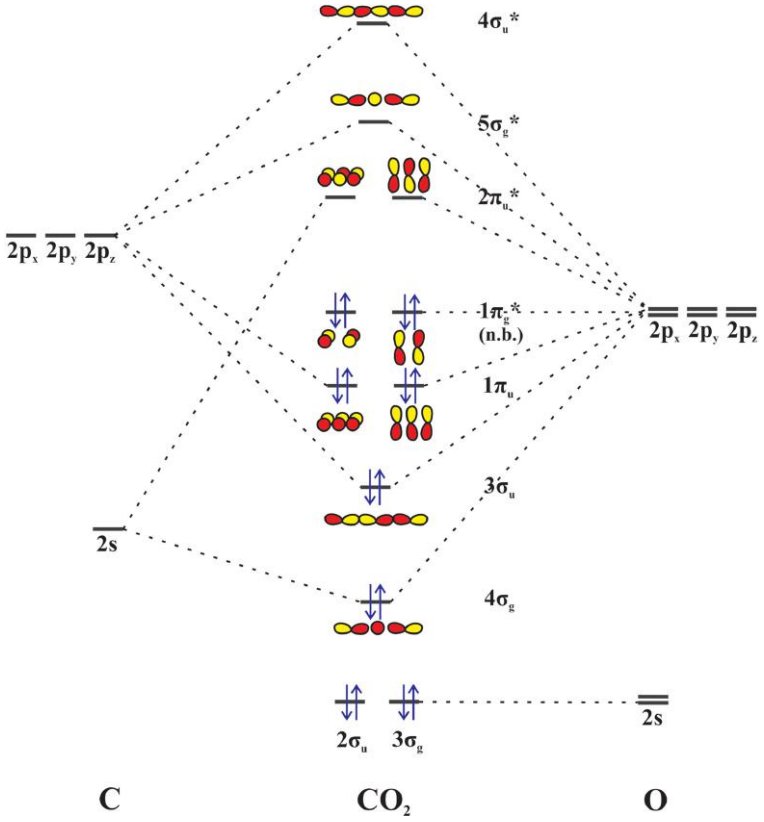

Figure 5.12: Molecular orbital diagram of linear (D1h symmetry) CO_2. Image from Taifan *et al.*.[218]

CO_2 at nanostructured reaction sites.[221] This has spurred considerable interest in the design, synthesis and control of biomimetic systems, which take advantage of chemical strategies present in natural systems, but can be handled and controlled in a laboratory. Fruitful approaches may be therefore based on biomimetic principles, taking inspiration from the architecture of reactive sites present in biomolecules widespread in Nature.[130] In a challenging perspective, catalytic cages in enzymes may be tuned or modified to yield specific selectivity or kinetic properties, in the view of merging chemical and biological catalysis.[222] Simple (electro)-catalysts for carbon dioxide conversion engineered on metallorganic macrocycles and porphyrin-like structures have already proven enhanced efficiency, stability, and selectivity with respect to conventional materials.[121,223] Recently, more complex, bioinspired self-assembled artificial nanostructures consisting of metal-organic frameworks have appeared as promising catalyst candidates, with the drawback of a yet poor engineering and predictable control on selectivity and conversion efficiency.[224] We propose here a concrete method to tune the properties of a 2D metallorganic crystal with respect to carbon dioxide adsorption and base our approach on the fast developing physics of heterostructures, consisting in the stacking of two-dimensional materials with peculiar, selected properties.[225] These results obtained on a model metallorganic framework imply applicative potentiality for CO_2 conversion processes based on (electro) catalytic approaches.[226]

In the following, we describe how we can oxidize graphene with molecular oxygen under near ambient pressure conditions, thus n-doping the FePc-graphene heterostack. The charge transfer at the organic/inorganic interface to the FeN_4 centers activates the framework towards CO_2 adsorption that becomes favored. Consequently, carbon dioxide binds chemically to Fe already at 0.05 mbar in a "V" shaped configuration, at variance with the uncharged system at which no adsorbed state is detected, at least up to two orders of magnitude higher pressure.

5.2.2 Oxidation of the graphene substrate.

In the specific, we chose to grow a self-assembled 2D crystal of iron phthalocyanine molecules (FePc) on a single graphene (GR) sheet, similarly to what has been performed in Section 4.3. By chemical vapor deposition and decomposition of ethylene on the Ir(111) single crystal surface,[227,228] it is possible to obtain an almost decoupled monolayer GR showing only slight p-doping, where Dirac points are found at a binding energy of only 0.067 eV above the Fermi level.[125,227,228] It is known that under model UHV conditions a gap can be artificially induced, together with a shift of the Dirac cones below or above the Fermi level, by oxidizing the graphene sheet,[228–230] or by intercalating oxygen beneath it,[227] thus by n- or p-doping it, respectively.

We propose a novel procedure to alter the GR carpet, consisting in a near ambient pressure (100 mbar) exposure to molecular oxygen at room temperature. The resulting layer presents spectroscopic fingerprints in line with previous findings concerning oxidized GR layers. Interestingly, most of these works relied on atomic oxygen sources,[228–230] where we employed molecular oxygen.

High pressure oxidation: stable graphene oxide (GRO) at room temperature. X-Ray Photoelectron Spectroscopy (XPS) core level spectra collected in UHV prior and after oxidation of bare graphene are presented in Fig. 5.13. A broad O 1s component appears at 532.5 $\pm$ 0.1 eV, while no feature could be detected in the corresponding UHV spectra. Concerning the C 1s region, the spectral feature associated with the pristine GR sheet slightly shifts from 284.01 to 284.09 eV, while new components appear at 284.67 , 285.50, and 286.19 eV (with an uncertainty of about $\pm$0.05 eV). Based on aforementioned literature, reporting UHV oxidation of GR/ Ir(111) by means of atomic oxygen beams,[228–230] we can conclude that graphene oxide (GRO) is obtained following this high pressure conditioning. We associate the new core level components at 532.5, 285.50, and 286.19 eV with the predominant presence of epoxy species at the "pores" and "wires" of a highly corrugated GRO sheet,[229,231] and the peak at 284.67 to other O-induced structures and defects.[229,230] Further considerations about GRO corrugation will be discussed in the following Section 5.2.3.

Oxygen intercalation at the GR/Ir(111) interface is excluded during the high pressure treatment: intercalated oxygen would decouple GR from the surface, lifting the sheet corrugation and the C 1s peak associated with GR would shift to lower binding energy (283.60 eV). Moreover, it would be associated also to an O 1s core level component at 529.8 eV due to atomic oxygen adsorbed at the Ir(111) metal surface.[227]

Oxygen-induced n/p- doping: GR band structure at the Fermi level. Concerning the band dispersion evolution, it is known from the literature that the oxidation process introduces a pronounced energy bandgap at the Fermi level (>0.35 eV), a deformation of the dispersion from linear to parabolic, and a downshift of the valence band below the Fermi edge, see Fig. 5.14, left panel.[228] This effect is associated with the sp^3-like character of the C atoms involved in the formation of the epoxy groups at the expense of the sp^2 graphene hybridization. Instead, on oxygen intercalated GR, the effect would be the opposite, resulting in a p-doping of the GR sheet and an upward shift of the GR Dirac cone across the Fermi level by 0.6 eV, see Fig. 5.14, right panel.[227]

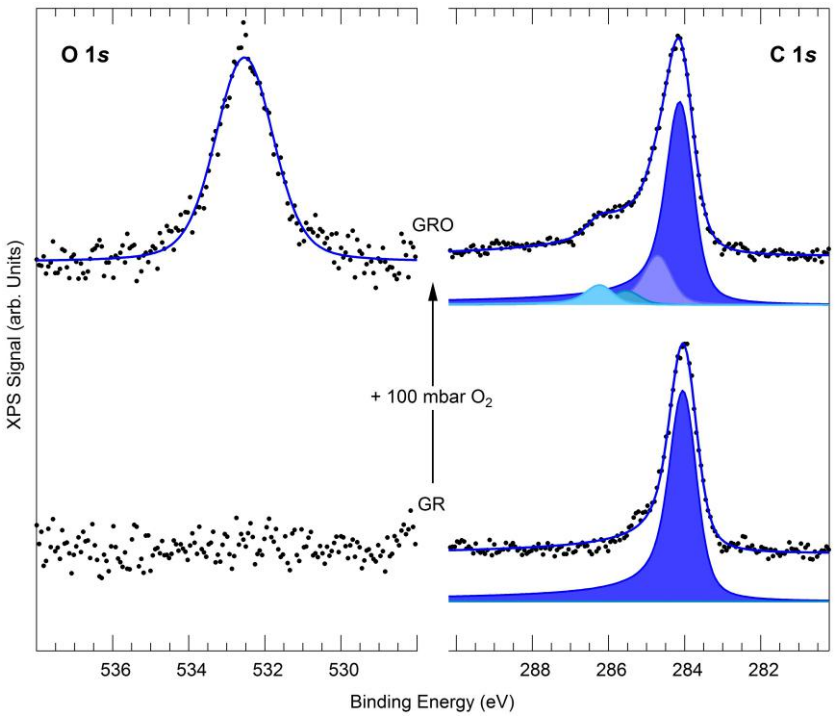

Figure 5.13: X-ray photoelectron spectroscopy data of bare graphene on Ir(111) (bottom) and of GRO, after oxidation at room temperature in 100 mbar O_2 (top). The O and C 1*s* core level signals are shown (left and right, respectively) together with the best fit (continuous line) and the deconvolution in the single core level shifted C 1*s* components (filled curves). The spectra were collected *ex situ* at room temperature in UHV (hν = 1253.6 eV).

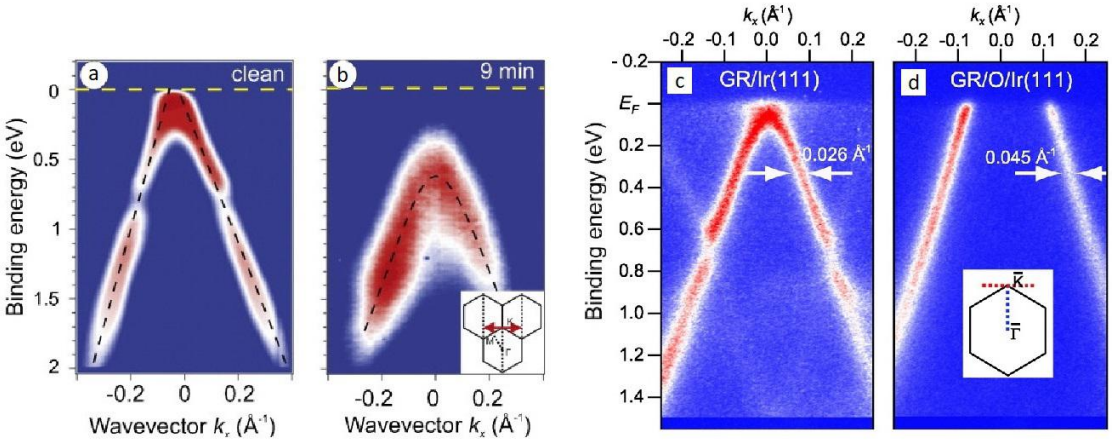

Figure 5.14: ARPES measurements of the oxidized and intercalated graphene on Ir(111) single crystall termination. In the left panel, photoemission intensity data around the K-point of the Brillouin zone (wavevector direction as indicated in the inset) of: (a) Clean graphene and (b) oxidized graphene after 9 min exposure to atomic oxygen. Image from Schulte *et al.*.[228] On the right, photoemission spectra acquired along a line orthogonal to the **ΓK** direction (see inset in (d)). In (c), dispersion of the as-grown graphene/Ir(111) and (d) of the lifted graphene due to O-intercalation. Image from Larciprete *et al.*.[227]

IR-Vis SFG: insight about the optical G mode of the GRO layer As preliminary control experiments, I collected IR-Vis SFG spectra at room temperature prior and after the high pressure O_2 treatment on the pristine graphene layer, without the molecular adlayer (Fig. 5.15).

The higher corrugation of the GRO sheet with respect to the pristine GR accounts for the increased SFG amplitude of its optical G mode, which also shifts from 1615 to 1609 cm^{-1}, as observed in Fig. 5.15a-b. Indeed, a more corrugated structure yields a larger dipole component in the direction of the surface normal, actually contributing to the SFG intensity.[232] The GRO system proves to be inactive towards CO_2 adsorption, as no additional vibrational features appears in the room temperature IR-Vis SFG spectrum collected *in situ* in 5 mbar CO_2 background pressure (Fig. 5.15c). Intriguingly, while the optical G mode of graphene appears to be affected by both oxygen exposure and FePc deposition, no effect of the near ambient pressure exposure to carbon dioxide can be highlighted in the line position (see Fig. 5.16), suggesting a passive role of graphene during CO_2 exposure.

After the system was brought back to UHV condition, an annealing was performed to 650 K to induce desorption of the oxygen species (see Fig. 5.15c).[228,230] We recover the initial spectral lineshape, in terms of both the optical G mode frequency and the SFG signal amplitude, in agreement with the removal of the epoxy groups as reported in the literature.

5.2.3 FePc monolayer on graphene oxide: enhancing CO_2 adsorption

The growth of the metallorganic FePc-framework on graphene yields a regular array of single metal atom reactive sites. These Fe centers are distributed on an almost square lattice with a Fe-Fe distance of about 15 Å. As determined by Scanning Tunneling Microscopy (see Fig. 4.13 and Section 4.3), the actual cell measures 14.1×13.6 $Å^2$, with an internal angle of 87°. The IR-Vis SFG vibronic spectrum of the as grown FePc/GR heterostack on Ir(111) shows under UHV the predominant presence of the GR optical G mode at 1615 cm^{-1} (Fig. 5.17a). At lower energy, two internal modes of the FePc are detected, associated with the benzene scissoring at 1335 cm^{-1} and with the B2 mode, involving the tetrapyrrole ring and the isoindoles, at 1398 cm^{-1}.[233] Upon exposure of the system at room temperature to 5 mbar CO_2, no significant modifications of the vibronic spectrum of the FePc are detected *in situ*, and we do not observe any vibrational fingerprint associated with adsorbed carbon dioxide (Fig. 5.17b'). The very weak CO_2 Fe interaction yields no significant adsorption at 5 mbar at room temperature.

When we expose the FePc/GR system to 100 mbar O_2, we observe the already discussed increase in the amplitude of the resonance associated with the GR phonon, undergoing again a redshift from 1615 to 1609 cm^{-1} (Fig. 5.17b and 5.18). In association with the aforementioned spectral modifications, already observed in Fig. 5.15a-b for the pristine GR monolayer, upon oxidation of the Fe/GR heterostack we also observe a phase change of the internal vibronic mode of the adsorbed FePcs (Fig. 5.18), an indirect proof of a modified electronic configuration of the system in proximity of the Fermi level. The phase shift by -60 ± 5° accounts for the shape change of the IR-Vis SFG spectral contribution (Fig. 5.17a-b, left, brownish deconvolution).

Both the increase of the SFG amplitude of the optical G mode and the phase shift of the FePc vibronic modes, together with XPS results presented in Fig. 5.13, fit with the n-doping of graphene induced by the oxidation process.

CO_2 adsorption at the FePc/GRO When we expose to 0.05 mbar of carbon dioxide the FePc/GRO heterostack, obtained by room temperature self assembly and near ambient

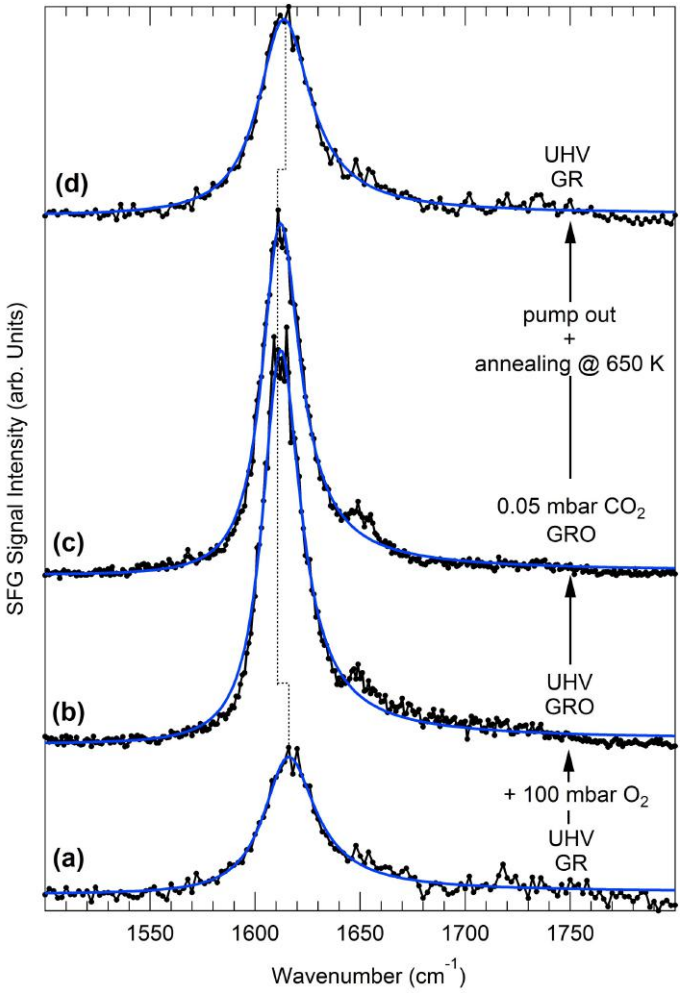

Figure 5.15: IR-Vis SFG spectra of the optical G mode of graphene. The spectra were collected *in situ* sequentially from (a) to (d): (a) bare GR/Ir(111) as prepared, under UHV conditions; (b) after oxidation in 100 mbar O_2 at room temperature; (c) GRO/Ir(111) in 0.05 mbar CO_2; (d) after evacuation, back to UHV and annealed. The best fit curve of the data, according to the lineshape described in the text, is also shown (cyan line). Apart from a shift of the GR line due to oxidation, no additional features related to CO_2 adsorption occur. Polarization: ppp.

pressure oxidation, several spectral modifications are observed *in situ*. In the specific, IR-Vis SFG reveals (Fig. 5.17c) the growth of two peaks at 1535 and 1729 cm^{-1} that, on the basis of literature data, can be associated, respectively, with an internal mode of the FePc (stretching of the porphyrazine),[125] and with the antisymmetric internal stretching mode of an activated, adsorbed carbon dioxide species.[216,218,220,226] The latter is expected to bind in a bent, "V"-shaped configuration at the Fe metal center, in association with a charge transfer from the metal to the molecule.[216,220,226] Adsorption of the ligand occurs at the macrocycle and this is confirmed by the SFG spectral features associated with the internal FePc modes (Fig. 5.17c, left). Indeed, we assist to a general increase of the resonant amplitudes of the features, possibly related with a further deformation of GR and of the tetrapyrrole macrocycle, and with a reorientation of the benzene rings. We also observe a further phase change of the vibronic fingerprint of the macrocycle mode, shifting by -260 ± 5° with respect to the pristine FePc/GR heterostack and by -200 ± 5° with respect to the modified FePc/GRO (Fig. 5.18).

The lineshape change appears clearly in the deconvolution (brownish) of the spectra shown

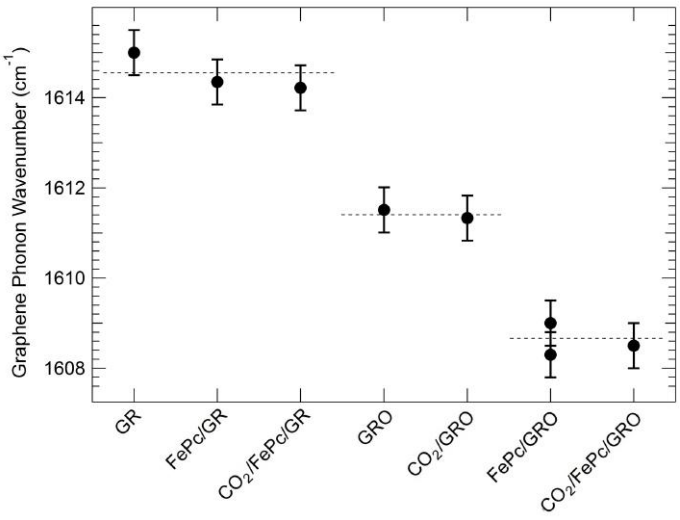

Figure 5.16: Wavenumber position of the resonance associated with the optical G mode of graphene, as obtained from the best fit of the IR-Vis SFG data collected *in situ*. An influence of both the oxidation and the growth of the 2D FePc crystal can be observed, yielding a progressive redshift of the phonon. Instead, adsorption of CO_2 at the iron site does not contribute.

in Fig. 5.17a-b-c. Furthermore, the process is reversible: when pumping out the CO_2 gas phase and recovering UHV condition, CO_2 desorption occurs (Fig. 5.17c-d) and all spectral features are accordingly restored.

The n-doping and the role of charge accumulation. *Ab initio* calculations (performed by the theoretical group of the condensed matter physics section of the Physics Department of the University of Trieste) based on the Density Functional Theory confirm and support the whole picture. We performed simulations of CO_2 interacting with the FePc monolayer in order to investigate adsorption geometries, binding energies, and charge redistribution effects. The FePc system was modeled in a periodically repeated cell, whose optimization gave planar molecular superstructure with an almost square periodicity, as observed in the experiments. Quite in agreement with the experiment, the high-symmetry molecular axes form an angle of about 26° with respect to the FePc lattice.

The GR support was not explicitly considered, but the effects of oxidation or possible oxygen intercalation were modeled by varying the electronic charge on the FePc. We studied the neutral, the positively charged (-2e), and the negatively charged (+2e) FePc systems (reported in Fig. 5.19) to mimic the as-grown, oxygen intercalated, and oxidized (n-doped) GR support, respectively. We estimate that two electrons can represent the maximum amount of charge transferred between GRO and each FePc, therefore hypothesizing, during the oxidation process, a possible shift of the GR Dirac cone across the Fermi level of 0.6 eV, in analogy to the oxygen intercalation case.[227,228] Following Ulstrup *et al.*,[234] we assume a linear behavior of the variation $\delta(\Delta\pi)$ of the π band amplitude, and consequently of the Dirac cone shift, with the number n_e of extra electrons per GR unit cell:

$$|\delta(\Delta\pi)| = 9 * n_e \tag{5.1}$$

In the self-assembled FePc layer, each FePc corresponds to about 40 GR cells, therefore a shift of $|\delta(\Delta\pi)| = 0.6$ eV, which gives $n_e = 0.06$ electrons, implies about 2 electrons in the GR area underlying each FePc.

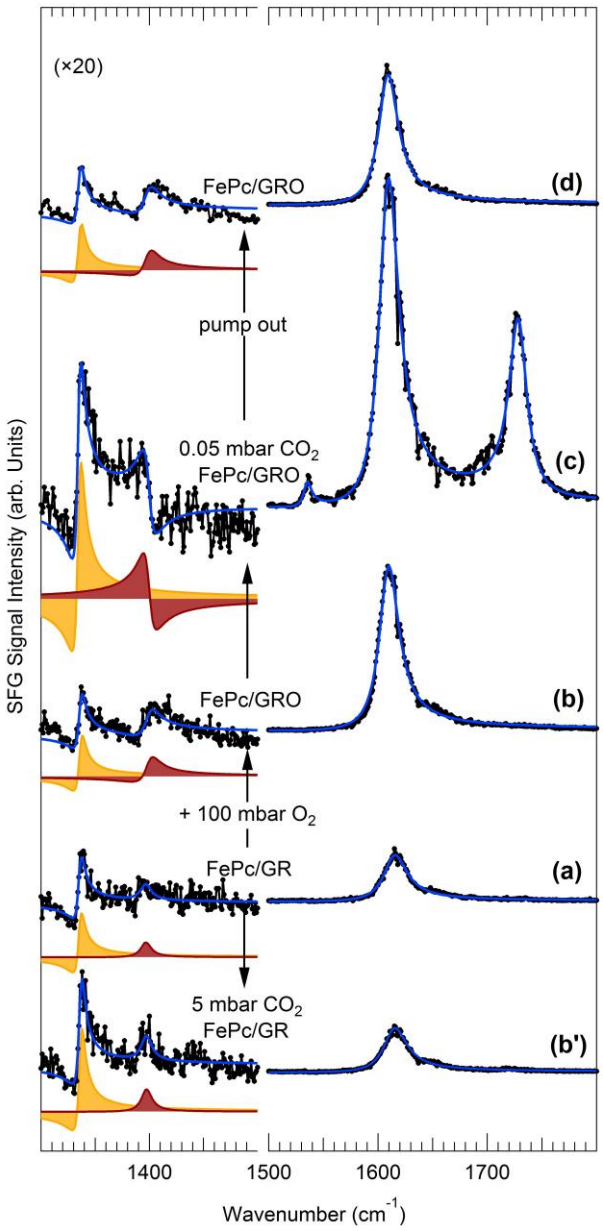

Figure 5.17: IR-Vis SFG spectra including the range of the FePc intramolecular modes, of the optical G mode of graphene, and of the internal CO_2 stretches. The spectra were collected *in situ* sequentially from (a) to (d): (a) FePc 2D crystal on GR/Ir(111) as prepared, under UHV conditions; (b') in 5 mbar CO_2; (b) after oxidation in 100 mbar O_2 at room temperature; (c) FePc 2D crystal on GRO/Ir(111) in 0.05 mbar CO_2; (d) FePc 2D crystal on GRO/Ir(111) after evacuation, back to UHV. The low wavenumber part of the spectra (left) has been magnified for clarity. The best fit curve of the data, according to the lineshape described in the text, is also shown (cyan line), together with the deconvolution (colored, filled curves) of the FePc internal modes (see text for details). Polarization: ppp.

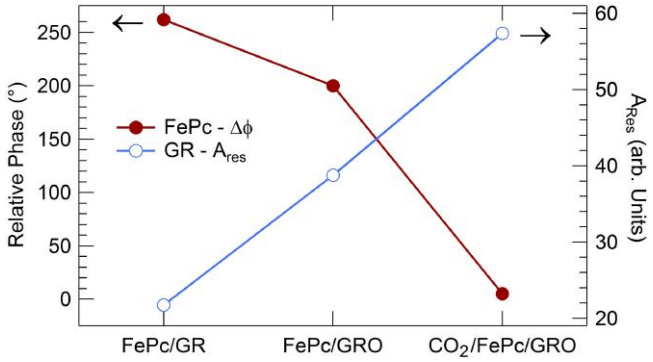

Figure 5.18: Red: evolution of the phase with respect to the non-resonant background of the IR-Vis SFG resonance at 1398 cm^{-1}, associated with the internal FePc modes, showing strong electronic and geometric effects associated with both oxidation and adsorption of CO_2. Cyan: evolution of the resonant signal originating from the graphene G mode at 1608-1615 cm^{-1}, associated with a progressive increase of the corrugation of the sheet.

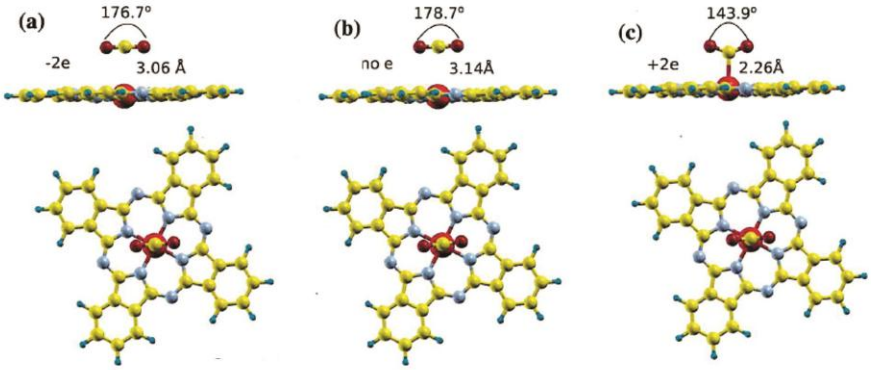

Figure 5.19: DFT results for the (a) positively, (b) zero, and (c) negatively charged FePc concerning its interaction with adsorbed CO_2 molecule. Side and top view of the stick-and-ball model of the linear or "V"-shaped CO_2 molecule adsorbed on FePc.

We found that carbon dioxide chemically binds only in the negatively charged case, in agreement with our experimental results and interpretation, whereas only physisorbed, linear CO_2 configurations are found in the neutral and positively charged cases (Fig. 5.19). By n-doping the stack, CO_2 adsorption is steered to the bent, "V" shaped configuration (O-C-O angle of 144°), in agreement with the general trend of CO_2 adsorption on metal surfaces,[220] and the molecule is stabilized via the carbon atom to the central Fe atom of the phthalocyanine at a distance of 2.26 Å (Fig. 5.20, left panel). The calculated adsorption energy is, however, rather weak (0.28 eV). The additional electronic charge available on the FePc thanks to the n-doping is initially distributed preferentially on the Fe atom, on the macrocycle, and, to a less amount, on the remaining atoms (Fig. 5.20, central panel). Upon formation of the CO_2-Fe bond, a dipole forms across the macrocycle plane and some electronic charge is transferred from the latter to the ligand (Fig. 5.20, right panel). A molecular trans-effect is therefore involved in the process,[116] where charge transfer can be chemically governed by oxidation of the underlying GR.

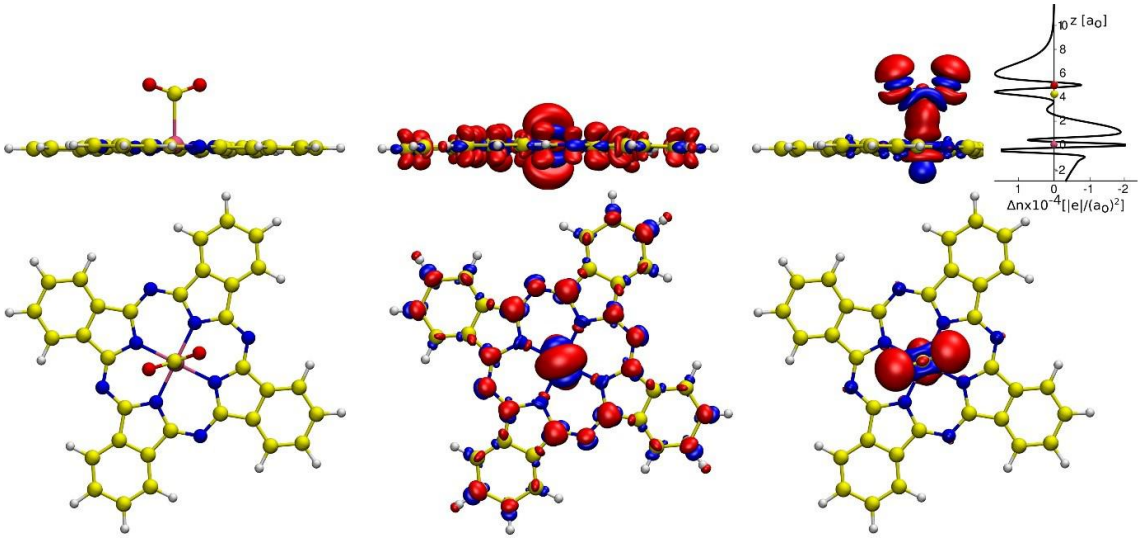

Figure 5.20: DFT results for the negatively charged FePc (+2e) and its interaction with adsorbed CO_2 molecule.
(a) Left panels: Side and top view of the stick-and-ball model of the "V"-shaped CO_2 molecule adsorbed on FePc.
(b) Middle panels: spatial distribution of the additional electronic density in the charge FePc molecule in absence of CO_2. Side and top view of isosurfaces of electron density difference calculated from the charged FePc minus the neutral FePc (isosurfaces at $\pm 0.002|e|/a_0^3$, red/blue for +/-). To avoid spurious effects in the difference, the geometry of the charged FePc is the same of the neutral molecule, although the addition of two electrons induces a small bending.
(c) Right panels: Charge transfer from the FePc to the adsorbed CO_2 molecule. Side and top view of isosurfaces of electron density difference calculated from the charged complex CO_2 on FePc minus the neutral CO_2 and the charged FePc separately considered, in the geometry of the complex (isosurfaces at $\pm 0.002|e|/a_0^3$, red/blue for +/-).
Top right inset: profile of the electron density difference averaged on planes parallel to FePc, with distances referred to the plane of the macrocycle, and the positions of Fe atom (brown) and of C (yellow) and O (red) atoms of the ligand shown for reference.

5.2.4 Conclusions

In conclusion, we have shown that we are able to tune the adsorption of carbon dioxide on a 2D bioinspired artificial system by chemical methods, i.e. by controlling the amount of oxygen present in the system. In this way, a weakly adsorbing system is turned into a system that efficiently binds carbon dioxide, but without being poisoned by it as desorption occurs when UHV is restablished. Oxidation of the graphene substrate leads to a charge transfer to the 2D system, which is responsible for the enhanced adsorption properties. Carbon dioxide chemisorbs in an activated ("V"-shape) configuration, thus lowering the barrier for further reaction.[216,235] The stabilization of the CO_2-Fe chemical bond is observed *in situ* at room temperature and at close to ambient pressure conditions. *Ab initio* simulations confirm the experimental picture, showing that both adsorption and activation result from governing the charge transfer across the graphene-metalorganic layer and exploiting a molecular trans-effect. The findings demonstrate that bioinspired principles can be successfully applied to artificial systems, opening a venue for technological sequestration and recycling of the carbon dioxide.

Chapter 6

Final remarks and future perspectives

This manuscript represents a summary of the research activity performed in the three years of my PhD project. While the details of the specific scientific findings are reported at the "Conclusions" section of each Chapter, here I intend to briefly discuss them and draw a general picture of the "take-home"messages.
Our efforts aimed to contribute to the precise and efficient design of model nano-architected surfaces to be exploited as new ideas for a possible future implementation as novel heterogeneous catalysts. High-level control over critical reactions is of utmost urgency to face the challenges rising in technological society, *e.g.* the increasing demand for an environment-friendly energy stream (production- transport- consumption). In this task, the contribution of surface science investigations is unfathomable, as the comprehension of the role of nanometric structures at a solid-gas interface may spill over to the world of applicative devices.[2]

In the specific, I focused on the atomic-scale characterization of the evolution occurring at nanopatterned model surfaces in a realistic pressure environment.
My goal was to investigate how model nanostructures synthesized in ultra-high vacuum (UHV) conditions (the highest achievable controlled environment) may evolve at close-to-ambient conditions, thus extending a fundamental approach to conditions closer to realistic ones. The task demanded high surface-sensitive techniques to investigate only surface-originated effects *in situ* in a complex (realistic) solid-gaseous interface. This approach could not be based only on classical surface science-methods. The latter provide indeed the desired resolution but are generally not applicable in the millibar pressure range.
At the same time, I tested different model systems and tried to infer about what novel, biomimetic nanosystems may offer with respect to other, already investigated, nanosized structures, as metal nanoparticles or carbon-nanocomposites. Even though innovative, the information obtained through "near ambient pressure techniques" would not have been sufficient for a thorough comprehension of the properties of interest. Therefore, in parallel, a solid, more conventional, characterization of the as-synthesized structures has been pursued exploiting widespread surface physics techniques.

We proved the activity of single metal atom sites embedded in 2D metal-organic frameworks in realistic model reaction conditions. Intriguingly, we have shown that it is possible to tune the properties of these systems through fascinating routes involving the supporting templates, as in the case of graphene and of the ultra-thin alumina oxide film. The support does not only stabilize the nanostructures acting as a template, but also clearly determines their properties, suggesting that it must be considered while inferring about the properties of novel materials. Important examples discussed in the manuscript are the NO interaction

with biomimetic single metal atom Ni centers and the tunable CO_2 adsorption threshold at mono-metallic iron centers on pristine or on oxidized graphene. Such phenomena stem from the delicate interaction between the bidimensional heterostructures and their support. Intriguingly, we present how these systems are in a certain way able to mimic processes that occur in Nature only at dedicate, complex biomolecules. In Nature, the stabilized single metal atoms perform their activity at biological conditions (far away from the UHV regime), thus in liquid environments and involving partial gas pressure in the mbar range.[43–46] Therefore, most of their properties have been characterized and predicted in the framework of state-of-the-art theoretical simulations.[48] Instead, as far as we know, our approach provided new experimental evidence of the potentialities of synthetic, biomimetic Single Metal Atom model Catalysts at realistic (and therefore appealing for potential technological applications) pressure/temperature ranges.

In addition, in this thesis I intended to highlight the role of pressure. It is indeed true that investigations performed in vacuum conditions are a valuable but limited tool from this point of view. We demonstrate that the good thermal, structural, and chemical stability characterizing graphene-supported Pt nanoparticles in vacuum is no longer valid in 0.1 mbar CO. Moreover, we provide direct evidence that, as only hypothesized before,[84–89] the mobility of the clusters is enhanced in non-negligible CO background pressure through the population of less-favorable adsorption sites. Specific active sites in fact may not be accessible in UHV conditions, while their importance is unquestioned at higher pressures ranges.[52,53] In these investigations, Infrared-Visible Sum Frequency Generation spectroscopy (IR-Vis SFG) emerges as a powerful tool allowing *in situ* studies even at conditions unaffordable for common surface science techniques.[54–56] The technique provides unique information concerning both vibrational and electronic properties of the interface and has been employed in my PhD research in a pressure range spanning from UHV to ambient pressures. It is indeed by means of this technique that we demonstrated, as mentioned above, how the role of biomimetic, single metal atom systems can be investigated at pseudo-biological conditions (*i.e.* room temperature and near ambient pressure). In the literature, the interaction of similar structures with simple diatomic ligands has been indeed observed, but preferentially only at UHV-compatible pressures and at cryogenic temperature.[107,114] In this manuscript instead, we show as carbon oxides (CO, CO_2) adsorption at heme-like centers starts at 300 K only above millibar pressure of reactants. Moreover, also thanks to the electronic information offered by IR-Vis SFG, both modifications of the substrate properties (as in the case of graphene oxidation) and unexpected properties of the single metal center in interaction with the ligand (as is the case of the observed Vis-induced excitonic population in 10 mbar of CO) could be unveiled.

Unfortunately, the thorough characterization of the synthesized structures and the meticulous investigation of the adsorption properties at the stable single metal centers required an extended period of study, and the characterization of a complete, complex chemical conversion could not be included in my PhD activity. However, the achieved, novel results suffice as a basis for new investigations, focusing on the role that these stable, self-assembling, and tunable biomimetic structures may play as heterogeneous catalysts. The role of temperature has yet to be taken into account, for example by thoroughly investigating the stability of the synthesized structures at "harsher" pressure/temperature conditions. The difficulties of *in situ* characterizations at these regimes demand a careful choice of complementary techniques (*e.g.* NEXAFS, in order to follow modifications of the molecular adsorption geometry or modification of the single metal centers) accompanied by a thoughtful experimental planning able to highlight the role of each parameter in such complex environments.

It is reasonable that a new project could start for example in order to investigate the evolution of NO/CO mixtures at single nickel centers. In fact, understanding the potentialities

of single metal centers with respect to the chemistry of these toxic molecules at realistic pressure conditions may lead to unexpected advances in their efficient conversion to less dangerous species.[117,118] On the other side, the FePc arrays could be further tested with respect to their CO_2 adsorption and conversion properties.[120,121] Ideally, a first important investigation may tackle the CO_2 reduction reaction at the iron centers exposed to CO_2/H_2 mixtures.

However, it has to be stressed that the approach followed during this thesis work may not be sufficient: surface-specific experiments may not give the full information about the reaction products. These species in fact, although efficiently catalyzed at the surface, may be characterized by a very short residence time at the surface, insufficient to be correctly detected. Therefore, complementary investigations sensible to the gas phase composition, as gas chromatography or mass spectrometry, could be the source of new and reliable information.

Appendix

6.1 Surface control at UHV conditions.

If we use the kinetic theory of gases, we can estimate the rate r of imping atoms on a surface per unit of time per unit area:

$$r = \frac{p}{\sqrt{2\pi k_B T m}} \tag{6.1}$$

where p is the pressure, m is the particle's mass, $k_B = 1.381 \times 10^{-23}\,\mathrm{JK}^{-1}$ is Boltzmann's constant and T is the temperature. Expressing p in mbar, T in K and substituting m by the molecular weight M multiplied by the atomic mass unit ($u = 1.661 \times 10^{-27}\,\mathrm{kg}$), we obtain r expressed in molecules $\mathrm{cm}^{-2}\ \mathrm{s}^{-1}$:

$$r = 2.63 \times 10^{22} \frac{p}{\sqrt{MT}} \tag{6.2}$$

Let us make the assumption that on an ideal surface every impinging atom will stick and that a well ordered surface presents $\sim 10^{15}$ atoms cm^{-2}. If we consider a pressure $p = 1 \times 10^{-6}\,\mathrm{mbar}$ of CO molecules (M=28) and insert the values in Eq.[6.2] we obtain an estimate of the rate of surface coverage per unit time per unit area. Dividing this by the estimated surface density allows to get the rate in terms of monolayers.
The result shows that at $p = 1 \times 10^{-6}\,\mathrm{mbar}$ every second a monolayer of contaminants is adsorbed. Enhancing the vacuum of 4 orders of magnitude, reaching, indeed, UHV conditions, allows to keep the surface clean for a reasonable time during which an experiment can be performed.

6.2 Adsorption and desorption at equilibrium

The equilibrium between the adsorption and the desorption process determines the net average population of adsorbates at a surface. In the following we propose a simple but rigorous model, where important parameters will be temperature, pressure, the energy of adsortpion and desorption (respectively Ea and Ed, see Fig. 6.1), and the heat of adsorption (Ha).

If we impose equilibrium between adsorption and desorption processes (that is the respective rates are equal) we obtain the following equation:

$$r \quad f(\theta, S_0) \quad e^{\frac{-E_a}{k_B T}} = \nu \quad g(\theta) \quad e^{\frac{-E_d}{k_B T}} \tag{6.3}$$

The adsorption rate (on the left side of Eq.[6.3]) depends upon the rate of impinging molecules per unit time ad area (see Appendix 6.1, Eq.[6.1]), upon a function f of the coverage (θ) and of the sticking coefficient (S_0), and exponentially upon the activation energy for adsorption,

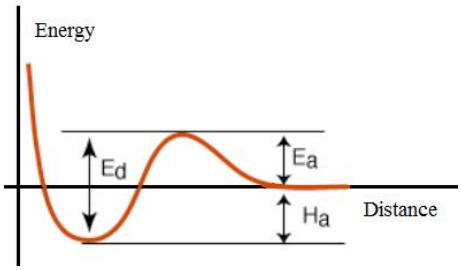

Figure 6.1: Pictorial representation of a generic potential energy profile of molecule as a function of the distance from a surface. E_a and E_d are the adsorption and desorption energies, respectively. H_a is the heat of adsorption, a measure of the stability of the bond of the adsorbed molecule.

that is the energy barrier that the molecule has to overcome in order to adsorb (see E_a in Fig. 6.1).
The desorption rate instead depends upon the coverage (through a function g), exponentially upon the energy of desorption (the energy barrier the molecule has to overcome in order to desorb, see E_d in Fig. 6.1), and upon a factor ν that can be interpreted as the "attempt frequency" to overcome the energy barrier of desorption (for simple molecular adsorption, it is the frequency of vibration of the bond between the molecule and the substrate and it is related to the second derivative of the potential energy profile).

Let us make some hypotheses in order to explicit the dependences on the surface relative coverage θ/θ_{sat}, where θ_{sat} is the coverage at saturation. If we suppose that the adsorption process can be described with the Langmuir's model (briefly: the impinging molecules attach with constant probability S_0 on a non-occupied adsorption site, whose population on the surface depends upon the coverage as $(1-\theta/\theta_{sat})$) and that the desorption/adsorption is a first order process (it involves only one molecule, therefore depends linearly on the coverage), we can substitute

$$f(\theta, S_0) = S_0\ (1 - \frac{\theta}{\theta_{sat}}) \tag{6.4}$$

$$g(\theta) = \frac{\theta}{\theta_{sat}} \tag{6.5}$$

into Eq.[6.3] and ,considering Eq.[6.1] obtain

$$\frac{p}{\sqrt{2\pi m k_B T}}\ S_0\ (1 - \frac{\theta}{\theta_{sat}})\ \ e^{\frac{-E_a}{k_B T}} = \nu \frac{\theta}{\theta_{sat}}\ e^{\frac{-E_d}{k_B T}} \tag{6.6}$$

Further manipulation allows to explicit the relative coverage as a function of p, T, and $E_{des} - E_{ads} = H_a$, namely

$$\frac{\theta}{\theta_{sat}} = \frac{pB_{(T,H_a)}}{1 + pB_{(T,H_a)}}, \qquad B_{(T,H_a)} = \frac{1}{\sqrt{2\pi k_B m T}} \frac{S_0}{\nu}\ e^{\frac{-H_a}{k_B T}} \tag{6.7}$$

A further approximation that can be done consists in assuming perfect sticking to the surface (S_0=1). Moreover, for a first order process, a reasonable choice for the pre-exponential factor could be $\nu \sim 10^{13} Hz$, and in the case of no activated adsorption, the adsorption energy E_a is zero. Therefore, we obtain, in the case of a first order process (assuming zero adsorption energy and that the Langmuir's hypotheses are valid), the following equation:

$$\frac{\theta}{\theta_{sat}} = \frac{pB_{(T,E_d)}}{1 + pB_{(T,E_d)}}, \qquad B_{(T,E_d)} = \frac{10^{-13}}{\sqrt{2\pi k_B m T}}\, e^{\frac{-E_d}{k_B T}} \tag{6.8}$$

which describes, at constant T, the relative surface coverage of atomic/molecular species as a function of the pressure.

6.3 Cooperative binding and the Hill model

Introduced by A. V. Hill as an empirical solution to describe the adsorption curve of oxygen in hemoglobin,[236] the Hill model has been widely used in biochemistry and physiology to infer about ligand-receptor interaction and about the number of ligand molecules that ideally saturate the binding sites of the receptor molecule.[157,237] A receptor molecule is said to exhibit cooperative binding if its binding to ligand scales non linearly with ligand concentration. Cooperativity is defined to be positive if the binding of a ligand molecule increases the receptor's apparent affinity, and hence increases the chance of another ligand molecule binding.[237]

Following Weiss,[157] let us suppose a binding reaction scheme were n ligand molecules (nL) bind to a receptor (R):

$$\mathrm{R} + \mathrm{nL} \rightleftharpoons \mathrm{RL}_n \tag{6.9}$$

If we consider the ratio of the bound to total (unbound and bound) receptors at the equilibrium, we can express the Hill equation as

$$\frac{\text{Bound}}{\text{Total}} = Y = \frac{[L]^n/K_d}{1 + [L]^n/K_d} \tag{6.10}$$

or

$$Y = \frac{[L]^n}{K + [L]^n} \tag{6.11}$$

where $K = 1/K_d$ and K_d is the dissociation constant related to reaction R.[6.9].
It has to be noted however that reaction R.[6.9] is unrealistic for $n > 1$, as it would imply the interaction of three molecules at the same time. In a more realistic model, within the hypotheses of a single interaction center on the receptor, the interaction can be approximated as a sequential process, i.e.

$$\mathrm{R} + 2\,\mathrm{L} \rightleftharpoons \mathrm{RL} + \mathrm{L} \rightleftharpoons \mathrm{RL}_2 \tag{6.12}$$

where we supposed $n = 2$. Intriguingly, this approximation holds as long as the lifetime of the RL state is negligible, that is if $K_{d_1} >> K_{d_2}$.

If this condition holds the Hill coefficient n can readily be estimated by means of Eq.[6.11], if the fractional occupancy of the interaction sites as a function of the concentration of the ligand is known. It has to be noticed however that the Hill coefficient, according to Weiss,[157] has to be considered as an "interaction coefficient" which reflects cooperativity more than a real estimate of the number of binding sites.

6.4 Second order polarizability: the Sum Frequency term.

Let us consider the full expression for the polarizability vector under the electric dipole approximation (no contributions from multipoles, magnetic terms, and interaction with other dipoles induced by the impinging radiation):

$$\begin{aligned}\boldsymbol{P}(t) &= \epsilon_0 \left[\chi^{(1)}\boldsymbol{E}(t) + \chi^{(2)}\boldsymbol{E}^2(t) + \chi^{(3)}\boldsymbol{E}^3(t) + \dots\right] \\ &= \boldsymbol{P}^{(1)}(t) + \boldsymbol{P}^{(2)}(t) + \boldsymbol{P}^{(3)}(t) + \dots\end{aligned} \tag{6.13}$$

Here we assume that we can represent the (real) electric field vector of the optical wave as the discrete sum of two frequency components:

$$\boldsymbol{E}(\boldsymbol{r},t) = \boldsymbol{E}(\omega_1)e^{-i(\omega_1 t+\phi_1)} + \boldsymbol{E}(\omega_2)e^{-i(\omega_2 t+\phi_2)} + c.c. \tag{6.14}$$

where the field amplitudes $\boldsymbol{E}(\omega_n)$ ($n = 1, 2$) are defined as follows:

$$\boldsymbol{E}(\omega_n) = \frac{1}{2}\boldsymbol{E}_n e^{i\boldsymbol{k}_n\cdot\boldsymbol{r}}, \qquad \boldsymbol{k}_n = \frac{\omega_n}{u}\hat{k}_n \tag{6.15}$$

u is the speed of light in the medium and the dependence of $\boldsymbol{E}(\omega_n)$ on $\boldsymbol{r}$ is understood. Note that according to the definition in Eq.[6.14], $\boldsymbol{E}(-\omega_n) = \boldsymbol{E}^\star(\omega_n)$. In our specific case ω_1 and ω_2 will be frequencies in the visible and mid-IR spectral range, respectively. We can write the total field in the more compact form

$$\boldsymbol{E}(\boldsymbol{r},t) = \sum_n \boldsymbol{E}(\omega_n)e^{-i(\omega_n t+\psi_n)}, \qquad n = -2,-1,+1,+2 \tag{6.16}$$

In Eq.[6.16] $\omega_{-n}(\psi_{-n})$ is a notation for $-\omega_n(-\psi_n)$. Thus the n-summation extends over all frequency components, both positive and negative, so that the complex conjugation *c.c.* term present in Eq.[6.14] is automatically included. Now we define the components of the second-order susceptibility tensor $\chi^{(2)}_{ijk}(\omega_n+\omega_m,\omega_n,\omega_m)$ as the constants of proportionality relating the amplitude of the second order nonlinear polarization to the product of the electric field amplitudes according to

$$P_i^{(2)}(\boldsymbol{r},t) = \epsilon_0 \sum_{jk}\sum_{nm} \chi^{(2)}_{ijk}(\omega_n+\omega_m,\omega_n,\omega_m)E_j(\omega_n)E_k(\omega_m)e^{-i[(\omega_n+\omega_m)t-(\phi_n+\phi_m)]} \tag{6.17}$$

Here the indices (i,j,k) refer to the cartesian components of the fields and, as above, n,m=-2,-1,+1,+2. Following convention, we have written $\chi^{(2)}$ as a function of three frequency arguments. This is technically unnecessary since the first argument is always the sum of the other two. By developing the nm summation in Eq.[6.17] it becomes evident that $\boldsymbol{P}^{(2)}(\boldsymbol{r};t)$ has components which oscillate at frequencies different from those of the incident fields: there are components oscillating at frequencies $2\omega_1$ and $2\omega_2$ (second harmonic generation, SHG), at frequency $\omega_1-\omega_2$ (difference frequency generation, DFG), at frequency $\omega_1+\omega_2=\omega_3$ (sum frequency generation, SFG). Moreover, there is a component not oscillating at all (optical rectification, OR).

Explicitly, the SFG component can be found to be:

$$\begin{aligned}P_i^{SFG}(\boldsymbol{r},t) = \epsilon_0 \sum_{jk}[&\chi^{(2)}_{ijk}(\omega_3,\omega_1,\omega_2)E_j(\omega_1)E_k(\omega_2)+ \\ &+\chi^{(2)}_{ijk}(\omega_3,\omega_2,\omega_1)E_j(\omega_2)E_k(\omega_1)]\;\; e^{-i(\omega_3 t-\phi_3)} + c.c\end{aligned} \tag{6.18}$$

In writing Eq.[6.18] we used the fact that $\chi^{(2)}_{ijk}(-\omega_3, -\omega_1, -\omega_2) = \chi^{(2)}_{ijk}(\omega_3, \omega_1, \omega_2)^\star$, as can be seen taking the complex conjugate of Eq.[6.17]. We now note that j and k are dummy indices and thus can be interchanged in the second term of Eq.[6.18]. We next assume that the nonlinear susceptibility possesses intrinsic permutation symmetry (see[238] for further details):

$$\chi^{(2)}_{ijk}(\omega_3, \omega_1, \omega_2) = \chi^{(2)}_{ijk}(\omega_3, \omega_2, \omega_1) \tag{6.19}$$

Through use of this relation, the expression for the SFG component of the nonlinear polarization becomes

$$\begin{aligned} P_i^{SFG}(\boldsymbol{r}, t) &= 2\epsilon_0 \sum_{jk} \chi^{(2)}_{ijk}(\omega_3, \omega_1, \omega_2) E_j(\omega_1) E_k(\omega_2) e^{-i(\omega_3 t - \phi_3)} + c.c \\ &= \frac{1}{2}\epsilon_0 \sum_{jk} \chi^{(2)}_{ijk}(\omega_3, \omega_1, \omega_2) \quad E_{1,j} \quad E_{2,k} \quad e^{i(\boldsymbol{k}_3 \cdot \boldsymbol{r} - \omega_3 t + \phi_3)} + c.c \end{aligned} \tag{6.20}$$

where we used Eq.[6.15]. From now on we'll neglect the phases and neglect to explicitly include the spatial and time dependence of the polarization field:

$$P_i^{SFG}(\boldsymbol{r}, t) = \frac{1}{2}\epsilon_0 \sum_{jk} \chi^{(2)}_{ijk} E_{1,j} E_{2,k} + c.c. \tag{6.21}$$

Eq.[6.21] represent the component of the second order polarization $\boldsymbol{P}^{(2)}(t)$ that modulates at the frequency $\omega_{SFG} = \omega_3 = \omega_1 + \omega_2$ and generates the Sum Frequency Field $\boldsymbol{E}^{SFG}(t)$.

6.5 The EKSPLA Laser

Laser source

The laser source is comprised of three functional parts: the master oscillator, the regenerative amplifier and the power amplifier (see Fig. 6.2). The master oscillator is a diode-pumped passively mode-locked laser employing Nd:YVO_4 (neodymium-doped yttrium orthovanadate) material. Mode-locking is achieved by means of a saturable absorber. The master oscillator has two output beams: one enters a photo-detector PHD1, which transforms this light to an electrical signal and delivers it to the synchronization board. The latter produces pulse sequences for laser modules. The second output beam is employed for seeding the regenerative amplifier. The regenerative amplifier is based on a diode pumped Nd:YAG rod (neodymium doped yttrium aluminium garnet, Nd:$Y_3Al_2(AlO_4)_3$). When the oscillator pulse is injected, the voltage on a Pockels cell is switched on, rapidly trapping the beam inside the cavity. After a pre-determined number of round trips, when the pulse is amplified to a maximum level, the voltage on the cell is switched off and the amplified pulse is dumped out of the regenerative amplifier cavity. The Faraday rotator FR1, half wave plate HWP1, and polarizer P1 prevent the regenerative amplifier output beam from entering back the master oscillator, and direct it instead to the power amplifier. Mirrors M5, M6, and M7 direct the picosecond pulse from the regenerative amplifier to the amplification stage based on diode pumped Nd:YAG rod R3. To adjust the laser output energy without affecting the other radiation parameters, pulse amplification is controlled by varying the delay between the amplifier and the regenerative amplifier flash lamps. When the amplification is off, the laser output is minimal ($\sim$ 2.0 mJ). Using the control pad the amplification level may be adjusted from 1 to 99 (arb. units).

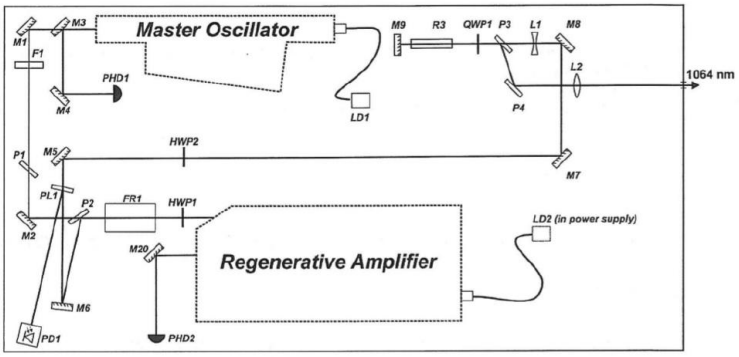

Figure 6.2: Layout of the laser source. Image from EKSPLA Manual.[239]

Harmonics unit (HU)

The fundamental IR radiation from the Nd:YAG enters the HU and polarizer P1 splits it into two beams (see Fig. 6.3). The first IR beam passes through the second harmonic generation crystal number 2 (SHG2), where the Vis beam is generated and directed to the SFG box. It is possible to attenuate the Vis beam power through HWP7 and Glan prism (GP). The second IR beam is again splitted in two by P2: one is the IR output and the other is sent towards SHG1 to generate the Vis output. Both of them are needed in the PG/DFG to generate the tunable mid-IR, and their ratio can be optimized through HWP2. HWP4 and HWP5 optimize the polarization of the pump radiation for the SHG crystals, while HWP3 optimizes the fundamental radiation energy for pumping the PG/DFG. The second

harmonic generation is realized in KD_2PO_4 (deuterated potassium dihydrogen phosphate) crystals. To maximize the conversion efficiency, the path of the input beam through the crystal must lay along a unique axis of fixed orientation relative to the crystalline axis (phase matching). The phase matching angle is also dependent on the crystal temperature. To keep the temperature (and consequently this angle) constant, all harmonics crystals are mounted in temperature-stabilized ovens, also to avoid water contamination. The prism PR1 and mirrors M11 and M12 form a remote-controlled delay line in order to ensure the temporal overlap of the Vis pulse and the mid-IR pulse on the sample.

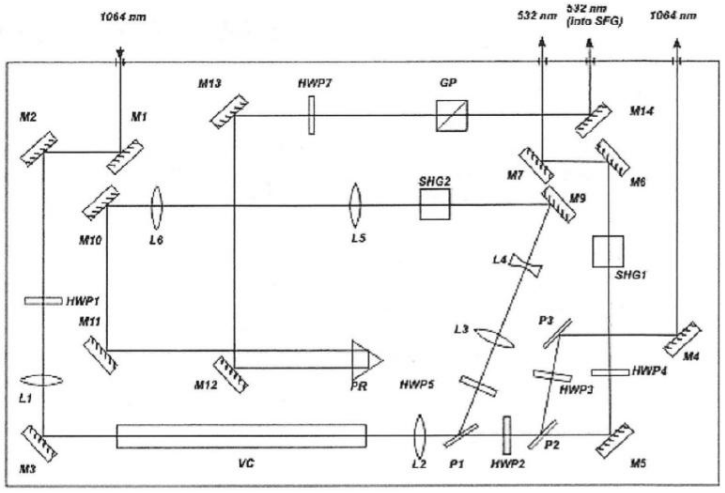

Figure 6.3: Layout of the HU. Image from EKSPLA Manual.[239]

Optical Parametric generator and difference frequency generator

The PG/DFG is comprised of two parts, namely the parametric generator and the difference frequency generator (see Fig. 6.4). Through parametric generation two light pulses (known as signal and idler) can be obtained from one single pulse. Energy conservation implies that the sum of the frequencies of the two generated pulses be equal to the frequency of the pumping pulse. Parametric generation is attained in nonlinear crystals and, as for SHG, by rotating the crystal the phase matching condition changes: in this way the signal (and consequently the idler) frequencies can be tuned.

In this particular setup, the pumping pulse is Vis at 532 nm and parametric generation is attained in BBO crystals ($\beta-$phase of barium borate, BaB_2O_4) (some technical details can be found in[239]). The obtained signal and idler beams are in the spectral range 680$\div$1064 nm and 1064$\div$2300 nm, respectively. The signal emerges through the output aperture S3 (and we don't use it), while the idler (1064$\div$2300 nm) can further be led in two ways: either to the DFG or to the output S5. We choose the former solution: in the DFG the idler mixes with the IR input at 1064 nm in a AGS (silver thiogallate, $AgGaS_2$) crystal and radiation in the 2300$\div$10000 nm spectral range is obtained 4. This corresponds to a spectroscopic wavenumber range $\nu = 1000\div4500$ cm^{-1}. The latter is finally the tunable mid-IR radiation needed for the SFG experiment.

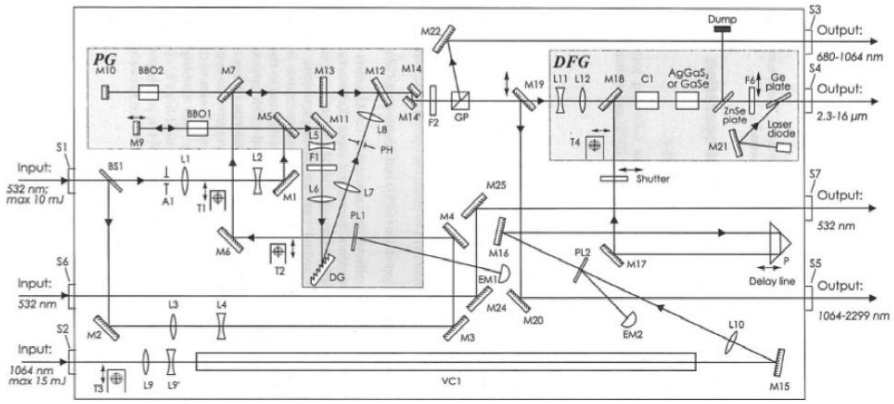

Figure 6.4: Layout of the PG/DFG. Image from EKSPLA Manual.[239]

SFG box and monochromator

The SFG box is where the SFG experiment takes place. Mirrors in the back side of the box (hidden in Fig. 6.5) direct the mid-IR beam inside and provide the desired polarization. Mirrors M7 and M8 direct the mid-IR on the sample. Beam splitter BS2 reflects a part of the mid-IR radiation to pyroelectric detector PD2 for continuous monitoring of the IR signal intensity. Lens L2 focuses IR radiation on the sample surface. The visible beam for the SFG is the second harmonic radiation of the HU. Laser diode LD overlaps SFG signal to help in obtaining proper sample alignment. Iris diaphragms ID3 and ID4 are used for beam guiding and elimination of unwanted laser radiation due to reflections. For the continuous monitoring of the Vis beam signal intensity, splitter BS1 directs part of the Vis beam to PD1. The SFG signal is directed to the signal monochromator by mirrors M10-M12. The optical signal detector features a photomultiplier tube (PMT) as main component.

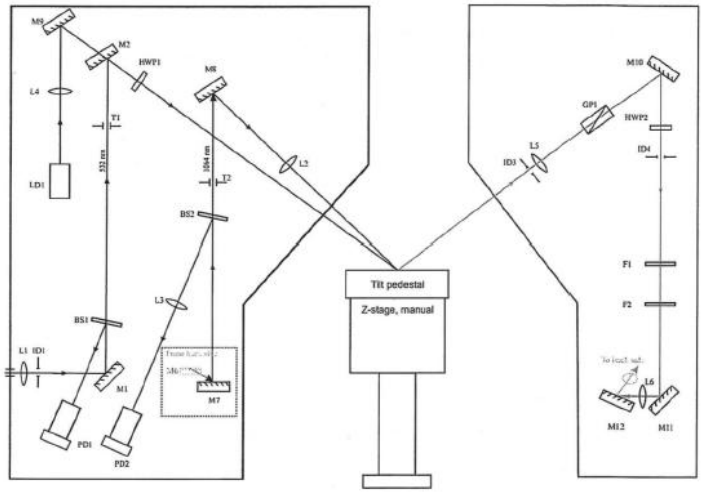

Figure 6.5: Front view of the SFG system layout. Image from EKSPLA Manual.[239]

6.6 NiTPP on Cu(100): the TPP internal modes.

This work		Phenyl Modes		Macrocycle Modes	
ω (cm^{-1})	*Δφ (°)*	*ω (cm^{-1})*	*Assignment*	*ω (cm^{-1})*	*Assignment*
1232 (*)	265	1235	ν(CC), δ(CCH)	1230, 1235	ν(C_m-Ph), δ(C_mPh), ν(NC_α), ν($C_\alpha C_\beta$), δ($C_\alpha C_\beta C_\beta$), δ($C_\alpha C_m$)
1246 (*)	23			1246, 1254	ν(NC_α), ν(C_m-Ph)
1276	288	1269	δ(CH)	1269	ν(C_m-Ph), ν(NC_α)
1291 (*)	297	1283, 1285, 1289	Out-of-plane B_{1u}, A_{2u}, E_g		
1304	350			1302	ν(pyr half-ring), ν(NC_α), ν($C_\alpha C_\beta$)
1315	224	1317, 1318	Out-of-plane B_{1u}, A_{2u}	1313	ν(pyr quarter-ring)
1356 (*)	49			1341, 1351	ν(pyr quarter-ring)$_{sym}$, ν($C_\alpha C_\beta$), δ(C_βH)
1374 (*)	328			1374, 1377	ν(pyr quarter-ring), ν(pyr half-ring)$_{sym}$, ν($C_\alpha C_\beta$), δ(C_βH), δ($C_\alpha C_\beta$), ν(NC_α), δ($C_\alpha C_m$), δ($C_\alpha NC_\alpha$)
1434	246	1438	Out-of-plane B_{1u}		
1436	97	1440	Out-of-plane A_{2u}		
1482	215	1470	δ(CCH), ν(CC)	1470, 1473, 1485	ν($C_\alpha C_m$)$_{sym}$, ν($C_\beta C_\beta$), ν(NC_α), ν($C_\alpha C_\beta$)
1573	105	1576, 1583, 1586	ν(CC), out-of-plane E_g, B_{1u}, A_{2u}	1572	ν($C_\beta C_\beta$), ν($C_\alpha C_m$), δ($C_\alpha C_m$)
1593	238	1586	out-of-plane A_{2u}	1586, 1594	ν($C_\alpha C_m$)$_{sym}$, ν($C_\alpha C_m$)$_{asym}$, δ($C_\alpha C_m$Ph)
2856	280				
2907	295				
3007	87	3039, 3047, 3063, 3068, 3069, 3071, 3073, 3075	ν(CH), out-of-plane E_g, B_{1u}, A_{2u}		
3046	97				
3069	131				
3086	155				

Table 6.1: Assignment of the observed vibronic modes to local coordinates and skeletal modes for the clean NiTPP molecules through comparison with previous literature data.[147–149] Modes associated with the multilayer are marked with an (*).

6.7 PM-IRAS and TR-2PPE setups.

PM-IRAS: Polarization-modulation infrared adsorption spectroscopy.

I performed the PM-IRAS experiments at the Institute for Materials Chemistry of the Technical University of Vienna in a custom-built UHV experimental chamber, previously described and successfully applied in various investigations. In brief, the chamber comprises two parts, a classical UHV chamber and an UHV-compatible high-pressure cell.[240] The upper UHV section allows sample preparation and characterization by standard tools of surface science such as ion bombardment and annealing, X-ray photoelectron spectroscopy (XPS), low energy electron diffraction (LEED) and temperature programmed desorption (TPD). The sample can be transferred under UHV to the lower section, a gold-coated spectroscopic high-pressure cell in which polarization-modulation IRAS (PM-IRAS) experiments can be performed in a pressure range from UHV to 103 mbar. PM-IRAS (Bruker IFS 66v/S FTIR spectrometer, liquid N_2-cooled HgCdTe detector, HINDS PEM-90 ZnSe photoelastic modulator) was exploited to investigate the vibrational properties of the species adsorbed on the sample. The basic principle of PM-IRAS is that the local electric field induced by s-polarized light, when impinging at near-grazing incidence on a metal surface, is vanishing.[241] Hence, no absorption of s-polarized light will occur by molecules adsorbed on the surface. On the other hand, p-polarized light will be absorbed by molecules both in the gas phase and adsorbed onother hand, p-polarized light will be absorbed by molecules both in the gas phase and adsorbed on the surface. Consequently, the demodulation of the signal obtained from s- and p-polarized light provides inherently surface specific information.

TR-2PPE: Time-resolved two-photon photoemission.

2PPE measurements were carried out in the SUNDYN-ANCHOR end-station of the ALOISA beamline at the Elettra synchrotron radiation facility. Pump and probe pulses were the second and fourth harmonic of the output of a Yb:YAG fiber laser (Amplitude Systèmes, Tangerine HP). The sample was excited by second harmonic pulses ($h\nu$ = 2.4 eV, 515 nm) and probed by fourth harmonic pulses ($h\nu$ = 4.8 eV, 257.5 nm) of the laser. The time delay between pump and probe pulses was varied via a motorized delay line. The repetition rate of the laser was 577 kHz, and the pulse width was 350 fs in the fundamental harmonic. We employed pump energies of about 0.1 μJ/pulse. The spot diameters for the pump and the probe beams were 350 μm and 250 μm, respectively. The emitted electrons were detected at normal emission through a hemispherical electron energy analyzer (PSP Vacuum, Resolve 120) equipped with a delay-line detection system. A bias of -1.2 V was applied to the sample and the spectra were acquired with a pass energy of 2 eV. TR-2PPE spectra have been acquired with p-polarized pump, while s-polarized probe was used to minimize the contribution of photoelectrons exclusively emitted by the probe photons, which are not pump-dependent. The energy scale of the 2PPE spectra has been aligned to the Fermi level by measuring the onset of the secondary electron cut-off with a low laser fluence and subsequently determining the work function of the sample with a conventional He discharge lamp.

6.8 *Ab initio* calculations supporting the spin-exciton scenario.

An extensive theoretical investigation was performed in the framework of a collaboration with the International Center of Theoretical Physics (ICTP) and the theoretical group of the condensed matter physics section of the Physics Department of the University of Trieste. The purpose was to to highlight and discuss possible effects involved in the generation of the vibronic multiplet observed in the IR-Vis SFG spectra. Here in the following I report a list of the obtained results, which led to the conclusions addressed in section 4.3.

Cooperative adsorption hypothesis.

The first hypothesis that we investigated consisted in assuming that the anomalous multiplicity was due to the cooperative adsorption of multiple CO molecules on a single FePc. The chemisorption of a first CO molecule would thus rearrange the structure of the system in such a way that further CO adsorption would become energetically favorable. This is the cooperative adsorption hypothesis.

The initial simulation system is composed of an isolated FePc molecule only. This is justified as, experimentally, the FePc molecules are decoupled from the Ir(111) surface by the graphene sheet and, since we have a $\pi - \pi$ bonding, the graphene layer is not expected to affect drastically the properties of the phthalocyanine.[125,170] The simulations show that the total magnetization is equal to $2.04\mu_B$, thus the system is in a triplet state. Moreover, the central iron atom has formally a +2 charge.
To probe the multiple carbonylation hypothesis, up to three CO molecules have been coadsorbed on FePc. The carbonylation of the FePc quenches the spin of the system, thus the magnetization becomes equal to $0.00\mu_B$, i.e. the system is in a singlet state. Calculations show that the only stable adsorption geometry is that reported in Fig. 4.15, while multiple adsorption is energetically unfavorable. The calculated adsorption energy for the single CO, $-0.34eV$, is in good agreement with the experimental value of $-0.3 \pm 0.1eV$. For di- and tri-carbonylation, the adsorption energy is $+0.23eV/CO$ and $+0.22eV/CO$ respectively, thus ruling out cooperative mechanisms.

***Ab initio* thermodinamics**

When describing finite, constant pressure and temperature conditions, the relevant quantity is the total Gibbs free energy G^*, rather than the adsorption energy.[242] The former is obtained from DFT total energies. For the adsorption of a single CO molecule at each metal center, the relevant quantity is the difference:

$$G^*(T,p) = G(T,p) - \mu_{FePc}(T,p) - \mu_{CO}(T,p) \tag{6.22}$$

where G is the Gibbs free energy of the adsorbed system, and μ_{FePc} and μ_{CO} are the chemical potentials of the FePc and CO molecules, respectively. The DFT total energies are evaluated within a given volume V of the unit cell and therefore the Gibbs free energy can be expressed in terms of the Helmholtz free energy plus the volume contributions, i.e.:

$$G(T,p) = F(T,V) + pV \tag{6.23}$$

The term pV can be neglected since p is of the order of 10 mbar in the present case, and V is smaller than $10^4 \mathring{A}^3$, yielding pV$< 6 \times 10^-5$ eV, much lower than the energy differences characterizing nonequivalent configurations (0.1 eV). The Helmholtz free energy can be further detailed as:

$$F(T,V) = E + F_{vibr}(T,V) \tag{6.24}$$

with

$$F_{vibr}(T,V) = E_{vibr}(T,V) - T \cdot S_{vibr}(T,V) \tag{6.25}$$

that includes energy and entropy contributions from the vibrational modes of the system. However, since vibrational energies F_{vibr} are generally small with respect to adsorption energies, they can be neglected as a first approximation.
Using all the assumptions above we obtain that

$$G^*(T,p) \cong E - \mu_{FePc} - \mu_{CO}(T,p) \tag{6.26}$$

The chemical potential for CO can be adequately parametrized with the expression valid for ideal gases where

$$\mu_{CO}(T,p) = E_{CO} + \mu_{CO}(T,p_{atm}) + k_B T \cdot ln(\frac{p}{p_{atm}}) \tag{6.27}$$

From thermochemical tables $\mu_{CO}(300K, p_{atm})$ = -0.53 eV. Collecting all the terms and setting the zero of the free energy scale for the clean FePc molecule (no CO adsorbed), the free energy difference that contributes in the CO adsorption process is

$$\Delta G(T,p) \cong E_{ads} - \mu_{CO}(T,p_{atm}) - k_B T \cdot ln(\frac{p}{p_{atm}}) \tag{6.28}$$

In the isothermal-isobaric ensemble, the probability of CO adsorption on a FePc molecule is

$$P = \frac{e^{-\beta \Delta G(T,p)}}{1 + e^{-\beta \Delta G^*(T,p)}} \tag{6.29}$$

with $\beta = 1/(k_B T)$. Consequently, the coverage of CO at the Fe sites of the FePc monolayer is

$$\frac{\theta}{\theta_{sat}} = \frac{r(T,p) e^{-\beta \Delta G^*(T,p)}}{1 + r(T,p) e^{-\beta \Delta G^*(T,p)}} \tag{6.30}$$

where r(T,p) is the ratio between the number of available molecules in the gas phase N_{gas}(p) and the number of available adsorption sites N_{sites}:

$$r(T,p) = \frac{N_{gas}(T,p)}{N_{sites}} = \frac{p \cdot V_{chamber}}{k_B T} \cdot \frac{A_{unitcell}}{A_{sample}} \tag{6.31}$$

In our setup the volume of the high pressure cell is $V_{chamber} \sim 10^{-3}\ m^3$, the surface area of the unit cell of the FePc monolayer is $A_{unitcell} \sim 200$ Å^2 and the sample surface is $A_{sample} \sim 50$ mm^2. The full *ab initio* thermodynamic expression for the surface coverage is finally

$$\begin{aligned} \frac{\theta}{\theta_{sat}} &= \frac{p \cdot B(T,p)}{1 + p \cdot B(T,p)} \\ B(T,p) &= r(T,p) \cdot \frac{e^{\beta[\mu_{CO}(T,p_{atm}) - E_{ads}]}}{p_{atm}} \end{aligned} \tag{6.32}$$

which is formally equivalent to the well-known Langmuir formula for isothermal adsorption. The curve plotted in Fig. 4.15 together with the experimental data points is directly obtained from this *ab initio* model, with no fitted parameters. This plot shows that the experimental data are well reproduced by the adsorption of only one CO molecule per iron phthalocyanine. Multiple carbonylation of FePc remains thermodynamically unfavorable, even when taking into account the effect of temperature and pressure. Further calculations of the adsorption energy as a function of the distance of the carbon atom of CO from the equilibrium adsorption length show no barrier for the single adsorption process, which is therefore not activated. The conclusions again confirm the exclusion of the cooperative adsorption hypothesis.

The dipole-dipole interaction hypothesis.

We have shown that the relative intensities of the multiple peaks observed in the SFG spectra depend on the degree of order of the FePc monolayer (see main text). Therefore, interaction between neighboring phthalocyanines plays a role. The dipole-dipole interaction hypothesis is based on a direct interaction of the dipoles of CO molecules adsorbed at adjacent phthalocyanines. We considered the potential energy for this interaction:

$$U(r) = p_{CO}^2/(4\pi\epsilon_0 r^3) \tag{6.33}$$

If we set r = 13.6 Å and p_{CO} = 0.112 D,[243] we obtain U = 3 $\times 10^{-6}$ eV, three orders of magnitude smaller than the peak spacing in the SFG spectra. Thus, the dipole-dipole interaction hypothesis had to be discarded.

The harmonic coupling hypothesis.

Another possible hypothesis about the nature of the interaction between the (CO)FePc molecules consists in assuming that the CO-CO interaction is indirectly mediated by the vibrations of the FePc 2D molecular lattice. We have calculated the frequency of the C-O stretching mode for this system by using density functional perturbation theory (DFPT). A finite dispersion of phonon modes in the first Brillouin zone would have demonstrated that intermolecular coupling is responsible for the appearance of several peaks in the SFG spectra. Instead, at different k-points the modes differ at most by 3 cm^{-1}, i.e. no direct effect on the vibrational modes could be observed, leading to the rejection of the harmonic coupling hypothesis, consistently with the PM-IRAS measurements.

The excitonic hypothesis.

After discarding the harmonic coupling hypothesis, where the interaction is of pure phononic nature, we analyze the influence of electronic effects. The excitonic hypothesis assumes that, upon illumination with visible light in a SFG experiment, a fraction of the molecules turns in an electronically excited state. Provided the lifetime of the latter is long enough, the SFG process occurs on the set of populated states. The multiplet of peaks would then originate from the non-equivalent vibrational modes of both the electronically excited and ground states. To prove the excitonic hypothesis, the vibrational modes of an excited state have been investigated. Since the ground state is a singlet, a virtually excited state was obtained by imposing a total magnetization of the system equal to 2.00 μ_B in the calculations. The vibrational frequencies were calculated both with DFT and with DFT+U. DFT yields frequencies of 1994, and 1996 cm^{-1} for the singlet and the lowest-lying triplet states, respectively. The obtained triplet state is associated with the HOMO to LUMO transition. DFT+U yields values of 2016 and 2049 cm^{-1}, respectively, and 2055 cm^{-1} for another excited configuration. As shown in Fig. 6.6, imposing a total magnetization of 2.00 μ_B in the calculation forces one electron originally occupying a HOMO-1 state to be lifted into a LUMO+1 state. The other excited state was instead obtained by imposing a fixed occupation on the orbitals, forcing the second highest minority spin state below the Fermi energy to be empty and the second lowest majority-spin state above the Fermi energy to be occupied. The vibrational energy differences are compatible with the experimentally observed values, thus lending support for the excitonic hypothesis.

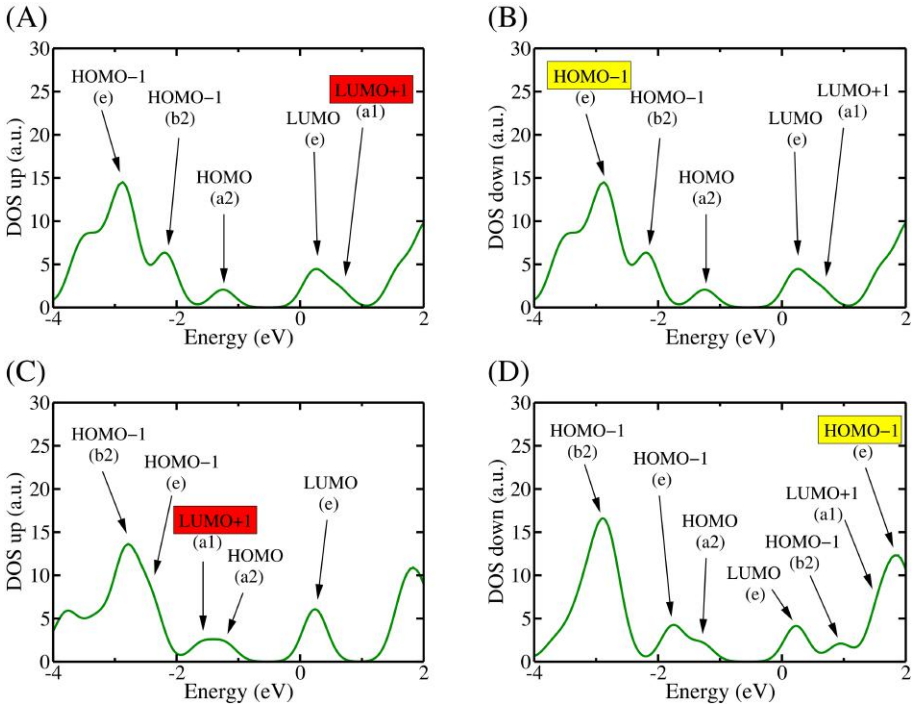

Figure 6.6: Singlet density of states for: **a** spin up and **b** spin down electrons and triplet density of states for **c** spin up and **d** spin down electrons. The classification of the orbitals is made according to the irreducible representation of the $C_{4\nu}$ group (which is the symmetry group of the isolated (CO)FePc molecule). The main differences between the singlet and the triplet states are highlighted in color, showing the emptying of a HOMO-1 state of the minority spins (yellow), and the filling of a LUMO+1 state of the majority spins (red). The Fermi level corresponds to the zero of the energy scale.

6.9 FePc on $Al_2O_3/Ni_3Al(111)$: fitting the XPS data

The C 1*s* XPS data were fitted by means of Voigt lineshapes. Starting from the FePc/alumina system, the best fit parameters were obtained for the satellite (288 eV), pyridinic (286.2 eV) and benzenic (284.7 eV) features, according to previous literature.[128,196] In order to extract the relevant information from the coverage, temperature, and cluster-size dependent measurements we introduced a set of constraints in the lineshape parameters in order to avoid overfitting. Thus, in a first approximation, we modeled the spectra as an additive superposition of a set of the three above features associated with the FePc molecules interacting with the substrate and with another set corresponding to the FePc molecules interacting with the Cu particles. The following parameters were constrained:

- the intensity ratio of the C 1*s* features associated with the pyrrolic and benzenic structures (0.3 : 1.0);
- the relative energy separation of the C 1*s* satellite (2.3 eV), and of the pyrrolic (1.5 eV) from the benzenic spectral contributions;
- the Lorentzian width (same valuefor all adiabatic features, 0.4 eV).

Within our approximation, we also neglected a second, smaller non-adiabatic satellite at intermediate binding energy. Depending on the experimental conditions (FePc coverage, Cu loading, and surface temperature) the binding energy of B1 was found to vary in the

284.4-284.7 eV range, and the B1-B2 separation varied from 0.7 to 0.9 eV.

Concerning the N 1s core level, as indicated in the main text, it is known that FePcs adsorbed on several substrates exhibit two features that are in most cases energetically unresolved and are centered at about 399 eV with a relative shift of 0.3-0.5 eV. They are associated with the two non-equivalent nitrogen atoms in the tetrapyrrolic ring. Accordingly, we fitted the N 1s spectrum of FePc molecules deposited on the pristine alumina surface with a doublet of Voigt-shaped features of equal intensity and centered at 399.3 and 399.0 eV, respectively, adding a second doublet in the presence of Cu. The Lorentzian width was optimized and fixed at 0.25 eV for all N 1s features.

List of Pubblications

The results obtained in the framework of this thesis have been partly published in:

1. Manuel Corva, Fatema Mohamed, Erika Tomsic, Matteo Rinaldi, Cinzia Cepek, Nicola Seriani, Maria Peressi, and Erik Vesselli
   "Learning from Nature: Charge Transfer and Carbon Dioxide Activation at Single, Biomimetic Fe Sites in Tetrapyrroles on Graphene."
   J. Phys. Chem. C, 2019, 123 (6), pp 3916–3922

2. Manuel Corva, Alberto Ferrari, Matteo Rinaldi, Zhijing Feng, Matteo Roiaz, Cristophe Rameshan, Guenther Rupprechter, Roberto Costantini, Martina Dell'Angela, Giorgio Pastore, Giovanni Comelli, Nicola Seriani, and Erik Vesselli
   "Vibrational fingerprint of localized excitons in a two-dimensional metal-organic crystal."
   Nature Comm., 2018, 9, 4703, doi: 10.1038/s41467-018-07190-1

3. Manuel Corva, Fatema Mohamed, Erika Tomsic, Zhijing Feng, Tomás Skála, Giovanni Comelli, Nicola Seriani, Maria Peressi, and Erik Vesselli
   "Substrate- to Laterally-Driven Self-Assembly Steered by Cu Nanoclusters: The Case of FePcs on an Ultrathin Alumina Film."
   ACS Nano, 2018 Sep 17. doi: 10.1021/acsnano.8b05992

4. Nicola Podda, Manuel Corva, Fatema Mohamed, Zhijing Feng, Carlo Dri , Filip Dvorák, Vladimir Matolin, Giovanni Comelli, Maria Peressi, and Erik Vesselli
   "Experimental and Theoretical Investigation of the Restructuring Process Induced by CO at Near Ambient Pressure: Pt Nanoclusters on Graphene/Ir(111)"
   ACS Nano, 2017, 11 (1), pp 1041–1053

Moreover, I contributed to the experimental findings (data acquisition and/or discussion) present in the following works (published or still in preparation):

- Manuel Corva and Erik Vesselli
  "Room Temperature Carbonylation of Iron–Phthalocyanines Adsorbed on a Single Crystal Metal Surface: An *in situ* SFG Investigation at Near Ambient Pressure"
  J. Phys. Chem. C, 2016, 120 (39), 22298–22303

- Manuel Corva, Zhijing Feng, Carlo Dri, Federico Salvador, Paolo Bertoch, Giovanni Comelli, and Erik Vesselli
  "Carbon dioxide reduction on Ir(111): stable hydrocarbon surface species at near ambient pressure"
  Phys.Chem.Chem.Phys., 2016, 18, 6763

- G. Zamborlini, S. Moro, E. Vesselli, M. Corva, M. Jugovac, A. Cossaro, A. Verdini, L. Floreano, Z. Feng, A. Sala, G. Comelli, D. Lüftner, P. Puschnig, C. M. Schneider, and V. Feyer
  "Synthesis of stable hyponitrite species at biomimetic single metal atom sites."
  In preparation

- S. Moro, M. Corva, M. Jugovac, G. Zamborlini, V. Feyer, and E. Vesselli
  "Adsorption and progressive nitrosylation of Ni tetraphenylporphyrins on Cu(100)"
  In preparation

- Anita Previdi, Manuel Corva, Manuela Bevilacqua, Vladimir Matolin, Erik Vesselli, Mykhailo Vorokhta, and Benedetto Bozzini
  "Cathodic oxygen reaction in a solid oxide fuel cell: *in situ* and *operando* spectroscopic characterization of the electrode's surface composition."
  In preparation

Acronyms

IR-Vis SFG Infrared-Visible Sum Frequency Generation

UHV Ultra High Vacuum

NAP Near Ambient Pressure

SMAC Single Metal Atom Catalyst

MOF Metal Organic Framework

XPS X-ray Photoemission Spectroscopy

NAP-XPS Near Ambient Pressure X-ray Photoemission Spectroscopy

STM Scanning Tunneling Mycroscope

DFT Density Functional Theory

NiTPP Nickel Tetra-Phenyl Porphyrin

FePc Iron Phthalocyanine

PVD Physical Vapour Deposition

PM-IRAS Polarization Modulation Infrared Adsorption Spectroscopy

TR-2PPE Time-Resolved Two-Photon Photoemission

Acknowledgments

My greatest thanks have to go to my PhD Supervisor Prof. Erik Vesselli for the suggestions, teachings, and support that I received in these last years. His enthusiasm and competence are one of the best synergies that a student may ask for.

Then, I would like to acknowledge the other Master and PhD students that contributed to my research activity, both "on the laboratory side" and for the theoretical simulations that they performed. Thank you Nicola, Erika, Stefania, Anita, Zhijing, Roberto, and Mattero Ro. Thank you Alberto, Matteo Ri., and Fatema.

I want to thank Prof. Maria Peressi and Dr. Nicola Seriani for the coordination of the state-of-the-art theoretical calculations complementing the experimental results of this Thesis.

In addition, I want to thank the staff of the ALOISA, NanoEsca, and Material Science beamlines at the ELETTRA synchrotron facility for their support and contribution.
My gratitude goes also to the Analytical Laboratory and Variable and Low Temperature Scanning Tunneling Microscopy groups at the CNR-IOM Institute in Trieste, together with the NAP-XPS Laboratory group at the Physics Department at the Charles University in Prague.
A particular mention to Dr. Tomás Skála and Dr. Filip Dvorák for the help that they provided to me.

As during my PhD I had the opportunity to spend two months at the Institute for Materials Chemistry at the University of Vienna, I want to thank Dr. Cristophe Rameshan and Prof. Guenther Rupprechter for their time and precious suggestions.

My last thanks go to the researchers, teachers, and administrative staff of my PhD School and of the University of Trieste, for the help that they provided me during these years.

Bibliography

[1] Chorkendorff, I. & Niemantsverdriet, J. W. *Concepts of Modern Catalysis and Kinetics* (Wiley-VCH Verlag GmbH & Co. KGaA, 2003). URL https://doi.org/10.1002%2F3527602658.

[2] Ertl, G. *Handbook of heterogeneous catalysis* (Wiley-VCH John Wiley, distributor, Weinheim Chichester, 2008).

[3] Maxwell, I. E. Driving forces for innovation in applied catalysis. In *11th International Congress On Catalysis - 40th Anniversary, Proceedings of the 11th ICC*, 1–9 (Elsevier, 1996). URL https://doi.org/10.1016%2Fs0167-2991%2896%2980210-2.

[4] C., V. G. L. & A., G. L. Fossil fuels. reserves and alternatives. a scientific approach (2005).

[5] Schmal, M. *Heterogeneous Catalysis and its Industrial Applications* (Springer International Publishing, 2016). URL https://doi.org/10.1007%2F978-3-319-09250-8.

[6] Houdry, E. J. Catalytic structure and composition (1956). URL http://www.freepatentsonline.com/2742437.html.

[7] Pardiwala, J. M., Paterl, F. & Patel, S. Review paper on catalytic converter for automotive exhaust emission. *International conference on currents trends in technology, "NUiCONE-2011"* (2011).

[8] Bragg, G., Charles D. (Newcastle upon Tyne. Bleach catalyst compositions and use thereof in laundry bleaching and detergent compositions (1984). URL http://www.freepatentsonline.com/4430243.html.

[9] Gray, J. I. & Russell, L. F. Hydrogenation catalysts-their effect on selectivity. *Journal of the American Oil Chemists' Society* **56**, 36–44 (1979). URL https://doi.org/10.1007%2Fbf02671758.

[10] Savchenko, V. I. & Makaryan, I. A. Palladium catalyst for the production of pure margarine. *Platinum Metals Review* **43**, 74–82 (1999).

[11] Modak, J. M. Haber process for ammonia synthesis. *Resonance* **7**, 69–77 (2002). URL https://doi.org/10.1007%2Fbf02836187.

[12] Ragsdale, S. W. Metals and their scaffolds to promote difficult enzymatic reactions. *Chemical Reviews* **106**, 3317–3337 (2006). URL https://doi.org/10.1021%2Fcr0503153.

[13] Kolasinski, K. W. *Surface Science* (John Wiley & Sons, Ltd, 2012). URL https://doi.org/10.1002%2F9781119941798.

[14] Zangwill, A. *Physics at Surfaces* (Cambridge University Press, 1988). URL https://books.google.it/books?id=KJj98B_3Dr8C.

[15] Lüth, H. *Solid Surfaces, Interfaces and Thin Films*. Graduate Texts in Physics (Springer International Publishing, 2014). URL https://books.google.it/books?id=nKYxBQAAQBAJ.

[16] Ferrari, A. *Ab-initio Investigation of reactivity, electronic and vibrational properties of iron pthalocyanines*. Master's thesis, University of Trieste (2016).

[17] Bentley, R. W. & Smith, R. World oil production peak - a supply-side perspective (2003).

[18] Davis, M. & Davis, R. *Fundamentals of Chemical Reaction Engineering*. Dover Civil and Mechanical Engineering (Dover Publications, 2013). URL https://books.google.it/books?id=szvDAgAAQBAJ.

[19] Masters, S., Eriksen, K. & Fehrmann, R. Hysteresis phenomena in sulfur dioxide oxidation over supported vanadium catalysts. *Journal of Molecular Catalysis A: Chemical* **120**, 227–233 (1997). URL https://doi.org/10.1016%2Fs1381-1169%2896%2900407-4.

[20] Mijangos, C., Hernández, R. & Martín, J. A review on the progress of polymer nanostructures with modulated morphologies and properties, using nanoporous AAO templates. *Progress in Polymer Science* **54-55**, 148–182 (2016). URL https://doi.org/10.1016%2Fj.progpolymsci.2015.10.003.

[21] Matsutani, K., Hayakawa, K. & Tada, T. Effect of particle size of platinum and platinum-cobalt catalysts on stability against load cycling. *Platinum Metals Review* **54**, 223–232 (2010). URL https://doi.org/10.1595%2F147106710x523698.

[22] Heiz, U. & Schneider, W.-D. Nanoassembled model catalysts. *Journal of Physics D: Applied Physics* **33**, R85–R102 (2000). URL https://doi.org/10.1088%2F0022-3727%2F33%2F11%2F201.

[23] Anderson, J. & Boudart, M. *Catalysis: Science and Technology*. Catalysis (Springer Berlin Heidelberg, 2012). URL https://books.google.it/books?id=wCH0CAAAQBAJ.

[24] Yang, X.-F. *et al.* Single-atom catalysts: A new frontier in heterogeneous catalysis. *Accounts of Chemical Research* **46**, 1740–1748 (2013). URL https://doi.org/10.1021%2Far300361m.

[25] Poppa, H. Nucleation, growth, and TEM analysis of metal particles and clusters deposited in UHV. *Catalysis Reviews* **35**, 359–398 (1993). URL https://doi.org/10.1080%2F01614949308013911.

[26] Bäumer, M. & Freund, H.-J. Metal deposits on well-ordered oxide films. *Progress in Surface Science* **61**, 127–198 (1999). URL https://doi.org/10.1016%2Fs0079-6816%2899%2900012-x.

[27] Haruta, M., Kobayashi, T., Sano, H. & Yamada, N. Novel gold catalysts for the oxidation of carbon monoxide at a temperature far below 0 °c. *Chemistry Letters* **16**, 405–408 (1987). URL https://doi.org/10.1246%2Fcl.1987.405.

[28] Herzing, A. A., Kiely, C. J., Carley, A. F., Landon, P. & Hutchings, G. J. Identification of active gold nanoclusters on iron oxide supports for CO oxidation. *Science* **321**, 1331–1335 (2008). URL https://doi.org/10.1126%2Fscience.1159639.

[29] Khanna, S. N. & Castleman, A. W. *Quantum Phenomena in Clusters and Nanostructures* (Springer Berlin Heidelberg, 2003). URL https://doi.org/10.1007%2F978-3-662-02606-9.

[30] Binns, C. Nanoclusters deposited on surfaces. *Surface Science Reports* **44**, 1–49 (2001). URL https://doi.org/10.1016%2Fs0167-5729%2801%2900015-2.

[31] Corain, B., Schmid, G. & Toshima, N. *Metal Nanoclusters in Catalysis and Materials Science: The Issue of Size Control* (Elsevier Science, 2011). URL https://books.google.it/books?id=CkhzxSGGcYgC.

[32] Das, N. K. & Mukherjee, S. Size-controlled atomically precise copper nanoclusters: Synthetic protocols, spectroscopic properties and applications. *Physical Sciences Reviews* **0** (2018). URL https://doi.org/10.1515%2Fpsr-2017-0081.

[33] Gates, B. C. Supported metal clusters: Synthesis, structure, and catalysis. *Chemical Reviews* **95**, 511–522 (1995). URL https://doi.org/10.1021%2Fcr00035a003.

[34] Qiao, B. *et al.* Single-atom catalysis: Pt1/FeOx for CO oxidation and preferential oxidation of CO in h2. *Microscopy and Microanalysis* **18**, 350–351 (2012). URL https://doi.org/10.1017%2Fs1431927612003601.

[35] Vincent, J. F., Bogatyreva, O. A., Bogatyrev, N. R., Bowyer, A. & Pahl, A.-K. Biomimetics: its practice and theory. *Journal of The Royal Society Interface* **3**, 471–482 (2006). URL https://doi.org/10.1098%2Frsif.2006.0127.

[36] Vincent, J. F. V. Biomimetics — a review. *Proceedings of the Institution of Mechanical Engineers, Part H: Journal of Engineering in Medicine* **223**, 919–939 (2009). URL https://doi.org/10.1243%2F09544119jeim561.

[37] Bhushan, B. Biomimetics: lessons from nature-an overview. *Philosophical Transactions of the Royal Society A: Mathematical, Physical and Engineering Sciences* **367**, 1445–1486 (2009). URL https://doi.org/10.1098%2Frsta.2009.0011.

[38] Gordon, J. E. & Mattis, D. C. The new science of strong materials, or, why you don't fall through the floor. *American Journal of Physics* **53**, 508–509 (1985). URL https://doi.org/10.1119%2F1.14221.

[39] Benyus, J. *Biomimicry: Innovation Inspired by Nature* (HarperCollins, 2009). URL https://books.google.it/books?id=mDHKVQyJ94gC.

[40] Autumn, K. *et al.* Evidence for van der waals adhesion in gecko setae. *Proceedings of the National Academy of Sciences* **99**, 12252–12256 (2002). URL https://doi.org/10.1073%2Fpnas.192252799.

[41] Bond, G. M., Richman, R. H. & McNaughton, W. P. Mimicry of natural material designs and processes. *Journal of Materials Engineering and Performance* **4**, 334–345 (1995). URL https://doi.org/10.1007%2Fbf02649071.

[42] Egan, P., Sinko, R., LeDuc, P. R. & Keten, S. The role of mechanics in biological and bio-inspired systems. *Nature Communications* **6** (2015). URL https://doi.org/10.1038%2Fncomms8418.

[43] Can, M., Armstrong, F. A. & Ragsdale, S. W. Structure, function, and mechanism of the nickel metalloenzymes, CO dehydrogenase, and acetyl-CoA synthase. *Chemical Reviews* **114**, 4149–4174 (2014). URL https://doi.org/10.1021%2Fcr400461p.

[44] Berg, J. *Biochemistry* (W.H. Freeman, New York, 2012).

[45] Zuliani, J. *Studio elettrochimico di citocromi c immobilizzati su elettrodi modificati con SAM di decantiolo in presenza di ossigeno e cardiolipina.* Master's thesis, Università di Trieste (2016).

[46] Li, N. *et al.* Overexpression, homology modeling and coenzyme docking studies of the cytochrome p450nor2 from cylindrocarpon tonkinense. *Molecular Biology* **50**, 320–327 (2016). URL https://doi.org/10.1134%2Fs002689331602014x.

[47] Kummer, J. Catalysts for automobile emission control. *Progress in Energy and Combustion Science* **6**, 177–199 (1980). URL https://doi.org/10.1016%2F0360-1285%2880%2990006-4.

[48] Li, Y. & Sun, Q. The superior catalytic CO oxidation capacity of a cr-phthalocyanine porous sheet. *Scientific Reports* **4** (2014). URL https://doi.org/10.1038%2Fsrep04098.

[49] Greeley, J. & Mavrikakis, M. A first-principles study of methanol decomposition on pt(111). *Journal of the American Chemical Society* **124**, 7193–7201 (2002). URL https://doi.org/10.1021%2Fja017818k.

[50] Isvoranu, C. *et al.* Comparison of the carbonyl and nitrosyl complexes formed by adsorption of CO and NO on monolayers of iron phthalocyanine on au(111). *The Journal of Physical Chemistry C* **115**, 24718–24727 (2011). URL https://doi.org/10.1021%2Fjp204461k.

[51] Corva, M. & Vesselli, E. Room temperature carbonylation of iron–phthalocyanines adsorbed on a single crystal metal surface: An in situ SFG investigation at near-ambient pressure. *The Journal of Physical Chemistry C* **120**, 22298–22303 (2016). URL https://doi.org/10.1021%2Facs.jpcc.6b05356.

[52] Rupprechter, G. & Weilach, C. Spectroscopic studies of surface–gas interactions and catalyst restructuring at ambient pressure: mind the gap! *Journal of Physics: Condensed Matter* **20**, 184019 (2008). URL https://doi.org/10.1088%2F0953-8984%2F20%2F18%2F184019.

[53] Peters, K. F. *et al.* Adsorption of carbon monoxide on ni(110) above atmospheric pressure investigated with surface x-ray diffraction. *Physical Review Letters* **86**, 5325–5328 (2001). URL https://doi.org/10.1103%2Fphysrevlett.86.5325.

[54] Shen, Y. R. Basic Theory of Surface Sum-Frequency Generation. *J. Phys. Chem. C* **116**, 15505–15509 (2012). URL http://pubs.acs.org/doi/10.1021/jp305539v.

[55] Wang *, H.-F., Gan † ‡, W., Lu † ‡ §, R., Rao † ‡ ¶, Y. & Wu †, B.-H. Quantitative spectral and orientational analysis in surface sum frequency generation vibrational

spectroscopy (SFG-VS). *Int. Rev. Phys. Chem.* **24**, 191–256 (2005). URL http://www.tandfonline.com/doi/abs/10.1080/01442350500225894.

[56] Lambert, A. G., Davies, P. B. & Neivandt, D. J. Implementing the Theory of Sum Frequency Generation Vibrational Spectroscopy: A Tutorial Review. *Appl. Spectrosc. Rev.* **40**, 103–145 (2005). URL http://www.tandfonline.com/doi/abs/10.1081/ASR-200038326.

[57] Vidal, F. & Tadjeddine, A. Sum-frequency generation spectroscopy of interfaces. *Reports Prog. Phys.* **68**, 1095–1127 (2005). URL http://stacks.iop.org/0034-4885/68/i=5/a=R03?key=crossref.203e5d07afffff2eb340f1f9102a3884b.

[58] Wang, H.-F., Velarde, L., Gan, W. & Fu, L. Quantitative Sum-Frequency Generation Vibrational Spectroscopy of Molecular Surfaces and Interfaces: Lineshape, Polarization, and Orientation. *Annu. Rev. Phys. Chem.* **66**, 189–216 (2015). URL http://www.annualreviews.org/doi/10.1146/annurev-physchem-040214-121322.

[59] Shen, Y. Phase-Sensitive Sum-Frequency Spectroscopy. *Annu. Rev. Phys. Chem.* **64**, 129–150 (2013). URL http://www.annualreviews.org/doi/10.1146/annurev-physchem-040412-110110. arXiv:1011.1669v3.

[60] Busson, B. & Tadjeddine, A. Non-Uniqueness of Parameters Extracted from Resonant Second-Order Nonlinear Optical Spectroscopies. *J. Phys. Chem. C* **113**, 21895–21902 (2009). URL http://pubs.acs.org/doi/10.1021/jp908240d.

[61] Gan, W., Zhang, Z., Feng, R.-r. & Wang, H.-f. Spectral Interference and Molecular Conformation at Liquid Interface with Sum Frequency Generation Vibrational Spectroscopy (SFG-VS) †. *J. Phys. Chem. C* **111**, 8726–8738 (2007). URL http://pubs.acs.org/doi/abs/10.1021/jp0670642.

[62] Backus, E. H. G., Garcia-Araez, N., Bonn, M. & Bakker, H. J. On the Role of Fresnel Factors in Sum-Frequency Generation Spectroscopy of Metal–Water and Metal-Oxide–Water Interfaces. *J. Phys. Chem. C* **116**, 23351–23361 (2012). URL http://pubs.acs.org/doi/10.1021/jp306273d.

[63] Corva, M. *et al.* Carbon dioxide reduction on ir(111): stable hydrocarbon surface species at near-ambient pressure. *Physical Chemistry Chemical Physics* **18**, 6763–6772 (2016). URL https://doi.org/10.1039%2Fc5cp07906c.

[64] Ito, M., Noguchi, H., Ikeda, K. & Uosaki, K. Substrate dependent structure of adsorbed aryl isocyanides studied by sum frequency generation (SFG) spectroscopy. *Phys. Chem. Chem. Phys.* **12**, 3156 (2010). URL http://xlink.rsc.org/?DOI=b920411c.

[65] Hüfner, S. *Photoelectron spectroscopy: principles and applications*. Springer Series in Solid-State Sciences Series (Springer-Verlag, 1996). URL https://books.google.it/books?id=1LfvAAAAMAAJ.

[66] Woodruff, D. P. *Modern Techniques of Surface Science* (Cambridge University Press, 2016), 3 edn.

[67] Bransden, B. & Joachain, C. *Quantum Mechanics* (Prentice Hall, 2000). URL https://books.google.it/books?id=K9f3F0EGACgC.

[68] Salmeron, M. & Schlögl, R. Ambient pressure photoelectron spectroscopy: A new tool for surface science and nanotechnology. *Surface Science Reports* **63**, 169–199 (2008).

[69] Hofmann, S. *Auger- and X-Ray Photoelectron Spectroscopy in Materials Science: A User-Oriented Guide*. Springer Series in Surface Sciences (Springer Berlin Heidelberg, 2012). URL https://books.google.it/books?id=t_AvLetz5-YC.

[70] Doniach, S. & Sunjic, M. Many-electron singularity in x-ray photoemission and x-ray line spectra from metals. *Journal of Physics C: Solid State Physics* **3**, 285–291 (1970). URL https://doi.org/10.1088%2F0022-3719%2F3%2F2%2F010.

[71] Shirley, D. A. High-resolution x-ray photoemission spectrum of the valence bands of gold. *Phys. Rev. B* **5**, 4709–4714 (1972). URL https://link.aps.org/doi/10.1103/PhysRevB.5.4709.

[72] Végh, J. The shirley background revised. *Journal of Electron Spectroscopy and Related Phenomena* **151**, 159 – 164 (2006). URL http://www.sciencedirect.com/science/article/pii/S0368204805005220.

[73] Phoibos 150 nap, near ambient pressure hemispherical energy analyzer. http://www.specs.de/cms/upload/PDFs/SPECS_Prospekte/2010_11_PHOIBOS_150_NAP_product_brochure_final_web.pdf.

[74] Malard, L., Pimenta, M., Dresselhaus, G. & Dresselhaus, M. Raman spectroscopy in graphene. *Physics Reports* **473**, 51–87 (2009). URL https://doi.org/10.1016%2Fj.physrep.2009.02.003.

[75] Grånäs, E. *et al.* CO intercalation of graphene on ir(111) in the millibar regime. *The Journal of Physical Chemistry C* **117**, 16438–16447 (2013). URL https://doi.org/10.1021%2Fjp4043045.

[76] Vajda, S. *et al.* Subnanometre platinum clusters as highly active and selective catalysts for the oxidative dehydrogenation of propane. *Nature Materials* **8**, 213–216 (2009). URL https://doi.org/10.1038%2Fnmat2384.

[77] Valden, M. Onset of catalytic activity of gold clusters on titania with the appearance of nonmetallic properties. *Science* **281**, 1647–1650 (1998). URL https://doi.org/10.1126%2Fscience.281.5383.1647.

[78] Stephens, I. E. L., Elias, J. S. & Shao-Horn, Y. The importance of being together. *Science* **350**, 164–165 (2015). URL https://doi.org/10.1126%2Fscience.aad3716.

[79] Calle-Vallejo, F. *et al.* Finding optimal surface sites on heterogeneous catalysts by counting nearest neighbors. *Science* **350**, 185–189 (2015). URL https://doi.org/10.1126%2Fscience.aab3501.

[80] Ding, K. *et al.* Identification of active sites in CO oxidation and water-gas shift over supported pt catalysts. *Science* **350**, 189–192 (2015). URL https://doi.org/10.1126%2Fscience.aac6368.

[81] Tyo, E. C. & Vajda, S. Catalysis by clusters with precise numbers of atoms. *Nature Nanotechnology* **10**, 577–588 (2015). URL https://doi.org/10.1038%2Fnnano.2015.140.

[82] N'Diaye, A. T. *et al.* A versatile fabrication method for cluster superlattices. *New Journal of Physics* **11**, 103045 (2009). URL https://doi.org/10.1088%2F1367-2630%2F11%2F10%2F103045.

[83] Linas, S. *et al.* Moiré induced organization of size-selected pt clusters soft landed on epitaxial graphene. *Scientific Reports* **5** (2015). URL https://doi.org/10.1038%2Fsrep13053.

[84] Gerber, T. *et al.* CO-induced smoluchowski ripening of pt cluster arrays on the graphene/ir(111) moiré. *ACS Nano* **7**, 2020–2031 (2013). URL https://doi.org/10.1021%2Fnn400082w.

[85] Knudsen, J. *et al.* Clusters binding to the graphene moiré on ir(111): X-ray photoemission compared to density functional calculations. *Physical Review B* **85** (2012). URL https://doi.org/10.1103%2Fphysrevb.85.035407.

[86] Gotterbarm, K. *et al.* Reactivity of graphene-supported pt nanocluster arrays. *ACS Catalysis* **5**, 2397–2403 (2015). URL https://doi.org/10.1021%2Facscatal.5b00245.

[87] Henry, C. R. 2d-arrays of nanoparticles as model catalysts. *Catalysis Letters* **145**, 731–749 (2014). URL https://doi.org/10.1007%2Fs10562-014-1402-6.

[88] Franz, D. *et al.* Atomic structure of pt nanoclusters supported by graphene/ir(111) and reversible transformation under CO exposure. *Physical Review B* **93** (2016). URL https://doi.org/10.1103%2Fphysrevb.93.045426.

[89] Gerber, T. *et al.* Stability and reactivity of graphene-templated nanoclusters. *The Journal of Physical Chemistry C* **120**, 26290–26299 (2016). URL https://doi.org/10.1021%2Facs.jpcc.6b07828.

[90] Rupprechter, G., Dellwig, T., Unterhalt, H. & Freund, H.-J. High-pressure carbon monoxide adsorption on pt(111) revisited: A sum frequency generation study†. *The Journal of Physical Chemistry B* **105**, 3797–3802 (2001). URL https://doi.org/10.1021%2Fjp003585s.

[91] Tao, F. *et al.* Break-up of stepped platinum catalyst surfaces by high CO coverage. *Science* **327**, 850–853 (2010). URL https://doi.org/10.1126%2Fscience.1182122.

[92] Crossley, A. & King, D. A. Infrared spectra for co isotopes chemisorbed on pt "111": Evidence for strong absorbate coupling interactions. *Surface Science* **68**, 528–538 (1977). URL https://doi.org/10.1016%2F0039-6028%2877%2990245-x.

[93] Chou, K. C., Westerberg, S., Shen, Y. R., Ross, P. N. & Somorjai, G. A. Probing the charge-transfer state of CO on pt(111) by two-dimensional infrared-visible sum frequency generation spectroscopy. *Physical Review B* **69** (2004). URL https://doi.org/10.1103%2Fphysrevb.69.153413.

[94] Kappers, M. J. & van der Maas, J. H. Correlation between CO frequency and pt coordination number. a DRIFT study on supported pt catalysts. *Catalysis Letters* **10**, 365–373 (1991). URL https://doi.org/10.1007%2Fbf00769171.

[95] Aizawa, H. & Tsuneyuki, S. First-principles study of CO bonding to pt(111): validity of the blyholder model. *Surface Science* **399**, L364–L370 (1998). URL https://doi.org/10.1016%2Fs0039-6028%2898%2900042-9.

[96] Su, X., Cremer, P. S., Shen, Y. R. & Somorjai, G. A. High-pressure CO oxidation on pt(111) monitored with infrared-visible sum frequency generation (SFG). *Journal of the American Chemical Society* **119**, 3994–4000 (1997). URL https://doi.org/10.1021%2Fja9638723.

[97] Klünker, C., Balden, M., Lehwald, S. & Daum, W. CO stretching vibrations on pt(111) and pt(110) studied by sumfrequency generation. *Surface Science* **360**, 104–111 (1996). URL https://doi.org/10.1016%2F0039-6028%2896%2900638-3.

[98] Schweizer, E., Persson, B., Tüshaus, M., Hoge, D. & Bradshaw, A. The potential energy surface, vibrational phase relaxation and the order-disorder transition in the adsorption system pt{111}-CO. *Surface Science* **213**, 49–89 (1989). URL https://doi.org/10.1016%2F0039-6028%2889%2990252-5.

[99] Hayden, B., Kretzschmar, K., Bradshaw, A. & Greenler, R. An infrared study of the adsorption of CO on a stepped platinum surface. *Surface Science* **149**, 394–406 (1985). URL https://doi.org/10.1016%2F0039-6028%2885%2990071-8.

[100] McCrea, K., Parker, J. S., Chen, P. & Somorjai, G. Surface structure sensitivity of high-pressure CO dissociation on pt(), pt() and pt() using sum frequency generation surface vibrational spectroscopy. *Surface Science* **494**, 238–250 (2001). URL https://doi.org/10.1016%2Fs0039-6028%2801%2901469-8.

[101] Hayden, B. & Bradshaw, A. The adsorption of CO on pt(111) studied by infrared-reflection-adsorption spectroscopy. *Journal of Electron Spectroscopy and Related Phenomena* **30**, 51 (1983). URL https://doi.org/10.1016%2F0368-2048%2883%2985033-6.

[102] Backus, E. H. G. Real-time observation of molecular motion on a surface. *Science* **310**, 1790–1793 (2005). URL https://doi.org/10.1126%2Fscience.1120693.

[103] Rupprechter, G. Surface vibrational spectroscopy from ultrahigh vacuum to atmospheric pressure: adsorption and reactions on single crystals and nanoparticle model catalysts monitored by sum frequency generation spectroscopy. *Physical Chemistry Chemical Physics* **3**, 4621–4632 (2001). URL https://doi.org/10.1039%2Fb104354b.

[104] Grånäs, E. *et al.* Oxygen intercalation under graphene on ir(111): Energetics, kinetics, and the role of graphene edges. *ACS Nano* **6**, 9951–9963 (2012). URL https://doi.org/10.1021%2Fnn303548z.

[105] Andersen, M., Hornekær, L. & Hammer, B. Understanding intercalation structures formed under graphene on ir(111). *Physical Review B* **90** (2014). URL https://doi.org/10.1103%2Fphysrevb.90.155428.

[106] Cavallin, A. *et al.* Local electronic structure and density of edge and facet atoms at rh nanoclusters self-assembled on a graphene template. *ACS Nano* **6**, 3034–3043 (2012). URL https://doi.org/10.1021%2Fnn300651s.

[107] Gottfried, J. M. Surface chemistry of porphyrins and phthalocyanines. *Surface Science Reports* **70**, 259–379 (2015). URL https://doi.org/10.1016%2Fj.surfrep.2015.04.001.

[108] Ivanov, A. S. & Boldyrev, A. I. Deciphering aromaticity in porphyrinoids via adaptive natural density partitioning. *Org. Biomol. Chem.* **12**, 6145–6150 (2014). URL https://doi.org/10.1039%2Fc4ob01018c.

[109] Lash, T. D. Origin of aromatic character in porphyrinoid systems. *Journal of Porphyrins and Phthalocyanines* **15**, 1093–1115 (2011). URL https://doi.org/10.1142%2Fs1088424611004063.

[110] Falk, J. & Smith, K. *Porphyrins and metalloporphyrins: a new edition based on the original volume by J. E. Falk.* BBA Library (Elsevier Scientific Pub. Co., 1975). URL https://books.google.it/books?id=dahqAAAAMAAJ.

[111] Raux, E., Schubert, H. L., Roper, J. M., Wilson, K. S. & Warren, M. J. Vitamin b12: Insights into biosynthesis's mount improbable. *Bioorganic Chemistry* **27**, 100–118 (1999). URL https://doi.org/10.1006%2Fbioo.1998.1125.

[112] Al-Karadaghi, S., Hansson, M., Nikonov, S., Jönsson, B. & Hederstedt, L. Crystal structure of ferrochelatase: the terminal enzyme in heme biosynthesis. *Structure* **5**, 1501–1510 (1997). URL https://doi.org/10.1016%2Fs0969-2126%2897%2900299-2.

[113] Gottfried, M. & Marbach, H. Surface-confined coordination chemistry with porphyrins and phthalocyanines: Aspects of formation, electronic structure, and reactivity. *Zeitschrift für Physikalische Chemie* **223**, 53–74 (2009). URL https://doi.org/10.1524%2Fzpch.2009.6024.

[114] Auwärter, W., Écija, D., Klappenberger, F. & Barth, J. V. Porphyrins at interfaces. *Nature Chemistry* **7**, 105–120 (2015). URL https://doi.org/10.1038%2Fnchem.2159.

[115] Hieringer, W. *et al.* The surface trans effect: Influence of axial ligands on the surface chemical bonds of adsorbed metalloporphyrins. *Journal of the American Chemical Society* **133**, 6206–6222 (2011). URL https://doi.org/10.1021%2Fja1093502.

[116] Deimel, P. S. *et al.* Direct quantitative identification of the "surface trans-effect". *Chemical Science* **7**, 5647–5656 (2016). URL https://doi.org/10.1039%2Fc6sc01677d.

[117] Mochida, I., Suetsugu, K., Fujitsu, H. & Takeshita, K. Enhanced catalytic activity of cobalt tetraphenylporphyrin on titanium dioxide by evacuation at elevated temperatures for intensifying the complex-support interaction. *The Journal of Physical Chemistry* **87**, 1524–1529 (1983). URL https://doi.org/10.1021%2Fj100232a015.

[118] Mochida, I., Suetsugu, K., Fujitsu, H. & Takeshita, K. Unusual activity of carbon monoxide on co-tetraphenylporphyrin supported by TiO2 for the reduction of nitric oxide. *Journal of the Chemical Society, Chemical Communications* 166 (1982). URL https://doi.org/10.1039%2Fc39820000166.

[119] Rezaeifard, A. & Jafarpour, M. The catalytic efficiency of fe-porphyrins supported on multi-walled carbon nanotubes in the heterogeneous oxidation of hydrocarbons and sulfides in water. *Catalysis Science & Technology* **4**, 1960 (2014). URL https://doi.org/10.1039%2Fc3cy00554b.

[120] Qiao, J., Liu, Y., Hong, F. & Zhang, J. A review of catalysts for the electroreduction of carbon dioxide to produce low-carbon fuels. *Chem. Soc. Rev.* **43**, 631–675 (2014). URL https://doi.org/10.1039%2Fc3cs60323g.

[121] Bevilacqua, M. *et al.* Energy savings in the conversion of CO2to fuels using an electrolytic device. *Energy Technology* **2**, 522–525 (2014). URL https://doi.org/10.1002%2Fente.201402014.

[122] Rosa, A., Ricciardi, G. & Baerends, E. J. Synergism of porphyrin-core saddling and twisting ofmeso-aryl substituents. *The Journal of Physical Chemistry A* **110**, 5180–5190 (2006). URL https://doi.org/10.1021%2Fjp060931i.

[123] Eaton, S. S. & Eaton, G. R. Rotation of phenyl rings in metal complexes of substituted tetraphenylporphyrins. *Journal of the American Chemical Society* **97**, 3660–3666 (1975). URL https://doi.org/10.1021%2Fja00846a016.

[124] Wölfle, T., Görling, A. & Hieringer, W. Conformational flexibility of metalloporphyrins studied by density-functional calculations. *Physical Chemistry Chemical Physics* **10**, 5739 (2008). URL https://doi.org/10.1039%2Fb800566b.

[125] Endlich, M. *et al.* Phthalocyanine adsorption to graphene on ir(111): Evidence for decoupling from vibrational spectroscopy. *The Journal of Chemical Physics* **141**, 184308 (2014). URL https://doi.org/10.1063%2F1.4901283.

[126] Sedona, F. *et al.* Tuning the catalytic activity of ag(110)-supported fe phthalocyanine in the oxygen reduction reaction. *Nature Materials* **11**, 970–977 (2012). URL https://doi.org/10.1038%2Fnmat3453.

[127] Mao, J. *et al.* Tunability of supramolecular kagome lattices of magnetic phthalocyanines using graphene-based moirè patterns as templates. *Journal of the American Chemical Society* **131**, 14136–14137 (2009). URL https://doi.org/10.1021%2Fja904907z.

[128] Scardamaglia, M. *et al.* Energetics and hierarchical interactions of metal–phthalocyanines adsorbed on graphene/ir(111). *Langmuir* **29**, 10440–10447 (2013). URL https://doi.org/10.1021%2Fla401850v.

[129] Zamborlini, G. *et al.* Publisher correction: Multi-orbital charge transfer at highly oriented organic/metal interfaces. *Nature Communications* **8** (2017). URL https://doi.org/10.1038%2Fs41467-017-01480-w.

[130] Hooley, R. J. Taking on the turnover challenge. *Nature Chemistry* **8**, 202–204 (2016). URL https://doi.org/10.1038%2Fnchem.2461.

[131] Moore, S. J. *et al.* Elucidation of the biosynthesis of the methane catalyst coenzyme f430. *Nature* **543**, 78–82 (2017). URL https://doi.org/10.1038%2Fnature21427.

[132] Meunier, B. Metalloporphyrins as versatile catalysts for oxidation reactions and oxidative DNA cleavage. *Chemical Reviews* **92**, 1411–1456 (1992). URL https://doi.org/10.1021%2Fcr00014a008.

[133] Hino, T. *et al.* Structural basis of biological n2o generation by bacterial nitric oxide reductase. *Science* **330**, 1666–1670 (2010). URL https://doi.org/10.1126%2Fscience.1195591.

[134] Wright, A. M. & Hayton, T. W. Understanding the role of hyponitrite in nitric oxide reduction. *Inorganic Chemistry* **54**, 9330–9341 (2015). URL https://doi.org/10.1021%2Facs.inorgchem.5b00516.

[135] Brown, W. A., Gardner, P. & King, D. A. Very low temperature surface reaction: N2o formation from NO dimers at 70 to 90 k on ag{111}. *The Journal of Physical Chemistry* **99**, 7065–7074 (1995). URL https://doi.org/10.1021%2Fj100018a045.

[136] Brown, W. A. & King, D. A. NO chemisorption and reactions on metal surfaces: a new perspective. *The Journal of Physical Chemistry B* **104**, 2578–2595 (2000). URL https://doi.org/10.1021%2Fjp9930907.

[137] Seufert, K. *et al.* Cis-dicarbonyl binding at cobalt and iron porphyrins with saddle-shape conformation. *Nature Chemistry* **3**, 114–119 (2011). URL https://doi.org/10.1038%2Fnchem.956.

[138] Seufert, K., Auwärter, W. & Barth, J. V. Discriminative response of surface-confined metalloporphyrin molecules to carbon and nitrogen monoxide. *Journal of the American Chemical Society* **132**, 18141–18146 (2010). URL https://doi.org/10.1021%2Fja1054884.

[139] Wäckerlin, C. *et al.* Controlling spins in adsorbed molecules by a chemical switch. *Nature Communications* **1**, 1–7 (2010). URL https://doi.org/10.1038%2Fncomms1057.

[140] Kim, H. *et al.* Visualizing tilted binding and precession of diatomic NO adsorbed to co-porphyrin on au(111) using scanning tunneling microscopy. *Chem. Sci.* **5**, 2224–2229 (2014). URL https://doi.org/10.1039%2Fc3sc52004h.

[141] Goubeaud, M., Schreiner, G. & Thauer, R. K. Purified methyl-coenzyme-m reductase is activated when the enzyme-bound coenzyme f430 is reduced to the nickel(i) oxidation state by titanium(III) citrate. *European Journal of Biochemistry* **243**, 110–114 (1997). URL https://doi.org/10.1111%2Fj.1432-1033.1997.00110.x.

[142] Santo, G. D. *et al.* Conformational adaptation and electronic structure of 2h-tetraphenylporphyrin on ag(111) during fe metalation. *The Journal of Physical Chemistry C* **115**, 4155–4162 (2011). URL https://doi.org/10.1021%2Fjp111151n.

[143] Diller, K. *et al.* Self-metalation of 2h-tetraphenylporphyrin on cu(111): An x-ray spectroscopy study. *The Journal of Chemical Physics* **136**, 014705 (2012). URL https://doi.org/10.1063%2F1.3674165.

[144] CHEN, B. *et al.* XPS and TPD study of NO interaction with cu(111): Role of different oxygen species. *Chinese Journal of Catalysis* **34**, 964–972 (2013). URL https://doi.org/10.1016%2Fs1872-2067%2812%2960585-3.

[145] Matloob, M. H. & Roberts, M. W. Electron spectroscopic study of nitrogen species adsorbed on copper. *Journal of the Chemical Society, Faraday Transactions 1: Physical Chemistry in Condensed Phases* **73**, 1393 (1977). URL https://doi.org/10.1039%2Ff19777301393.

[146] Johnson, D. W., Matloob, M. H. & Roberts, M. W. Study of the interaction of nitric oxide with cu(100) and cu(111) surfaces using low energy electron diffraction and electron spectroscopy. *Journal of the Chemical Society, Faraday Transactions 1: Physical Chemistry in Condensed Phases* **75**, 2143 (1979). URL https://doi.org/10.1039%2Ff19797502143.

[147] Rush, T. S. *et al.* Computational modeling of metalloporphyrin structure and vibrational spectra: porphyrin ruffling in NiTPP. *The Journal of Physical Chemistry B* **104**, 5020–5034 (2000). URL https://doi.org/10.1021%2Fjp000266s.

[148] Li, X. Y., Czernuszewicz, R. S., Kincaid, J. R., Su, Y. O. & Spiro, T. G. Consistent porphyrin force field. 1. normal-mode analysis for nickel porphine and nickel tetraphenylporphine from resonance raman and infrared spectra and isotope shifts. *The Journal of Physical Chemistry* **94**, 31–47 (1990). URL https://doi.org/10.1021%2Fj100364a007.

[149] Scudiero, L., Barlow, D. E. & Hipps, K. W. Physical properties and metal ion specific scanning tunneling microscopy images of metal(II) tetraphenylporphyrins deposited from vapor onto gold (111). *The Journal of Physical Chemistry B* **104**, 11899–11905 (2000). URL https://doi.org/10.1021%2Fjp002292w.

[150] Zamborlini, G. *et al. In preparation* .

[151] Daskalakis, V., Ohta, T., Kitagawa, T. & Varotsis, C. Structure and properties of the catalytic site of nitric oxide reductase at ambient temperature. *Biochimica et Biophysica Acta (BBA) - Bioenergetics* **1847**, 1240–1244 (2015). URL https://doi.org/10.1016%2Fj.bbabio.2015.06.014.

[152] Berto, T. C. *et al.* Characterization of the bridged hyponitrite complex {[fe(OEP)]2(μ-n2o2)}: Reactivity of hyponitrite complexes and biological relevance. *Inorganic Chemistry* **53**, 6398–6414 (2014). URL https://doi.org/10.1021%2Fic5002573.

[153] Yi, J., Campbell, A. L. & Richter-Addo, G. B. Nitric oxide coupling to generate n 2 o promoted by a single-heme system as examined by density functional theory. *Nitric Oxide* **60**, 69–75 (2016). URL https://doi.org/10.1016%2Fj.niox.2016.09.004.

[154] Varotsis, C., Ohta, T., Kitagawa, T., Soulimane, T. & Pinakoulaki, E. The structure of the hyponitrite species in a heme fe-cu binuclear center. *Angewandte Chemie* **119**, 2260–2264 (2007). URL https://doi.org/10.1002%2Fange.200602963.

[155] McCleverty, J. A. Chemistry of nitric oxide relevant to biology. *Chemical Reviews* **104**, 403–418 (2004). URL https://doi.org/10.1021%2Fcr020623q.

[156] Tian, C. & Shen, Y. Recent progress on sum-frequency spectroscopy. *Surface Science Reports* **69**, 105–131 (2014). URL https://doi.org/10.1016%2Fj.surfrep.2014.05.001.

[157] Weiss, J. N. The hill equation revisited: uses and misuses. *The FASEB Journal* **11**, 835–841 (1997). URL https://doi.org/10.1096%2Ffasebj.11.11.9285481.

[158] Reed, D. A. *et al.* A spin transition mechanism for cooperative adsorption in metal–organic frameworks. *Nature* (2017). URL https://doi.org/10.1038%2Fnature23674.

[159] Scholes, G. D. & Rumbles, G. Excitons in nanoscale systems. *Nature Materials* **5**, 683–696 (2006). URL https://doi.org/10.1038%2Fnmat1710.

[160] Bakulin, A. A. *et al.* Mode-selective vibrational modulation of charge transport in organic electronic devices. *Nature Communications* **6** (2015). URL https://doi.org/10.1038%2Fncomms8880.

[161] Bakulin, A. A. *et al.* Real-time observation of multiexcitonic states in ultrafast singlet fission using coherent 2d electronic spectroscopy. *Nature Chemistry* **8**, 16–23 (2015). URL https://doi.org/10.1038%2Fnchem.2371.

[162] Jortner, J. Electronic relaxation in large molecules. In *Radiationless Processes*, 103–156 (Springer US, 1980). URL https://doi.org/10.1007%2F978-1-4613-3174-2_4.

[163] Gütlich, P., Hauser, A. & Spiering, H. Thermal and optical switching of iron(II) complexes. *Angewandte Chemie International Edition in English* **33**, 2024–2054 (1994). URL https://doi.org/10.1002%2Fanie.199420241.

[164] Gütlich, P., Gaspar, A. B. & Garcia, Y. Spin state switching in iron coordination compounds. *Beilstein Journal of Organic Chemistry* **9**, 342–391 (2013). URL https://doi.org/10.3762%2Fbjoc.9.39.

[165] Gütlich, P., Garcia, Y. & Goodwin, H. A. Spin crossover phenomena in fe(ii) complexes. *Chemical Society Reviews* **29**, 419–427 (2000). URL https://doi.org/10.1039%2Fb0035041.

[166] Inyushin, M. *et al.* Superparamagnetic properties of hemozoin. *Scientific Reports* **6** (2016). URL https://doi.org/10.1038%2Fsrep26212.

[167] Smith, M. B. & Michl, J. Singlet fission. *Chemical Reviews* **110**, 6891–6936 (2010). URL https://doi.org/10.1021%2Fcr1002613.

[168] Miyata, K. *et al.* Coherent singlet fission activated by symmetry breaking. *Nature Chemistry* **9**, 983–989 (2017). URL https://doi.org/10.1038%2Fnchem.2784.

[169] Wäckerlin, C. *et al.* Two-dimensional supramolecular electron spin arrays. *Advanced Materials* **25**, 2404–2408 (2013). URL https://doi.org/10.1002%2Fadma.201204274.

[170] Scardamaglia, M. *et al.* Graphene-induced substrate decoupling and ideal doping of a self-assembled iron-phthalocyanine single layer. *The Journal of Physical Chemistry C* **117**, 3019–3027 (2013). URL https://doi.org/10.1021%2Fjp308861b.

[171] Scardamaglia, M. *et al.* Metal-phthalocyanine array on the moiré pattern of a graphene sheet. *Journal of Nanoparticle Research* **13**, 6013–6020 (2011). URL https://doi.org/10.1007%2Fs11051-011-0384-1.

[172] Siegert, B., Donarini, A. & Grifoni, M. Nonequilibrium spin crossover in copper phthalocyanine. *Physical Review B* **93** (2016). URL https://doi.org/10.1103%2Fphysrevb.93.121406.

[173] Swart, I., Sonnleitner, T. & Repp, J. Charge state control of molecules reveals modification of the tunneling barrier with intramolecular contrast. *Nano Letters* **11**, 1580–1584 (2011). URL https://doi.org/10.1021%2Fnl104452x.

[174] Qiu, X. H., Nazin, G. V. & Ho, W. Vibronic states in single molecule electron transport. *Physical Review Letters* **92** (2004). URL https://doi.org/10.1103%2Fphysrevlett.92.206102.

[175] Stróżecka, A., Soriano, M., Pascual, J. I. & Palacios, J. J. Reversible change of the spin state in a manganese phthalocyanine by coordination of CO molecule. *Physical Review Letters* **109** (2012). URL https://doi.org/10.1103%2Fphysrevlett.109.147202.

[176] Kuch, W. & Bernien, M. Controlling the magnetism of adsorbed metal–organic molecules. *Journal of Physics: Condensed Matter* **29**, 023001 (2016). URL https://doi.org/10.1088%2F0953-8984%2F29%2F2%2F023001.

[177] Hämäläinen, S. K. *et al.* Self-assembly of cobalt-phthalocyanine molecules on epitaxial graphene on ir(111). *The Journal of Physical Chemistry C* **116**, 20433–20437 (2012). URL https://doi.org/10.1021%2Fjp306439h.

[178] Podda, N. *et al.* Experimental and theoretical investigation of the restructuring process induced by CO at near ambient pressure: Pt nanoclusters on graphene/ir(111). *ACS Nano* **11**, 1041–1053 (2016). URL https://doi.org/10.1021%2Facsnano.6b07876.

[179] Isvoranu, C. *et al.* Tuning the spin state of iron phthalocyanine by ligand adsorption. *Journal of Physics: Condensed Matter* **22**, 472002 (2010). URL https://doi.org/10.1088%2F0953-8984%2F22%2F47%2F472002.

[180] Silvernail, N. J., Roth, A., Schulz, C. E., Noll, B. C. & Scheidt, W. R. Heme carbonyls: environmental effects on ν c-o and fe-c/c-o bond length correlations. *Journal of the American Chemical Society* **127**, 14422–14433 (2005). URL https://doi.org/10.1021%2Fja053148x.

[181] Linder, D. P. *et al.* The diagnostic vibrational signature of pentacoordination in heme carbonyls. *Journal of the American Chemical Society* **136**, 9818–9821 (2014). URL https://doi.org/10.1021%2Fja503191z.

[182] Chan, W.-L. *et al.* Observing the multiexciton state in singlet fission and ensuing ultrafast multielectron transfer. *Science* **334**, 1541–1545 (2011). URL https://doi.org/10.1126%2Fscience.1213986.

[183] Altenburg, S. J., Lattelais, M., Wang, B., Bocquet, M.-L. & Berndt, R. Reaction of phthalocyanines with graphene on ir(111). *Journal of the American Chemical Society* **137**, 9452–9458 (2015). URL https://doi.org/10.1021%2Fjacs.5b05558.

[184] Rao, S. V. & Rao, D. N. Excited state dynamics in phthalocyanines studied using degenerate four wave mixing with incoherent light. *Journal of Porphyrins and Phthalocyanines* **06**, 233–237 (2002). URL https://doi.org/10.1142%2Fs1088424602000270.

[185] Ma, G., He, J., Kang, C.-H. & Tang, S.-H. Excited state dynamics studies of iron(III) phthalocyanine using femtosecond pump–probe techniques. *Chemical Physics Letters* **370**, 293–299 (2003). URL https://doi.org/10.1016%2Fs0009-2614%2803%2900130-1.

[186] Noomnarm, U. & Clegg, R. M. Fluorescence lifetimes: fundamentals and interpretations. *Photosynthesis Research* **101**, 181–194 (2009). URL https://doi.org/10.1007%2Fs11120-009-9457-8.

[187] Shen, T., li Yuan, Z. & jun Xu, H. Fluorescent properties of phthalocyanines. *Dyes and Pigments* **11**, 77–80 (1989). URL https://doi.org/10.1016%2F0143-7208%2889%2985027-2.

[188] Vincett, P. S., Voigt, E. M. & Rieckhoff, K. E. Phosphorescence and fluorescence of phthalocyanines. *The Journal of Chemical Physics* **55**, 4131–4140 (1971). URL https://doi.org/10.1063%2F1.1676714.

[189] Tritsch, J. R., Chan, W.-L., Wu, X., Monahan, N. R. & Zhu, X.-Y. Harvesting singlet fission for solar energy conversion via triplet energy transfer. *Nature Communications* **4** (2013). URL https://doi.org/10.1038%2Fncomms3679.

[190] Chan, W.-L., Ligges, M. & Zhu, X.-Y. The energy barrier in singlet fission can be overcome through coherent coupling and entropic gain. *Nature Chemistry* **4**, 840–845 (2012). URL https://doi.org/10.1038%2Fnchem.1436.

[191] Monahan, N. R. *et al.* Dynamics of the triplet-pair state reveals the likely coexistence of coherent and incoherent singlet fission in crystalline hexacene. *Nature Chemistry* **9**, 341–346 (2016). URL https://doi.org/10.1038%2Fnchem.2665.

[192] Busby, E. *et al.* A design strategy for intramolecular singlet fission mediated by charge-transfer states in donor–acceptor organic materials. *Nature Materials* **14**, 426–433 (2015). URL https://doi.org/10.1038%2Fnmat4175.

[193] Joshi, S. *et al.* Control of molecular organization and energy level alignment by an electronically nanopatterned boron nitride template. *ACS Nano* **8**, 430–442 (2013). URL https://doi.org/10.1021%2Fnn406024m.

[194] Järvinen, P., Hämäläinen, S. K., Ijäs, M., Harju, A. & Liljeroth, P. Self-assembly and orbital imaging of metal phthalocyanines on a graphene model surface. *The Journal of Physical Chemistry C* **118**, 13320–13325 (2014). URL https://doi.org/10.1021%2Fjp504813v.

[195] Cheng, Z. H. *et al.* Adsorption behavior of iron phthalocyanine on au(111) surface at submonolayer coverage. *The Journal of Physical Chemistry C* **111**, 9240–9244 (2007). URL https://doi.org/10.1021%2Fjp0703881.

[196] Snezhkova, O. *et al.* Iron phthalocyanine on cu(111): Coverage-dependent assembly and symmetry breaking, temperature-induced homocoupling, and modification of the adsorbate-surface interaction by annealing. *The Journal of Chemical Physics* **144**, 094702 (2016). URL https://doi.org/10.1063%2F1.4942121.

[197] Bazarnik, M., Brede, J., Decker, R. & Wiesendanger, R. Tailoring molecular self-assembly of magnetic phthalocyanine molecules on fe- and co-intercalated graphene. *ACS Nano* **7**, 11341–11349 (2013). URL https://doi.org/10.1021%2Fnn405172q.

[198] Wiltner, A. *et al.* Growth of copper and vanadium on a thin al2o3-film on ni3al(111). *Thin Solid Films* **400**, 71–75 (2001). URL https://doi.org/10.1016%2Fs0040-6090%2801%2901453-5.

[199] Olmos-Asar, J. A., Vesselli, E., Baldereschi, A. & Peressi, M. Towards optimal seeding for the synthesis of ordered nanoparticle arrays on alumina/ni3al(111). *Physical Chemistry Chemical Physics* **17**, 28154–28161 (2015). URL https://doi.org/10.1039%2Fc5cp00304k.

[200] Olmos-Asar, J. A., Vesselli, E., Baldereschi, A. & Peressi, M. Self-seeded nucleation of cu nanoclusters on al2o3/ni3al(111): an ab initio investigation. *Phys. Chem. Chem. Phys.* **16**, 23134–23142 (2014). URL https://doi.org/10.1039%2Fc4cp03271c.

[201] Vesselli, E., Baraldi, A., Lizzit, S. & Comelli, G. Large interlayer relaxation at a metal-oxide interface: The case of a supported ultrathin alumina film. *Physical Review Letters* **105** (2010). URL https://doi.org/10.1103%2Fphysrevlett.105.046102.

[202] Degen, S. *et al.* Determination of the coincidence lattice of an ultra thin al2o3 film on ni3al(111). *Surface Science* **576**, L57–L64 (2005). URL https://doi.org/10.1016%2Fj.susc.2004.12.020.

[203] Schmid, M. *et al.* Nanotemplate with holes: Ultrathin alumina onNi3al(111). *Physical Review Letters* **99** (2007). URL https://doi.org/10.1103%2Fphysrevlett.99.196104.

[204] Moors, M. *et al.* Scanning tunneling microscopy and spectroscopy investigations of copper phthalocyanine adsorbed on al2o3/ni3al(111). *Applied Surface Science* **254**, 4251–4257 (2008). URL https://doi.org/10.1016%2Fj.apsusc.2008.01.029.

[205] Becker, C. *et al.* Al 2 o 3 -films on ni 3 al(111): a template for nanostructured cluster growth. *New Journal of Physics* **4**, 75 (2002). URL http://stacks.iop.org/1367-2630/4/i=1/a=375.

[206] Corva, M. *et al.* Vibrational fingerprint of localized excitons in a 2d metalorganic crystal. *submitted* .

[207] Néel, N., Lattelais, M., Bocquet, M.-L. & Kröger, J. Depopulation of single-phthalocyanine molecular orbitals upon pyrrolic-hydrogen abstraction on graphene. *ACS Nano* **10**, 2010–2016 (2016). URL https://doi.org/10.1021%2Facsnano.5b06153.

[208] Åhlund, J. *et al.* The electronic structure of iron phthalocyanine probed by photoelectron and x-ray absorption spectroscopies and density functional theory calculations. *The Journal of Chemical Physics* **125**, 034709 (2006). URL https://doi.org/10.1063%2F1.2212404.

[209] Weilach, C., Spiel, C., Föttinger, K. & Rupprechter, G. Carbonate formation on al2o3 thin film model catalyst supports. *Surface Science* **605**, 1503–1509 (2011). URL https://doi.org/10.1016%2Fj.susc.2011.05.025.

[210] Wang, W., Wang, S., Ma, X. & Gong, J. Recent advances in catalytic hydrogenation of carbon dioxide. *Chemical Society Reviews* **40**, 3703 (2011). URL https://doi.org/10.1039%2Fc1cs15008a.

[211] Centi, G. & Perathoner, S. Opportunities and prospects in the chemical recycling of carbon dioxide to fuels. *Catalysis Today* **148**, 191–205 (2009). URL https://doi.org/10.1016%2Fj.cattod.2009.07.075.

[212] Sakakura, T., Choi, J.-C. & Yasuda, H. Transformation of carbon dioxide. *Chemical Reviews* **107**, 2365–2387 (2007). URL https://doi.org/10.1021%2Fcr068357u.

[213] Federsel, C., Jackstell, R. & Beller, M. State-of-the-art catalysts for hydrogenation of carbon dioxide. *Angewandte Chemie International Edition* **49**, 6254–6257 (2010). URL https://doi.org/10.1002%2Fanie.201000533.

[214] Dri, C. *et al.* Imaging and characterization of activatedCO2species on ni(110). *Physical Review B* **82** (2010). URL https://doi.org/10.1103%2Fphysrevb.82.165403.

[215] Monachino, E. *et al.* Reactivity of carbon dioxide on nickel: Role of CO in the competing interplay between oxygen and graphene. *The Journal of Physical Chemistry Letters* **5**, 1929–1934 (2014). URL https://doi.org/10.1021%2Fjz5007675.

[216] Vesselli, E. *et al.* Carbon dioxide hydrogenation on ni(110). *Journal of the American Chemical Society* **130**, 11417–11422 (2008). URL https://doi.org/10.1021%2Fja802554g.

[217] Song, C. Global challenges and strategies for control, conversion and utilization of CO2 for sustainable development involving energy, catalysis, adsorption and chemical processing. *Catalysis Today* **115**, 2–32 (2006). URL https://doi.org/10.1016%2Fj.cattod.2006.02.029.

[218] Taifan, W., Boily, J.-F. & Baltrusaitis, J. Surface chemistry of carbon dioxide revisited. *Surface Science Reports* **71**, 595–671 (2016). URL https://doi.org/10.1016%2Fj.surfrep.2016.09.001.

[219] deB Darwent, B. Bond dissociation energies in simple molecules. Tech. Rep. (1970). URL https://doi.org/10.6028%2Fnbs.nsrds.31.

[220] Ding, X. *et al.* Interaction of carbon dioxide with ni(110): A combined experimental and theoretical study. *Phys. Rev. B* **76**, 195425 (2007). URL https://link.aps.org/doi/10.1103/PhysRevB.76.195425.

[221] Doukov, T. I. A ni-fe-cu center in a bifunctional carbon monoxide dehydrogenase/acetyl-CoA synthase. *Science* **298**, 567–572 (2002). URL https://doi.org/10.1126%2Fscience.1075843.

[222] Dydio, P. *et al.* An artificial metalloenzyme with the kinetics of native enzymes. *Science* **354**, 102–106 (2016). URL https://doi.org/10.1126%2Fscience.aah4427.

[223] Wang, Z., Zhao, J. & Cai, Q. CO2 electroreduction performance of a single transition metal atom supported on porphyrin-like graphene: a computational study. *Physical Chemistry Chemical Physics* **19**, 23113–23121 (2017). URL https://doi.org/10.1039%2Fc7cp04299j.

[224] Trickett, C. A. *et al.* The chemistry of metal–organic frameworks for CO2 capture, regeneration and conversion. *Nature Reviews Materials* **2**, 17045 (2017). URL https://doi.org/10.1038%2Fnatrevmats.2017.45.

[225] Novoselov, K. S., Mishchenko, A., Carvalho, A. & Neto, A. H. C. 2d materials and van der waals heterostructures. *Science* **353**, aac9439 (2016). URL https://doi.org/10.1126%2Fscience.aac9439.

[226] Liu, Y. *et al.* Chemical adsorption enhanced CO2 capture and photoreduction over a copper porphyrin based metal organic framework. *ACS Applied Materials & Interfaces* **5**, 7654–7658 (2013). URL https://doi.org/10.1021%2Fam4019675.

[227] Larciprete, R. *et al.* Oxygen switching of the epitaxial graphene–metal interaction. *ACS Nano* **6**, 9551–9558 (2012). URL https://doi.org/10.1021%2Fnn302729j.

[228] Schulte, K., Vinogradov, N., Ng, M., Mårtensson, N. & Preobrajenski, A. Bandgap formation in graphene on ir(111) through oxidation. *Applied Surface Science* **267**, 74–76 (2013). URL https://doi.org/10.1016%2Fj.apsusc.2012.07.122.

[229] Vinogradov, N. A. *et al.* Impact of atomic oxygen on the structure of graphene formed on ir(111) and pt(111). *The Journal of Physical Chemistry C* **115**, 9568–9577 (2011). URL https://doi.org/10.1021%2Fjp111962k.

[230] Larciprete, R. *et al.* Dual path mechanism in the thermal reduction of graphene oxide. *Journal of the American Chemical Society* **133**, 17315–17321 (2011). URL https://doi.org/10.1021%2Fja205168x.

[231] Barinov, A. *et al.* Initial stages of oxidation on graphitic surfaces: Photoemission study and density functional theory calculations. *The Journal of Physical Chemistry C* **113**, 9009–9013 (2009). URL https://doi.org/10.1021%2Fjp902051d.

[232] Lambert, A. G., Davies, P. B. & Neivandt, D. J. Implementing the theory of sum frequency generation vibrational spectroscopy: A tutorial review. *Applied Spectroscopy Reviews* **40**, 103–145 (2005). URL https://doi.org/10.1081%2Fasr-200038326.

[233] Tackley, D. R., Dent, G. & Smith, W. E. Phthalocyanines: structure and vibrations. *Physical Chemistry Chemical Physics* **3**, 1419–1426 (2001). URL https://doi.org/10.1039%2Fb007763l.

[234] Ulstrup, S. *et al.* Manifestation of nonlocal electron-electron interaction in graphene. *Physical Review B* **94** (2016). URL https://doi.org/10.1103%2Fphysrevb.94.081403.

[235] Vesselli, E. *et al.* Hydrogen-assisted transformation of CO2 on nickel: The role of formate and carbon monoxide. *The Journal of Physical Chemistry Letters* **1**, 402–406 (2009). URL https://doi.org/10.1021%2Fjz900221c.

[236] Hill, A. V. The combinations of haemoglobin with oxygen and carbon monoxide, and the effects of acid and carbon dioxide. *Biochemical Journal* **15**, 577–586 (1921). URL https://doi.org/10.1042%2Fbj0150577.

[237] Stefan, M. I. & Novère, N. L. Cooperative binding. *PLoS Computational Biology* **9**, e1003106 (2013). URL https://doi.org/10.1371%2Fjournal.pcbi.1003106.

[238] Boyd, R. & Prato, D. *Nonlinear Optics*. Nonlinear Optics Series (Elsevier Science, 2008). URL https://books.google.it/books?id=uoRUi1Yb7ooC.

[239] EKSPLA. *SFG Spectrometer: Technical Description and User's Manual* (2013).

[240] Rupprechter, G. Sum frequency generation and polarization–modulation infrared reflection absorption spectroscopy of functioning model catalysts from ultrahigh vacuum to ambient pressure. In *Advances in Catalysis*, 133–263 (Elsevier, 2007). URL https://doi.org/10.1016%2Fs0360-0564%2806%2951004-1.

[241] Greenler, R. G. Infrared study of adsorbed molecules on metal surfaces by reflection techniques. *The Journal of Chemical Physics* **44**, 310–315 (1966). URL https://doi.org/10.1063%2F1.1726462.

[242] Reuter, K. & Scheffler, M. Composition, structure, and stability of RuO_2(110)as a function of oxygen pressure. *Physical Review B* **65** (2001). URL https://doi.org/10.1103%2Fphysrevb.65.035406.

[243] Lovas, F. J. & Tiemann, E. Microwave spectral tables i. diatomic molecules. *Journal of Physical and Chemical Reference Data* **3**, 609–770 (1974). URL https://doi.org/10.1063%2F1.3253146.